An analysis of the ZACube-2 mission operations

by

Gregory Jordan Naidoo

Dissertation submitted in partial fulfilment of the requirements for the degree

Master of Engineering: Satellite Systems and Applications

in the **Faculty of Engineering and the Built Environment**

at the **Cape Peninsula University of Technology**

Supervisor: Professor Robert R van Zyl

Technical Co-Supervisor: Dr Gunjan Gupta

Bellville Campus

DECLARATION

I, Gregory Jordan Naidoo, declare that the contents of this dissertation/thesis represent my own unaided work and that the dissertation/thesis has not previously been submitted for academic examination towards any qualification. Furthermore, it represents my own opinions and not necessarily those of the Cape Peninsula University of Technology.

14 March 2023

Signed **Date**

ABSTRACT

This research entails a comprehensive analysis of ZACube-2 operational mission data that addresses on-orbit operations. Mission operations evaluation criteria will be investigated, including all available telemetry, tracking, and command data sets at system and subsystem levels, the orbital dynamics of the system, and the ground segment operations.

An auxiliary analysis will investigate space weather and its effects on the mission, pertaining to how the system reacts in the presence of solar activity over specific areas of the Earth; therefore, giving an overall assessment of system robustness. From the data analysis that was completed on the various telemetry channels and subsequently the various resource budgets, there was no instance found in which any of the subsystems acted abnormally to an extent where the satellite was at risk for complete failure.

A comparison of the various calculated resource budgets such as the link, power and thermal in relation to the designed resource budgets proved, that the resource budgets the engineering team used to design ZACube-2 were more conservative in nature than the respective resource budgets that were calculated using the provided telemetry values.

The method in which the link budget was shown to be conservative was in comparing the UHF RSSI values for both ZACube-2 and the ground station. The UTRXC RSSI values aboard the satellite were compiled in a CDF graph which was then compared RSSI to the received power values conversion table found in the user manual.

The downlink UHF RSSI values of the ground station were compared to downlink values stated in the link budget to validate the link margin. This method proved that the link budget was conservative, however, while the received power values were larger than the link margin the disparity was far too large for it to be realistic. It was found that there was an inherent offset, in the range of 50 dB to 60 dB, due to the RSSI values recorded by the mission control software are not absolute but rather, comparative, or relative to the ADC’s full scale. To standardize to an absolute value, calibration of the ground station's UHF receiver with a signal generator both at the receiver and along the downlink path to the antenna would be required.

The power budget like the link budget was demonstrated to be conservative in addition to the calculation of the various power profiles, orbital parameters such as sunlit minimum, eclipse maximum, average power generated by the solar panels and orbital duration which was described in the said budget were calculated.

To calculate the orbital parameters, the battery charging and discharging telemetry was used to check when the satellite was in either sunlit minimum or eclipse maximum, respectively. This process was completed over a span of a day with the respective times averaged, the output of this process showed that the largest variance was approximately 2.613 minutes, which is within the margin of error of 3 minutes as this was the interval at which telemetry data was recorded.

With the confirmation of the orbital parameters, the various solar panel configurations had to be verified of which each configuration yields a different total power generated, which is dependent on the number of solar panels generating power. For ZACube-2 the minimum required power generated is 6.4717 Wh. This value is achieved when a single 3U solar panel is in view of the Sun. Two separate telemetry-based samples were calculated and both sample power calculations did not meet the minimum power requirement. However, this deficiency was attributed to several factors such as the interval at which the telemetry was recorded, the incorrect combination of current and/or voltage readings belonging to a specific pair of solar panels, if the telemetry recorded was during solar declination and if the Sun was in a state of solar maximum or solar minimum.

In total there are four power consumption profiles with each profile having a sun and eclipse variant specifying the minimum required power generated to satisfy the optimal operation of the satellite. The resultant power consumption profile calculations showed that the values described in the power budget were greater than the telemetry-based profiles with the smallest and largest discrepancy for the profiles “Downlink Eclipse” and “Payload Sun” being 1.6% and 53.8% respectively. Additionally, on average profiles that were reserved for when ZACube-2 was in sunlit minimum conditions used less power, with the smallest variation being 3.1%, than the profiles operated in eclipse maximum conditions, with the smallest variation being 1.6%.

Lastly, while it may not be a resource budget in comparison to the budget used to calculate the required link and power needed, the thermal aspect of the satellite proved to be within manufacturers and design constraints. While no formal thermal simulation was finalized for the satellite, using a combination of telemetry and thermal calculations based on techniques described by Fortescue, Swinerd and Stark (2011) and Gilmore (2002), the thermal environment was characterised

In regard to the thermal-related telemetry the various subsystems operated well within the respective thermal limits described by both the subsystems user manuals and aforementioned techniques manufacturer, implying that the passive thermal management techniques employed on ZACube-2 worked as desired. The hottest and coldest subsystems were the

HSTXC of 37.2°C and K-line imager of -15.1°C, respectively, with the imager having the largest thermal difference when comparing the maximum and minimum temperatures experienced.

Comparing these values to the maximum and minimum temperature limits from both methods resulted in the telemetry values demonstrating that the technique by Fortescue, Swinerd and Stark (2011) is more conservative than that described by Gilmore (2002), with the thermal range between the maximum and minimum temperature variation being smaller in the latter technique.

The budgets being conservative is a positive, demonstrating that the techniques used by the engineering team when designing the satellite and future satellites are viable, with some areas to improve. There were multiple occasions in which telemetry channels shared the same period in which no data was recorded, or outliers were present in the data set with these instances not being mutually exclusive with documented space weather events leading to the causes for lapses in the recorded telemetry data. Overall, these lapses were attributed to system issues rather than an external environmental matter.

In closing, while there is an opportunity to further improve and increase operational efficiency, ZACube-2 operated as intended without any major incident that resulted in the satellite being temporarily inoperable. The output of the research will provide an objective assessment of the operational performance of the system comprising space and ground segments against the mission design specifications and will compare as-designed features of the satellite with actual system performance.

Design improvements will be recommended for incorporation in the design cycle of future missions further improving the forthcoming satellites operational functionality as well as the engineering team design methodology.

Keywords: Telemetry, ZACube-2, Mission Operations, System Performance, Mission Analysis, Orbital Dynamics, South Africa Economic Exclusive Zone, MATLAB.

ACKNOWLEDGEMENTS

I wish to thank:

- Professor Robert R van Zyl, for providing direction in every step of the research process.
- Dr. Gunjan Gupta, for providing direction, providing insightful comments and suggestions.
- Dr. Morne Roman, with the provision and aid in the understanding of ZACube-2 telemetry data.
- Shane Martin, with the provision and help in the understanding of ZACube-2 telemetry data.
- Stephen Cupido with the provision and assistance in the understanding of ZACube-2 telemetry data.
- Sinamandla Maqina with the provision of telemetry, assistance in the understanding of the various ZACube-2 telemetry and subsystem operations.
- Leon Steenkamp with the provision and aid in the understanding of ZACube-2 telemetry data.
- Kanyisa Mtshemla with the provision and assistance in the understanding of ZACube-2 telemetry data.
- Etnard Louw with the provision and help in the understanding of ZACube-2 telemetry data.
- Johann Lochner in the verification and explanation of the mission control software operations.
- Nyameko Royi with helping in the understanding of the link budget and how it can be compared to telemetry.
- Donovan Cogan with the understanding of thermal aspect of modelling the satellite.
- Robert Daniels with the understanding of the different thermal equilibrium modelling techniques used for satellite design.
- Other members of F'SATI that have directly or indirectly influenced the shape of this work.
- Finally, and most importantly my parents and family for their continuous support through this arduous yet rewarding journey.

The financial assistance of the National Research Foundation towards this research is acknowledged. Opinions expressed in this thesis and the conclusions arrived at, are those of the author, and are not necessarily to be attributed to the National Research Foundation.

TABLE OF CONTENTS

LIST OF FIGURES

LIST OF TABLES

ABBREVIATIONS AND ACRONYMS

ADCS	- Attitude Determination and Control System
AIS	- Automatic Identification System
CME	- Coronal Mass Ejections
cm	- Centimetre
CDF	- Cumulative Density/Distribution Function
CEOS	- Committee on Earth Observation Satellites
CNES	- Centre National D'Etudes Spatiales (French Space Agency)
COTS	- Commercial Off-The-Shelf or Commercially Available Off-The-Shelf
CPU	- Central Processing Unit
CPUT	- Cape Peninsula University of Technology
dB	- Decibel
dBm/dBmW	- Decibel-milliwatt
DET	- Direct Energy Transfer
DoD	- Depth of Discharge
EKF	- Extended Kalman Filter
EPS	- Electronic Power System
ESA	- European Space Agency
EUV	- Extreme Ultraviolet
FPGA	- Field Programmable Gate Array
GCR	- Galactic Cosmic Rays
GHz	- Gigahertz
IADC	- Inter-Agency Space Debris Coordination Committee
JSON	- JavaScript Object Notation
kg	- Kilogram
LCL	- Latching Current Limiter
LEO	- Low Earth Orbit
MHz	- Mega Hertz
MCS	- Mission Control Software
mm	- Millimetre
NASA	- National Aeronautics and Space Administration
NDP	- National Development Plan
NIR	- Near-Infrared
NOAA	- North Oceanic and Atmosphere Administration
NORAD	- North American Aerospace Defence Command
OBC	- On-Board Computer
PA	- Power Amplifier
PDF	- Probability Density Function
PMAD	- Power Management and Distribution
PP	- Primary Payload
PPT	- Peak Power Trackers
R^2	- R-Square or Co-efficient of Determination
RAAN	- Right Ascension of Ascending Node
RF	- Radio Frequency
RMSE	- Root Mean Square Error

Rx	- Receive
SA	- Solar Array
SDR	- Software Defined Radio
SLA	- Service-Level Agreement
SMAD	- Space Mission Analysis and Design
SMPS	- Switched Mode Power Supply
STK	- System Tool Kit
STELA	- Semi-analytic Tool for End of Life Analysis
TEC	- Total Electron Content
TLE	- Two-Line Element
TT&C	- Telemetry, Tracking and Control
Tx	- Transmit
UI	- User Interface
UTC	- Co-ordinated Universal Time or Universal Time Co-ordinated
UX	- User Experience
VIS	- Visible
VDES	- VHF Data Exchange System
W	- Watt
Wh	- Watt-hour(s)

GLOSSARY

Terms/Acronyms/Abbreviations	Definition/Explanation
Apoapsis (Apogee)	The furthest distance between an orbiting object in relation to the central body that it is orbiting.
COTS (Commercially Off The Shelf)	Commercially available packaged solution(s).
EFK (Extended Kalman Filter) Estimator	Is an algorithm-based process that Is used to estimate the satellite orientation (roll, pitch, and yaw) attitude angle and angular rates.
Gray (Gy)	Unit of dosed ionized radiation.
Kp Index	An index of global geomagnetic activity with a rating of 0 being the lowest and a rating of 9 being the highest.
LCL (Latch-up Current Limiter)	A current limiter that is to prevent current overload between a power source and components.
NOAA (National Oceanic and Atmospheric Administration)	A regulatory body of the United States of America Department of Commerce which monitors and observes Earth's weather including space weather.
Periapsis (Perigee)	The shortest distance between an orbiting object about the central body that it is orbiting.
R^2/R-Squared	A measurement of how successful the data fits in accordance with the regression model. Where a value close to 1 show that the model accounts for all data variation.
RMSE (Root Mean Square Error)	A metric used to determine the deviation between the data and the model. Where a value close to 0 shows that the fit can be used for prediction.
RSSI (Received Signal Strength Indicator)	A measurement of the integrity of the received signal.
Turnkey	A complete and operational-ready product.
UTC (Universal Time Coordinated)	A worldwide adopted time standard.

CHAPTER ONE
INTRODUCTION

1.1 Introduction

The ZACube-2 mission is the second satellite developed in the Cape Peninsula University of Technology (CPUT) Satellite Programme, hosted by F'SATI (French South African Institute of Technology) with funding from the Department of Science and Innovation. The satellite is a 3-unit (3U) CubeSat and was launched in 2018 with the prime objective of providing sovereign maritime domain awareness services in support of Operation Phakisa, which is an initiative in support of the National Development Plan (Operation Phakisa, n.d.). As a secondary mission objective, a novel fire detection imager was also demonstrated.

The technology and mission roadmap of the CPUT Satellite Programme aims to continually support national imperatives, such as the National Development Plan. The immediate development is toward a constellation of satellites that deems /aims to complement and further develop the maritime communications services as demonstrated by ZACube-2. The mission, therefore, is of key strategic importance to the South African space industry as it serves as the baseline design for future missions and programmes.

To this end, it is imperative to evaluate the operations of the satellite against its primary mission objectives and to validate and improve the design approach that will be incorporated in future missions. By doing so, more effective, and reliable methods across the full design lifecycle of the mission can be adopted, contributing to the longevity of the South African space industry.

1.2 Research Statement

The research aims to analyse the mission operations of ZACube-2 which consists of telemetry relating to the daily operations of ZACube-2. The output of the analysis will be compared against the primary mission objectives to validate and improve the design approach to be used for future missions.

1.3 Research Questions

The research questions are as follows:

- How accurate were the resource budgets in comparison to the actual performance?

- Did the CubeSat's COTS or in-house manufactured subsystems operate within the designed limits?
- What was the cause of any outlying recorded subsystem performance parameters(s)?
- How well did the spacecraft bus and the respective subsystems function during the mission duration?
- What effect did space weather have on ZACube-2 operations?
- How well did the ground segment function and what improvements can be made?
- How accurate were the orbital simulations in contrast to actual orbital behaviour?

1.4 Key Research Objectives

The key research findings and/or deliverables are as follows:

- Analysis of on-orbit operations categorised as "commissioning," "early operations" and "nominal operations."
- Performance evaluation of the satellite bus and the respective subsystems.
- Investigation of orbital dynamic behaviour.
- Performance of the mass, power, thermal and communication budget in comparison to model estimation.
- Statistical analysis of operational mission data.
- Evaluation of existing ground segment operations.
- Investigation of the effects of space weather on the satellite and mission performance.

1.5 Methodology

With the copious amount of data that needs to be analysed, a structured approach needs to be implemented for the analysis of the mission. The process will be broken down into four distinctive steps.

1. Acquisition of both raw and simulation data.
2. Processing of data sets.
3. Statistical analysis of data.
4. Recommendations based on findings.

The data in question is that of the ZACube-2 telemetry data sets, for the period 1 January 2019 UTC to 28 July 2020 UTC. Telemetry data sets are available for the following subsystems:

- S-band transmitter (HSTX)

- UHF transceiver (UTRX)
- Attitude determination and control system (ADCS)
- Software defined radio (SDR) payload
- On-board K-line near-infrared imager
- Electrical power systems (EPS)
- X-band transmitter (XTX)
- On-board computer (OBC)

The values from the aforementioned data sets are to be processed and analysed using MathWorks MATLAB suite with various equations that are described in *CHAPTER 3: DATA ANALYTICS METHODOLOGY*. The deliverables that are not subject to mathematical modelling will be done through a literature review where the results can benefit the findings from the statistical modelling.

The table below lists all the telemetry channels with the respective designation that will be used in the analysis period.

Table 1.1: ZACube-2 Telemetry Channels

Telemetry Channel	Data Recorded	Unit	Designation	Description
ADCS	X-axis angular rate	°/s	ADCS_X_AR	Angular rate of X-axis
	Y-axis angular rate	°/s	ADCS_Y_AR	Angular rate of Y-axis
	Y-axis attitude angle	degree	ADCS_Y_AA	Attitude angle of Y-axis
	Z-axis attitude angle	degree	ADCS_Z_AA	Attitude angle of Z-axis
	Z-axis angular rate	°/s	ADCS_Z_AR	Angular rate of Z-axis
Battery	Board temperature	°C	BATT_MB_TEMP	The temperature of the battery motherboard
	Battery temperature 0	°C	BATT_TEMP_0	The temperature of the battery itself
	Battery temperature 1	°C	BATT_TEMP_1	The temperature of the battery itself
	Battery temperature 2	°C	BATT_TEMP_2	The temperature of the battery itself
	Reset count	Value	BATT_RESET	Number of battery resets
	Battery current	mA	BATT_CURRENT	The current output of the battery
	Battery current direction	Value	BATT_CURRENT_DIRECTION	Battery current direction
	Battery heater status 0	Value	BATT_HEATER_STATUS_0	If the battery heater is on/off
	Battery heater status 1	Value	BATT_HEATER_STATUS_1	If the battery heater is on/off
	Battery heater status 2	Value	BATT_HEATER_STATUS_2	If the battery heater is on/off
	Battery voltage	V	BATT_VOLTAGE	Battery output voltage value
	Brown out reset count	Value	BATT_BORC	The number of times a brown out has caused a reset
	Last error	Value	BATT_LAST_ERROR	Number of errors
	Status	Value	BATT_STATUS	If the battery is on/off
EPS	Bus current 0	mA	EPS_CURRENT_0	Bus current value
	Bus current 1	mA	EPS_CURRENT_1	Bus current value
	Bus current 2	mA	EPS_CURRENT_2	Bus current value
	Bus voltage 3	V	EPS_VOLTAGE	Bus voltage value
HSTX	Mode	Value	S-BAND_MODE	The mode of the S-band transmitter where 0=Sync 1= Data, 2= Test data, 3= SPI test, 4= DAC mode

	Enabled	State	S-BAND_ENABLED	If the S-band transmitter is on for transmission
	Battery current	mA	S-BAND_CURRENT	Current draw of the S-band transmitter
	Voltage	V	S-BAND_VOLTAGE	Voltage draw of the S-band transmitter
	Board temperature 0	°C	S-BAND_BOARD_TEMP_0	S-band motherboard temperature
	Board temperature 1	°C	S-BAND_BOARD_TEMP_1	S-band motherboard temperature
	Modulation	State	S-BAND_MODULATION	S-band modulation state
	Offset frequency	MHz	S-BAND_OFFSET_FREQUENCY	S-band offset frequency
	On time remaining	Seconds	S-BAND_TIME_ON	Time remaining for S-band operation
	Power amplifier current	mA	S-BAND_PA_CURRENT	Amplifier current reading
	Power amplifiers enable	State	S-BAND_PA_ENABLED	If the amplifier is on/off
	Power amplifier power	mW	S-BAND_PA_POWER	Power usage of amplifier
	Power amplifier temperature	°C	S-BAND_PA_TEMP	Amplifier temperature
	Power amplifier voltage	V	S-BAND_PA_VOLTAGE	Amplifier electric potential
K-Line Imager	Enabled	State	K-LINE_ENABLED	K-line imager is on/off
	On time remaining	Seconds	K-LINE_TIME_ON	Time remaining for K-line imager operation
OBC	Failsafe boot image	Value	OBC_BOOT_IMAGE	There are 2 OBC images. 1-primary and 2-failsafe
	MRAM non-correctable error count	Value	OBC_MRAM_COUNT_1	Error count of the MRAM 1
	MRAM non-correctable error count	Value	OBC_MRAM_COUNT_2	Error count of the MRAM 2
	Primary boot image	Value	OBC_PRIMARY_BOOT	If the primary boot image is active
SDR	Enabled	State	SDR_ENABLED	If the SDR has been enabled
	On time remaining	Seconds	SDR_TIME_ON	Time remaining for SDR operation
	SDR interface	State	SDR_INTERFACE_STATE	If the SDR interface has been enabled
	SDR interface delays 0	Seconds	SDR_INTERFACE_DELAY_0	Time of the SDR interface delay
	SDR interface delays 1	Seconds	SDR_INTERFACE_DELAY_1	Time of the SDR interface delay
	SDR interface delays 2	Seconds	SDR_INTERFACE_DELAY_2	Time of the SDR interface delay

	AIS buffer storage transfer size	Value	SDR_AIS_BUFFER_SIZE	Size of the transmitter buffer storage
Solar Array	Panel SA1A current	mA	SA_SA1A_CURRENT	Current generated by panel SA1A
	Panel SA1B current	mA	SA_SA1B_CURRENT	Current generated by panel SA1B
	Panel SA2A current	mA	SA_SA2A_CURRENT	Current generated by panel SA2A
	Panel SA2B current	mA	SA_SA2B_CURRENT	Current generated by panel SA2B
	Panel SA3A current	mA	SA_SA3A_CURRENT	Current generated by panel SA3A
	Panel SA3B current	mA	SA_SA3B_CURRENT	Current generated by panel SA3B
	Panels SA1A and SA1B voltage	V	SA_SA1_VOLTAGE	Combined voltage generated by panels SA1A and SA1B
	Panels SA2A and SA2B voltage	V	SA_SA2_VOLTAGE	Combined voltage generated by panels SA2A and SA2B
	Panels SA3A and SA3B voltage	V	SA_SA3_VOLTAGE	Combined voltage generated by panels SA3A and SA3B
Time	Time	Seconds	TIME_ON_0	Time since the satellite has been switched on
	Time 1	Seconds	TIME_ON_1	Time since the satellite has been switched on
Utility	HK16 time	Seconds	UTILITY_HK16_TIME	
	Uptime	Seconds	UTILITY_UPTIME	
XTX	Enabled	State	X-BAND_ENABLED	If the X-band transmitter has been enabled
	On time remaining	Seconds	X-BAND_TIME_ON	Time remaining for X-band operation
	RF control	State	X-BAND_RF_CONTROL	If RF control has been enabled

1.6 Delineation of Research

The research boundaries are as follows.

- Only data that has been recorded can be attained and compared; the cost of the satellite may have restricted the addition of certain sensors as it is either not necessary for the mission or the cost of the sensor does not justify its usage within the parameters of the mission.
- The temporal range and resolution of sets of telemetry vary.
- Telemetry data is specific to ZACube-2 and cannot be exchanged for data from another satellite.
- The investigation is limited to operational mission data and excludes a payload performance assessment.
- The research will only investigate the factors as stated in section *1.4 Key Research Deliverables.*

1.7 Significance of Research

ZACube-2 is a seminal mission used for both Earth observation and a demonstration of machine-to-machine communication in the form of automatic identification system (AIS) services. However, minimal validation of the platform exists as it is only the second mission developed at CPUT and the first 3U satellite.

Therefore, an evaluation of the operations of the satellite against its primary mission objectives is imperative, which will yield valuable data that can be used to increase the operational efficiency of the following missions. An additional aspect of the research significance relates to the pending development of a constellation of nanosatellites to complement and further develop the maritime communications services as demonstrated by ZACube-2.

The results from the evaluation period will both validate and improve future mission operations and the design approach, leading to a refinement of in-house manufactured CubeSats with an increase in mission reliability. This is especially critical due to the nature associated with the sustainable utilisation of space as a resource.

Hence, the overarching key strategic importance of the project is the contribution it makes to the emerging South African space industry as it will inform the baseline design and life cycle execution of future missions that will ultimately be in support of the national imperatives stated earlier.

CHAPTER TWO
LITERATURE REVIEW

This section deals with the multiple aspects that will aid in the analysis of the mission.

2.1 Various Types of Satellites

The first satellite, called “Sputnik”, was launched by the now-dissolved Soviet Union in 1957. The mission was the by-product of the space race. Since then, satellites have been an instrumental tool in both the understanding of the environment and its surrounding, i.e., remote sensing, but also the development of societal infrastructures, such as communications networks.

With a vast array of applications that modern satellites fulfil, distinct types of satellites come in a range of sizes. Classification of satellites’ size based on mass is as follows (Kulu, 2020):

- Large satellites: > 1000kg
- Medium: 500kg – 1000kg
- Small satellites: < 500kg

Small satellites are then further categorised by mass, resulting in the list below (Kulu, 2020):

- Minisatellites: 500kg – 100kg
- Microsatellites: 100kg – 10kg
- Nanosatellites: 10kg – 1kg
- Picosatellites: 1kg – 100g
- Femtosatellites: 100g – 10g
- Attosatellites: 10g – 1g
- Zeptosatellites: 1g – 0.1g

A popular example of a nanosatellite that has risen in popularity is the CubeSat. CubeSats are built to an industry-standard set of specifications (CubeSat Design Specification Rev. 13, 2015).

2.2 CubeSat Subsystems

There are multiple subsystems on board a CubeSat that contribute to the success of the mission objectives through supporting the payload. The payload is the defining feature that characterises the mission.

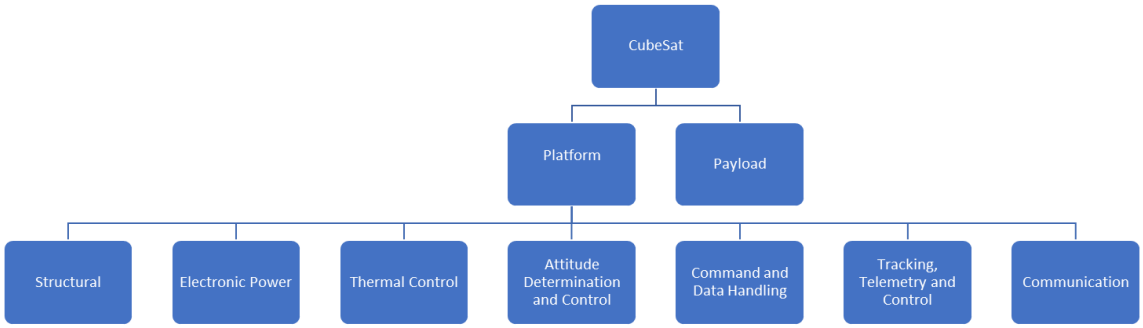

Figure 2.1: CubeSat Subsystems

(Addaim, Kherras and Bachir, 2010)

As can be seen from Figure 2.1 there are in total seven subsystems that contribute to the success of the mission objectives. However, as per the delineation of the research, the payload will not be considered. The subsystems are as follows:

- Structure – all components are affixed externally or internally to the structure.
- Electronic Power Supply– responsible for the generation, control, and distribution of power.
- Thermal Control – used to regulate the internal temperature of the satellite due to the heat produced by the subsystems.
- Attitude Determination and Control – commonly abbreviated to ADCS, this subsystem is responsible for making sure that the orientation and attitude of the satellite are correct, and if not, correct any deviations experienced.
- Command and Data Handling – this can be surmised as the brains of the entire satellite that as the name suggests, sends commands, and handles the flow of data from the other subsystems.
- Tracking, Telemetry and Control – this is a key subsystem that connects the satellite to the ground operations by providing a way to both oversee and control satellite operations.
- Communication – responsible for enabling communication between the CubeSat and ground segment.

2.2.1 Spacecraft Structure

The structural subsystem is the anchor point that the components are attached to both externally and/or internally. As previously mentioned in section *2.1 Various Types of Satellites,* CubeSats have standard dimensions for a singular module in the form of a cube where the outermost dimensions are 10 cm x 10 cm x 10 cm.

The images below show the standard dimensions for a CubeSat “U” or 1U as taken from the CubeSat design specification version 13 documents published by CubeSat.

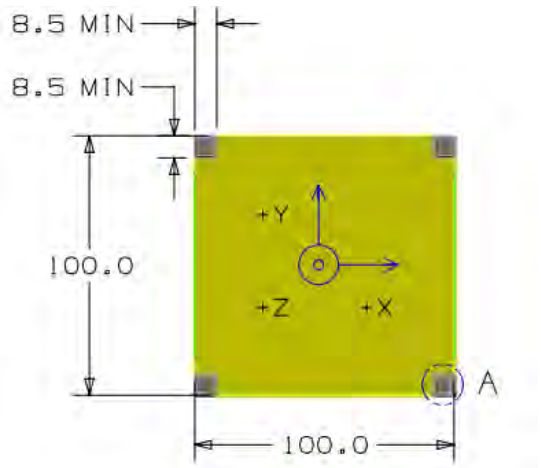

Figure 2.2: 1U CubeSat Design Dimension

(CubeSat Design Specification Rev. 13, 2015)

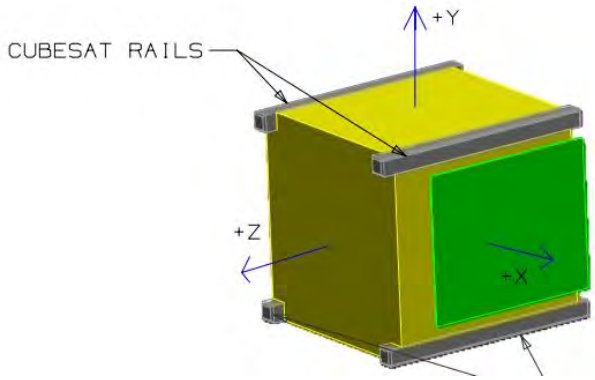

Figure 2.3: 3D View of 1U CubeSat

(CubeSat Design Specification Rev. 13, 2015)

As can be seen from both *Figure 2.2 1U CubeSat Design Dimension* and *Figure 2.3: 3D View of 1U CubeSat,* there are rails connected to the module itself. These are beneficial aspects of a standard modular design. Each “U” or unit can be stacked; hence, a CubeSat can have multiple modules resulting in designs such as 3U or 2U CubeSats, where the maximum mass is 4 kg and 2.66 kg, respectively, as detailed in the CubeSat design specification rev. 13 in section 3.2.13 and 3.2.12.

A mass and volume budget of ZACube-2, which is the summation of the aforementioned values for the required subsystems both operational and payload, was calculated showing that the total inclusive mass is 2906 g and the overall stack height of 266 mm. These values are following the CubeSat standards for a 3U as described in CubeSat design specifications.

2.2.2 Electronic Power Subsystem

The electronic power subsystem (EPS) is responsible for all aspects regarding the satellite’s power generation, storage, and distribution to the various satellite buses. The basic components of an EPS are as follows:

- Solar array
- Power storage
- Power management and distribution (PMAD) system

An EPS comprises of the following, in particular, the system used on ZACube-2 procured from Clyde Space as a COTS product:

- Solar arrays
- Battery charge regulator (BCR)
- Battery (BAT)
- Power conducting module (PCM)
- Power distribution module (PDM)
- Communication (Telemetry)
- Satellite buses which are 3.3V, 5V, 12V and the unregulated battery voltage.

The image below shows, graphically, the interrelationships between the various subsystems of the EPS:

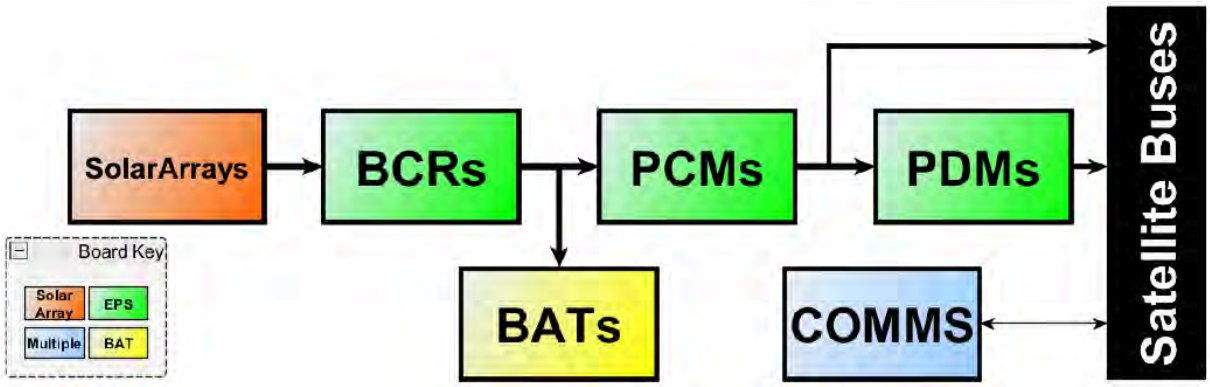

Figure 2.4: Electronic Power Subsystem Components

(Clyde Space, n.d.)

The following subsections delve into what each of these components does and the several types that can be used on a CubeSat.

2.2.2.1 Solar Array

Solar panels are used to capture photons emitted by the sun and generate electrical energy using semiconductors. Solar panels have constraints that limit their efficiency, such as effective surface area, mass, cost, solar intensity, and eclipse periods, to name a few.

There are two types of solar cells, namely, single, and multiple junction cells. These types of solar cells differ in the number of materials used, respectively. Single junction cells are low cost, and have low efficiency, and are used predominantly in terrestrial applications. Multiple junction solar cells are used more in extra-terrestrial applications; although costing much more than their counterpart, the price per performance justifies the usage on spacecraft.

The aerospace industry now employs triple-junction solar cells on spacecraft with efficiencies ranging from 28.3% to 30.7% (State Of The Art Small Spacecraft Technology, 2018). ZACube-2 makes use of five triple-junction cells that are body-mounted with each countering panel being paired resulting in a voltage being generated.

The image below is the solar array (SA) configuration for ZACube-2. From the image it can be seen that the nadir side of the ZACube-2 is designated as SA1B; this is due to telemetry being generated even though there is no solar panel fixed to the nadir face.

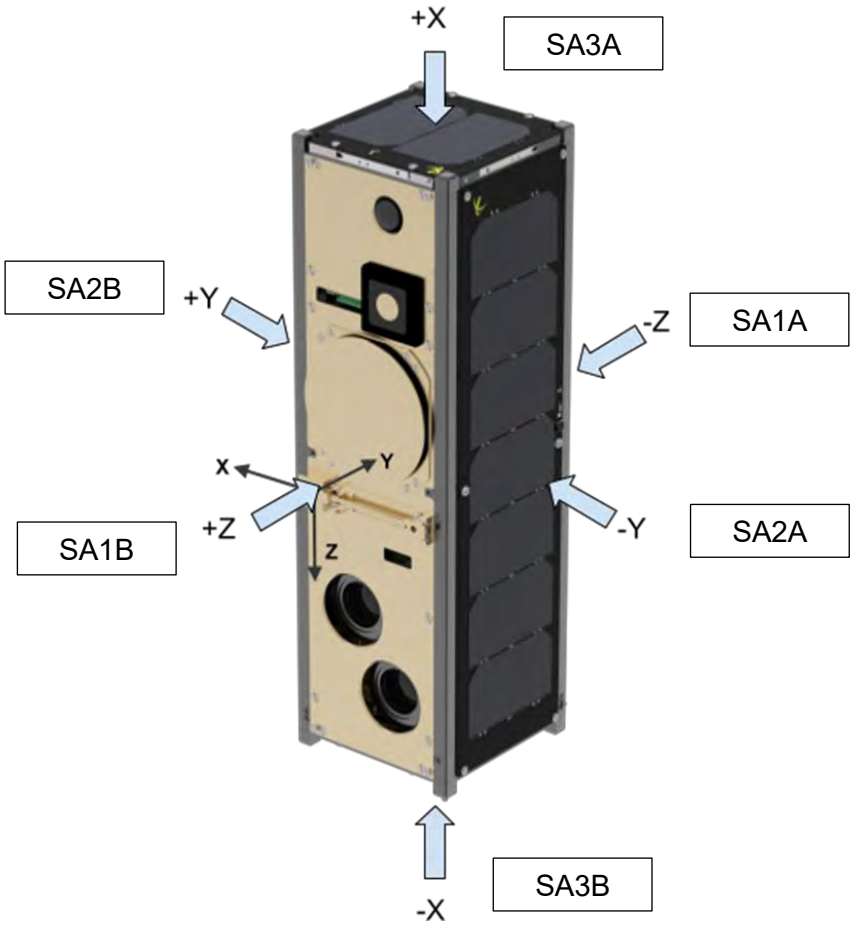

Figure 2.5: ZACube-2 Solar Array Configuration

The blue arrows represent the CubeSats cartesian co-ordinate reference frame, whereas the reference frame that can be seen at the +Z-axis is a fixed body frame in relation to the spherical co-ordinates.

2.2.2.2 Power Storage

Once power has been generated, there needs to be a method to store energy that can be used to either supplement direct power consumption from the solar panels if said panels are not operating at the maximum output or for usage during an eclipse when vital subsystem still needs the power to operate. Typically, there is a primary and secondary battery onboard to facilitate excess power production and ensure that there is enough power when the satellite is in eclipse.

The chemical composition of these batteries varies between both primary and secondary batteries due to the respective usages, with the former not being rechargeable and therefore used only for mission durations that last at a maximum of one week. It can also be used to supplement the satellite as it transitions from deployment to final orbit.

The latter, secondary batteries, are rechargeable and most commonly lithium-based due to their low weight and high energy density properties, although lithium can be used in primary batteries. However, other battery types, such as the ones seen in Figure 2.6, can be used in place of lithium-based batteries.

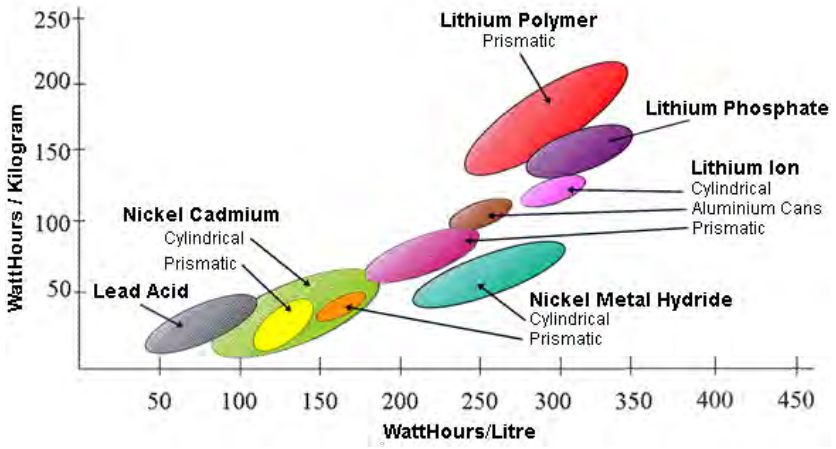

Figure 2.6: Energy Densities of Varies Secondary Batteries

(Wagner, 2006)

2.2.2.3 Power Management and Distribution (PMAD) System

Due to the sensitive nature of electronics onboard satellites, especially CubeSats, a direct link from either the solar panel or batteries to the various subsystem can be determinantal, leading to periods of the payload not operating efficiently or ultimately leading to a total system failure.

Therefore, an intermediatory module that administers and monitors electrical energy from both the solar panels and batteries is needed. This intermediatory module is the power management and distribution (PMAD) system that controls the flow of power to the respective subsystem, making certain that only the rated power per subsystem is delivered.

There are two types of power regulation systems, namely direct energy transfer (DET) and peak power trackers (PPT). DET systems use shunt resistors to maintain a predetermined bus voltage and are typically utilised in systems less than 100 W, where unneeded power is dissipated. The PPT system obtains the required power directly from the solar array by dynamically changing the arrays operating point; however, does require from 4% to 7% of the power generated (Miller and Keesee, 2003).

The COTS PMAD system that ZACube-2 utilises PPT as the power regulatory method enabling an efficient way of charging the batteries and increasing battery longevity. ZACube-2 has four bus lines:

- 3.3V
- 5V
- 12V
- Unregulated battery bus.

2.2.3 Thermal Control

The hostility that outer space poses in terms of drastic temperature changes when the satellite is in view of the sun and an eclipse can affect the operational performance of the satellite. Satellite components have a range of temperatures at which operational efficiency is nominal; however, once those limits have been reached by either the system being too hot or too cold, sub-components' performance begin to deteriorate, reducing overall system operations.

To combat the system experiencing either end of the temperature scale, active and passive thermal management systems can be employed by either using conductive or radiative means.

2.2.3.1 Passive Thermal Control

As the name implies, passive thermal control systems transfer the thermal energy from one subsystem to another using conduction or by shielding the satellite from external sources of radiation such as the sun. Various passive thermal control solutions are listed below (State Of The Art Small Spacecraft Technology, 2018):

- Thermal straps
- Sunshields
- Thermal insulation and coatings
- Thermal louvers
- Deployable radiators
- Heat pipes
- Stacking of different subsystems

Passive thermal control was used as the thermal control method for ZACube-2 with stacking different subsystems as the primary method and using heat straps and/or pipes as a secondary

method. Each subsystem/component as it operates, radiates thermal energy and some components emit more thermal energy than others, i.e., some components get hotter than others.

If all these “hot” components are stacked together in the configuration, summation of the thermal energy being generated by the components and the sun can exceed the operating temperature of the various components, which can greatly increase the risk of individual components operating inefficiently or an overall system failure occurring. This notion also applies to components that do not emit excessive amounts of thermal energy.

Therefore, stacking components that emit excessive amounts of thermal energy with subsystems that generate low thermal energy helps to mitigate the effects of excessive heating or cooling within the CubeSat stack/ structure while operational.

In addition, thermal straps or heat pipes are implemented to further distribute thermal energy such that components neither experience either end of the specified operating temperature spectrum as extremes will drastically affect performance.

2.2.3.2 Active Thermal Control

Whilst a passive thermal control system uses the available thermal energy to control the satellite’s thermodynamics, active thermal control solutions operate with an electrical input and require an extensive thermal analysis of the effectiveness as said system is an additional system producing heat.

However, active thermal control solutions are effective in maintaining optimal thermal limits defined by the user ensuring that the subsystem and the system overall operates without being thermally restricted. Examples of various active thermal control solutions are listed below (State Of The Art Small Spacecraft Technology, 2018):

- Thermal straps
- Electrical heaters
- Cryocoolers

2.2.4 Guidance, Navigation and Control

This subsystem is responsible for ensuring the orientation of the satellite is in the optimum orientation for payload performance in addition to stabilizing the CubeSat.

Commonly known as an attitude determination and control subsystem (ADCS), the satellite's orientation can be manipulated by using a combination of sensors and actuators to adjust the spacecraft's attitude, the attitude being the orientation of the spacecraft's fixed co-ordinate system to a reference co-ordinate system (Dachwald, 2010). Examples of the aforementioned sensors and actuators used in attitude adjustment are listed below (Wertz and Larson, 1999):

- Earth sensors
- Sun sensors
- Magnetometers
- Horizon sensors
- Gyros
- Star trackers
- Atomic clocks

With some examples of actuators being (State Of The Art Small Spacecraft Technology, 2018):

- Reaction wheels
- Magnetorquers

Individual components can be used to build custom-made ADCS units, however, COTS integrated units can be utilized that are produced in packages, such as the ADCS unit that ZACube-2 employs. Reference orientation in which the ADCS operates, can be seen in Figure 2.7 below.

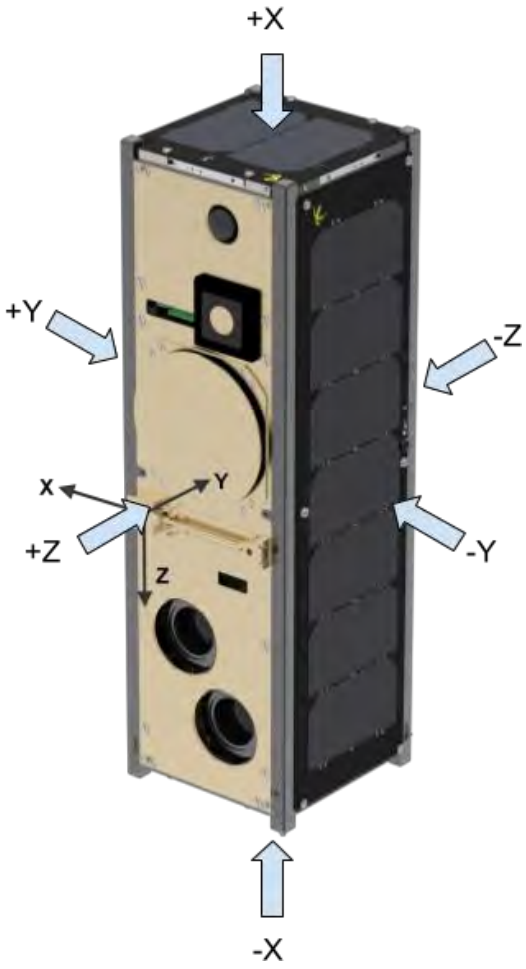

Figure 2.7: ZACube-2 Spacecraft Bus Orientation

From Figure 2.7 there are two cartesian reference frames; the reference frame or co-ordinate system with the blue arrows is spacecraft fixed, whilst the other co-ordinate system is Earth fixed. The ADCS unit that ZACube-2 employs, contains the following components:

- Deployable magnetometer that measures the Earth's magnetic field.
- Two variations of magnetorquers induce motion by interacting with the Earth's geomagnetic field to control the satellite's orientation.
- Coarse sun sensors output the sun's position in relation to the spacecraft's position.
- The reaction wheel adjusts the CubeSats attitude by producing angular momentum through a wheel attached to an electric motor.

2.2.5 Command and Data Handling

What can be regarded as the brain of the satellite in the form of an on-board computer (OBC), this unit is responsible for managing the operational and payload operations of the satellite.

This particular Common functions of an OBC are as follows (Command & Data Handling, 2019):

- Decoding, authentication, decryption, and distribution of on-board telecommands.
- Generation, formatting, encoding and transmission of on-board satellite telemetry.
- The maintenance and distribution of on-board time and synchronisation signals.
- Control software resource allocation.
- Memory function for the payload and telemetry or housekeeping data.
- Managing operational control modes of the satellite.
- Interfacing of integrated ADCS units or individual ADCS components.

2.2.6 Telemetry, Tracking and Control

Satellite telemetry, or “housekeeping data”, are important sets of data collected at regular intervals that relay the health of the satellite to the ground segment where the data is reviewed to make sure the satellite is operating within the defined parameters. This data is transmitted through the radio spectrum via a transceiver in frequency bands that vary from 30 MHz to 40 GHz.

Various powered subsystems generate different sets of data that are particular to that subsystem, e.g., EPS telemetry data sets can be current readings for the different buses. ZACube-2 telemetry data is continuously recorded at three second intervals with the data being stored onboard and available for download at periodic transmission.

2.3 Communication

This subsystem enables communication between the satellite or CubeSat and ground control. As expressed in section *8.2.6 Telemetry, Tracking and Control (TT&C),* frequency bands in the radio spectrum vary from 30 MHz to 40 GHz for spacecraft communication. Within the aforementioned range there are multiple individual bands that each have a respective usage (State Of The Art Small Spacecraft Technology, 2018):

- Very high frequency (VHF): 30 MHz – 300 MHz
- Ultra-high frequency (UHF): 300 MHz – 3 GHz
- L-band: 1 GHz – 2 GHz
- S-band: 2 GHz – 4 GHz
- C-band: 4 GHz – 8GHz
- X-band: 8 GHz – 12 GHz

- Ku-band: 12 GHz – 18 GHz
- K-band: 18 GHz – 27 GHz
- Ka-band: 27 GHz – 40 GHz

ZACube-2 makes use of the following bands for the downlink and uplink of telecommands, TT&C and payload data:

- UHF for tracking, telemetry, and command (TT&C).
- S-band for payload data transmission.
- VHF to obtain AIS and VDES (VHF data exchange system) messages.

2.4 Analysis of Ground Control

Ground control is an important aspect as a way of monitoring and controlling the satellite's behaviour to ensure optimal payload performance and spacecraft longevity. To accomplish this, mission control software (MCS) is used which automates, controls, monitors, and supports the CubeSat, to name a few, through a graphical interface. Whilst companies do offer fully built front-end and back-end MCS solutions, other enterprises such as NASA have released partially built back-end open-source MCS that can be tailored to the user's requirements.

The following subsections will delve into the two MCS options available and the subsequent scalability as more ground stations and/or satellites are added.

2.4.1 Licensed Mission Control Software

Licensed MCS are robust turnkey solutions that use propriety software developed by an enterprise, which either offers other services in addition to providing MCS or specialises in MCS by having multiple deployment options that are tiered with each tier having a rigid support system, e.g., the cost of satellite support per month or extensiveness of service-level agreement (SLA) support. Generally, the higher the tier, the higher the cost, and the more support the end-user is given.

What can be seen is that the financial aspect ultimately becomes a constraint experienced by the end-user. However, whilst this option is commonly more expensive than open-source alternatives, there are multiple advantages. One of these advantages is the speed at which it can be implemented with a turnkey solution as little to no time needs to be spent tailoring the product to the end user's specification. This comes down to dedicated support provided by the seller.

Dedicated support is a major factor that can significantly improve the chances of success for the mission. An advantageous feature is continual updates and patches to the MCS, ensuring that the software remains stable and, in case of additional satellites being incorporated, that the software can manage the additional flow of data whilst making all generated data available.

This results in minimal downtime, guaranteeing that operations run smoothly, and if there happens to be downtime due to software complications that the problem is immediately addressed and fixed promptly. This allows the mission operations team to focus on more pressing matters.

Security is an important deciding factor as any data generated can be sensitive. With licensed MCS, digital security is of the utmost importance where multiple industry-standard safeguards are implemented to keep the data safe.

Therefore, by using a licensed MCS, the end-user is bound by the budget that is allocated to the MCS and the relative service, and if said service satisfies the needs of the operation. Nevertheless, both the customisability and cost are offset by the support provided, through continuous software support, access to facilities, implementation time and quality of service.

2.4.2 Open-Source Mission Control Software

Unlike licensed MCS, open-source MCS is typically the back-end portion of the software also known as the source code, which can be inspected and modified by the public. While open-source MCS has no licensing cost, the reality is that there can be a minimal cost associated, which is dependent on the publisher. With little to no cost, this avails the software to a wider audience, aligning with the low-cost ethos of CubeSats.

Along with the lower cost of open-source MCS, the opportunities to modify and find the code to fit the mission’s needs are highly desirable. As mentioned previously, some licensed MCS is based on a tiered system, where each tiered is essentially restricted by the number of features, such as satellites per plan and ground stations or gateways. Customisability is infinite and can be tailored to fit the mission’s characteristics and even future missions, allowing scalability.

Negative aspects of having an infinitely modifiable program are where additional costs can be found. Firstly, expertise in coding both in front-end and back-end is vital and with the MCS being used daily, a clear and concise user interface (UI) and user experience (UX) are

required. These design features must be intuitive and meaningful to improve the quality of the user's experience.

Second is MCS stability and support over the mission lifetime. These two factors are dependent on the size of the team responsible for MCS oversight and previous experience maintaining an MCS. Although updates/upgrades can come from the community of related MCS users, long term solutions are still needed, which in turn must be modified to fit the mission's needs. This fluctuating workload can be subject to a third party that provides formal support, but this can result in expensive ad-hoc support where updates either do not suffice or there is significant downtime.

Open source has disadvantages, such as needing to satisfy the software development process to tailor the solution to the respective mission and no formal support resulting in additional time spent by the mission team/third-party to mitigate and fix problems. Nevertheless, the low-cost aids smaller, less financially backed teams to build and launch satellites. Software features are not bound by budget and the customisability limit is only bound by the level of competency of the software development team.

2.5 Modes of Operation

As ZACube-2 orbits, it will not always be in contact with the ground station and the respective payload targets; therefore, for the spacecraft to be in a constant "ON" state where all subsystems are operating instead of essential systems would cause unwarranted risk on the system, such as increased thermal activity.

To this end, different operating modes are needed for both the spacecraft, ZACube-2, and the ground segment. The modes for both the ground segment and ZACube-2 were detailed by the engineering team in the proprietary preliminary design review documentation.

2.5.1 Ground Segment Operations

The ground segment is used to provide support and relays both spacecraft data, i.e., TT&C, and payload data to the respective users, whilst there can be multiple ground stations that support this role. ZACube-2 has only one ground station, which is located at Cape Peninsula University of Technology's Bellville campus.

The ground station has four operating modes that are used during a single satellite overpass. These four modes from the beginning of the overpass to the end of the overpass are tabulated below.

Table 2.1: Ground Segment Operations

Ground Segment Operational mode	Description
Idle mode	In idle mode, some of the ground segment's equipment is either in a low-power mode or switched off to conserve power to prepare for the satellite flying overhead. A transition from idle mode to prep mode takes place.
Prep mode	Prep mode is initiated five minutes before the satellite reaches the horizon. During this phase, the two Yagi antennas are automatically positioned into place to where the satellite will cross the horizon, which is calculated from its two-line element (TLE) published by the North American Aerospace defence command (NORAD). Relevant equipment is switched from the low-power mode to standard power mode and configured to transmit and receive data to and from ZACube-2.
Tracking mode	As ZACube-2 crosses the horizon, the ground station shifts into tracking mode. This means that the ground station actively points the two Yagi antennas and assumes control of the equipment. During this tracking phase, any operations such as the downlink of telemetry/payload data, uplink of the onboard payload's operation schedule and other scheduled operations take place.
Park mode	Once ZACube-2 falls below the horizon, a delay of 30 seconds is initiated before the ground station transitions into park mode where the two antennas are parked, and some equipment is switched off entirely or put into a low-power mode.

2.5.2 ZACube-2 Operations

The satellite fulfils the mission objective by virtue of a payload. The payload can be any device(s), such as the one onboard ZACube-2, which is a software-defined radio (SDR) as primary payload (PP), and a near-infrared (NIR) imager as hosted (secondary) payload.

However, these payloads are only operated within a specific region of the globe; hence, operational modes are implemented. These modes are specified by either onboard events, telecommands received by the ground station, or scheduled events that are uploaded to the ZACube-2 OBC from the ground station. These operational modes with the respective actions are tabulated below:

Table 2.2: ZACube-2 Operational Modes

ZACube-2 Operational Mode	Description
Safe mode	The safe mode results in a low power mode, which is triggered by a low battery event to prevent the EPS from being depleted. This ensures that ZACube-2 is safe, i.e., can still operate all subsystems and maximise the batteries recharging abilities. A low battery event can comprise either inefficient power

	generation or the operation of both the PP and the hosted imager payload simultaneously, leading to the depth of discharge (DoD) falling below the 20% specified threshold.
Primary payload mode	Primary payload mode is dictated by the aforementioned schedule of events. This schedule has all the relevant information to operate the payload effectively and efficiently, such as the time that the payload should activate and deactivate, which is set according to the coordinated universal time (UTC), the payload data transmitter and subsequent instructions to the ADCS subsystem so that the bus orientates to the region of interest.
Hosted imager payload mode	Scheduled events dictate the operation of the hosted imager payload. These events can once again relay both activation and deactivation times of the imager, which can be specified by either time or attitude and different methods of NIR imaging, e.g., single sensor single image, dual-sensor dual image series or multiple dual-sensor images. The operation of the imager is additionally restricted by the availability of power, such that it does not interfere with the operation of the primary payload, e.g., if the operation of both payloads results in a decreased operational efficiency of the primary payload the imager is subsequently turned off.
ADCS mode	ADCS mode is to ensure that the bus is three-axes stabilised with the integrated ADCS unit, by using a combination of reaction wheels, magnetorquers, magnetometers and coarse sun sensors that use actuators to adjust the CubeSat's attitude.

2.6 Data Analytics Methodology

With sizable volumes of data that need to be processed to gain an understanding of system performance, a data analytics approach needs to be taken. In total there are six steps to the process with each step being iterative. The six steps are as follows:

- Data requirement specifications
- Data collection
- Data processing
- Data cleaning
- Data analysis
- Communication

The figure below shows the interrelationship and iterative phases:

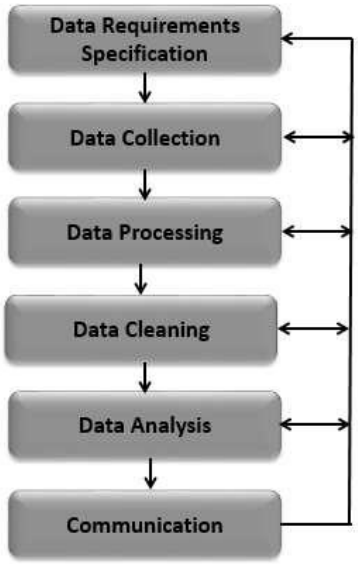

Figure 2.8: Data Analytics Phases

(tutorialspoint, 2020)

The first two steps have already been completed, with the remainder being the purpose of this work. Data processing and cleaning refer to the organization of the data that can be understood by the processing utility, which was chosen to be MATLAB.

The goal of the data processing step is to establish the reliability and functionality of ZACube-2, over a specific temporal range, when compared to specifications and investigation of any outlying values. To this end, statistical models must be employed, such as:

- Mean
- Median
- Mode
- Minimum value
- Maximum value
- Standard deviation
- Range
- Variance
- Gaussian probability model
- Cumulative density function
- Fault tree analysis (FTA)
- Correlation

The usage of these various data analytics methodologies is to ascertain the performance of the various telemetry being recorded in comparison to the expected/calculated values in the various budgets. Whilst the resource budgets represent an ideal system, actual system performs various on a multitude of factors ranging from human error to external factors such the environment.

While the practice of using basic statistical analysis such as mean, mode, median and etc shows a singular piece of data within, in this instance, a vast dataset. This, alone, does not show the performance of the respective subsystem over a span of time at which the telemetry was recorded.

Therefore, utilising other statistical models such as the Gaussian probability model and the cumulative density function demonstrates the frequency at which certain values are being recorded and the probability of said value occurring, respectively. Put simplistically this can be used to identify how well a particular system is operating above the design threshold and how often in turn showing whether improvements are to be made to make the system more reliable or if said system is operating nominally with no further required design changes.

An in-depth detailing of how the telemetry data was processed from the raw data sets to which the aforementioned tools have been applied, can be found in *CHAPTER THREE: DATA ANALYTICS METHODOLOGY*.

2.7 Effect of Space Weather on CubeSats

Space weather is the effect that the sun has on the magnetosphere, ionosphere, and thermosphere that influences both space and ground systems. Figure 2.9 gives a representation of space weather phenomena and their respective origins.

Figure 2.9: Space Weather Cause and Effect

(Hill, n.d.)

The Sun's influence on space weather includes, but are not limited to (Space Weather Phenomena | NOAA / NWS Space Weather Prediction Center, 2020):

- Solar flares
- Solar wind
- Solar radiation storms
- Coronal holes
- Sunspots
- Solar extreme ultraviolet (EUV) irradiance
- Coronal mass ejections (CME)
- Galactic cosmic rays (GCR)

These phenomena emit highly charged particles that, when interacting with the Earth's magnetosphere, can give the following events at high altitudes (Space Weather Phenomena | NOAA / NWS Space Weather Prediction Center, 2020):

- Geomagnetic storms
- Ionospheric scintillation
- Radiation belts
- Total electron content (TEC)

An example of space weather influencing a system is that of solar flares, which produce strong X-rays. These X-rays tamper with the propagation of high-frequency radio waves as the signal travels through the plasma of the ionosphere, resulting in either a weak signal or the signal being completely blocked. This phenomenon is referred to as scintillation, or ionospheric scintillation, where the signal goes under rapid modification of electron density, ultimately leading to the waves being refracted or diffracted, impacting the power and phase of the receiving signal.

In total there are two ways that radiation influences on-board electronics; namely, lattice displacement and ionisation effects, with the former causing lasting damage by changing the components' arrangement of atoms from collisions with neutrons, protons, alpha particles, heavy ions, and gamma photons.

Radiation mitigation is an important factor as electronics that experience radiation damage, in the form of ionizing particles, experience four end-effects (State Of The Art Small Spacecraft Technology, 2018), (Radiation hardening, 2020):

- Total ionizing dose (TID) is the total amount of ionizing radiation received, measured in rad, where 1 rad equates to 0.01 Gy (Gray) or 0.01 J/kg.
- Single event effects (SEE) are the disturbances created by a single particle hitting the on-board electronics.
- Single event upsets (SEU) have an effect where the logic state of the memory is disrupted.
- Single event latch-up (SEL) affects the CMOS (complementary metal–oxide–semiconductor) logic state on the output transistor that leaves the component in a "shorted" state, which is responsible for potential high-current values.

To prevent the aforementioned events from damaging electronics, suppliers of commercial off-the-shelf (COTS) products utilise radiation hardening, commonly abbreviated to "rad-hard", which protects the product from ionizing radiation by a way of either modifying physical attributes or logical processing. The table below describes what each process entails.

Table 2.3: Physical and Logical Process of Radiation Hardening

(Radiation hardening, 2020)

Physical	Logical
Processing chips are manufactured on insulting substrate materials, such as silicon oxide (silicon-on-insulator) or sapphire (silicon-on-sapphire).	Using error-correcting code (ECC) memory

Shielding the device with a cover.	Implementing redundant system-level elements such as a limited number of microprocessor boards using voting logic to determine the correct result
Using static RAM instead of dynamic RAM that is capacitor-based.	Implementing redundant circuit-level elements that implement the same voting logic to determine the result. The implementation of redundant elements acts as an additional fail-safe.
Using a substrate that has a large band or energy gap, such as silicon carbide or gallium nitride.	
Using a shielding medium on the chips, such as Boron-11 in the chip's borophosphosilicate glass (BPSG) layer.	

CHAPTER THREE
DATA ANALYTICS METHODOLOGY

This chapter deals with the methodology in which the raw telemetry was processed, and the respective data analytics tools.

3.1 Telemetry Processing Methodology

As previously mentioned in section *2.6 Data Analytics Methodology,* the phases when undergoing data analysis are as follows:

- Data requirement specifications
- Data collection
- Data processing
- Data cleaning
- Data analysis
- Communication

Each phase will be elaborated further within the following subsections as to the steps taken and functions used within a numeric computing environment, such as MATLAB, in aid of data analysis.

3.2 Data Requirement Specifications

The initial step was done by the engineering team in the proprietary preliminary design review (PDR) documentation, which details the systems requirements to achieve mission objectives. For ZACube-2, these were the technological demonstrations of both the AIS messaging reception using the SDR (software-defined radio) payload and the medium resolution near-infrared imager, also referred to as the K-line imager.

3.3 Data Collection

Telemetry data is downloaded through a scheduled downlink session when ZACube-2 is over the ground station at the CPUT Bellville campus. During a 24-hour cycle, there are typically two 2-hour opportunities available to download the generated telemetry data; the first window is from 10:00 am to 12:00 pm and the second window is from 10:00 pm to 00:00 am.

3.4 Data Processing

The received telemetry files are in .csv (comma-separated value) file format, which contains specific recorded values for each of the telemetry channels. The relevant telemetry channels and the values recorded for each telemetry channel are listed in *Table 2: Telemetry Channels*.

These .csv files can be used to exchange information across multiple forms of applications; however, it was found that some telemetry channels were combined into a single .csv file. The two images below show the list of raw telemetry data with an example of the pre-processed telemetry data supplied.

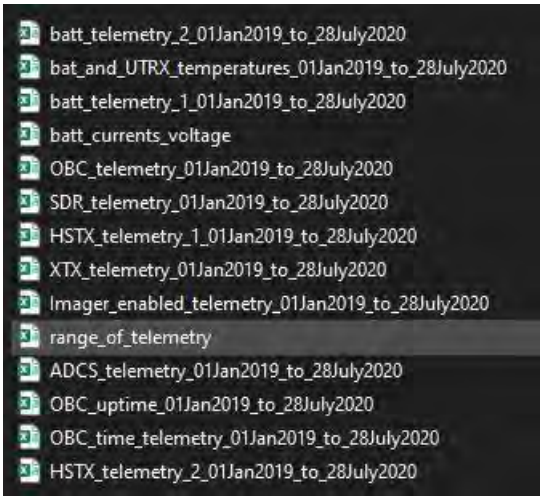

Figure 3.1: Example List of Supplied Telemetry

Figure 3.2: Example of Pre-processed Telemetry Data

As can be seen in the Figure 3.2, all the data is placed within the first column; however, to discern the different data and which subsystem these values belong to, the text-to-column wizard in the data tab of Excel was used. All data within the supplied .csv files are delimited, meaning that the commas or tabs separate the respective data points.

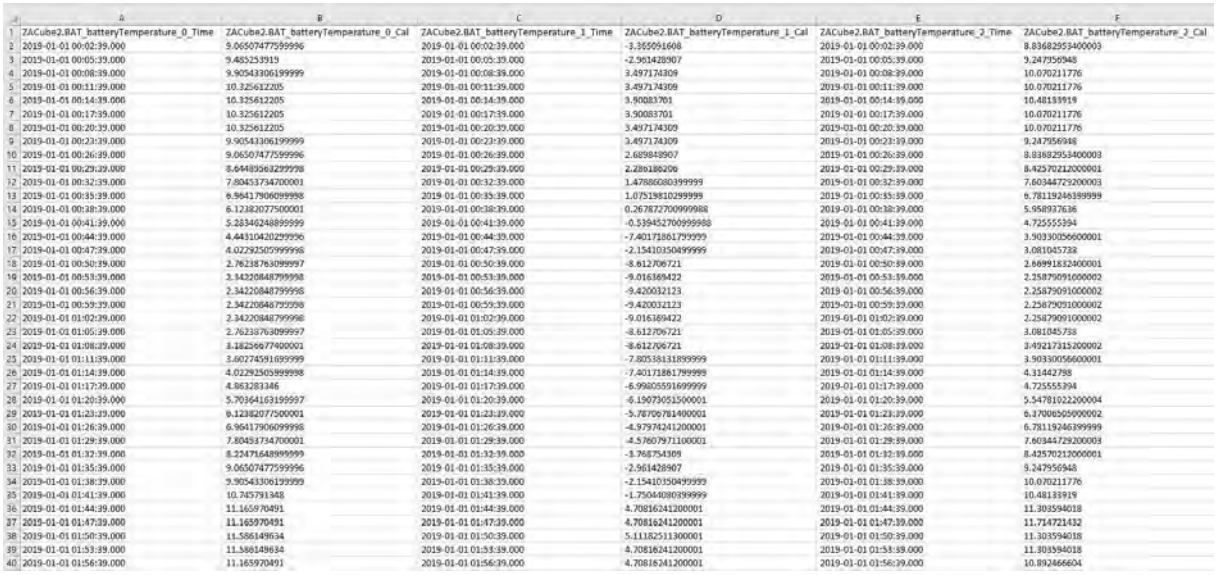

	A	B	C	D	E	F
1	ZACube2.BAT_batteryTemperature_0_Time	ZACube2.BAT_batteryTemperature_0_Cal	ZACube2.BAT_batteryTemperature_1_Time	ZACube2.BAT_batteryTemperature_1_Cal	ZACube2.BAT_batteryTemperature_2_Time	ZACube2.BAT_batteryTemperature_2_Cal
2	2019-01-01 00:02:39.000	9.06507477599996	2019-01-01 00:02:39.000	-3.365091608	2019-01-01 00:02:39.000	8.83682953400003
3	2019-01-01 00:05:39.000	9.485253919	2019-01-01 00:05:39.000	-2.961428907	2019-01-01 00:05:39.000	9.247956948
4	2019-01-01 00:08:39.000	9.90543306199999	2019-01-01 00:08:39.000	3.497174309	2019-01-01 00:08:39.000	10.070211776
5	2019-01-01 00:11:39.000	10.325612205	2019-01-01 00:11:39.000	3.497174309	2019-01-01 00:11:39.000	10.070211776
6	2019-01-01 00:14:39.000	10.325612205	2019-01-01 00:14:39.000	3.90083701	2019-01-01 00:14:39.000	10.48133919
7	2019-01-01 00:17:39.000	10.325612205	2019-01-01 00:17:39.000	3.90083701	2019-01-01 00:17:39.000	10.070211776
8	2019-01-01 00:20:39.000	10.325612205	2019-01-01 00:20:39.000	3.497174309	2019-01-01 00:20:39.000	10.070211776
9	2019-01-01 00:23:39.000	9.90543306199999	2019-01-01 00:23:39.000	3.497174309	2019-01-01 00:23:39.000	9.247956948
10	2019-01-01 00:26:39.000	9.06507477599996	2019-01-01 00:26:39.000	2.689848907	2019-01-01 00:26:39.000	8.83682953400003
11	2019-01-01 00:29:39.000	8.64489363299998	2019-01-01 00:29:39.000	2.289186206	2019-01-01 00:29:39.000	8.425702120000001
12	2019-01-01 00:32:39.000	7.80453734700001	2019-01-01 00:32:39.000	1.47886080399999	2019-01-01 00:32:39.000	7.603447292000003
13	2019-01-01 00:35:39.000	6.96417906099998	2019-01-01 00:35:39.000	1.07519810299999	2019-01-01 00:35:39.000	6.781192463999999
14	2019-01-01 00:38:39.000	6.12182077500001	2019-01-01 00:38:39.000	0.267827709999988	2019-01-01 00:38:39.000	5.958937636
15	2019-01-01 00:41:39.000	5.28346248899999	2019-01-01 00:41:39.000	-0.539452709999988	2019-01-01 00:41:39.000	4.725555394
16	2019-01-01 00:44:39.000	4.44310420299996	2019-01-01 00:44:39.000	-1.40171861799999	2019-01-01 00:44:39.000	3.903300566000001
17	2019-01-01 00:47:39.000	4.02292505999998	2019-01-01 00:47:39.000	-2.15410350499999	2019-01-01 00:47:39.000	3.081045738
18	2019-01-01 00:50:39.000	2.76238763099997	2019-01-01 00:50:39.000	-8.612706721	2019-01-01 00:50:39.000	2.689818324000001
19	2019-01-01 00:53:39.000	3.34220848799998	2019-01-01 00:53:39.000	-9.016369422	2019-01-01 00:53:39.000	2.258790910000002
20	2019-01-01 00:56:39.000	2.34220848799998	2019-01-01 00:56:39.000	-9.420032123	2019-01-01 00:56:39.000	2.258790910000002
21	2019-01-01 00:59:39.000	2.34220848799998	2019-01-01 00:59:39.000	-9.420032123	2019-01-01 00:59:39.000	2.258790910000002
22	2019-01-01 01:02:39.000	2.34220848799998	2019-01-01 01:02:39.000	-9.016369422	2019-01-01 01:02:39.000	2.258790910000002
23	2019-01-01 01:05:39.000	2.76238763099997	2019-01-01 01:05:39.000	-8.612706721	2019-01-01 01:05:39.000	3.081045738
24	2019-01-01 01:08:39.000	3.18226677400001	2019-01-01 01:08:39.000	-8.612706721	2019-01-01 01:08:39.000	3.492173152000002
25	2019-01-01 01:11:39.000	3.60274591699999	2019-01-01 01:11:39.000	-7.805381131899999	2019-01-01 01:11:39.000	3.903300566000001
26	2019-01-01 01:14:39.000	4.02292505999998	2019-01-01 01:14:39.000	-7.401718617999999	2019-01-01 01:14:39.000	4.31442798
27	2019-01-01 01:17:39.000	4.863283346	2019-01-01 01:17:39.000	-6.998055919999999	2019-01-01 01:17:39.000	4.725555394
28	2019-01-01 01:20:39.000	5.70364163199997	2019-01-01 01:20:39.000	-6.190730515000001	2019-01-01 01:20:39.000	5.547810222000004
29	2019-01-01 01:23:39.000	6.12182077500001	2019-01-01 01:23:39.000	-5.787067814000001	2019-01-01 01:23:39.000	6.370065059000002
30	2019-01-01 01:26:39.000	6.96417906099998	2019-01-01 01:26:39.000	-4.97974241200001	2019-01-01 01:26:39.000	6.781192463999999
31	2019-01-01 01:29:39.000	7.80453734700001	2019-01-01 01:29:39.000	-4.57607971100001	2019-01-01 01:29:39.000	7.603447292000003
32	2019-01-01 01:32:39.000	8.22471648999999	2019-01-01 01:32:39.000	-3.768754309	2019-01-01 01:32:39.000	8.425702120000001
33	2019-01-01 01:35:39.000	9.06507477599996	2019-01-01 01:35:39.000	-2.961428907	2019-01-01 01:35:39.000	9.247956948
34	2019-01-01 01:38:39.000	9.90543306199999	2019-01-01 01:38:39.000	-2.154103504999999	2019-01-01 01:38:39.000	10.070211776
35	2019-01-01 01:41:39.000	10.745791348	2019-01-01 01:41:39.000	-1.750440803999999	2019-01-01 01:41:39.000	10.48133919
36	2019-01-01 01:44:39.000	11.165970491	2019-01-01 01:44:39.000	4.70816241200001	2019-01-01 01:44:39.000	11.303594018
37	2019-01-01 01:47:39.000	11.165970491	2019-01-01 01:47:39.000	4.70816241200001	2019-01-01 01:47:39.000	11.714721432
38	2019-01-01 01:50:39.000	11.586149634	2019-01-01 01:50:39.000	5.11182511300001	2019-01-01 01:50:39.000	11.303594018
39	2019-01-01 01:53:39.000	11.586149634	2019-01-01 01:53:39.000	4.70816241200001	2019-01-01 01:53:39.000	11.303594018
40	2019-01-01 01:56:39.000	11.165970491	2019-01-01 01:56:39.000	4.70816241200001	2019-01-01 01:56:39.000	10.892466604

Figure 3.3: Example of Splitting Telemetry Data into Different Columns

After completing this step for each file listed in *Figure 3.1: Example List of Supplied Telemetry*, individual files were generated by separating each value with the respective DateTime and designated appropriately. This resulted in *Table 1.1: ZACube-2 Telemetry Channels* which lists the telemetry channel, data recorded, the unit of measurement, designation, and description of the data being recorded. Below is an example of the end-product of the processing stage.

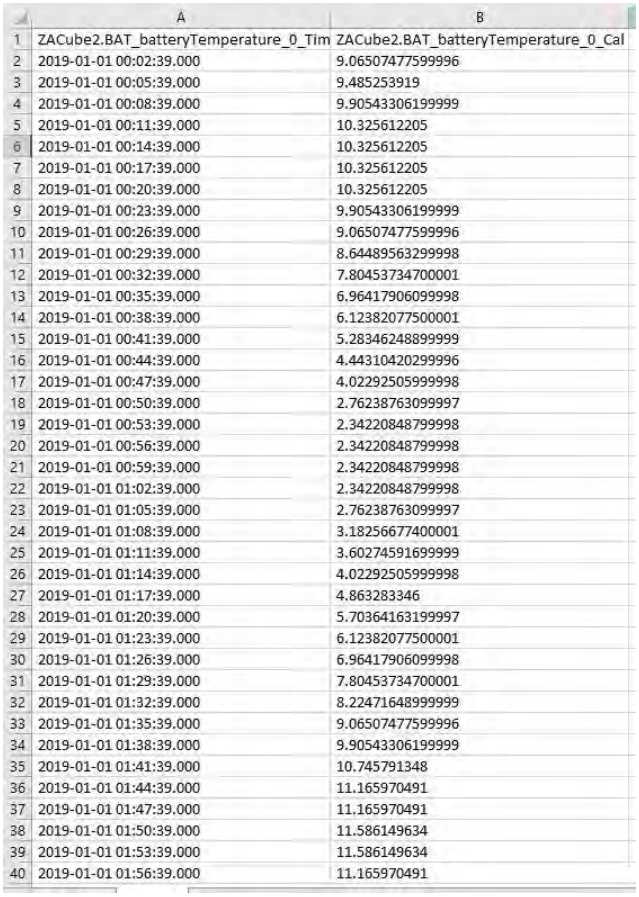

	A	B
1	ZACube2.BAT_batteryTemperature_0_Tim	ZACube2.BAT_batteryTemperature_0_Cal
2	2019-01-01 00:02:39.000	9.06507477599996
3	2019-01-01 00:05:39.000	9.485253919
4	2019-01-01 00:08:39.000	9.90543306199999
5	2019-01-01 00:11:39.000	10.325612205
6	2019-01-01 00:14:39.000	10.325612205
7	2019-01-01 00:17:39.000	10.325612205
8	2019-01-01 00:20:39.000	10.325612205
9	2019-01-01 00:23:39.000	9.90543306199999
10	2019-01-01 00:26:39.000	9.06507477599996
11	2019-01-01 00:29:39.000	8.64489563299998
12	2019-01-01 00:32:39.000	7.80453734700001
13	2019-01-01 00:35:39.000	6.96417906099998
14	2019-01-01 00:38:39.000	6.12382077500001
15	2019-01-01 00:41:39.000	5.28346248899999
16	2019-01-01 00:44:39.000	4.44310420299996
17	2019-01-01 00:47:39.000	4.02292505999998
18	2019-01-01 00:50:39.000	2.76238763099997
19	2019-01-01 00:53:39.000	2.34220848799998
20	2019-01-01 00:56:39.000	2.34220848799998
21	2019-01-01 00:59:39.000	2.34220848799998
22	2019-01-01 01:02:39.000	2.34220848799998
23	2019-01-01 01:05:39.000	2.76238763099997
24	2019-01-01 01:08:39.000	3.18256677400001
25	2019-01-01 01:11:39.000	3.60274591699999
26	2019-01-01 01:14:39.000	4.02292505999998
27	2019-01-01 01:17:39.000	4.863283346
28	2019-01-01 01:20:39.000	5.70364163199997
29	2019-01-01 01:23:39.000	6.12382077500001
30	2019-01-01 01:26:39.000	6.96417906099998
31	2019-01-01 01:29:39.000	7.80453734700001
32	2019-01-01 01:32:39.000	8.22471648999999
33	2019-01-01 01:35:39.000	9.06507477599996
34	2019-01-01 01:38:39.000	9.90543306199999
35	2019-01-01 01:41:39.000	10.745791348
36	2019-01-01 01:44:39.000	11.165970491
37	2019-01-01 01:47:39.000	11.165970491
38	2019-01-01 01:50:39.000	11.586149634
39	2019-01-01 01:53:39.000	11.586149634
40	2019-01-01 01:56:39.000	11.165970491

Figure 3.4: Example of Separated Telemetry Data

However, due to the sheer number of data points, any data manipulation and/or process processed in Microsoft Excel is challenging. Due to these reasons, an alternative was used, namely MATLAB, specifically MATLAB R2020a due to the program being powerful and comprehensive with the vast majority of functions, especially analytical-based functions, already included in the program with the opportunity to download specialised add-ons or toolboxes to further augment functions.

Each of the telemetry channels as listed in *Table 1.1: ZACube-2 Telemetry Channels* was imported into the MATLAB workspace with the selected data being outputted as several types as listed in the table below.

Table 3.1: MATLAB Import Variable Selection
(Read Spreadsheet Data Using Import Tool- MATLAB & Simulink, 2021)

Option	**Data Type**
Column vectors	Import each column as an individual m-by-1 vector
Numeric array	Import as m-by-n numeric array
String array	Import as m-by-n string array
Cell array	Import as cell array which can contain multiple data types
Table	Import as table

*m = number of rows
n = number of columns

It should be noted that when importing data in tabular form, each column can be assigned a specific data type as recognised by MATLAB. These data types are text, number, categorical, DateTime, which has several different DateTime formats, or assigning a custom date format that is not listed in the drop-down menu that can be seen in the figure below:

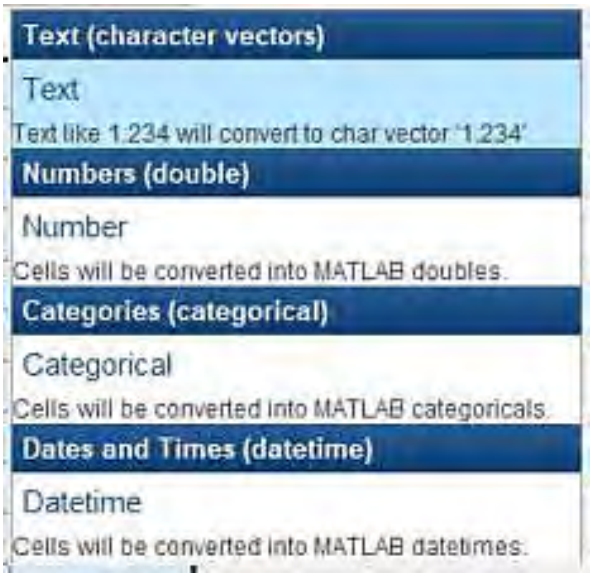

Figure 3.5: Data Type

However, as the spreadsheets being imported were still in the original .csv format, data types were automatically recognized, e.g., the data and time of the variable being recorded, and did not have to be declared.

The import interface has additional features, such as specifying the range of the selected data, row location of the name of the variables, output type as per discussed, and the rules regarding what to do with cells that cannot be imported either because MATLAB does not recognise it as a number represented as NaN (Not-a-Number) or a DateTime value, represented at NaT (Not-a-Time).

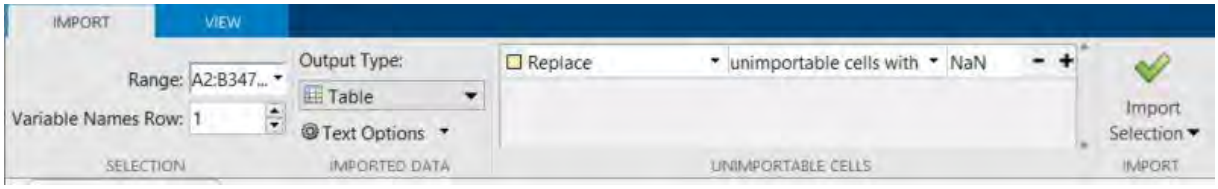

Figure 3.6: Import Tool Interface

Once the range of data has been selected and imported, it is now found in the workspace window. Several types of data outputs are stored in the workspace where they can be recalled in MATLAB's command window. The workspace also gives the variables value, class, median and range values. An example can be seen below.

Workspace

Name	Value	Class	Median	Range
ADCSYAA	*34796x2 table*	table		
ZACube2ADCS_estAttAngleY_Cal	*34796x1 double*	double	-1.1300	359.7500
ZACube2ADCS_estAttAngleY_Time	*34796x1 datetime*	datetime		

Figure 3.7: Workspace Interface

The resulting file can be seen below. What is evident is that there are missing values that are populated with the respective NaT for missing DateTime values and NaN for missing number values; these various absent values will be addressed during the data cleaning phase.

	1 ZACube2ADCS_estAttAngleY_	2 ZACube2ADCS_estAttAngleY_
1	10-May-2019 21:59:51	-1.789999961853030
2	NaT	NaN
3	11-May-2019 09:24:58	-2.759999990463260
4	NaT	NaN
5	11-May-2019 11:01:04	-2.660000085830690
6	NaT	NaN
7	11-May-2019 21:30:37	-0.029999999329448
8	NaT	NaN
9	12-May-2019 10:37:00	-2.869999885559080
10	NaT	NaN
11	12-May-2019 21:09:34	-0.300000011920929
12	NaT	NaN
13	12-May-2019 22:44:10	-0.579999983310699
14	NaT	NaN
15	13-May-2019 10:14:15	-3.009999990463260
16	13-May-2019 10:16:55	-2.700000047683720
17	NaT	NaN
18	13-May-2019 20:48:02	-0.219999998807907
19	NaT	NaN
20	13-May-2019 22:21:30	-0.209999993443489
21	NaT	NaN
22	14-May-2019 09:52:31	-3.119999885559080
23	NaT	NaN
24	14-May-2019 11:34:21	-2.430000066757200
25	NaT	NaN
26	14-May-2019 20:28:12	-1.009999990463260
27	NaT	NaN
28	14-May-2019 21:59:19	-0.119999997317791

Figure 3.8: Example of Imported Data File

The last step prior to the cleaning of data is converting the tables into what MATLAB calls a timetable; a *timetable* is a type of table where the data in each row is associated with a specific date and/or time, making it possible to generate graphs that have the values for the respective telemetry channel on the Y-axis and the corresponding date and time on the X-axis.

3.5 Data Cleaning

Data cleaning is an important process in any form of data science as it removes unnecessary noise from the data whilst preparing the data for the analysis period. As mentioned in *3.4 Data Processing*, missing values for either a number or datetime are replaced with NaN and NaT, respectively.

To remove these NaN and NaT entries, which are essentially missing data, the function "*rmmissing*" is used that removes missing entries regardless of whether it is a NaN or NaT. To use this function, as an example *Figure 3.8: Example of Imported Data File* is used, which relates to the ADCS_Y_AA data, the general syntax follows as where *A* is the input and *R* is the output (Remove missing entries - MATLAB rmmissing, 2021).

- R=rmmissing(A);

Though, for this purpose, variables *A* and *R* can be the same variable name; in terms of this example, *R* and *A* will become ADCS_Y_AA, resulting in a new syntax.

- ADCSYAA=rmmissing(ADCSYAA);

Usage of this function yields a table that is void of NaN and/or NaT, which can then be processed by MATLAB. The result of this function can be seen in the figure below.

	ZACube2ADCS_estAttAngleY_Time	1 ZACube2ADCS_estAttAngleY_Cal
1	10-May-2019 21:59:51	-1.7900
2	11-May-2019 09:24:58	-2.7600
3	11-May-2019 11:01:04	-2.6600
4	11-May-2019 21:30:37	-0.0300
5	12-May-2019 10:37:00	-2.8700
6	12-May-2019 21:09:34	-0.3000
7	12-May-2019 22:44:10	-0.5800
8	13-May-2019 10:14:15	-3.0100
9	13-May-2019 10:16:55	-2.7000
10	13-May-2019 20:48:02	-0.2200
11	13-May-2019 22:21:30	-0.2100
12	14-May-2019 09:52:31	-3.1200
13	14-May-2019 11:34:21	-2.4300
14	14-May-2019 20:28:12	-1.0100
15	14-May-2019 21:59:19	-0.1200

Figure 3.9: Resultant of Data Cleaning

Correctly naming the file with the included appropriate underscore can be done in the workspace by right-clicking and selecting the rename option. This process of removing empty entries was repeated for each data set.

Additionally, in cases where outliers are present in the data, and subsequently skewing the data or compressing most of the data relaying a false narrative in behavioural characteristics, these values were replaced with value(s) preceding the outlier.

3.6 Data Analysis Techniques

With the data now prepped and cleaned for the analysis phase, the method(s) of data analysis must be chosen. As elaborated in section *2.6 Data Analytics Methodology,* the following statistical techniques will be employed in aid of analysing the telemetry data in a performance review of ZACube-2 operations compared to design specifications:

- Mean
- Median
- Mode
- Range
- Minimum value
- Maximum value
- Variance

- Standard deviation
- Gaussian probability model
- Fault tree analysis (FTA)

Whilst there exists a large variety of techniques or methods of analysis data, the techniques were chosen due to the fact that these formulas have been used before in similar publications as demonstrated in Castet and Saleh (2009) and Kaminskiy and Kashem (2015), in which the aim was to review telemetry data to benefit future missions.

Most of these techniques can be accomplished with the usage of MATLAB's add-ons, called *Apps*. These apps are toolboxes both developed from MathWorks and the community alike; each serving a purpose to a respective field. The *Statistics and Machine Learning Toolbox* was used to make the analysis easier with built-in functions, such as generating Gaussian probability models and cumulative density functions, to name a few.

The following subsections will delve into the aforementioned data analysis techniques clarifying the purpose and subsequent mathematical equation.

3.6.1 Basic Statistics

Basic statistics can be used to show the basic behavioural characteristics of the generated telemetry. Calculated values will also be used as a gauge when compared to the designed specifications. Basic statistics give insight that can be incorporated into future design iterations.

While several statistical tools can be called basic, for this application basic statistics used are:

- Mean
- Median
- Mode
- Range
- Minimum value
- Maximum value
- Variance
- Standard deviation

Formulas for the applicable abovementioned statistical tools are provided below.

- Mean:

$$\bar{x} = \frac{\sum x}{n}$$ **(Equation 3.1)**

Where:

$$\sum x = summation\ of\ the\ values$$

$$n = number\ of\ values$$

- Median:

$$n^{th} = \frac{n+1}{2}$$ **(Equation 3.2)**

Where:

$$n = number\ of\ values$$

- Mode:

$$Most\ frequently\ occuring\ value$$

- Range:

The range will also be used to highlight the variety of the recorded data. The function is given as:

$$maximum\ value - minimum\ value$$

- Variance:

$$\sigma^2 = \frac{\sum(x_i - \bar{x})^2}{n-1}$$ **(Equation 3.3)**

3.6.2 Gaussian Probability Model

Also known as the bell curve or probability density function, the Gaussian probability model will give the distribution of the telemetry data points. It comprises the mean, which dictates the location of the centre of the curve, and the standard deviation, which determines the width of the curve. These functions are given as (Normal Distribution- MATLAB & Simulink, 2020):

- Standard deviation:

$$\sigma = \sqrt{\frac{\sum(x_i - \bar{x})^2}{n-1}} \qquad \textbf{(Equation 3.4)}$$

Where:

$$x_i = \ value\ at\ a\ certain\ point$$
$$\bar{x} = mean$$
$$n = number\ of\ values$$

- Gaussian probability:

$$f(x) = \frac{1}{\sigma\sqrt{2\pi}} e^{\frac{-(x-\mu)^2}{2\sigma^2}} \qquad \textbf{(Equation 3.5)}$$

Where:

$$\mu = mean$$
$$\sigma = standard\ deviation$$

Equation 3.5 is also known as the probability density function (PDF), which when integrated is the cumulative density function, or CDF.

3.6.3 Cumulative Density Function (CDF)

The cumulative density or distribution function, commonly abbreviated to CDF, is as explained in the previous subsection, the integration of the probability density function, or PDF. The CDF,

as the name suggests, relays information on the cumulative distribution of a variable where the variable can either be discrete or continuous.

- Cumulative probability density function:

$$F(x) = \int_{-\infty}^{x} f(x)\,dx = \int_{-\infty}^{x} \frac{1}{\sigma\sqrt{2\pi}} e^{\frac{-(x-\mu)^2}{2\sigma^2}} \quad \textbf{(Equation 3.6)}$$

This can be written in an alternative way as:

$$F(x) = P(X \leq x) \quad \textbf{(Equation 3.7)}$$

This formula, in laymen's terms, describes the probability of X in which X is a random variable that is smaller than or equal to some specific value denoted as x (DeCook, 2020). An example of how the CDF would be applied, is by finding the probability that the minimum amount of power from the solar array as stated in the power budget is being generated.

3.6.4 Correlation

As covariances describe joint variability, correlation is the quantification of the relationship between the two variables. This degree is denoted as a coefficient "r" where an "r" value of +1 indicates a strong relationship and conversely, -1 indicates a strong negative relationship. The function is given as (Orlof and Bloom, 2014):

$$Cor(X, Y) = \frac{\rho}{\sigma_x \sigma_y} \quad \textbf{(Equation 3.8)}$$

Where:

$$\rho = covarinace\ of\ the\ varibales\ X\ and\ Y$$
$$\sigma_x, \sigma_y = Standard\ deviation\ of\ either\ X\ or\ Y\ respectively$$

3.7 Communication

This phase is vital as it shows the results that were generated during the analysis phases. Due to the MathWorks toolboxes, most of the results can be represented in graphs, which are done using the MATLAB “plot” function to generate the graphs. With the “plot” function various graphs can be used to plot data. Applicable graphs are automatically selected once the range of data has been chosen.

The reasoning behind using graphs as a form of communication is that the data sets for the various telemetry channels are large with multiple data entries, since data sets contain years’ worth of information. Graphic representation serves to represent these large data sets in a condensed manner where patterns are discernible and can be further investigated for abnormalities.

CHAPTER FOUR
RAW TELEMETRY DATA AND DATA ANALYSIS RESULTS

This section details the transformation of raw telemetry data from numerical to graphical in addition to providing a performance overview of the various applicable subsystems through the application of the data analysis methodologies. This transformation provides an ease of use when spotting potential areas of interest as the various datasets are vast.

The chapter is divided into the respective telemetry channels as described in *Table 1.1: ZACube-2 Telemetry Channels*. Each telemetry section is divided into two sections; raw telemetry data and results of the data analysis, which is the provision of basic statistics, probability density function and the cumulative density function.

4.1 Attitude Determination Control System (ADCS)

The ADCS is responsible for the orientation of the satellite. ZACube-2 is configured to have a sun-synchronous orbit, which means that the satellite will pass over a geographic location at the same time of day. For ZACube-2, this location was the ground station located at the Cape Peninsula University of Technology in Cape Town, South Africa, where the over-pass occurs twice daily from approximately 10:00 to 12:00 UTC and 22:00 to 00:00 UTC.

There were five sets of data recorded from the ADCS subsystem, namely the angular rate for the X-axis, both the attitude angle and the angular rate for the Y-axis, and the attitude angle for the Z-axis. Telemetry values span from 10 May 2019 21:59:48.260 UTC to 28 July 2020 21:42:19.961 UTC at an inconsistent time internal.

4.1.1 ADCS Angular Rate X-Axis

This section shows the raw telemetry graphical data as well as the resultant of the data analysis process for the ADCS angular rate X-axis

4.1.1.1 Raw Telemetry

Figure A.1 in Appendix A shows the X-axis angular rate for ZACube-2. From the graph, several outliers are seen that visually compress the data. By replacing these outliers with the previous data point value, the behaviour of the angular rate in relation to the X-axis can be properly displayed.

Figure 4.2 shows that prior to May 2020 UTC the variation in the angular was minimal; however, post-May 2020 UTC the angular rate varied between approximately +0.07°/second and -0.07°/second. For ease of reference, the same figure can be seen below.

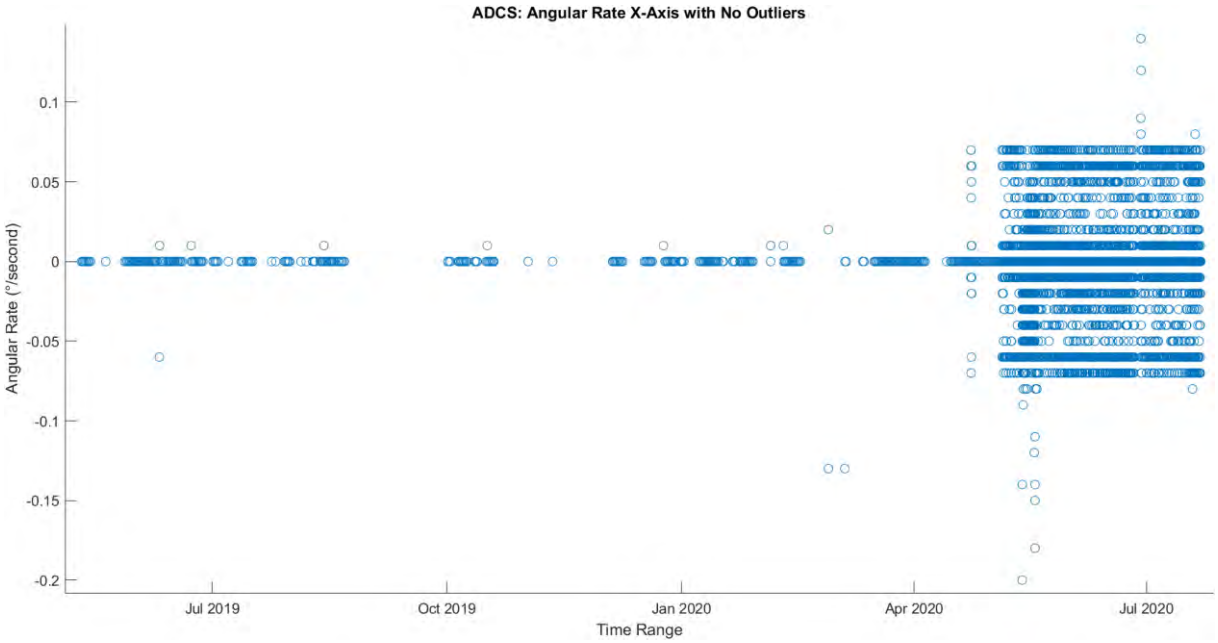

Figure 4.1: ADCS Angular Rate X-Axis with No Outliers

4.1.1.2 Data Analysis

This section gives details regarding the basic statistic, probability density function and cumulative density function for the ADCS angular rate of the X-axis.

4.1.1.2.1 Basic Statistics

The basic statistics for the ADCS angular rate for the X-axis can be referred to in Table 4.1 below.

Table 4.1: ADCS Angular Rate X-Axis Basic Statistics

Statistic	Angle (°/s)
Mean	-0.002
Median	0
Mode	0
Range	0.340
Minimum value	-0.200
Maximum value	0.140
Variance	0

Standard deviation	0.021

4.1.1.2.2 Probability Density Function

The PDF for the ADCS angular rate for the X-axis is presented in Figure 4.2.

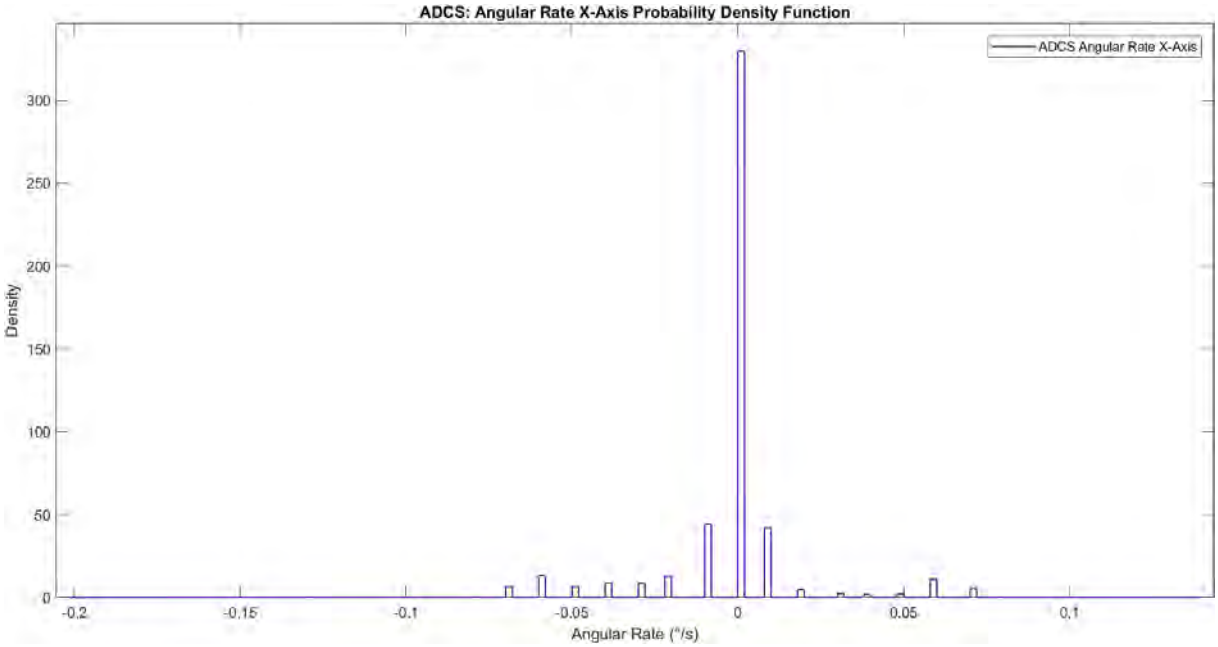

Figure 4.2 ADCS Angular Rate X-Axis Probability Density Function

4.1.1.2.3 Cumulative Density Function

The CDF for the ADCS angular rate for the X-axis is presented in Figure B.1 in Appendix B.

4.1.2 ADCS Attitude Angle Y-Axis

This section shows the raw telemetry graphical data, as well as the resultant of the data analysis process for the ADCS attitude angle in the Y-axis

4.1.2.1 Raw Telemetry

The figure below is the Y-axis attitude angle for ZACube-2. The attitude angle for the Y-axis increased noticeably during the middle of May 2020.

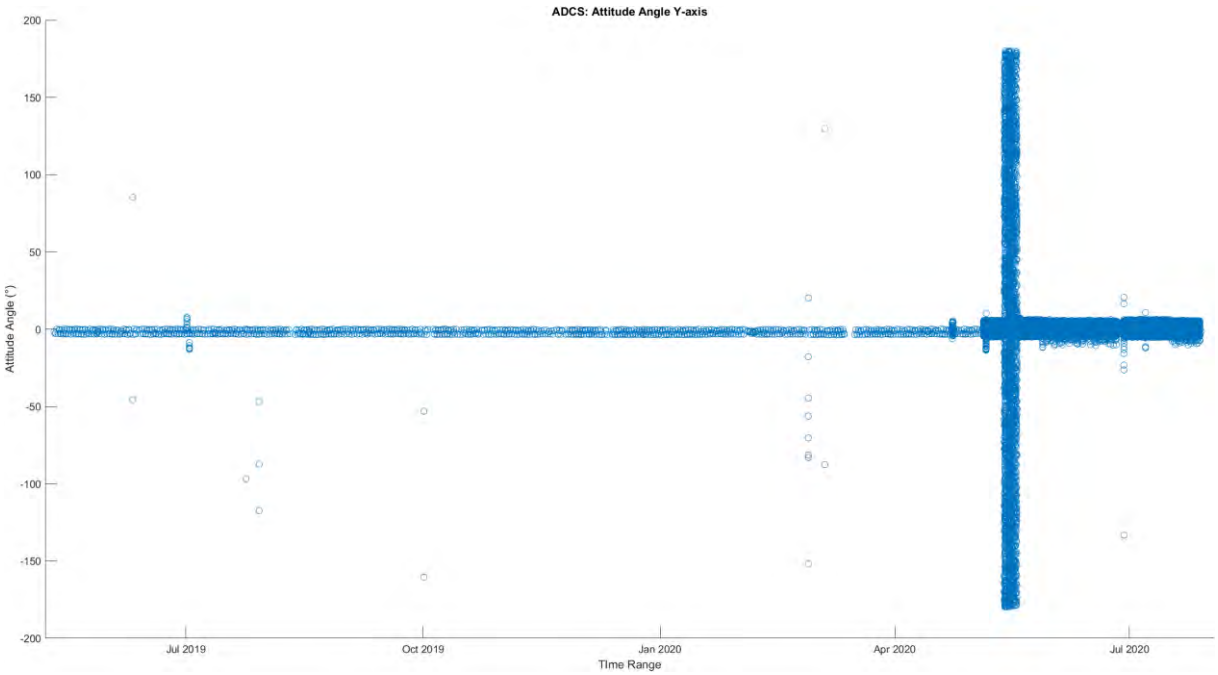

Figure 4.3: ADCS Attitude Angle Y-axis

By expanding this column of data, an area of interest spanning from May 2020 to July 2020 becomes present, resulting in Figure 4.4.

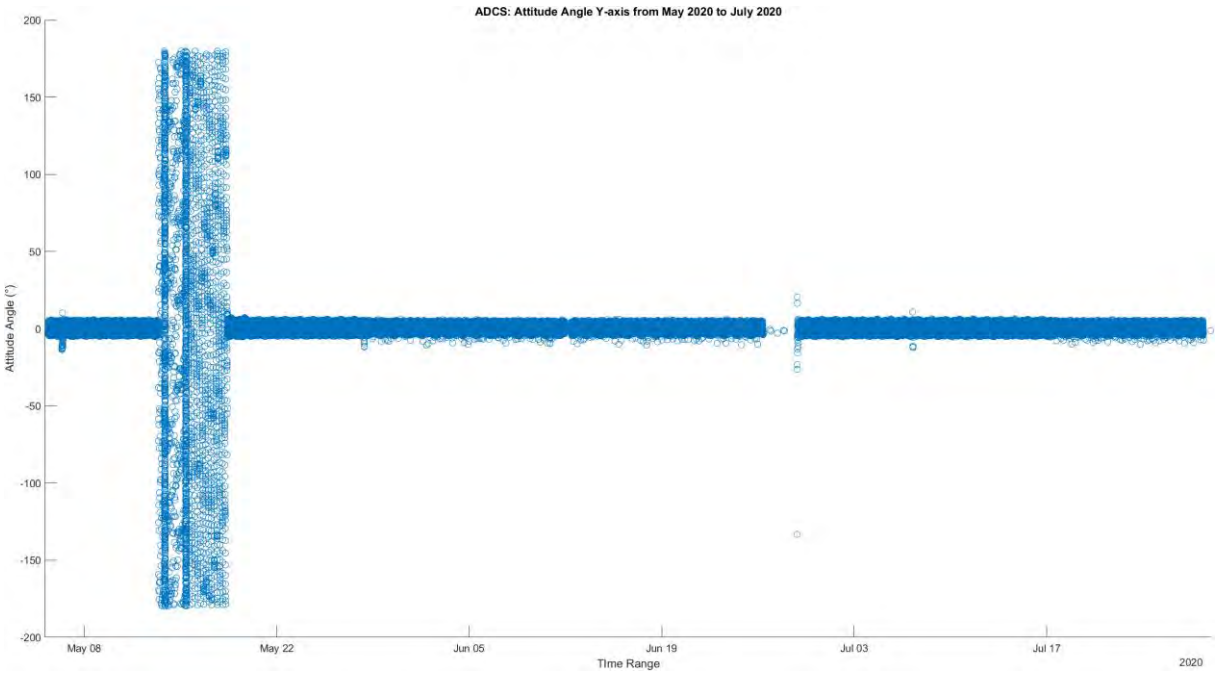

Figure 4.4: ADCS Attitude Angle Y-axis from May 2020 to July 2020

However, with the data being highly compressed during the period in which the attitude angle significantly increased, it is better to expand this section such that a better understanding can be had. Figure 4.5 is the expansion of this dense column of data.

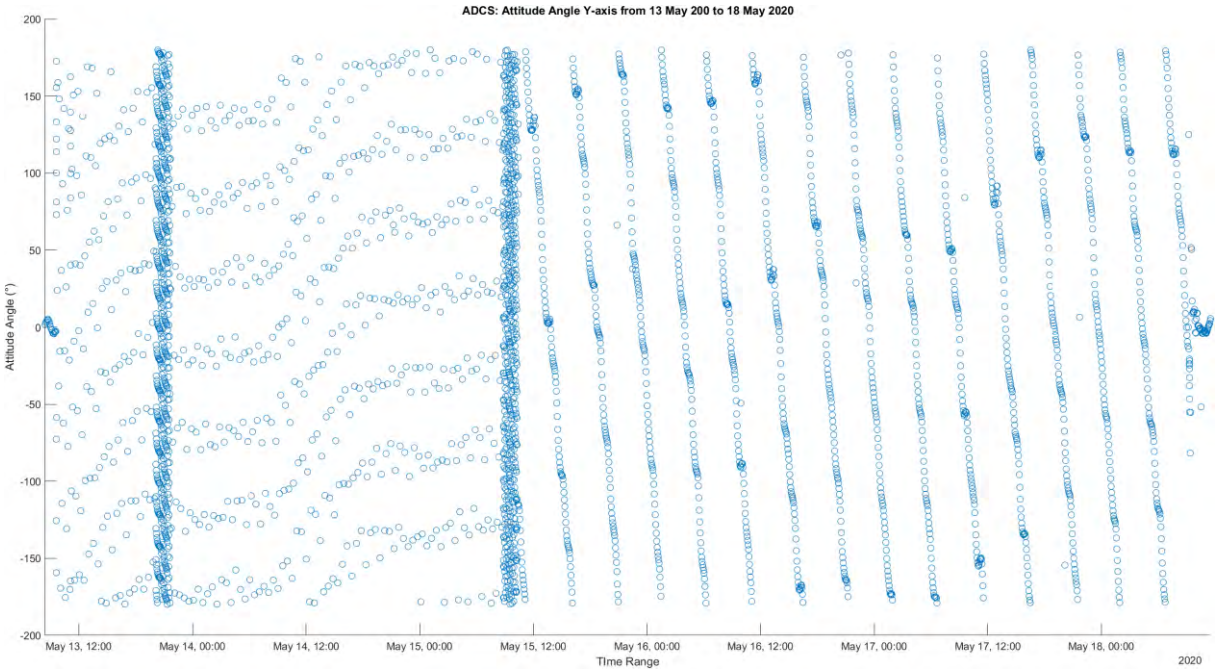

Figure 4.5: ADCS Attitude Angle Y-axis Increase from 13 May 2020 to 18 May 2020

From Figure 4.5, the attitude angle fluctuates consistently from -180° to +180° during the period of 13th May 2020 09:42:56 UTC to 18th May 2020 09:22:40 UTC in a linear manner.

4.1.2.2 Data Analysis

This section gives details regarding the basic statistic, PDF and CFDF for the ADCS attitude angle of the Y-axis.

4.1.2.2.1 Basic Statistics

The basic statistic for the ADCS attitude angle of the Y-axis is given in Table 4.2.

Table 4.2: ADCS Attitude Angle Y-Axis Basic Statistics

Statistic	Angle (°)
Mean	0.429
Median	0.300
Mode	0
Range	262.980

Minimum value	-178.360
Maximum value	84.620
Variance	1.219
Standard deviation	4.268

4.1.2.2.2 Probability Density Function

The PDF for the ADCS attitude angle of the Y-axis is presented in Figure 4.6.

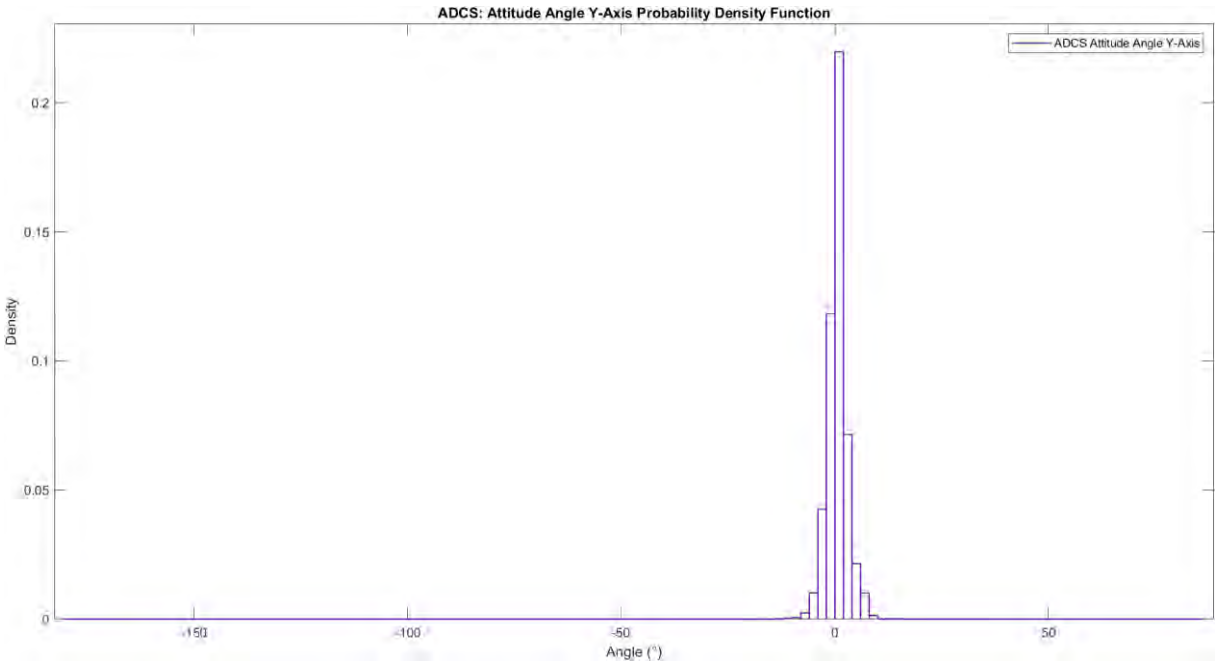

Figure 4.6: ADCS Attitude Angle Y-Axis Probability Density Function

4.1.2.2.3 Cumulative Density Function

The CDF for the ADCS attitude angle of the Y-axis is presented in Figure B.2 in Appendix B.

4.1.3 ADCS Angular Rate Y-Axis

This section shows the raw telemetry graphical data as well as the resulting data analysis for the ADCS angular rate in the Y-Axis

4.1.3.1 Raw Telemetry

The Y-axis angular rate for ZACube-2 is given in Figure 4.10. As with the attitude angle for the Y-axis, a common trend that can be seen from the raw telemetry is that during the middle of May 2020 to July 2020, ZACube-2 started to experience excessive rotation.

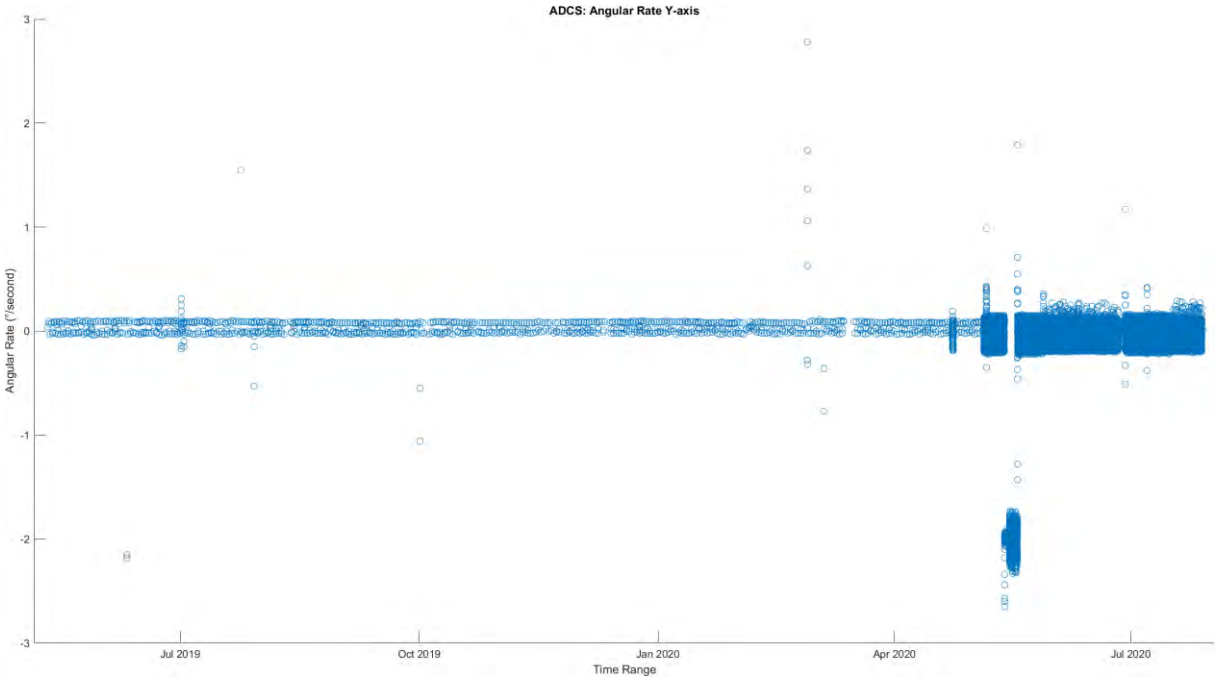

Figure 4.7: ADCS Angular Rate Y-axis

As was done for previous graphs where data was highly compressed, an expansion of the area was performed as for the other telemetry channels. These were taken from May 2020 UTC to July 2020 UTC. The expansion of this area of interest can be seen in Figure 4.8.

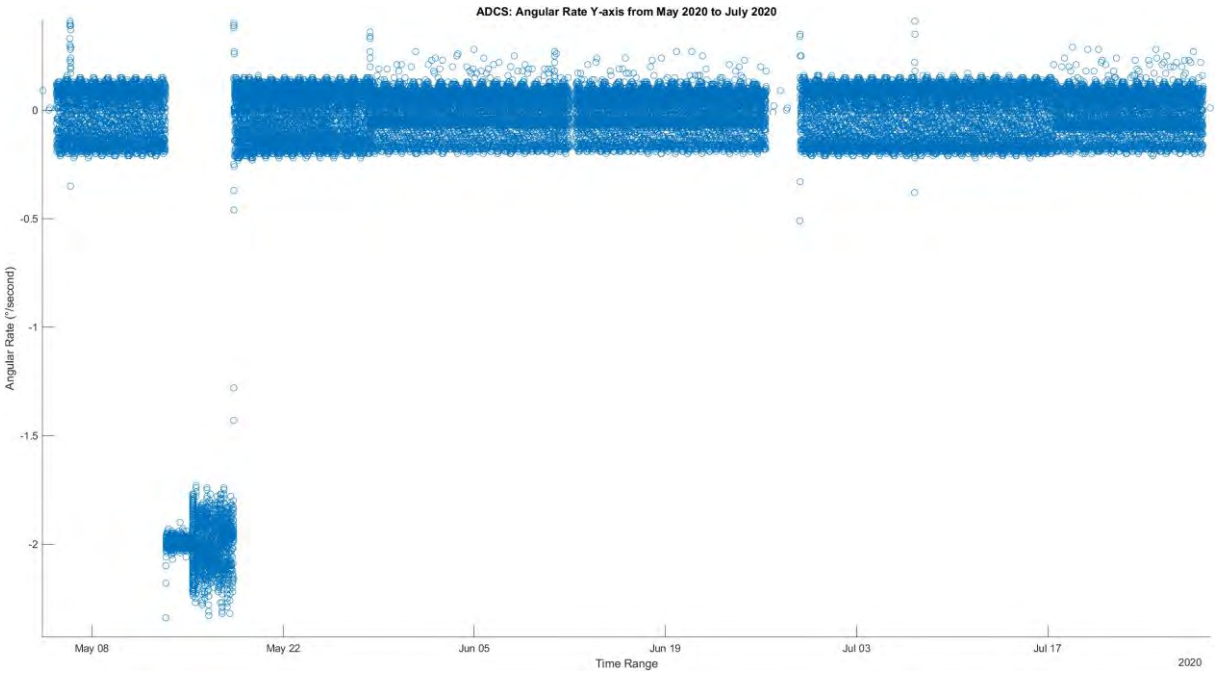

Figure 4.8: ADCS Angular Rate Y-axis from May 2020 to July 2020

4.1.3.2 Data Analysis

This section gives details regarding the basic statistic, probability density function and cumulative density function for the ADCS angular rate Y-axis.

4.1.3.2.1 Basic Statistics

The basic statistic for the ADCS angular rate of the Y-axis is summarised in Table 4.3.

Table 4.3: ADCS Angular Rate Y-Axis Basic Statistics

Statistic	Angle (°/s)
Mean	-0.191
Median	0
Mode	0.090
Range	5.430
Minimum value	-2.650
Maximum value	2.780
Variance	0.347
Standard deviation	0.589

4.1.3.2.2 Probability Density Function

The PDF for the ADCS angular rate of the Y-axis can be referred to in Figure 4.9.

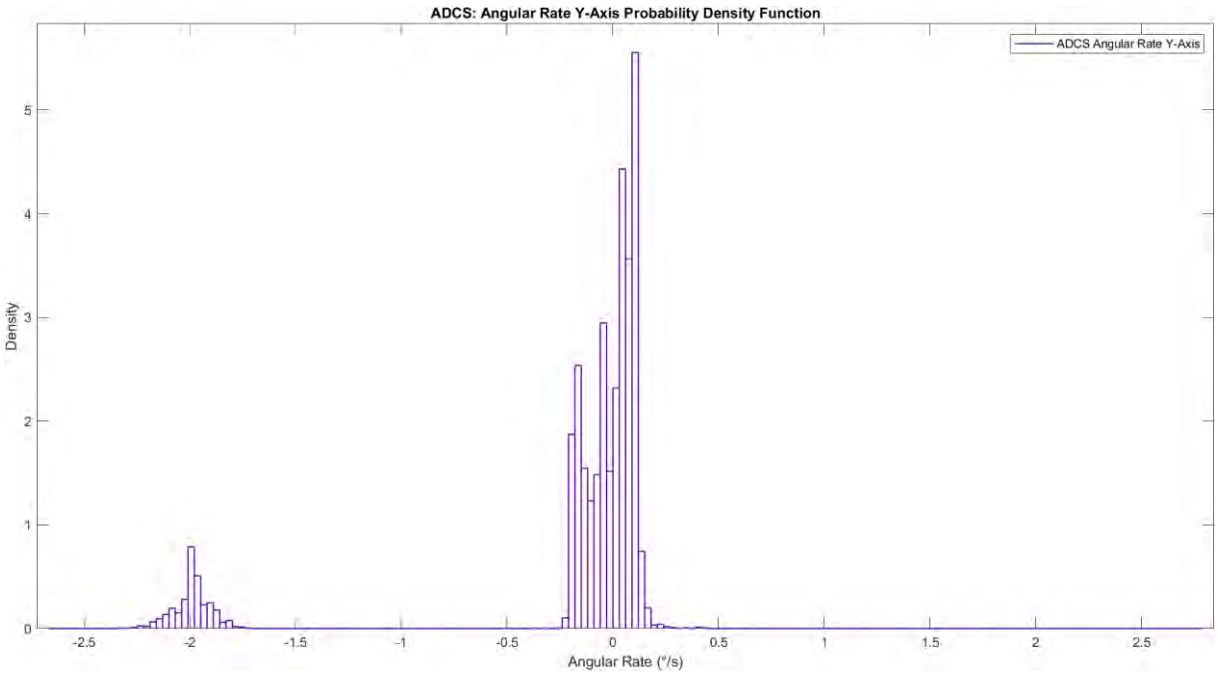

Figure 4.9: ADCS Angular Rate Y-Axis Probability Density Function

4.1.3.2.3 Cumulative Density Function

The CDF for the ADCS angular rate of the Y-axis is given in Figure B.3 in Appendix B.

4.1.4 ADCS Attitude Angle Z-Axis

This section shows the raw telemetry as well as the resulting data analysis for the ADCS attitude angle in the Z-Axis

4.1.4.1 Raw Telemetry

The Z-axis attitude angle for ZACube-2 can be seen in Figure 4.14. During May 2020 UTC until the end of the telemetry set, which was July 2020 UTC, the attitude angle increased in comparison to earlier operations.

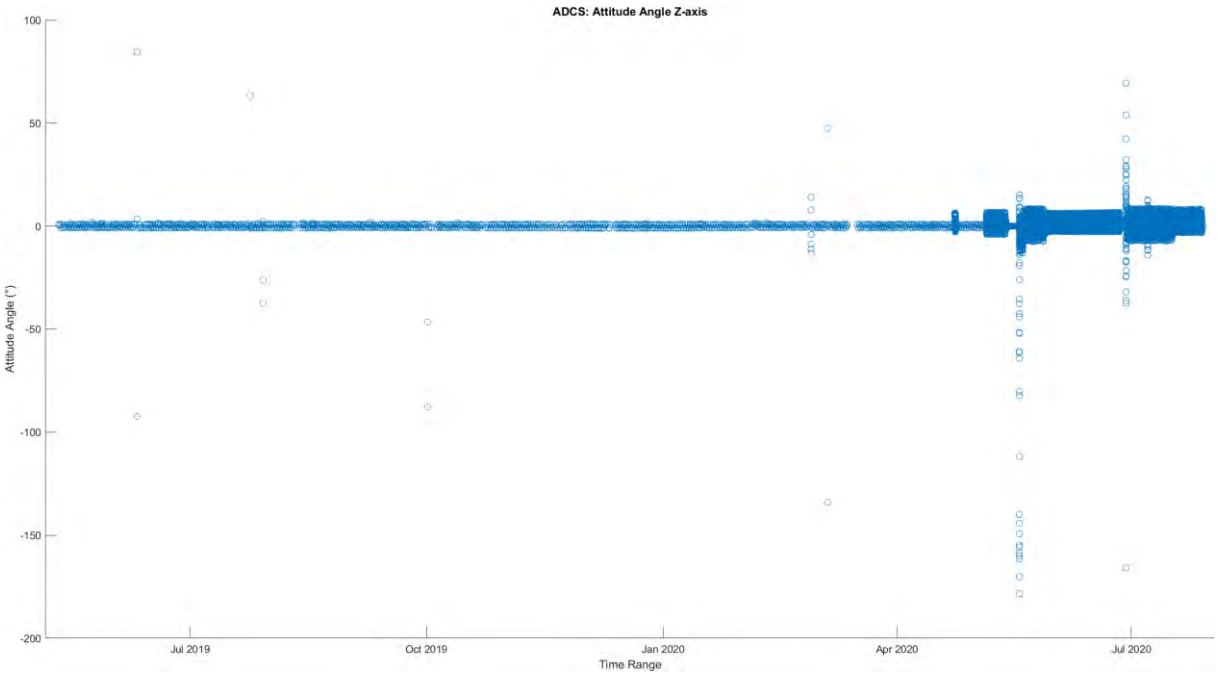

Figure 4.10: ADCS Attitude Angle Z-axis

Figure 4.10 depicts the area of interest spanning from May 2020 to July 2020 where the attitude angle fluctuates between approximately +8° and -8°.

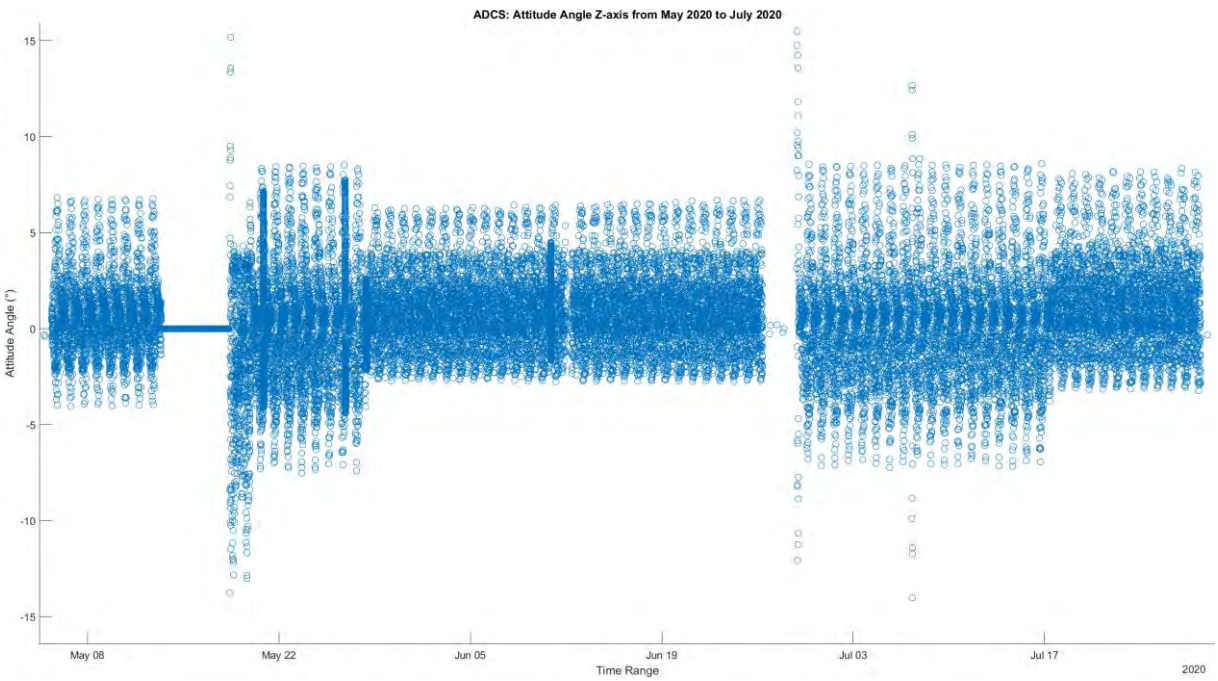

Figure 4.11: ADCS Attitude Angle Z-axis from May 2020 to July 2020

4.1.4.2 Data Analysis

This section gives details regarding the basic statistic, probability density function and cumulative density function for the ADCS attitude angle Z-axis

4.1.4.2.1 Basic Statistics

The basic statistics for the ADCS attitude angle of the Z-axis are listed in Table 4.4.

Table 4.4: ADCS Attitude Angle Z-Axis Basic Statistics

Statistic	Angle (°)
Mean	-0.397
Median	-1.130
Mode	-2.950
Range	359.750
Minimum value	176.950
Maximum value	-179.800
Variance	1038.400
Standard deviation	32.224

4.1.4.2.2 Probability Density Function

The PDF for the ADCS attitude angle of the Z-axis is presented in Figure 4.12.

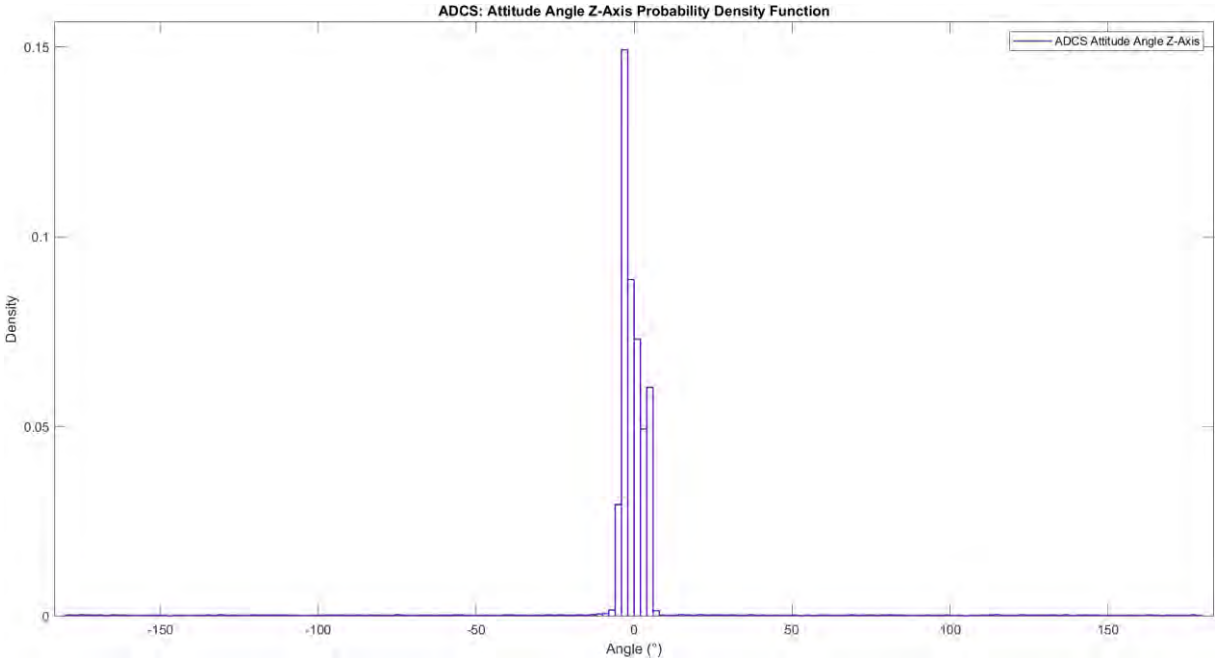

Figure 4.12: ADCS Attitude Angle Z-Axis Probability Density Function

4.1.4.2.3 Cumulative Density Function

The CDF for the ADCS attitude angle of the Z-axis is presented in Figure B.4 in Appendix B.

4.1.5 ADCS Angular Rate Z-Axis

This section shows the raw telemetry data as well as the resulting data analysis of the ADCS angular rate in the Z-Axis.

4.1.5.1 Raw Telemetry

The Z-axis angular rate for ZACube-2 is presented Figure A.2. The figure shows that there are several outliers present in the compressed data. By removing the outliers, the behaviour can be seen clearly, as shown in Figure 4.13.

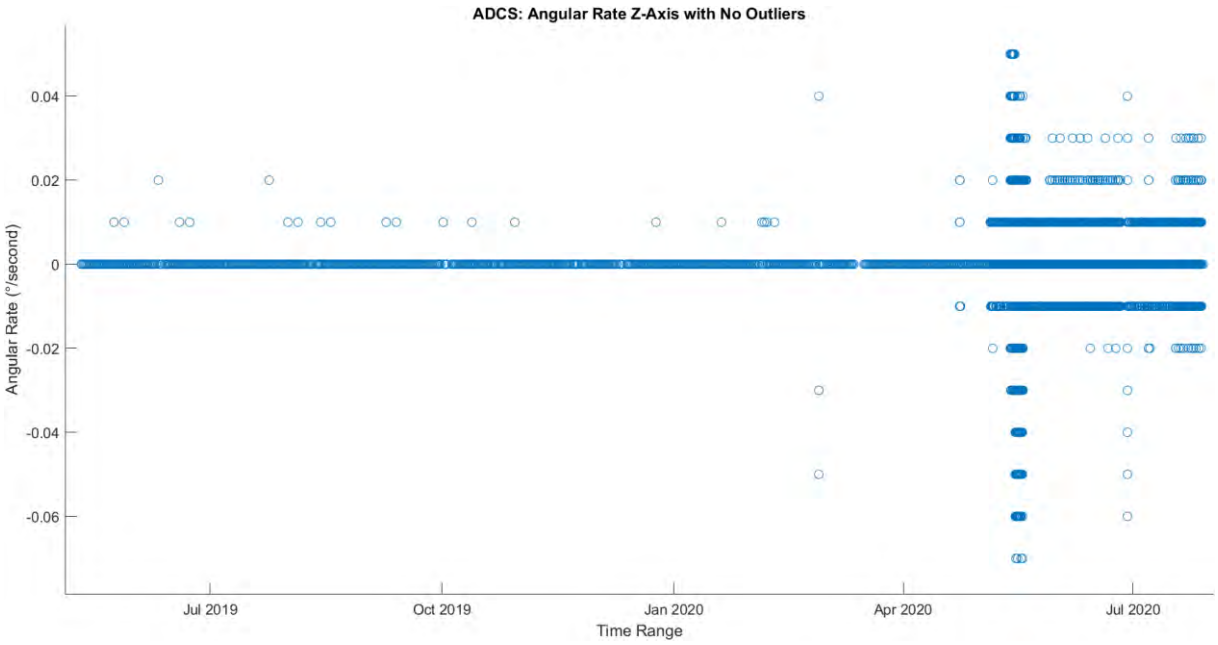

Figure 4.13: ADCS Angular Rate Z-Axis

4.1.5.2 Data Analysis

This section gives details regarding the basic statistic, probability density function and cumulative density function for the ADCS angular rate Z-axis.

4.1.5.2.1 Basic Statistics

The basic statistics for the ADCS angular rate are presented in Table 4.5.

Table 4.5: ADCS Angular Rate Z-Axis

Statistic	Angle (°/s)
Mean	0
Median	0
Mode	0
Range	0.210
Minimum value	-0.080
Maximum value	0.130
Variance	0
Standard deviation	0.009

4.1.5.2.2 Probability Density Function

The PDF for the ADCS angular rate of the Z-axis is presented in in Figure 4.14.

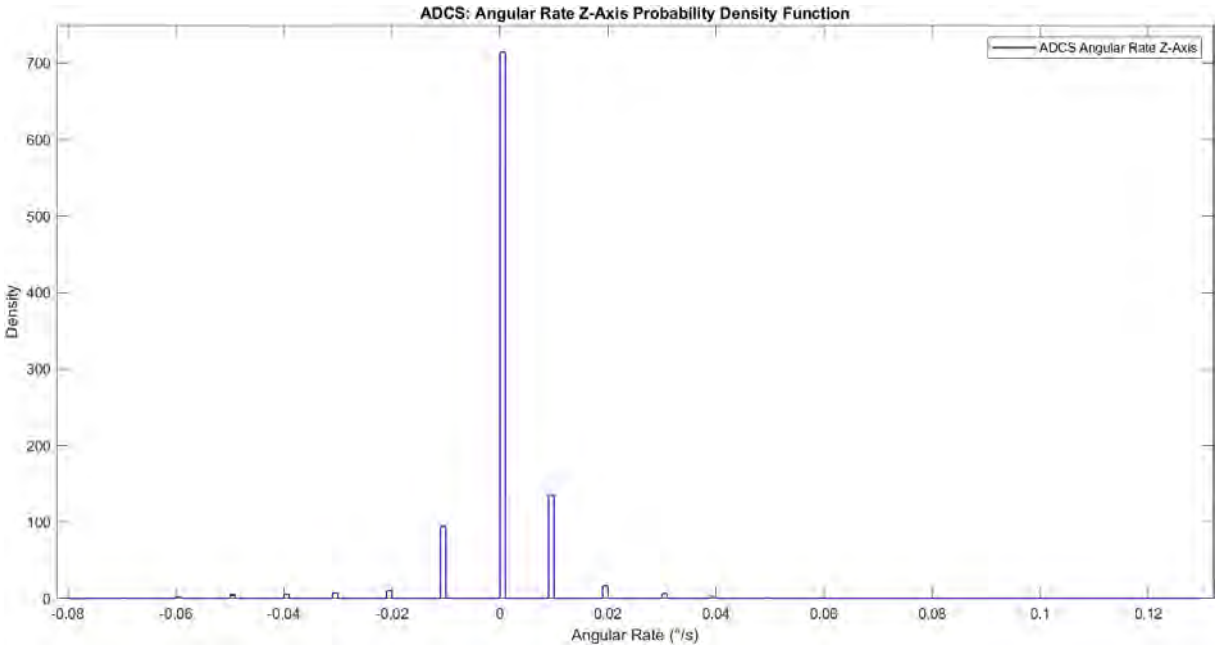

Figure 4.14: ADCS Angular Rate Z-Axis Probability Density Function

4.1.5.2.3 Cumulative Density Function

The CDF for the ADCS angular rate of the Z-axis is given in Figure B.5 in Appendix B.

4.1.6 ADCS Telemetry Correlation

The correlation between the five telemetry channels can be seen in the table below.

Table 4.6: ADCS Telemetry Correlation

Telemetry Channel		X-Axis		Y-Axis	Z-Axis	
		Angular Rate	Attitude Angle	Angular Rate	Attitude Angle	Angular Rate
X-Axis	Angular Rate	1	0,015	0.210	-0.002	0.043
	Attitude Angle	0.015	1	0.002	-0.008	-0.042
Y-Axis	Angular Rate	0.210	0.002	1	0.020	0.150
Z-Axis	Attitude Angle	-0.002	-0.008	0.020	1	-0.047
	Angular Rate	0.043	-0.042	0.150	-0.047	1

4.2 Battery

The battery has multiple telemetry data sets. However, only half of those telemetry channels were used, namely the current and voltage. Telemetry values span from 01 January 2019 00:02:39 UTC to 28 July 2020 09:30:15 UTC at a time step of 3 minutes.

4.2.1 Battery Current

This section shows the raw telemetry data as well as the resulting data analysis for the battery current.

4.2.1.1 Raw Telemetry

Figure 4.15 shows the raw battery current telemetry with a few outliers present in the data range.

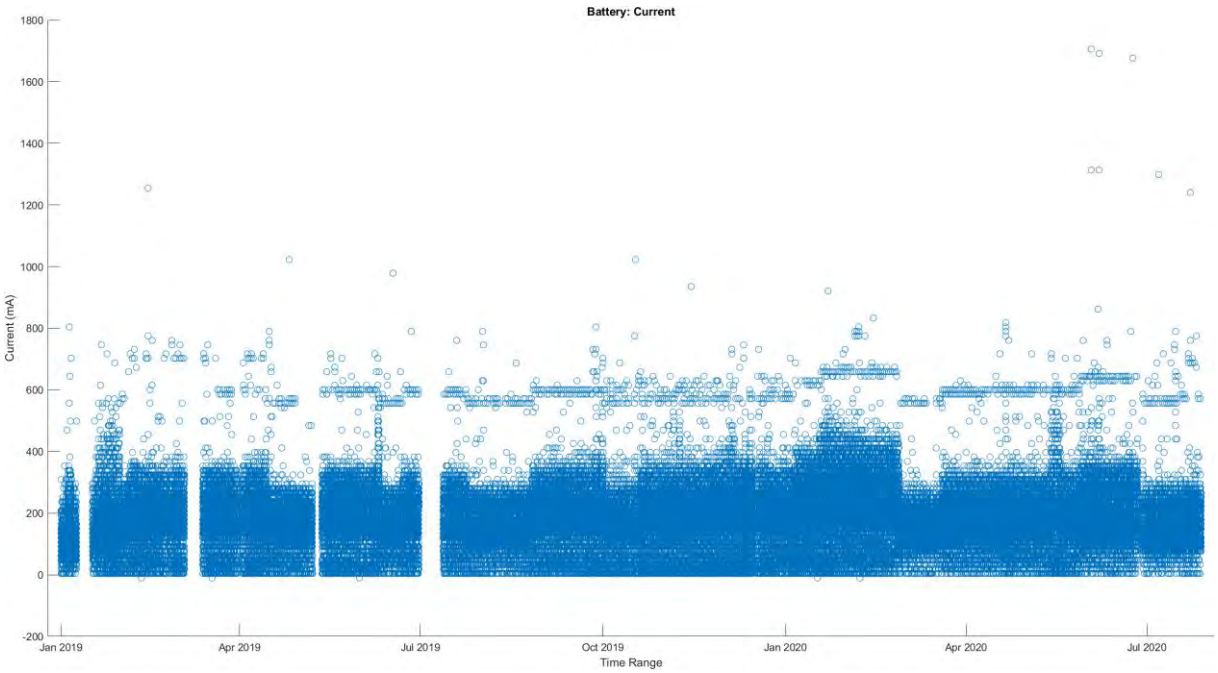

Figure 4.15: Battery Current

Removing the outliers, a clearer depiction of the behaviour, as seen in Figure 4.16.

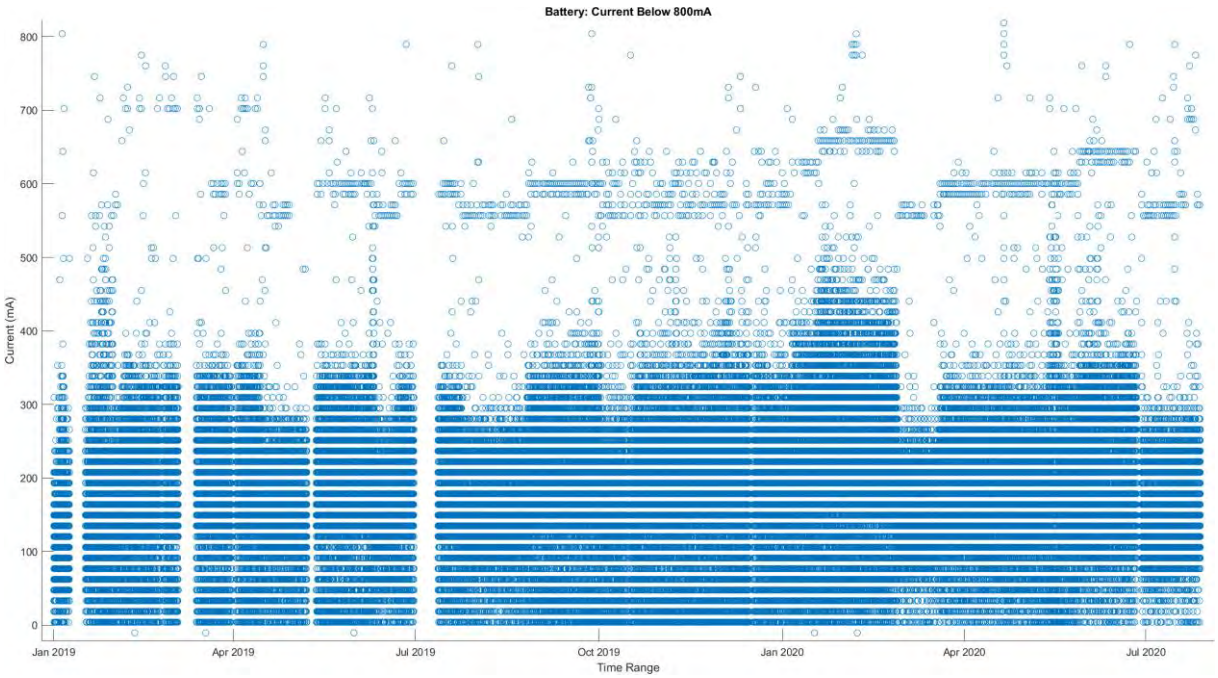

Figure 4.16: Battery Current Below 800 mA

By choosing and expanding a random sample, an insight into the average performance is obtained, such as for 24 November 2019 UTC. This is presented in the figure below.

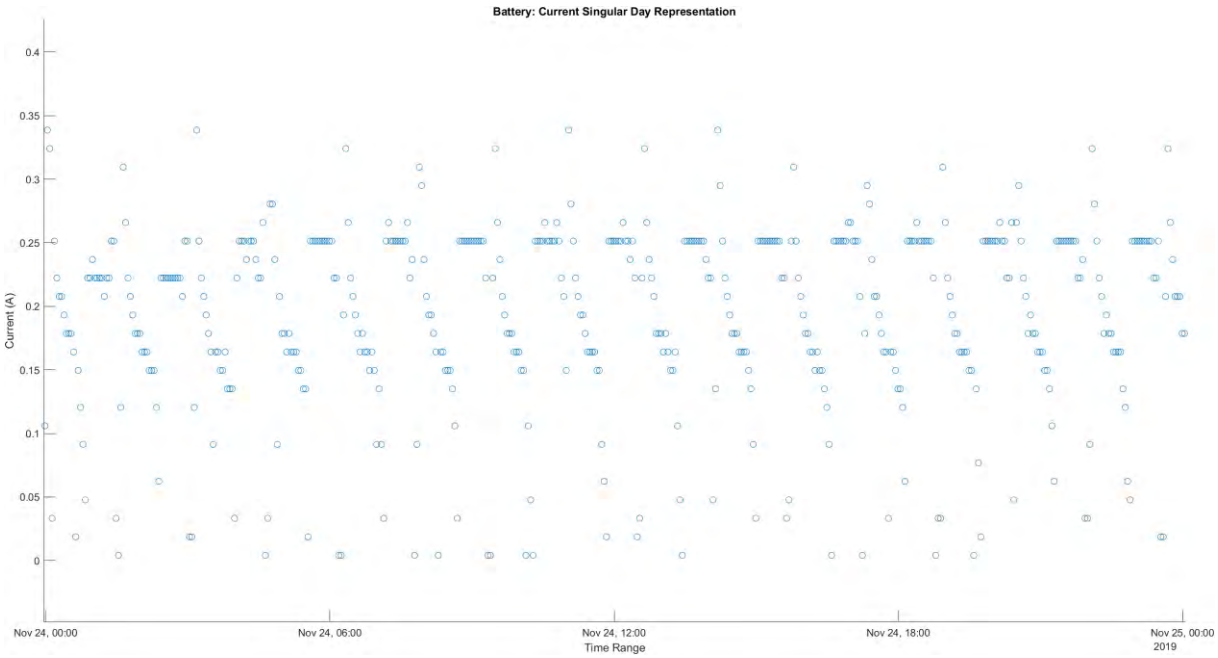

Figure 4.17: Battery Current Singular Day Representation

It can be seen that the battery's current ranges from 0A to 0.35A.

4.2.1.2 Data Analysis

This section gives details regarding the basic statistic, probability density function and cumulative density function for the battery current

4.2.1.2.1 Basic Statistics

The basic statistics for the battery current is presented in Table 4.7.

Table 4.7: Battery Current Basic Statistics

Statistic	Current (A)
Mean	0.192
Median	0.208
Mode	0.251
Range	1.716
Minimum value	-0.010
Maximum value	1.706
Variance	0.007
Standard deviation	0.082

4.2.1.2.2 Probability Density Function

The PDF for the battery current is presented in Figure 4.18.

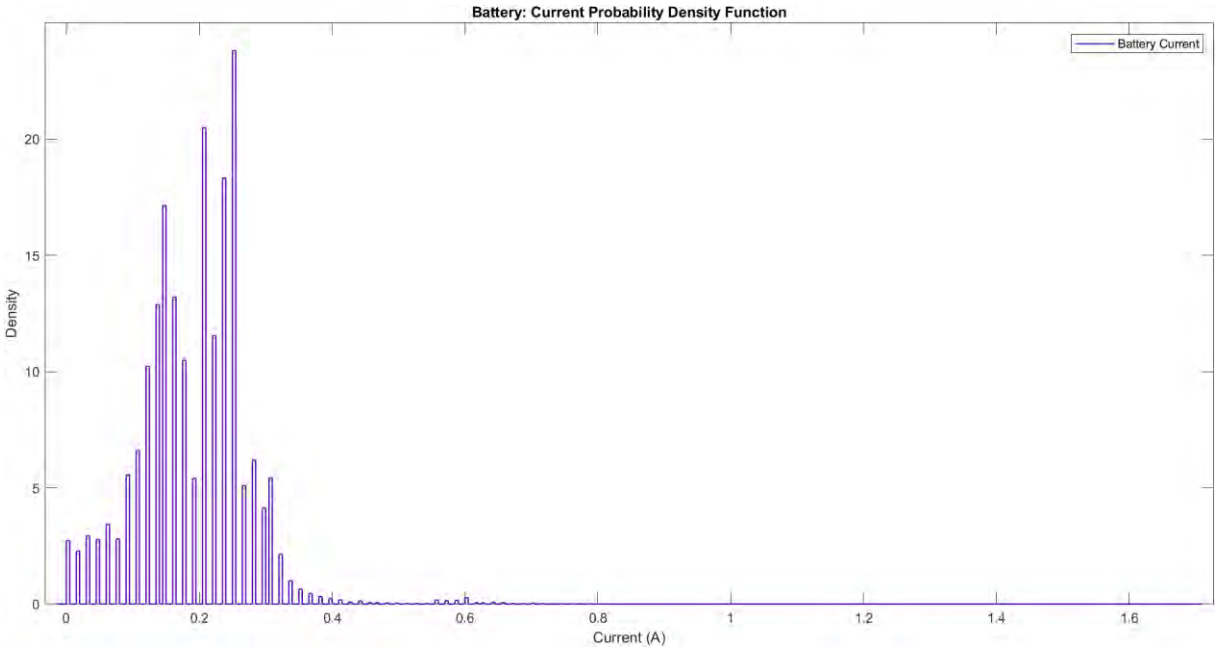

Figure 4.18: Battery Current Probability Density Function

4.2.1.2.3 Cumulative Density Function

The CDF for the battery current is presented in Figure B.6 in Appendix B.

4.2.2 Battery Voltage

This section shows the raw telemetry data as well as the resulting data analysis for the battery voltage

4.2.2.1 Raw Telemetry

Evident from the battery voltage telemetry shown in Figure A.3 (Appendix A) are outliers, causing most of the data to be visually compressed. When these outliers are removed, as described earlier, a clearer behavioural pattern is presented in Figure 4.19.

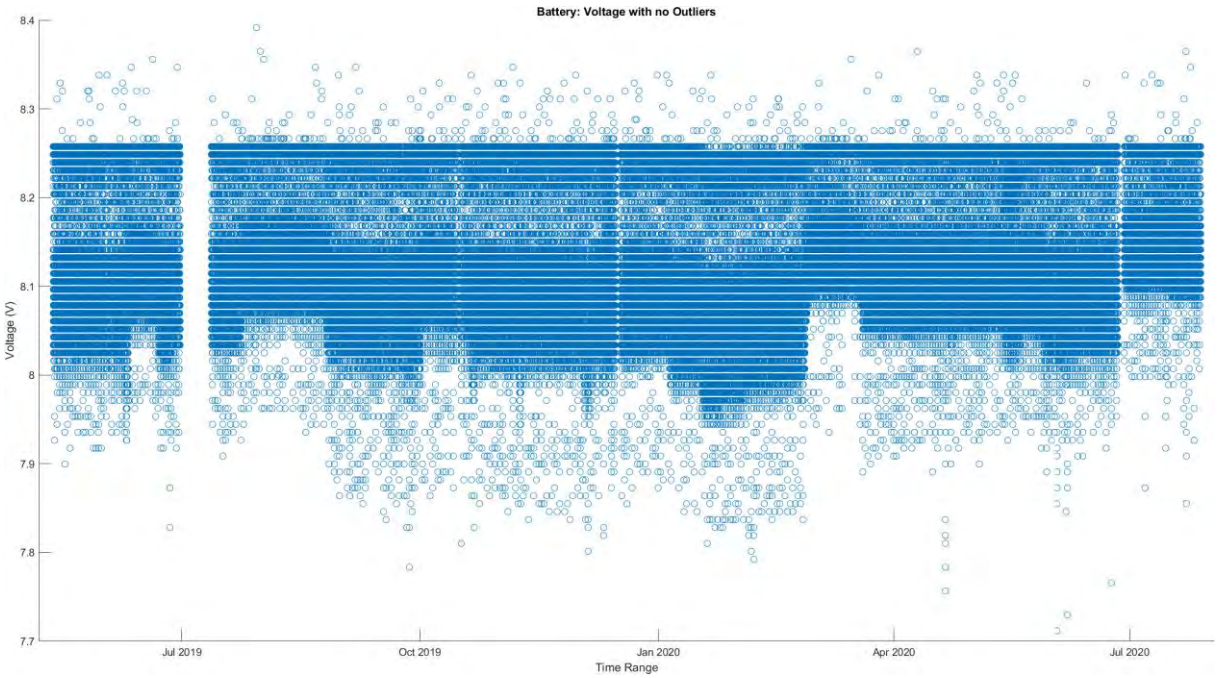

Figure 4.19: Battery Voltage with no Outliers

Even with the removal of any outliers, the data being presented was still dense. Therefore, a single day (12 December 2019 UTC) was chosen to represent the typical behavioural characteristics. This is presented in Figure 4.20.

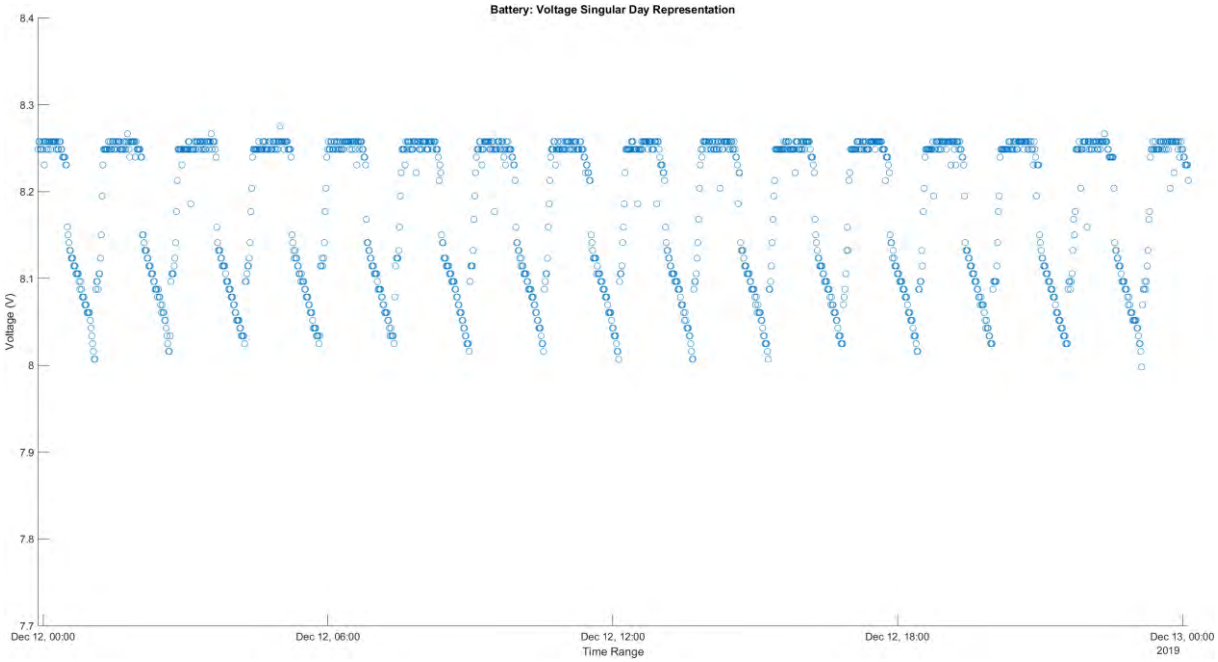

Figure 4.20: Battery Voltage Singular Day Representation

As described in the power budget of ZACube-2, it was stated that the maximum DoD, or depth of discharge, for the battery was to be 20%. The battery used for ZACube-2 has a charge limit of 8.4 V, therefore, this equates to a minimum battery charge of 6.72V.

The maximum and minimum battery charge values were found to be 8.392V and 7.685V, respectively, indicating that the maximum discharge voltage experienced is 0.707V, or 8.42%, which is less than that of the maximum designed discharge value of 20%.

Figure 4.21 is a depiction in which the data represented in orange is the battery telemetry voltage, whilst the blue line is the DoD voltage value of 6.72V.

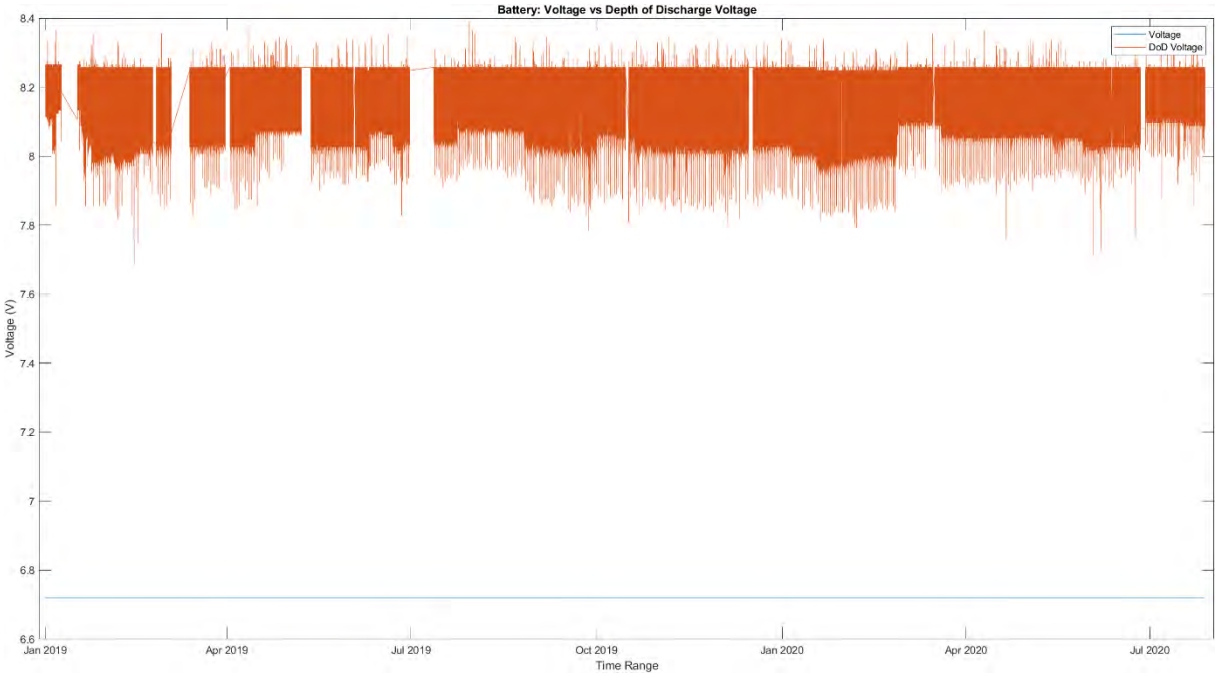

Figure 4.21: Battery Voltage vs Depth of Discharge Voltage

4.2.2.2 Data Analysis

This section gives details regarding the basic statistic, probability density function and cumulative density function for the battery voltage.

4.2.2.2.1 Basic Statistics

The basic statistics for the battery voltage is summarised in Table 4.8.

Table 4.8: Battery Voltage Basic Statistics

Statistic	Voltage (V)
Mean	8.180
Median	8.240
Mode	8.258
Range	0.707
Minimum value	7.685
Maximum value	8.392
Variance	0.007
Standard deviation	0.084

4.2.2.2.2 Probability Density Function

The PDF for the battery voltage is presented in Figure 4.22.

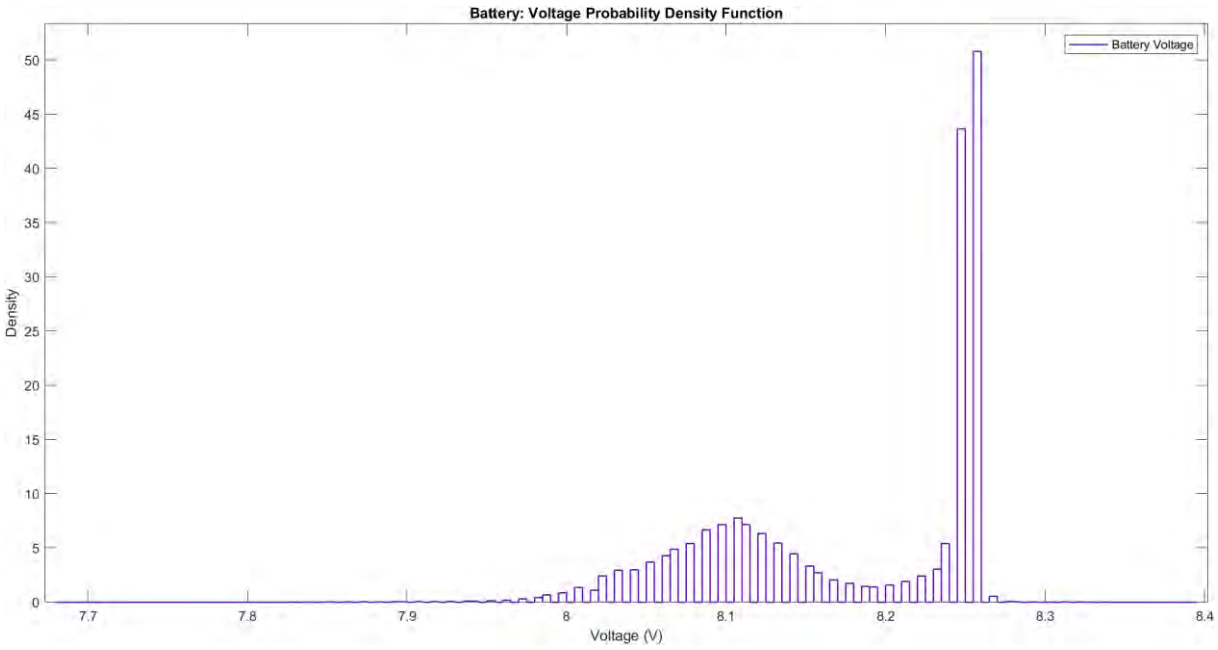

Figure 4.22: Battery Voltage Probability Density Function

4.2.2.2.3 Cumulative Density Function

The CDF for the battery voltage is given in Figure B.7 in Appendix B.

4.2.3 Battery Power

This section shows the raw telemetry data as well as the resulting data analysis for the battery power.

4.2.3.1 Raw Telemetry

With the current and voltage values for the battery known, the battery power can be calculated and plotted as seen in Figure 4.23.

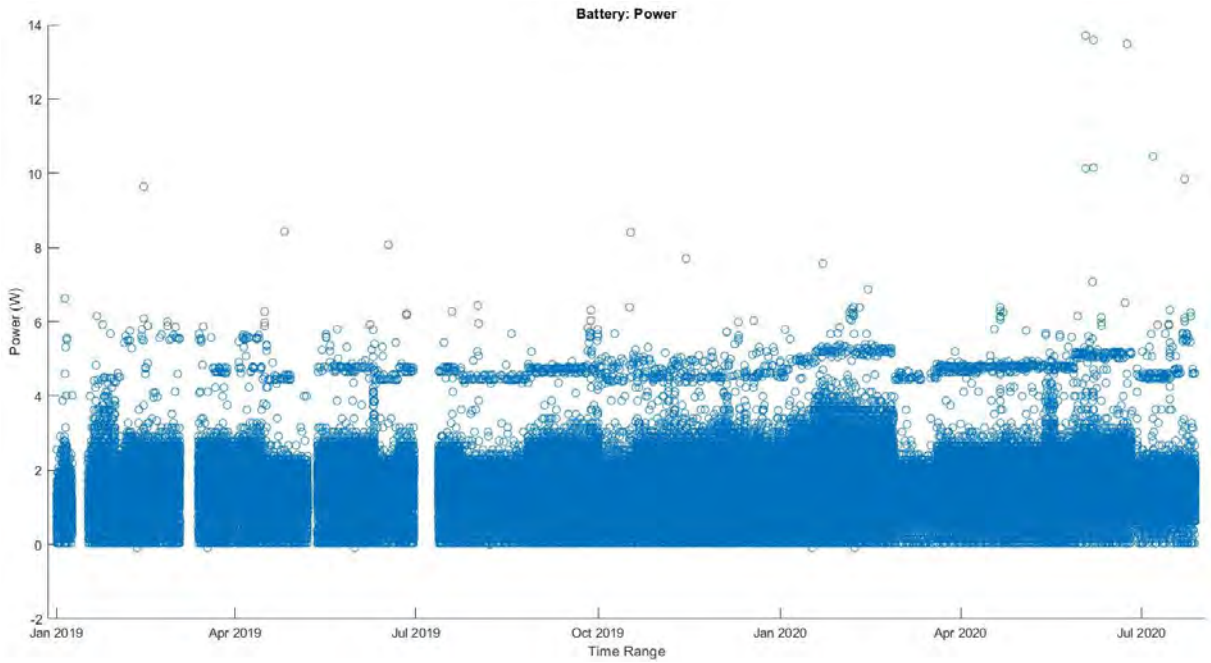

Figure 4.23: Battery Power

Most of the values for the battery power are below 6W. Figure 4.24 shows the behaviour of the battery's power below 6W to gain insight into how the battery is utilised over the selected temporal period.

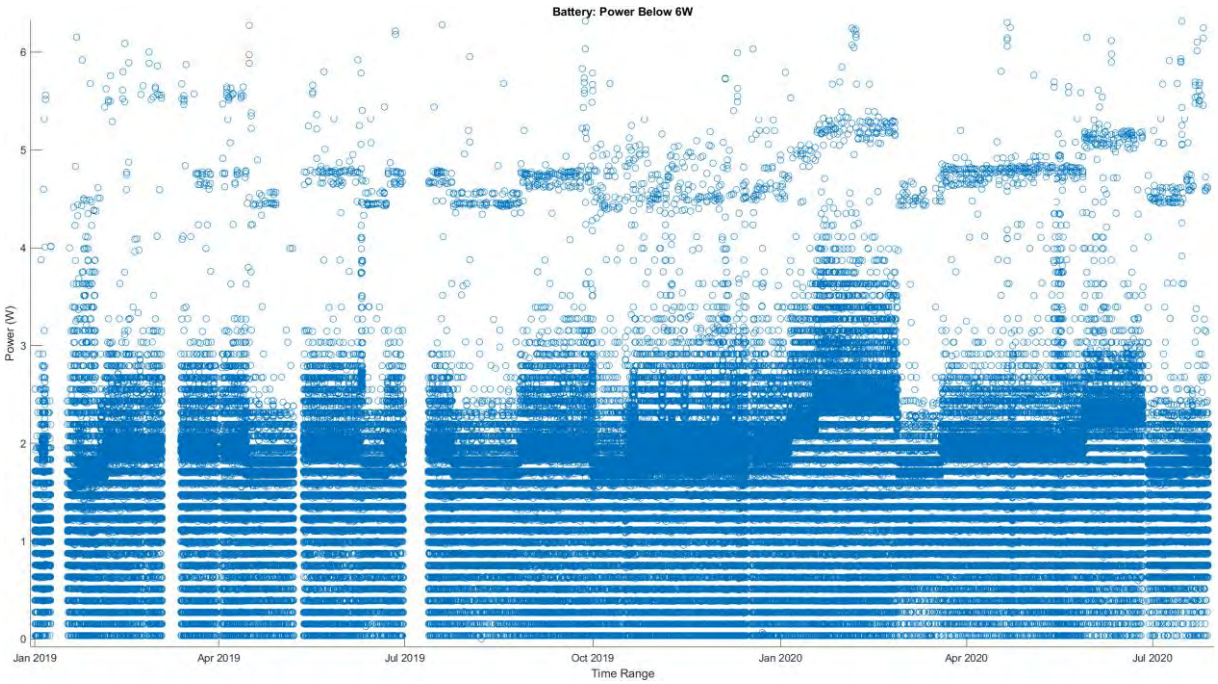

Figure 4.24: Battery Power Below 6W

4.2.3.2 Data Analysis

This section gives details regarding the basic statistic, probability density function and cumulative density function for the battery power

4.2.3.2.1 Basic Statistics

The basic statistics of the battery power is summarised in Table 4.8.

Table 4.8: Battery Power Basic Statistics

Statistic	Power (W)
Mean	1.564
Median	1.677
Mode	1.235
Range	13.790
Minimum value	-0.086
Maximum value	13.704
Variance	0.433
Standard deviation	0.658

4.2.3.2.2 Probability Density Function

The PDF for the battery power is presented in Figure 4.25.

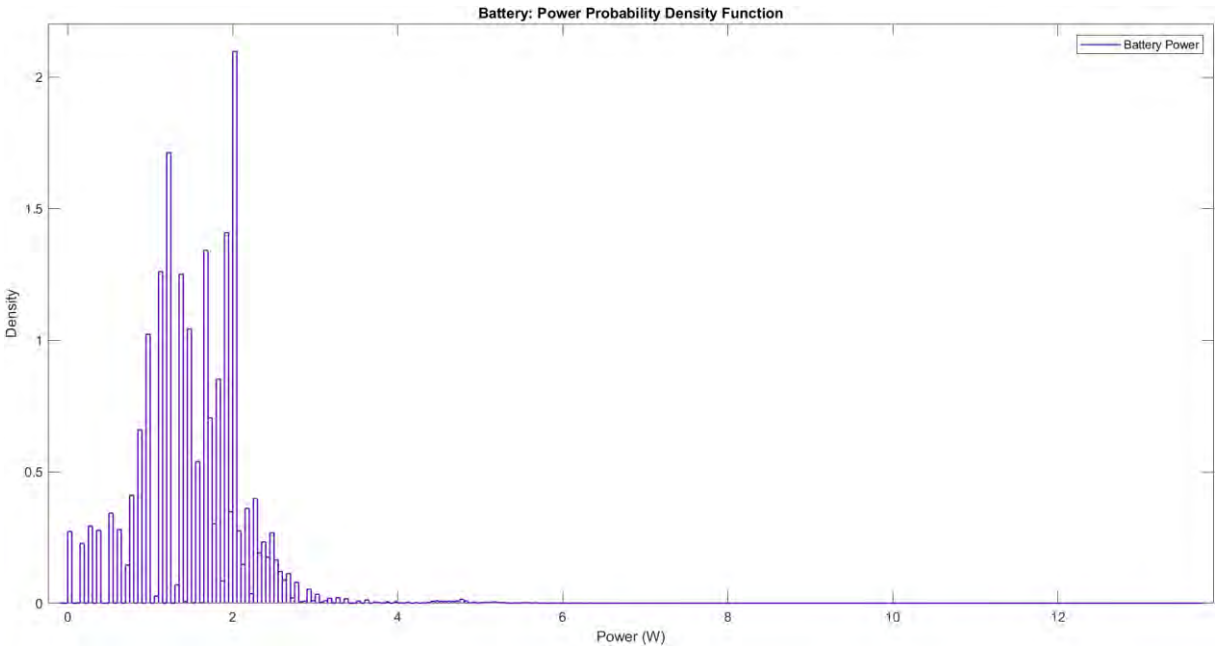

Figure 4.25: Battery Power Probability Density Function

4.2.3.2.3 Cumulative Density Function

The CDF for the battery power can be referred to in Figure B.8 in Appendix B.

4.2.4 Battery Daughterboards' Temperature

This section shows the raw telemetry data as well as the resulting data analysis for the battery's daughterboards' temperature.

4.2.4.1 Raw Telemetry

The battery consists of three daughterboards, each with a temperature sensor. Figure A.4 in Appendix A depicts the three respective daughterboard temperatures. With outliers removed, the telemetry is presented in Figure 4.25.

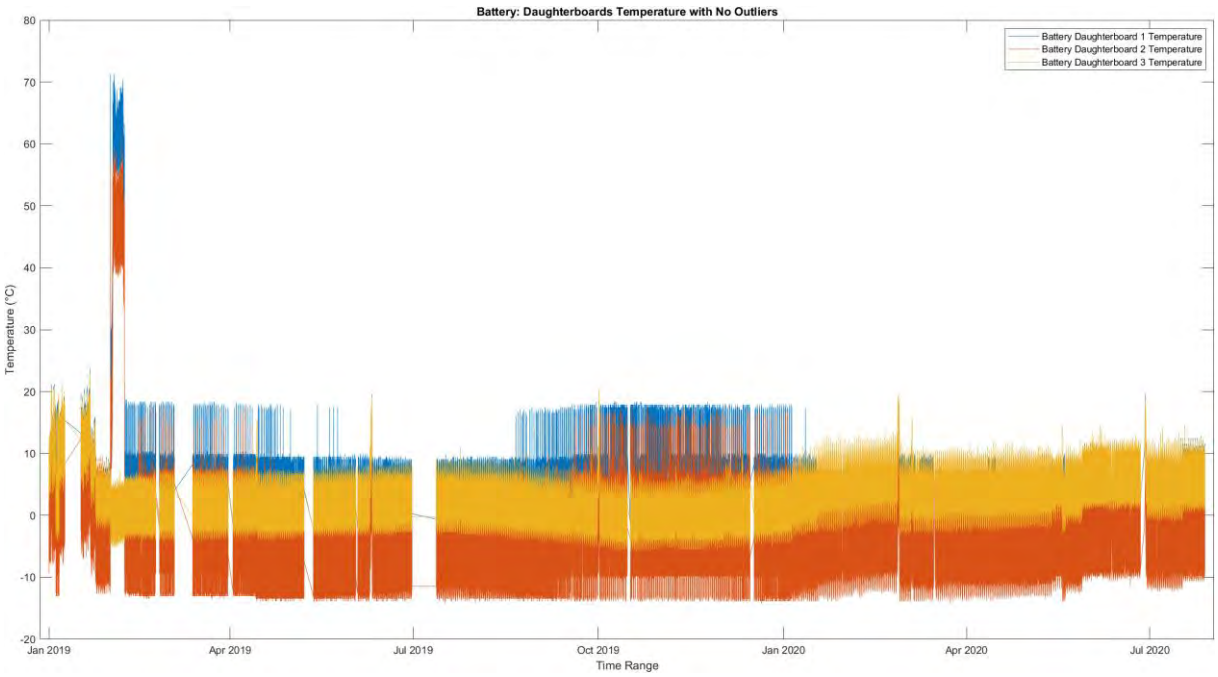

Figure 4.25: Daughterboards Temperatures with No Outliers

4.2.4.2 Data Analysis

This section gives details regarding the basic statistic, probability density function and cumulative density function for the temperature of the battery daughterboard.

4.2.4.2.1 Basic Statistic

The basic statistic for the combined average battery daughterboard temperatures is summarised in the table below.

Table 4.9: Battery Average Daughterboards Temperature Basic Statistics

Statistic	**Temperature (°C)**
Mean	2.3
Median	1.7
Mode	-1.4
Range	51.5
Minimum value	-6.6
Maximum value	44.9
Variance	30.7
Standard deviation	5.5

4.2.4.2.2 Probability Density Function

The PDF for the average of the battery daughterboard temperatures can be seen in the figure below.

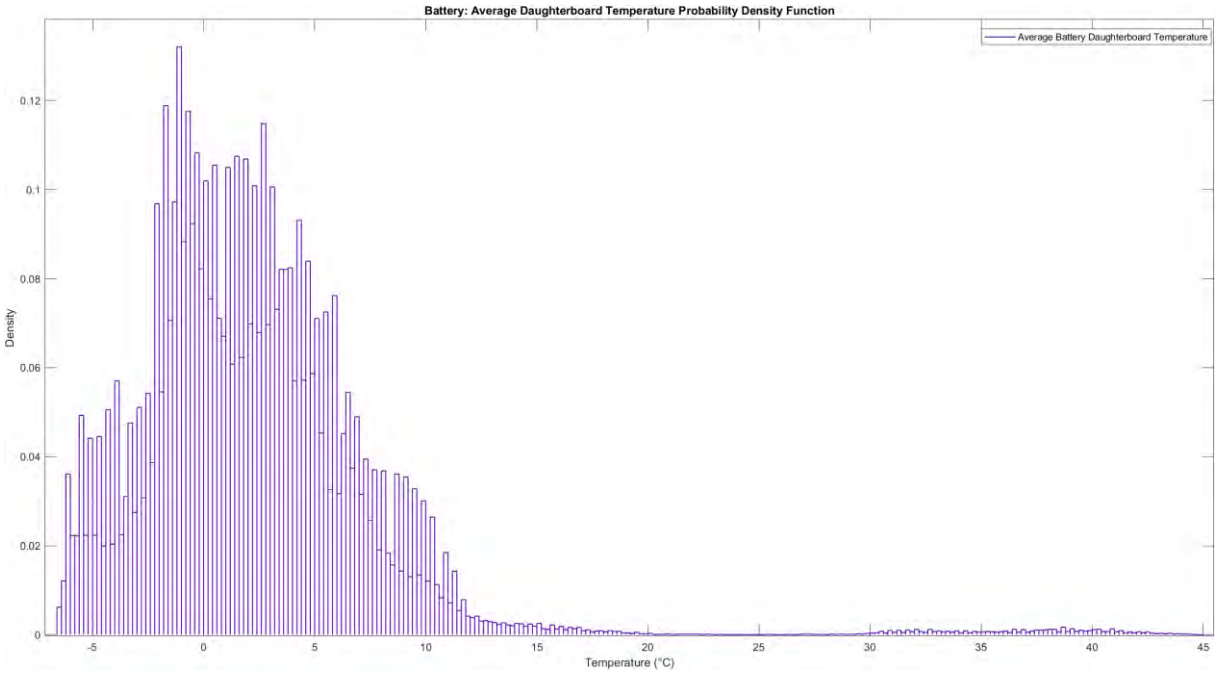

Figure 4.26: Battery Average Daughterboard Temperature Probability Density Function

4.2.4.2.3 Cumulative Density Function

The CDF for the average battery daughterboard temperature is presented in Figure B.9 in Appendix B.

4.2.5 Battery Motherboard Temperature

This section shows the raw telemetry data as well as the resulting data analysis for the battery's motherboard temperature.

4.2.5.1 Raw Telemetry

The temperature for the battery can be seen in Figure A.5. With outliers removed, a clearer presentation is provided in Figure 4.27.

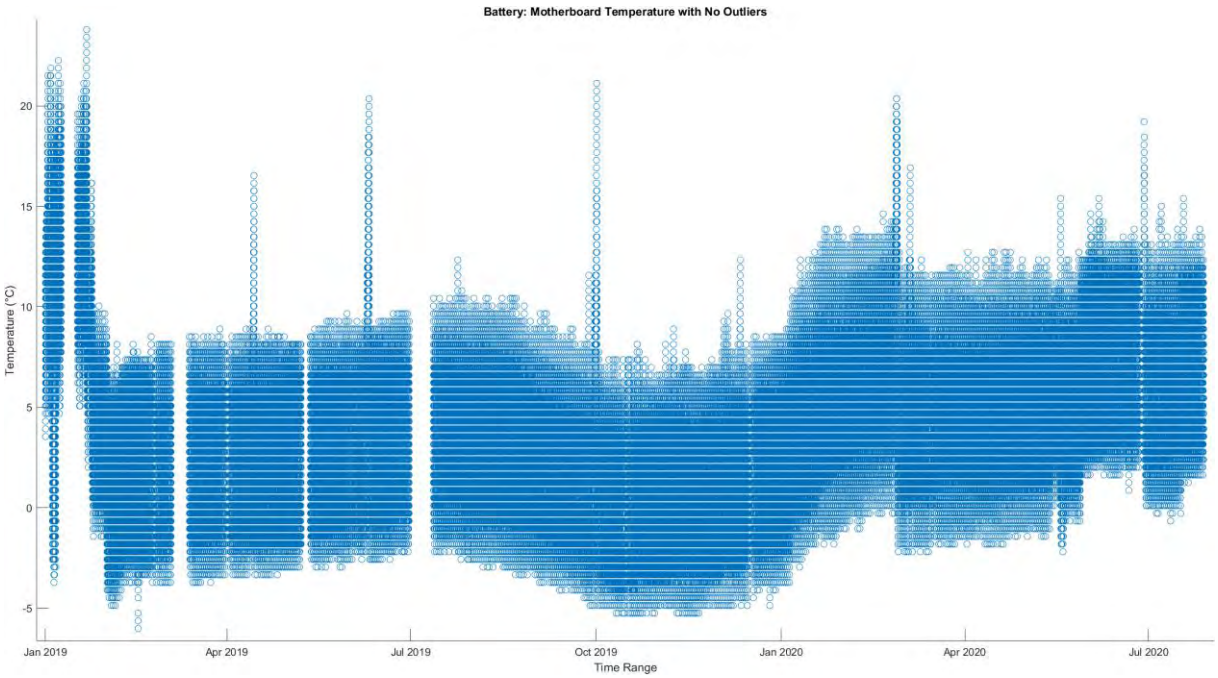

Figure 4.27: Battery Motherboard Temperature with No Outliers

4.2.5.2 Data Analysis

This section gives details regarding the basic statistic, probability density function and cumulative density function for the battery's motherboards' temperature.

4.2.5.2.1 Basic Statistics

The basic statistics for the motherboard temperature of the battery is summarised in Table 4.10.

Table 4.10: Battery Motherboard Temperature Basic Statistics

Statistic	**Temperature (°C)**
Mean	4.2
Median	4.31
Mode	4.7
Range	29.8
Minimum value	-6.0
Maximum value	23.8
Variance	17.3
Standard deviation	4.2

4.2.5.2.2 Probability Density Function

The PDF for the temperature of the battery is presented in Figure 4.28.

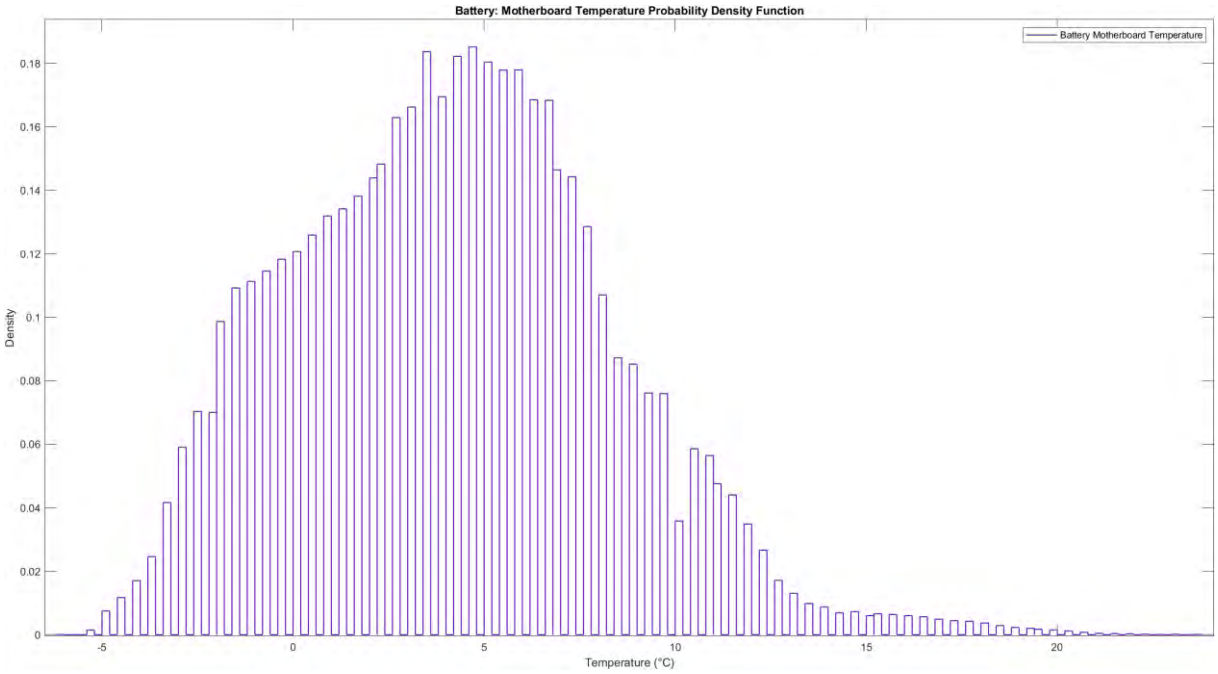

Figure 4.28: Battery Motherboard Temperature Probability Density Function

4.2.5.2.3 Cumulative Density Function

The CDF for the motherboard temperature of the battery can be found in Figure B.10 in Appendix B.

4.2.6 Battery Correlation

The correlation between these three telemetry channels is summarised in Table 4.11.

Table 4.11: Battery Telemetry Correlation

Telemetry Channel	Current	Voltage	Power	Ave DB Temp	MB Temp
Current	1	-0,022	-0,003	0,136	-0,038
Voltage	-0,022	1	0,733	-0,064	-0,239
Power	-0,003	0,733	1	-0,038	-0,159
Ave DB Temp	0,136	-0,064	-0,038	1	0,480
MB Temp	-0,038	-0,239	-0,159	0,480	1

Please note that DB and MB have been used as shorthand for the daughterboard and motherboard, respectively.

4.3 Electrical Power System (EPS)

The EPS comprises four regulated power bus lines; 3.3V, 5V, 12V, and an unregulated battery bus that is directly connected to the battery. The various subsystems that are being supplied with power from the four bus lines are listed in Table 4.12.

Table 4.12: EPS Bus Powered Subsystems

EPS Power Bus	Subsystems Powered
3.3V regulated	Attitude determination control system (ADCS)
	UTRX (UHF)
	Deployable antenna
5V regulated	K-line imager
	HSTX (S-band)
	XTX (X-band)
	On board computer (OBC)
	UTRX (UHF)
	Attitude determination control system (ADCS)
12V regulated	EPS motherboard
Unregulated	Software defined radio (SDR)

The following subsections highlight the raw telemetry data from each of the power buses, showing the current and subsequent power generation from the respective power bus from 12 May 2019 09:06:05 UTC to 28 July 2020 09:30:15 UTC with a 3-minute time step.

4.3.1 3.3V Regulated Bus

This section shows the raw telemetry data as well as the resulting data analysis for the 3.3V regulated bus for the EPS.

4.3.1.1 Raw Telemetry

The 3.3V bus current is shown in Figure 4.29.

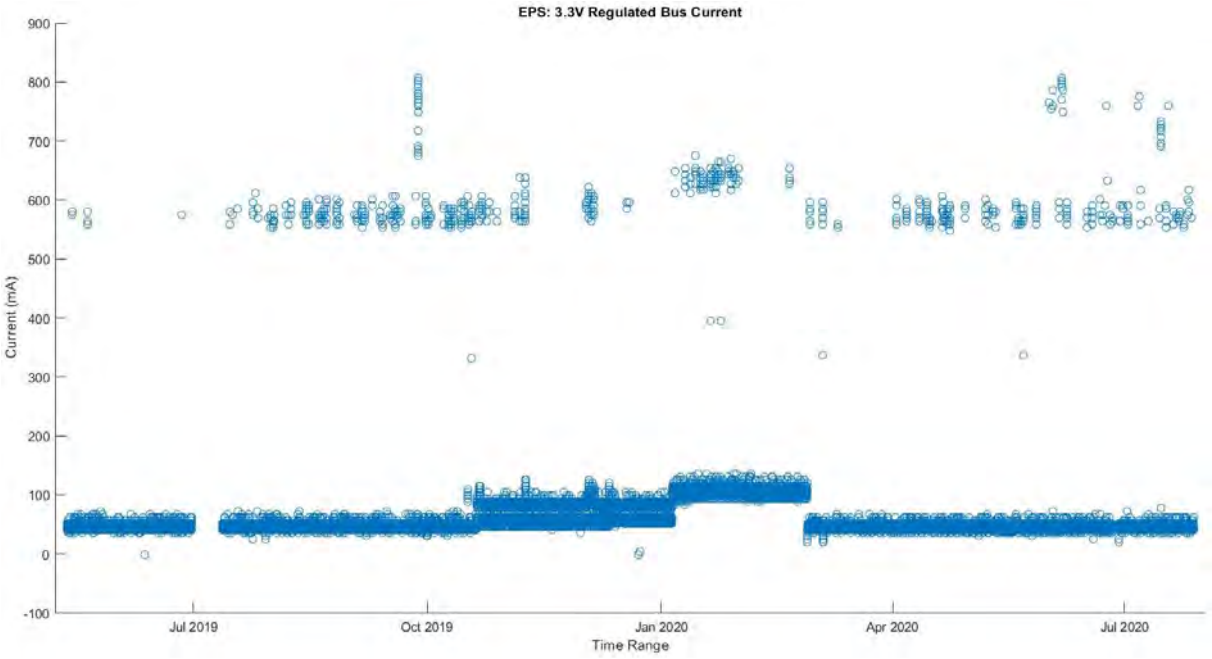

Figure 4.29: EPS 3.3V Regulated Bus Current

With the current and the known voltage, the power is calculated and shown in Figure 4.30.

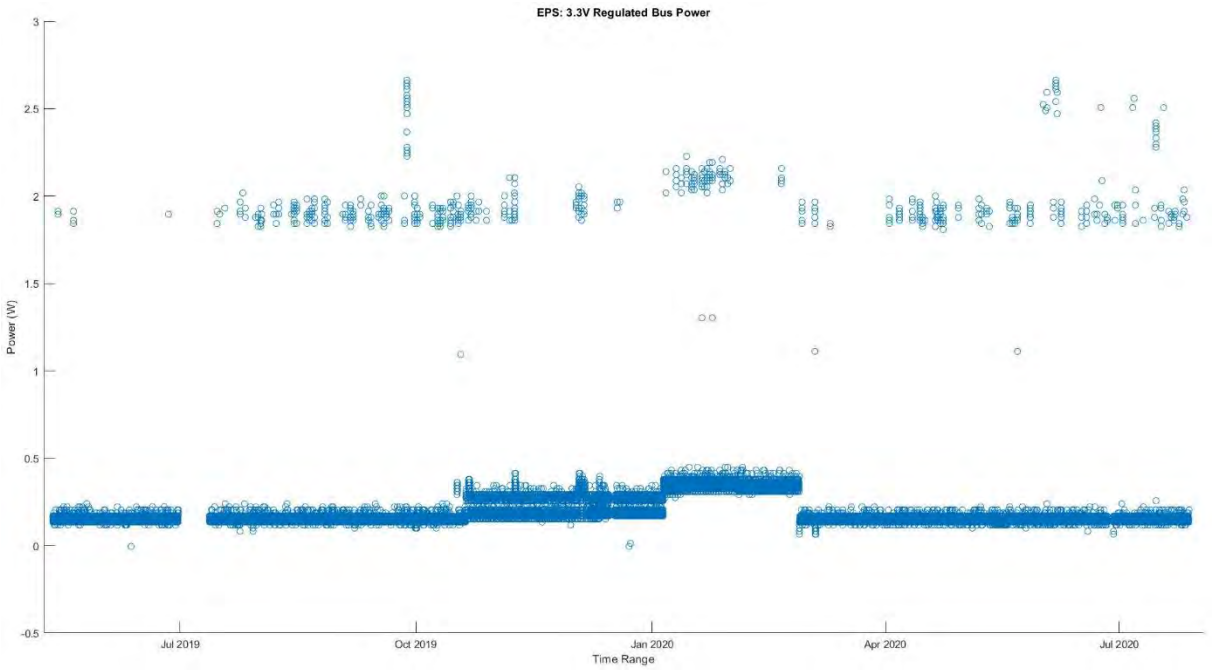

Figure 4.30: EPS 3.3V Regulated Bus Power

From these figures, most of the current and power data points lie below 0.5A and 0.5W, respectively. From the current graph, the maximum current is approximately 2.7A, which

occurred at a single instance and is below the manufacturer's minimum rated LCL trip point of 4.4A.

4.3.1.2 Data Analysis

This section gives details regarding the basic statistic, probability density function and cumulative density function for the EPS 3.3V regulated bus current and power.

4.3.1.2.1 Basic Statistics

The basic statistic for the 3.3V regulated bus current and power is summarised in Table 4.13 and Table 4.14, respectively.

Table 4.13: EPS 3.3V Regulated Bus Current Basic Statistics

Statistic	Current (A)
Mean	0.192
Median	0.208
Mode	0.251
Range	1.716
Minimum value	-0.010
Maximum value	1.706
Variance	0.007
Standard deviation	0.082

Table 4.14: EPS 3.3V Regulated Bus Power Basic Statistics

Statistic	Power (W)
Mean	0.191
Median	0.153
Mode	0.153
Range	2.668
Minimum value	-0.004
Maximum value	2.664
Variance	0.015
Standard deviation	0.122

4.3.1.2.2 Probability Density Function

The PDF for the 3.3V regulated bus current and power are presented in Figure 4.31 and Figure 4.32, respectively.

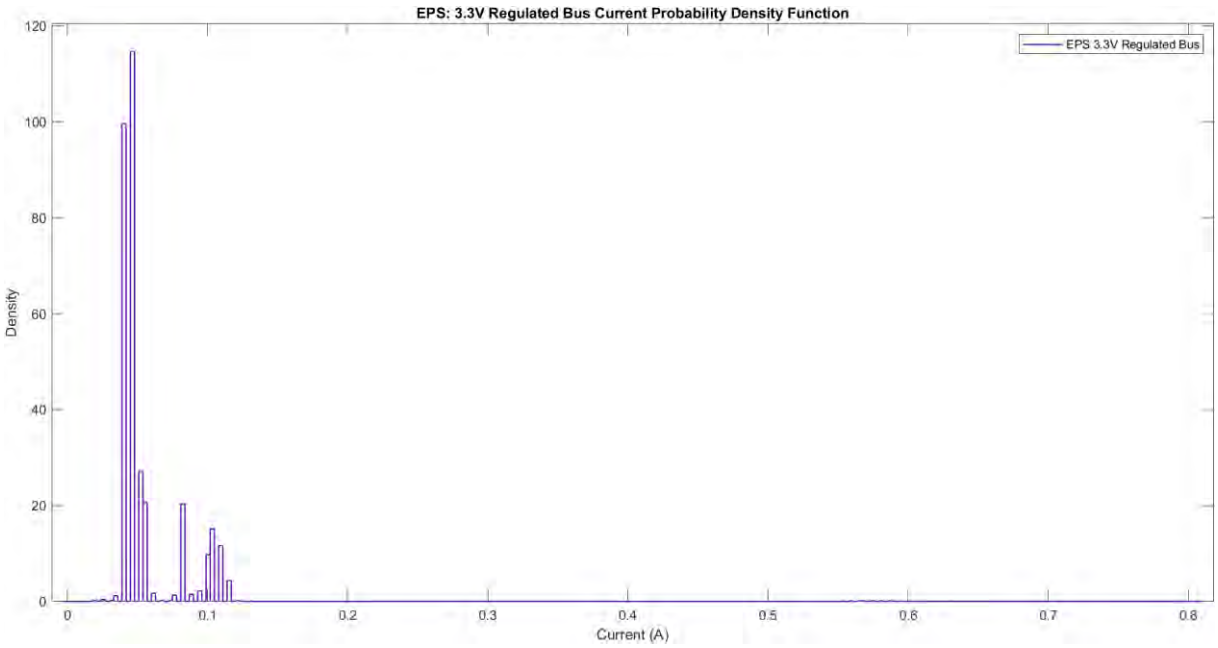

Figure 4.31: EPS 3.3V Regulated Bus Current Probability Density Function

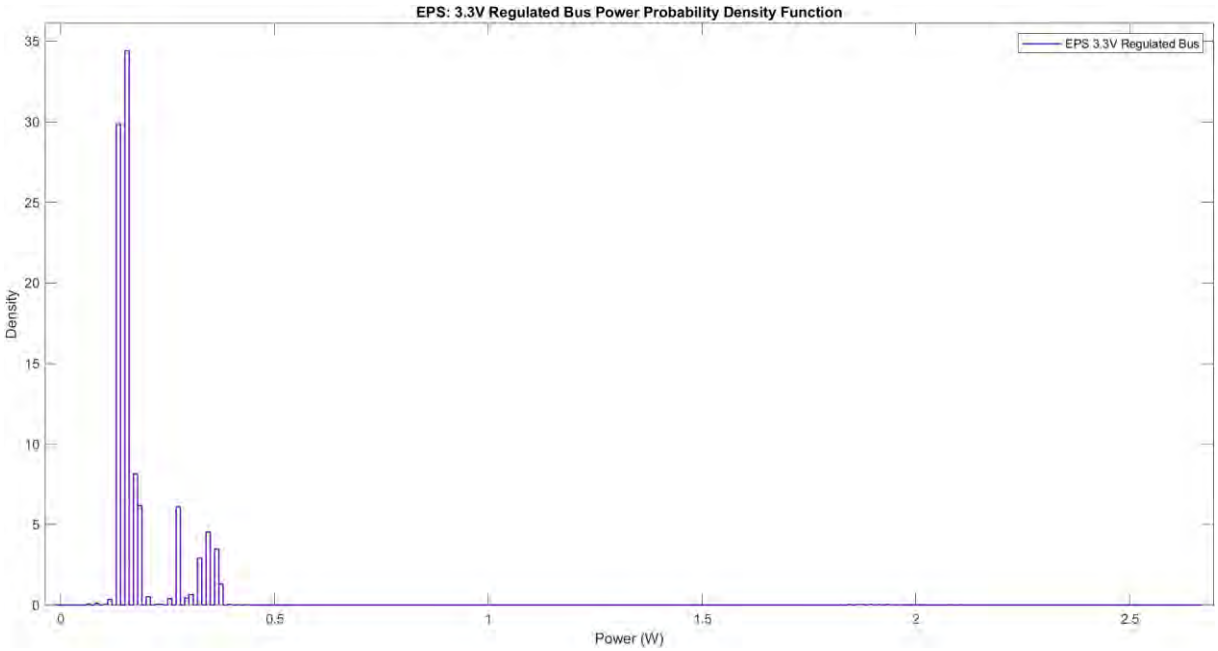

Figure 4.32: EPS 3.3V Regulated Bus Power Probability Density Function

4.3.1.2.3 Cumulative Density Function

The CDF for the 3.3V regulated bus current and power are presented in Figure B.11 and B.12 in Appendix B, respectively.

4.3.2 5V Regulated Bus

This section shows the raw telemetry data as well as the resulting data analysis for the EPS 5V regulated bus.

4.3.2.1 Raw Telemetry

Figure A.6 in Appendix A shows the raw current values for the regulated 5V bus. With outliers removed and displayed in Figure 4.33, a maximum current of approximately 550mA is evident, which is below the minimum rated LCL trip point of 4.4A.

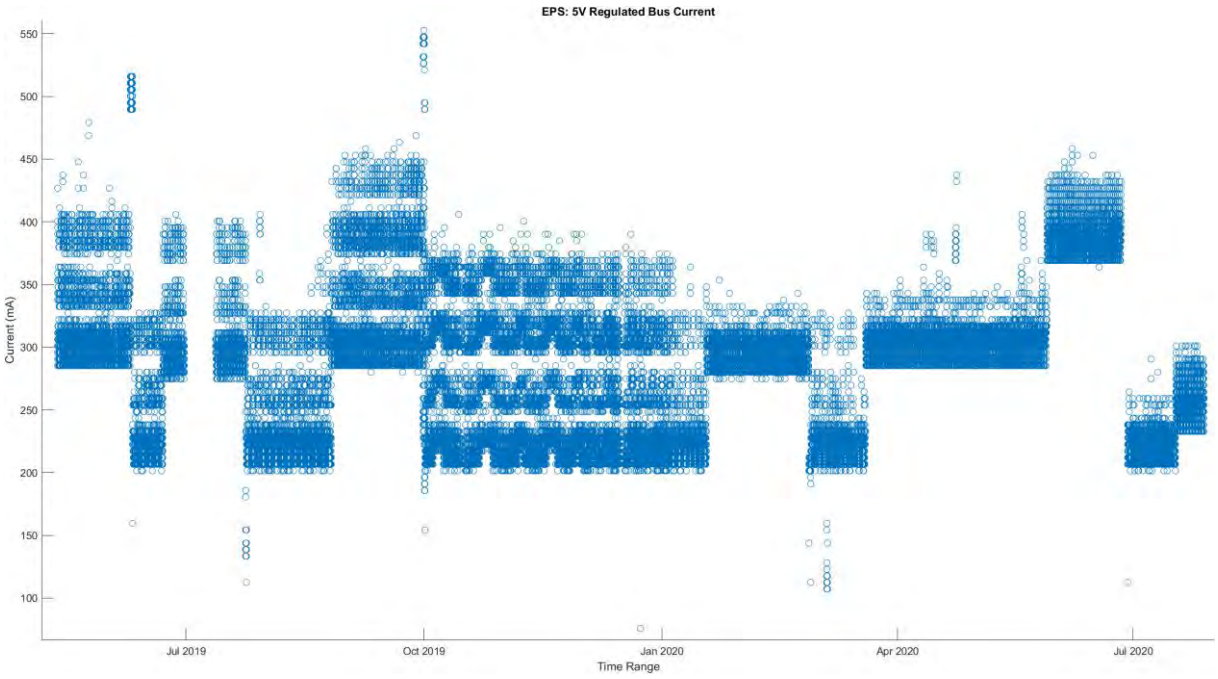

Figure 4.33: EPS 5V Regulated Bus Current with No Outliers

Using the 5V regulated bus current data set that contains no outliers present, the power can be calculated, as presented in Figure 4.34.

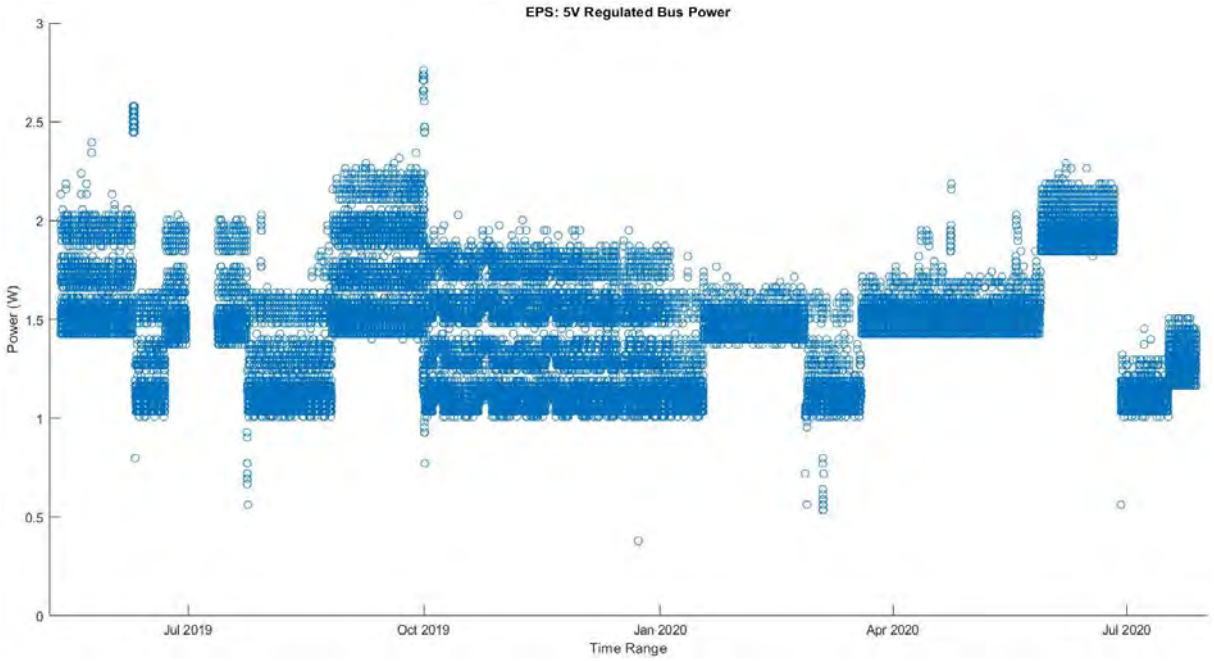

Figure 4.34: EPS 5V Regulated Bus Power

4.3.2.2 Data Analysis

This section gives details regarding the basic statistic, probability density function and cumulative density function for the EPS 5V regulated bus current and power.

4.3.2.2.1 Basic Statistics

The basic statistics for the 5V regulated bus current and power are summarised in Table 4.15 and Table 4.16, respectively.

Table 4.15: EPS 5V Regulated Bus Current Basic Statistics

Statistic	Current (A)
Mean	0.279
Median	0.291
Mode	0.291
Range	0.553
Minimum value	0
Maximum value	0.553
Variance	0.003
Standard deviation	0.057

Table 4.16: EPS 5V Regulated Bus Power Basic Statistics

Statistic	Power (W)
Mean	1.395
Median	1.453

Mode	1.453
Range	2.763
Minimum value	0
Maximum value	2.673
Variance	0.083
Standard deviation	0.287

4.3.2.2.2 Probability Density Function

The PDF for the 5V regulated bus current and power are presented in Figure 4.35 and Figure 4.36, respectively.

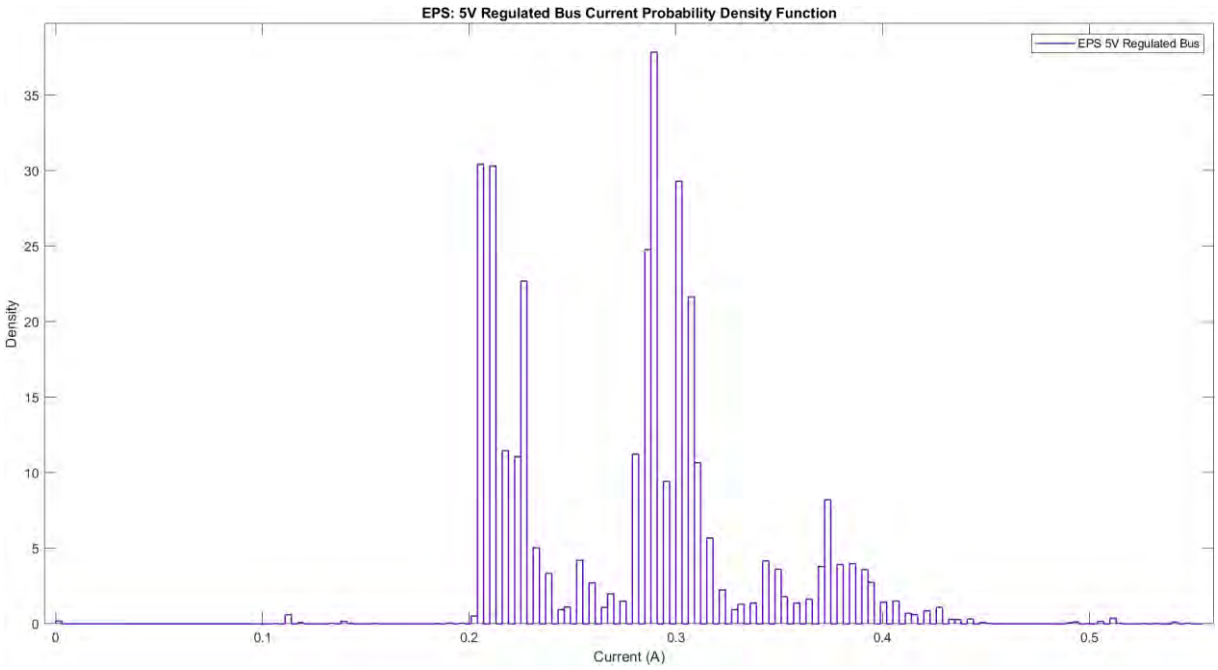

Figure 4.35: EPS 5V Regulated Bus Current Probability Density Function

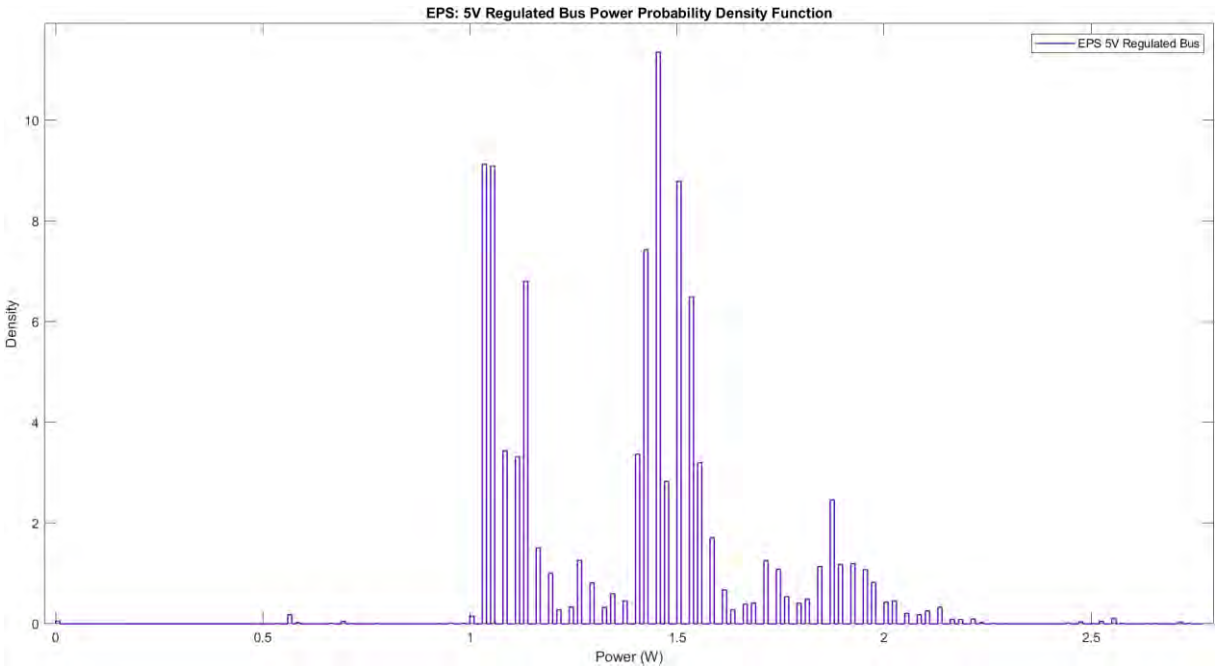

Figure 4.36: EPS: 5V Regulated Bus Power Probability Density Function

4.3.2.2.3 Cumulative Density Function

The CDF for the 5V regulated bus current and power are presented in Figure B.13 and Figure B.14 in Appendix B. respectively.

4.3.3 12V Regulated Bus

This section shows the raw telemetry data as well as the resulting data analysis for the EPS 12V regulated bus.

4.3.3.1 Raw Telemetry

The 12V bus is a regulated bus that is assigned to the EPS motherboard, meaning that a constant voltage is needed because the motherboard oversees the operation of the EPS.

Raw voltage telemetry for this bus can be seen in Figure A.7. With outliners removed, the behaviour of the telemetry data can be seen in Figure 4.37.

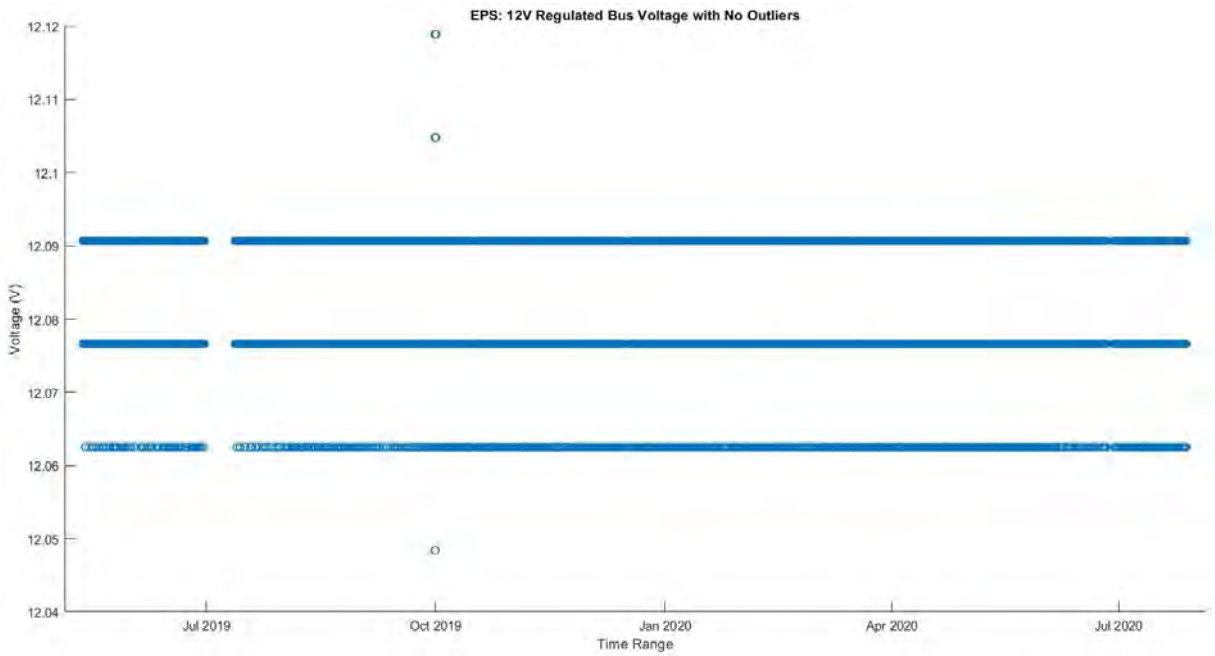

Figure 4.37: EPS 12V Regulated Bus Voltage without Outliers

Unlike the other buses, the 12V bus telemetry only captured the bus voltage and not the current. Due to this fact, no power graph could be calculated.

4.3.3.2 Data Analysis

This section gives details regarding the basic statistic, probability density function and cumulative density function for the EPS 12V regulated bus voltage.

4.3.3.2.1 Basic Statistics

The basic statistics for the 12V regulated bus voltage is summarised in Table 4.17.

Table 4.17: EPS 12V Regulated Bus Voltage Basic Statistic

Statistic	Voltage (V)
Mean	12.081
Median	12.077
Mode	12.077
Range	0.071
Minimum value	12.048
Maximum value	12.119
Variance	0
Standard deviation	0.007

4.3.3.2.2 Probability Density Function

The PDF for the 12V regulated bus voltage is presented in Figure 4.38.

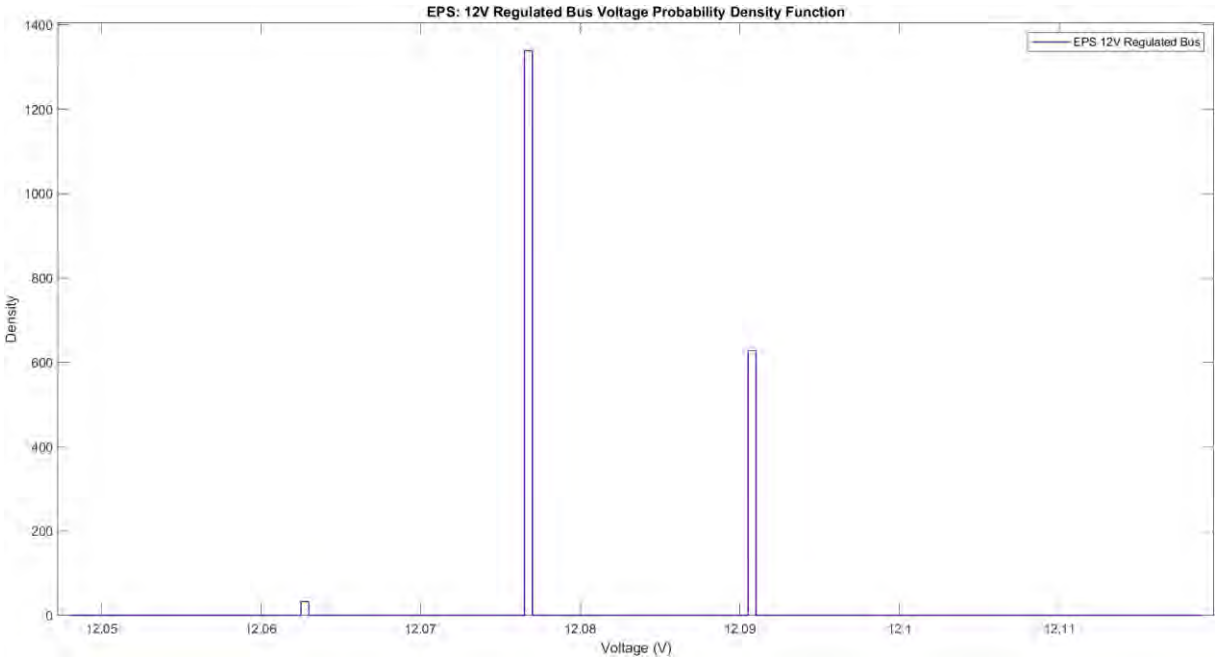

Figure 4.38: EPS 12V Regulated Bus Voltage Probability Density Function

4.3.3.2.3 Cumulative Density Function

The CDF for the 12V regulated bus voltage is presented in Figure B.15 in Appendix B.

4.3.4 Unregulated Battery Bus

This section shows the raw telemetry data as well as the resulting data analysis for the unregulated battery bus.

4.3.4.1 Raw Telemetry

The unregulated bus line's voltage, unlike the other bus lines, is as the name suggests unregulated and directly associated with the status of the battery voltage. The current graph for the unregulated bus is presented in Figure A.8. With outliers removed, the resulting data set is graphically displayed in Figure 4.39.

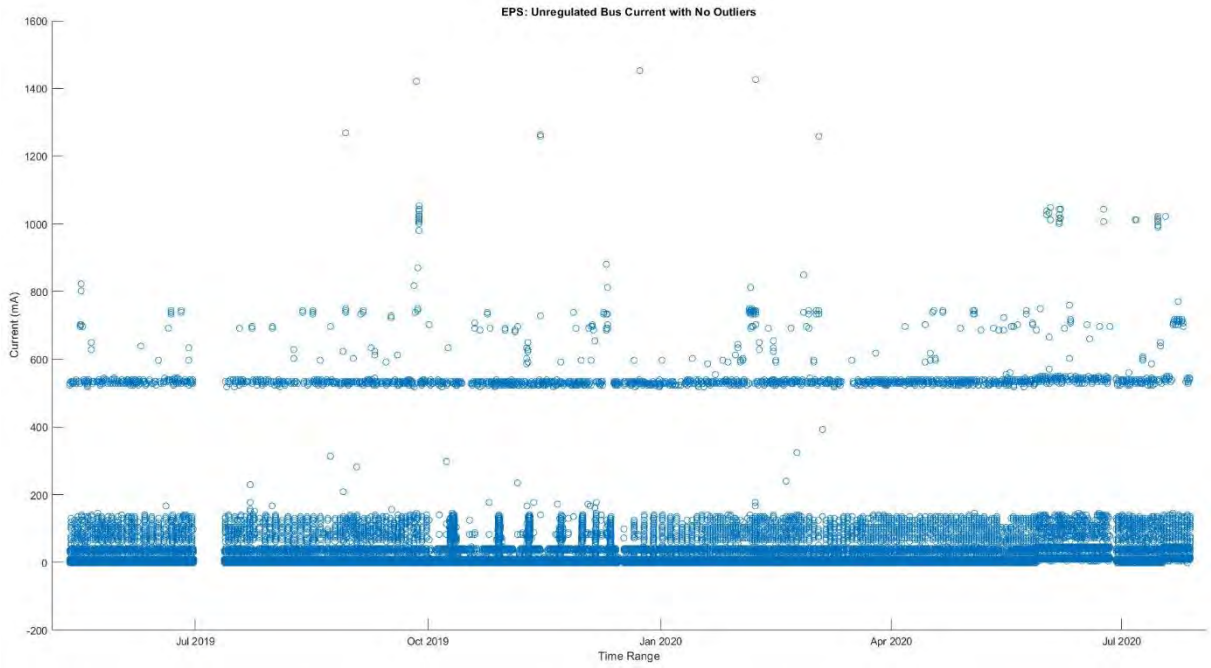

Figure 4.39: EPS Unregulated Battery Bus Current with No Outliers

Using the unregulated battery bus current that contained no outliers, the power generated from this bus was calculated and plotted in Figure 4.40.

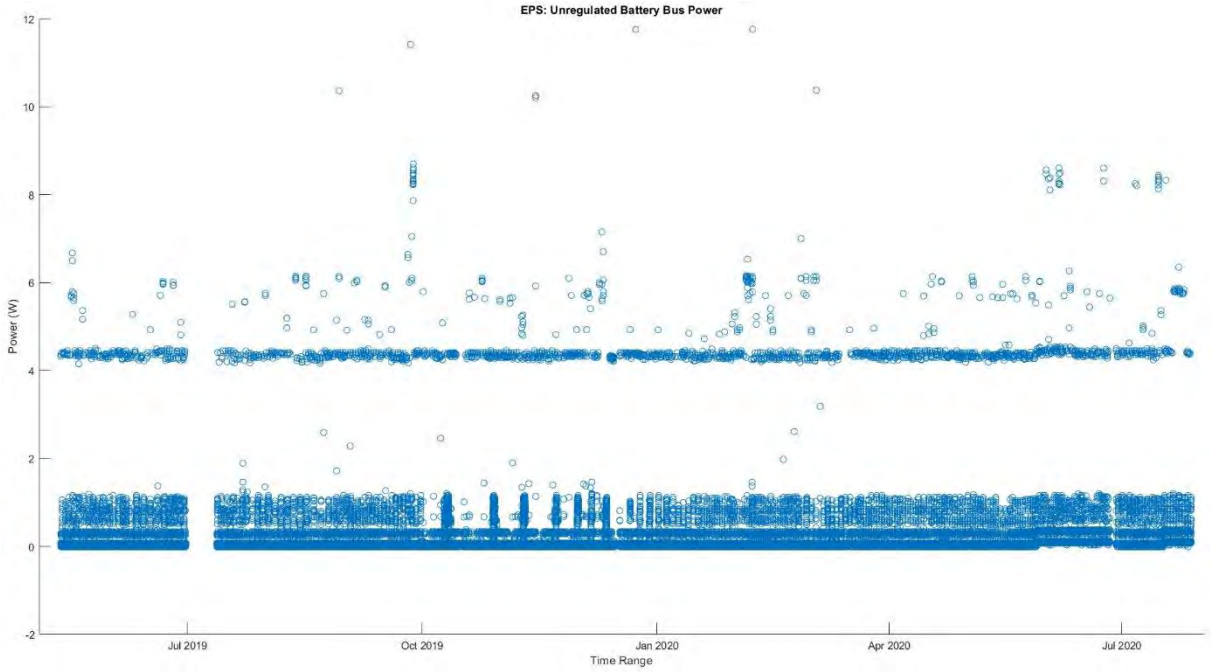

Figure 4.40: Unregulated Battery Bus Power

4.3.4.2 Data Analysis

This section gives details regarding the basic statistic, probability density function and cumulative density function for the EPS unregulated bus current and power.

4.3.4.2.1 Basic Statistics

The basic statistics for the unregulated bus current and power are summarised in Table 4.18 and Table 4.19, respectively.

Table 4.18: EPS Unregulated Bus Current Basic Statistics

Statistic	Current (A)
Mean	0.019
Median	0.009
Mode	0.009
Range	1.454
Minimum value	-0.001
Maximum value	1.453
Variance	0.004
Standard deviation	0.062

Table 4.19: EPS Unregulated Bus Power Basic Statistics

Statistic	Power (W)
Mean	0.151
Median	0.075
Mode	0.033
Range	11.775
Minimum value	-0.011
Maximum value	11.765
Variance	0.259
Standard deviation	0.509

4.3.4.2 Probability Density Function

The PDF for the unregulated bus current and power are presented in Figure 4.41 and Figure 4.42, respectively.

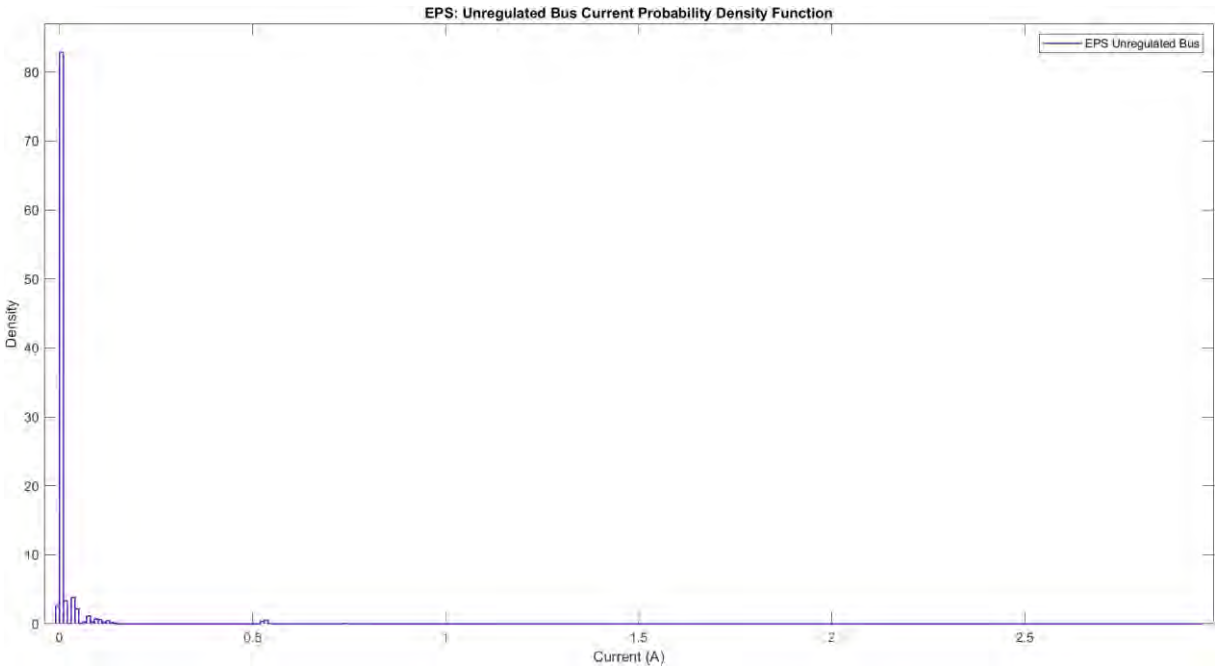

Figure 4.41: EPS Unregulated Bus Current Probability Density Function

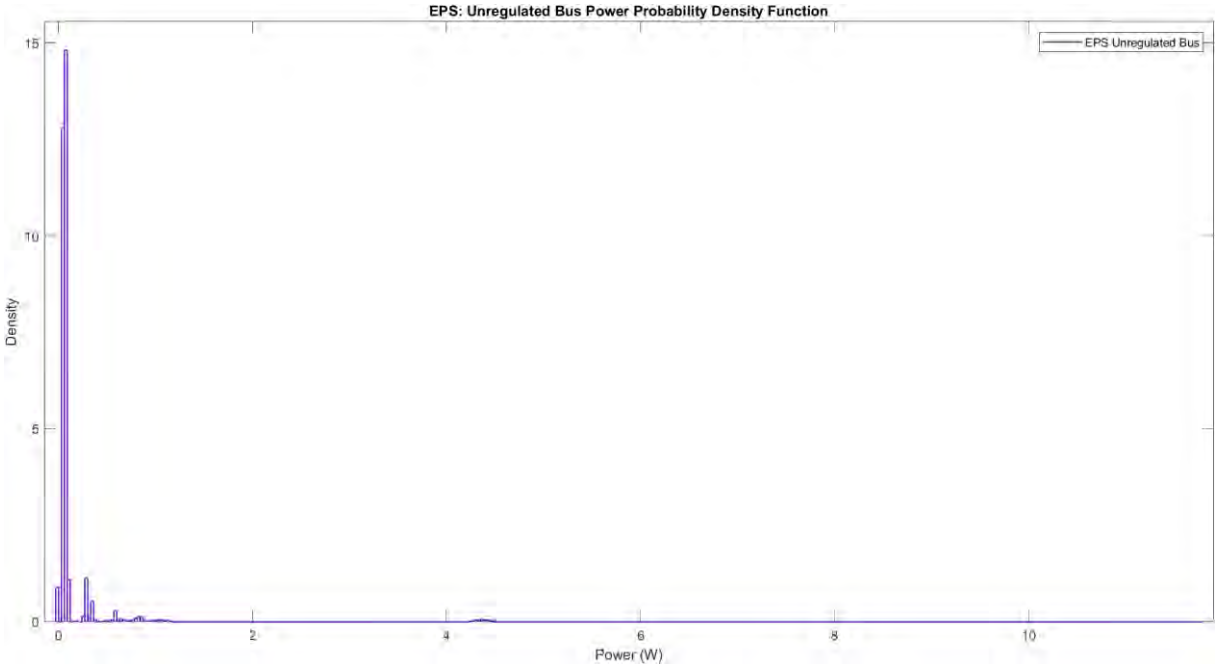

Figure 4.42: EPS Unregulated Bus Power Probability Density Function

4.3.4.3 Cumulative Density Function

The CDF for the unregulated bus current and power are presented in Figure B.16 and B.17 in Appendix B, respectively.

4.3.5 Combined EPS Bus Power

This section shows the raw telemetry data as well as the resulting data analysis for the combined EPS bus power.

4.3.5.1 Raw Telemetry

With all the power values calculated for each of the four buses, the combined instantaneous bus power can be calculated and plotted in Figure 4.43.

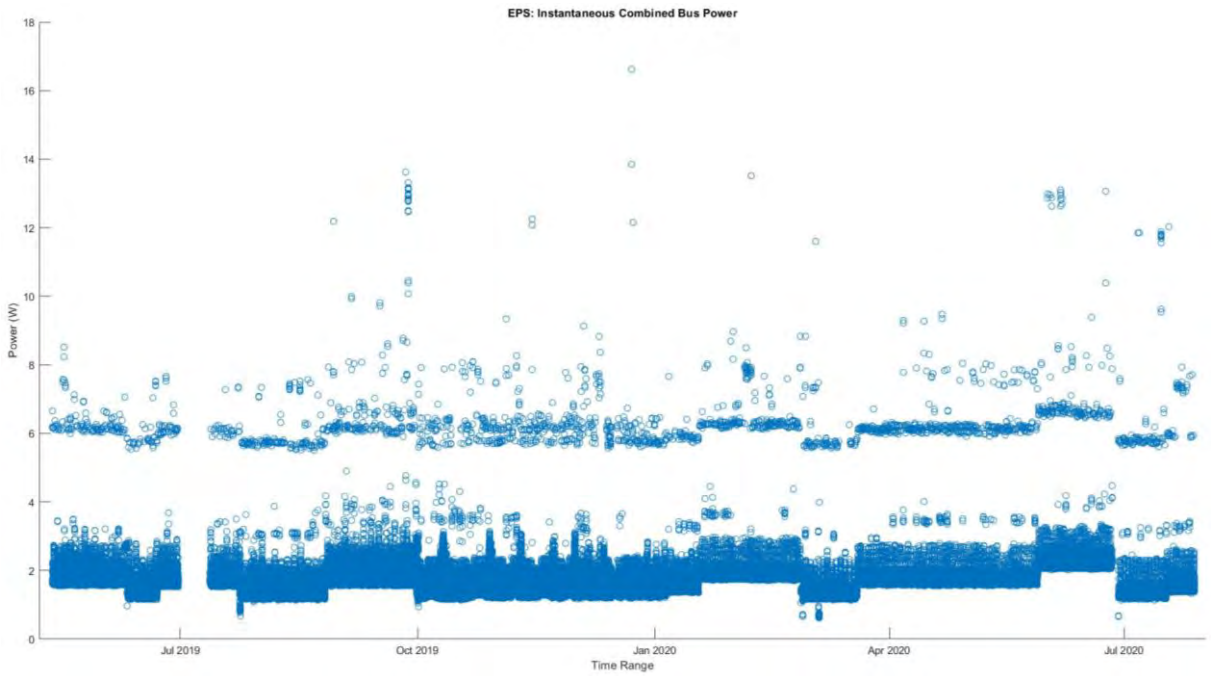

Figure 4.43: EPS Instantaneous Combined Bus Power

4.3.5.2 Data Analysis

This section gives details regarding the basic statistic, probability density function and cumulative density function for the instantaneous EPS combined bus power.

4.3.5.2.1 Basic Statistics

The basic statistics for the combined instantaneous EPS bus power are summarised in Table 4.20.

Table 4.20: EPS Instantaneous Combined Bus Power Basic Statistic

Statistic	Power (W)
Mean	1.736
Median	1.673
Mode	1.639
Range	16.618
Minimum value	0
Maximum value	16.618
Variance	0.389
Standard deviation	0.624

4.3.5.2.2 Probability Density Function

The PDF for the instantaneous combined bus power can be seen in Figure 4.44

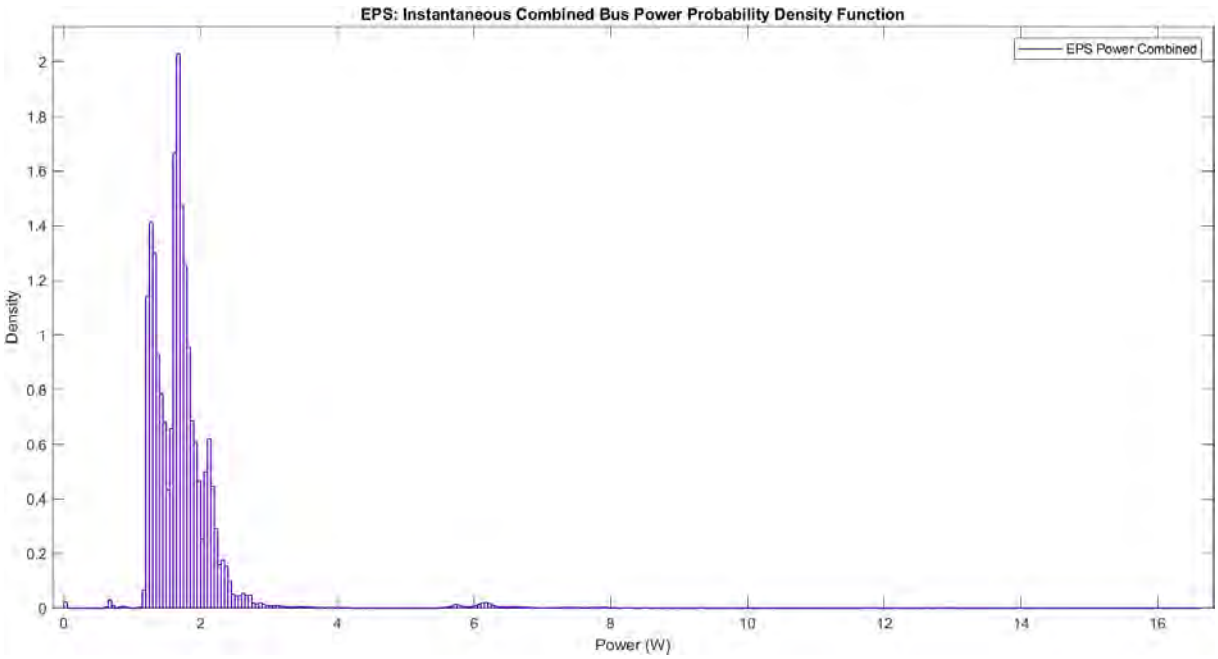

Figure 4.44: EPS Instantaneous Combined Bus Power Probability Density Function

4.3.5.2.3 Cumulative Density Function

The CDF for the instantaneous combined bus power is shown in Figure B.18 in Appendix B.

4.3.6 EPS Bus Telemetry Correlation

The current correlation between these three telemetry channels is summarised in Table 4.21.

Table 4.21: EPS Bus Current Telemetry Correlation

Telemetry Channel	3.3V Regulated Bus	5V Regulated Bus	Unregulated Bus
3.3 Regulated Bus	1	-0.0924	0.1043
5V Regulated Bus	-0.0924	1	00769
Unregulated Bus	0.1043	0.0769	1

The power correlation between these three telemetry channels is summarised in Table 4.22.

Table 4.22: EPS Bus Power Telemetry Correlation

Telemetry Channel	3.3V Regulated Bus	5V Regulated Bus	Unregulated Bus
3.3 Regulated Bus	1	-0.092	0.105
5V Regulated Bus	-0.092	1	0.077
Unregulated Bus	0.105	0.077	1

The voltage correlation between the 12V regulated bus and unregulated bus telemetry channels is summarised in Table 4.23.

Table 4.23: EPS Bus Voltage Telemetry Correlation

Telemetry Channel	12V Regulated Bus	Unregulated Bus
12V Regulated Bus	1	0,018
Unregulated Bus	0,018	1

4.4 K-Line Imager

The K-line imager is an imager used to detect vegetation fires by detecting elevated levels of potassium emissions and is only active when ZACube-2 is in the stabilised Y-momentum mode. The imager consists of two infrared sensors, namely a visible (VIS) and a near infrared (NIR) sensor that are used in two modes of imaging; continuous and single mode.

4.4.1 K-Line Imager Enabled

Single mode is where a single image is captured per sensor, whilst continuous mode takes a series of images such that the images overlap and is to be used primarily for fire detection over land, in particular in Southern Africa.

The telemetry range spans from 01 January 2019 00:02:39 UTC to 28 July 2020 09:30:15 UTC at an interval of 3 minutes. The frequency at which the K-line imager was enabled can be seen in Figure 4.45.

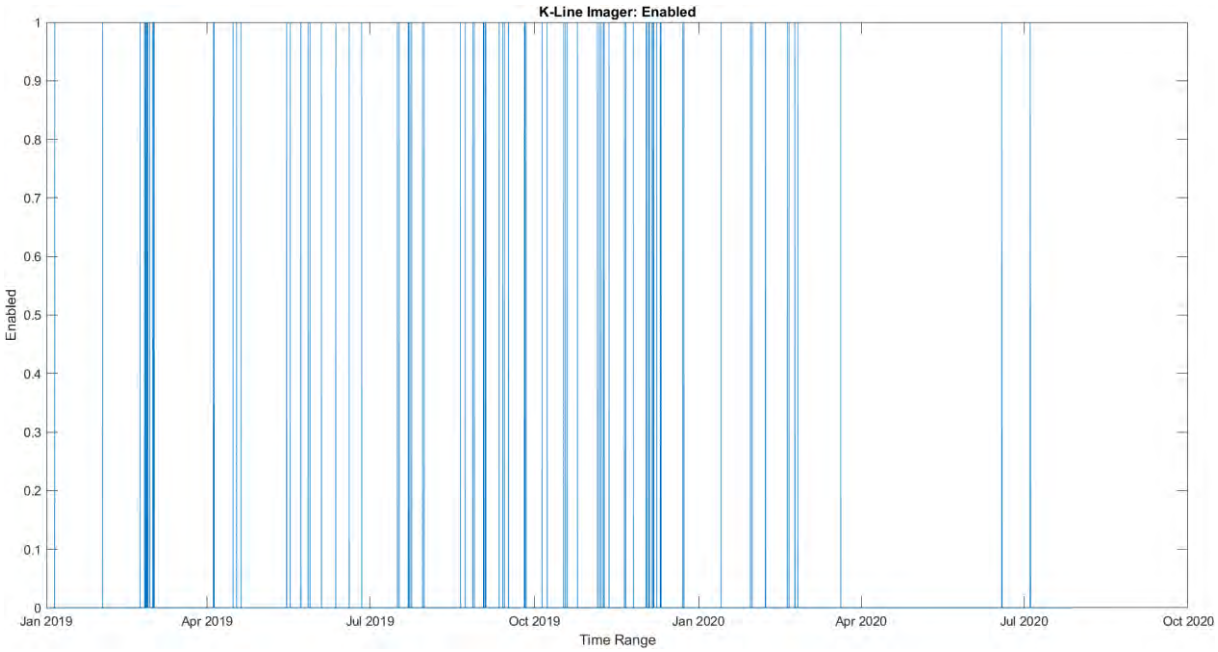

Figure 4.45: K-Line Imager Enabled

In total, the imager was enabled 465 times from September 2019 to May 2020.

4.4.2 K-Line Imager Temperature

Temperature is a critical factor when it comes to the operation of the imager and, especially, the image quality produced. At both low and elevated temperatures, the camera's operability decreases as components cease to work as efficiently when operating in the optimal thermal operating limits as specified in the manufacturer's manuals, causing incorrect emissivity readings in addition to the image looking "hazy" due to the increased image noise. The focal point of the imager is also extremely sensitive to temperature variation.

To this end, the thermal operation of the imager must be monitored. The graph in Figure 4.46 shows sample telemetry readings from on-board temperature sensors that were logged from 29 October 2020 20:21:36 UTC to 29 October 2020 21:19:36 UTC.

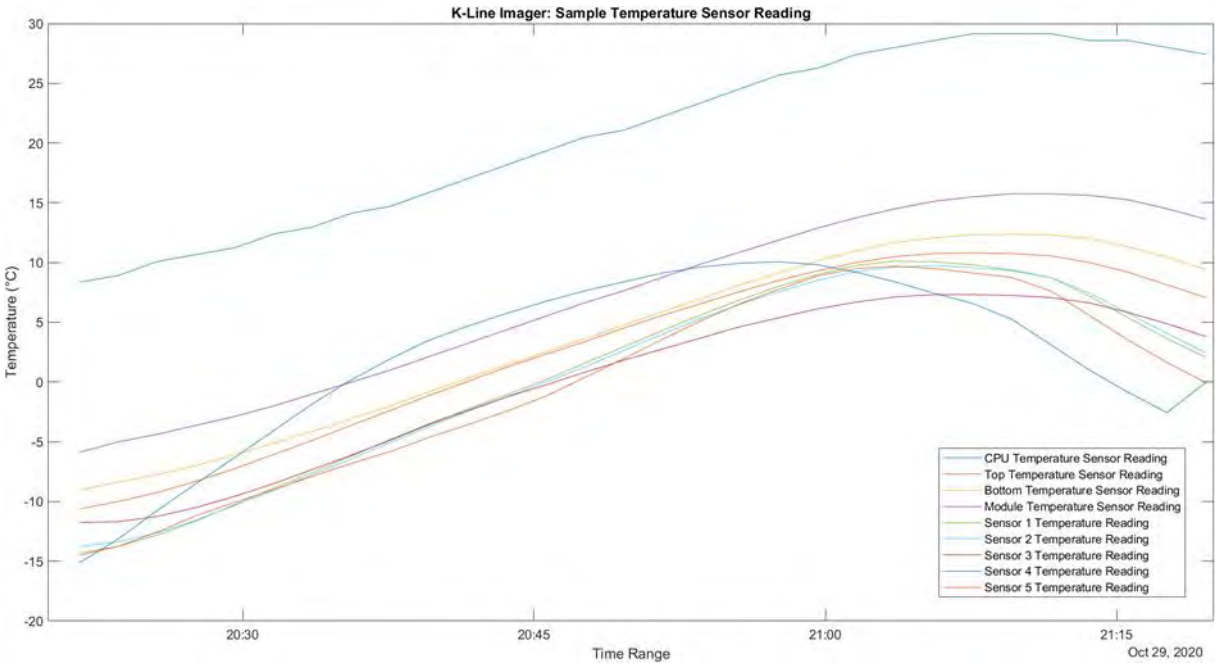

Figure 4.46: K-Line Imager Sample Temperature Sensor Reading

From Figure 4.46, the CPU experiences the highest temperature as expected due to the amount of information needing to be processed. The highest temperature recorded for the CPU was 29.15°C from 29 October 2021 21:07:36 UTC to 29 October 2021 21:11:36 UTC. The lowest temperature recorded was by sensor 4 at -15.1°C on 29 October 2021 20:21:36 UTC.

4.5 S-Band Transmitter (HSTXC)

The HSTXC, or high-speed S-band transmitter, is used to primarily downlink or send payload data to the ground segment, with the UHF band being used as a redundant channel although at a reduced rate. The telemetry range for the HSTXC spans from 12 May 2019 09:06:05 UTC to 28 July 2020 09:30:15 UTC at a timestep of 3 minutes.

The frequency at which the HSTXC was enabled can be seen in Figure 4.47. In total, the HSTXC was enabled 196 times.

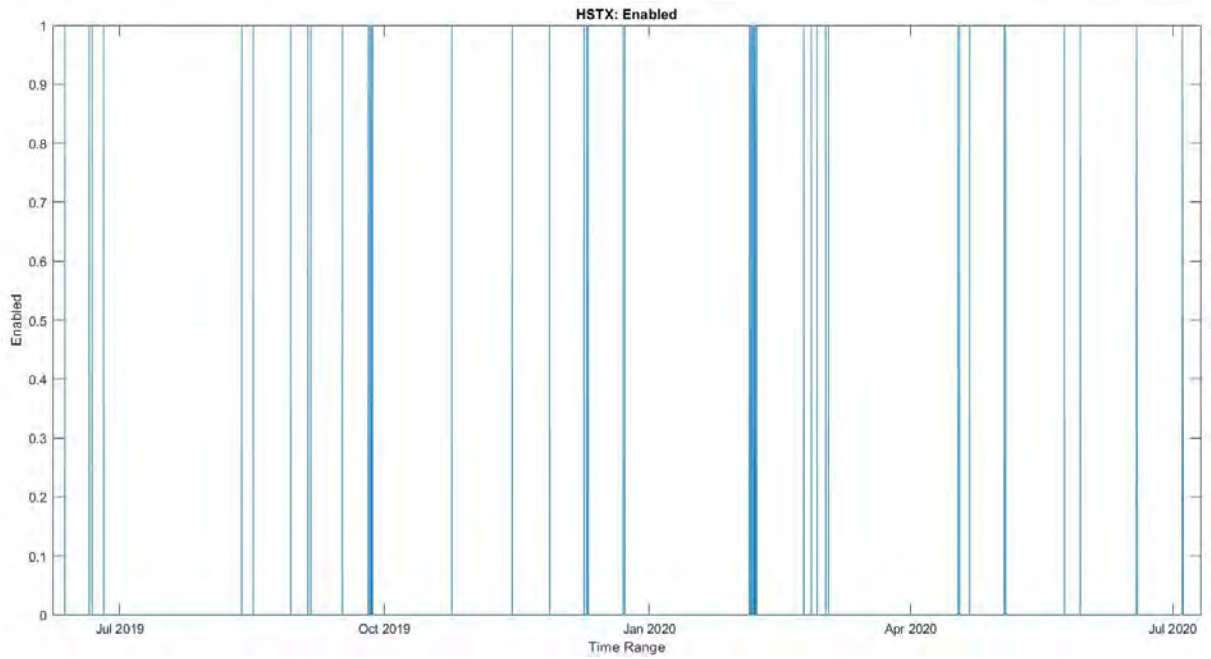

Figure 4.47: HSTXC Enabled

During September 2019 and February 2020, the HSTXC was used frequently, which is presented in Figure 4.48 and Figure 4.49, respectively.

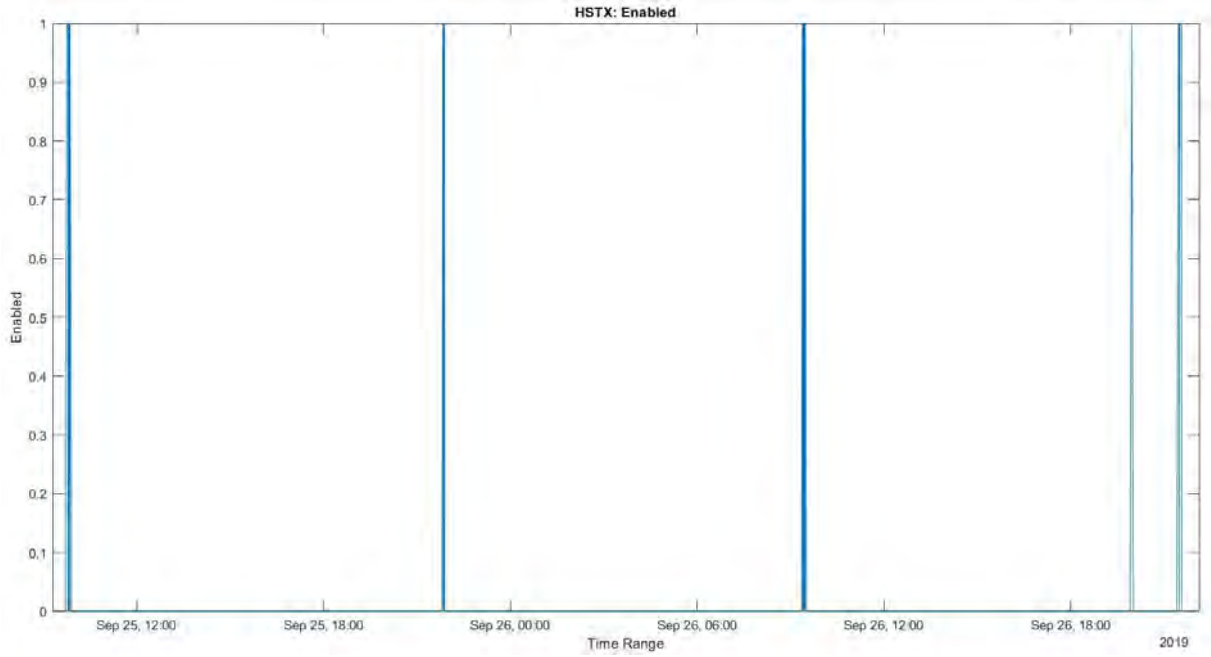

Figure 4.48: HSTXC Enabled September 2019

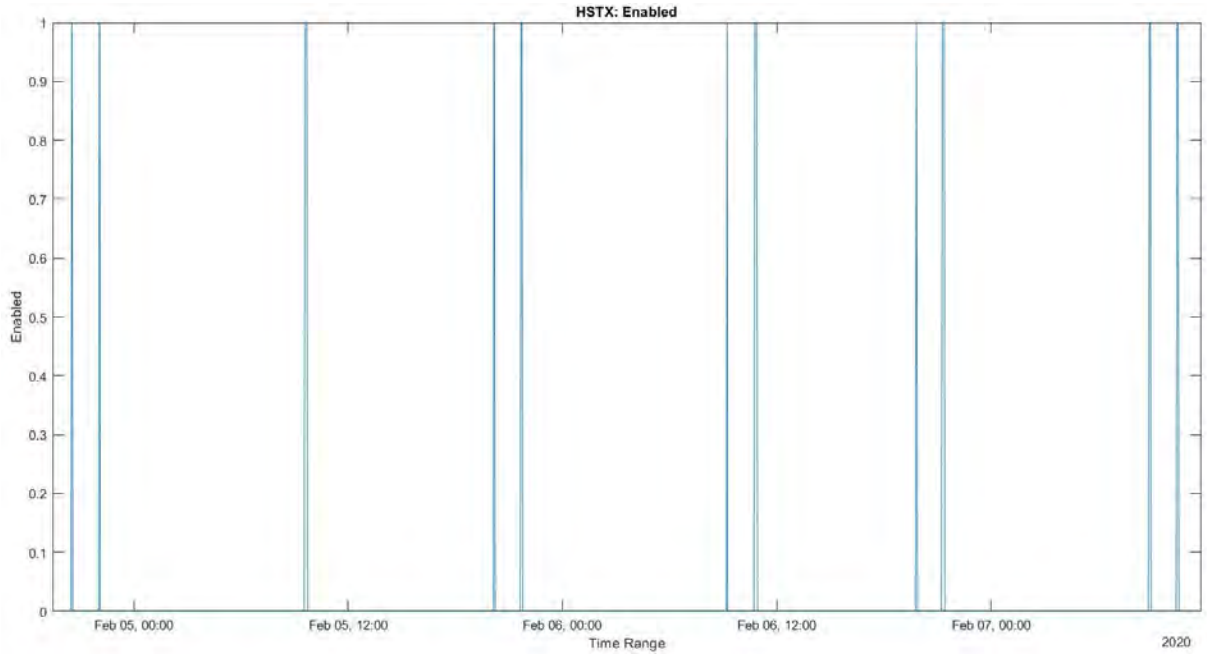

Figure 4.49: HSTXC Enabled February 2020

4.6 Software Defined Radio (SDR)

The SDR is the primary payload that is used to obtain transmitted shipborne AIS messages, which contain a ship's position, status as well as other relevant information, within the South African Exclusive Economic Zone (EEZ).

The SDR is switched on and off 30 seconds, respectively, before and after the satellite footprint enters the EEZ, ensuring that it is not only active when covering the area, but the area covered is larger than the EEZ for optimal coverage. Telemetry data spans from 01 January 2019 00:02:39 UTC to 29 July 2020 09:30:15 at a timestep of 3 minutes.

The frequency at which the SDR was enabled can be seen in Figure 4.50. In comparison to the other payload, the K-line imager, the SDR was used repeatedly. Relaying AIS information was frequently utilized.

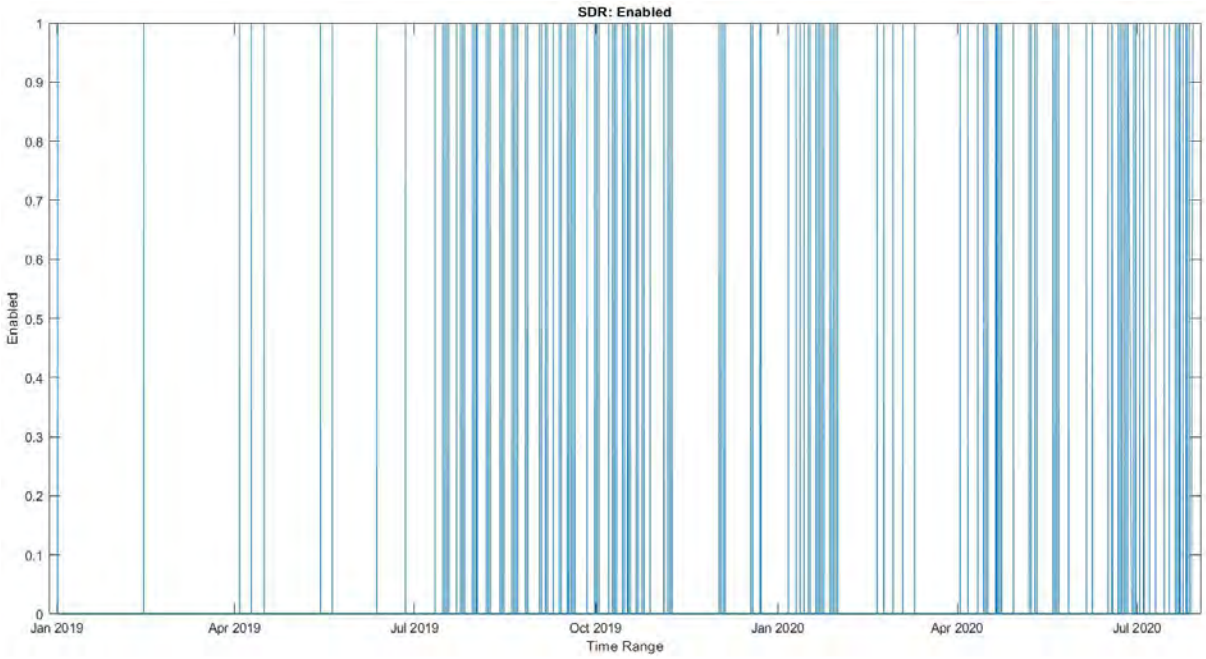

Figure 4.50: SDR Enabled

4.7 Solar Array

As mentioned in section *2.2.2.1 Solar Array*, ZACube-2 has five body-mounted solar panels, which form the solar array responsible for providing the spacecraft bus with power. Since solar panel SA1B is nadir pointing and therefore not installed, only five sets of data were used. The telemetry from the respective panels spans from 01 January 2019 00:02:39 to 29 July 2020 00:51:15, where each value is recorded at a timestep of 3 minutes.

4.7.1 Solar Panels SA1A and SA1B

This section shows the raw telemetry data as well as the resulting data analysis for solar panels SA1A.

4.7.1.1 Current and Voltage Raw Telemetry

Figure 4.51 shows the current being generated from solar panels SA1A. As explained previously, there is no solar panel SA1B and therefore does not generate a current. The voltage presented in Figure 4.52 therefore depicts the voltage produced solely from solar panel SA1A.

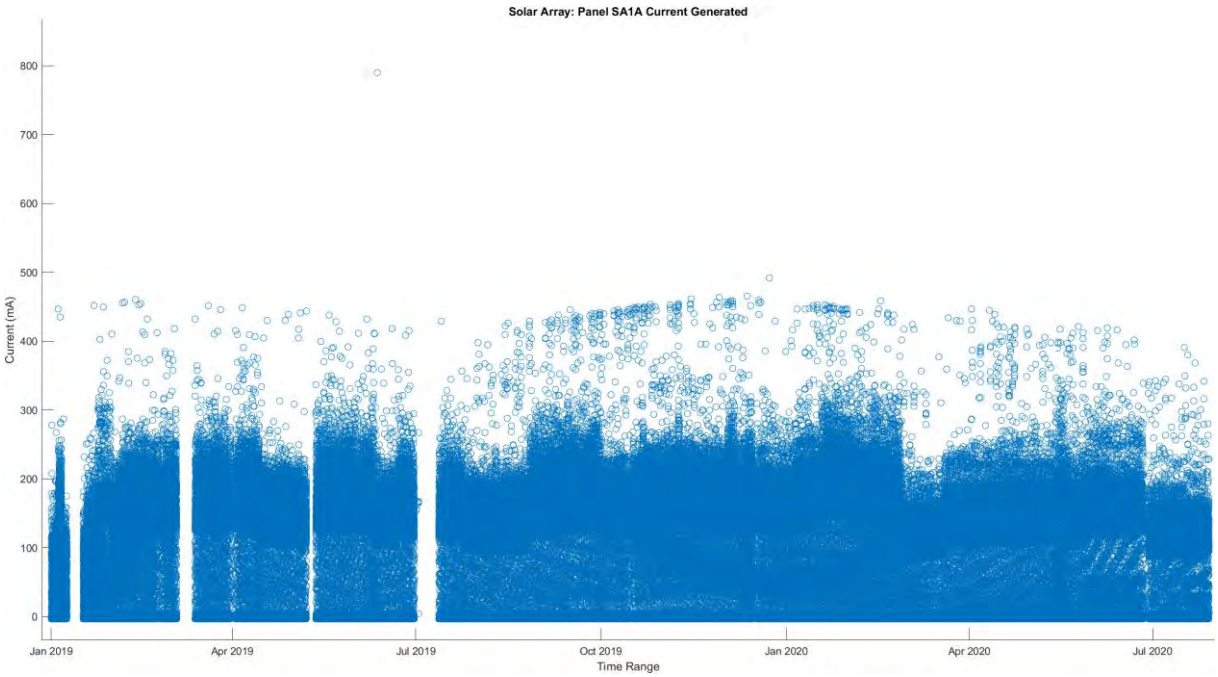

Figure 4.51: Solar Panel SA1A Current Generated

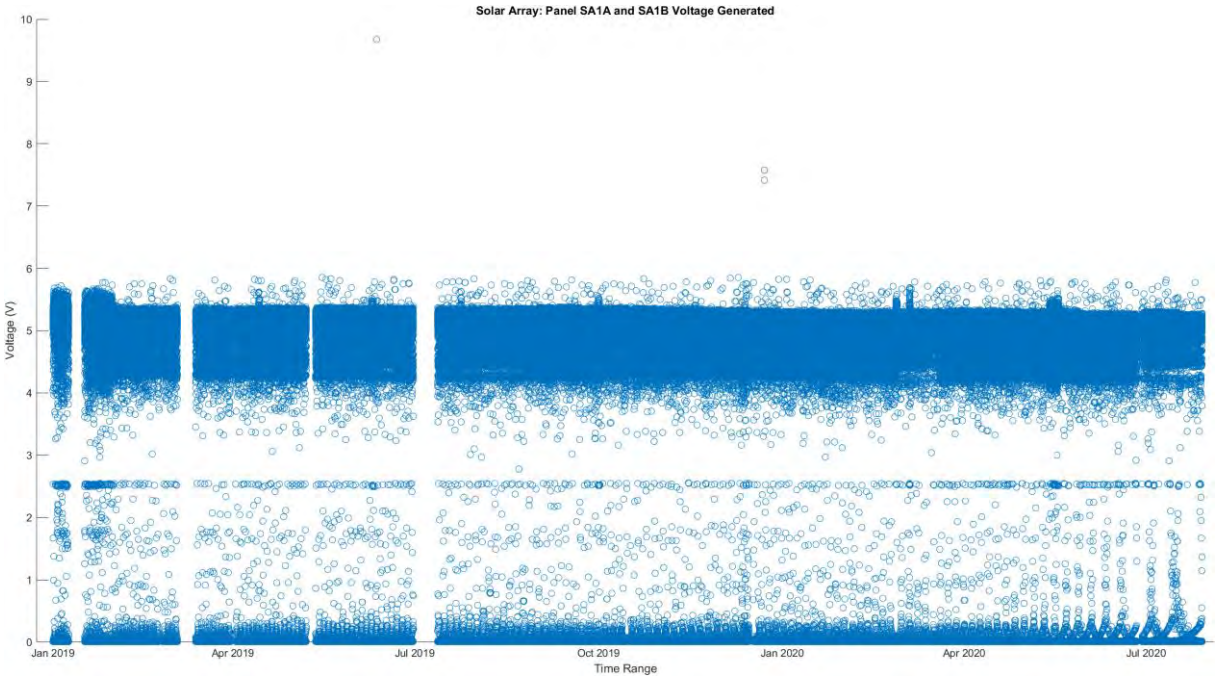

Figure 4.52: Solar Panel SA1A and SA1B Voltage Generated

4.7.1.2 Current and Voltage Data Analysis

The following section presented the resulting data analytics of the various telemetry channels for solar panel SA1A.

4.7.1.2.1 Basic Statistics

The basic statistics for solar panel SA1A current and voltage are summarised in Tables 4.24 and 4.25, respectively.

Table 4.24: Solar Panels SA1A and SA1B Current Basic Statistics

Statistic	Current (A)
Mean	0.077
Median	0.059
Mode	-0.002
Range	0.793
Minimum value	-0.003
Maximum value	0.790
Variance	0.007
Standard deviation	0.082

Table 4.25: Solar Panels SA1A and SA1B Voltage Basic Statistics

Statistic	Voltage (V)
Mean	3.107
Median	4.563
Mode	0.016
Range	9.667
Minimum value	0.006
Maximum value	9.673
Variance	5.699
Standard deviation	2.387

4.7.1.2.2 Probability Density Function

The PDF for solar panel SA1A current and voltage is presented in Figure 4.53 and 4.54, respectively.

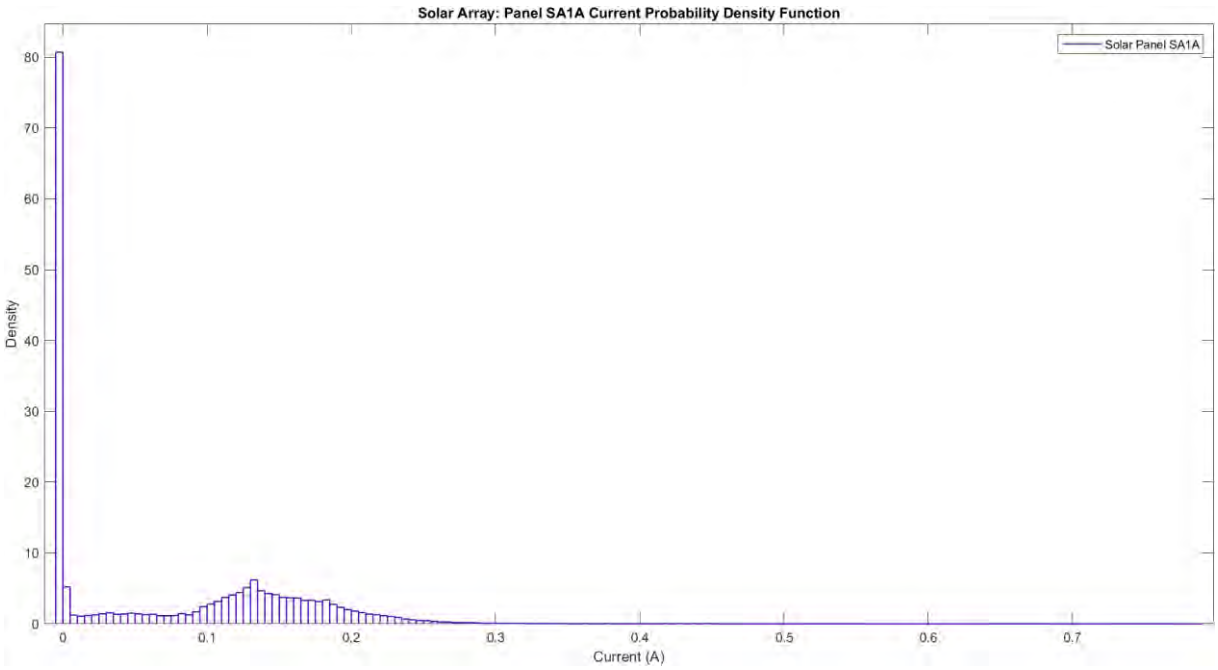

Figure 4.53: Solar Array Panels SA1A and SA1B Current Probability Density Function

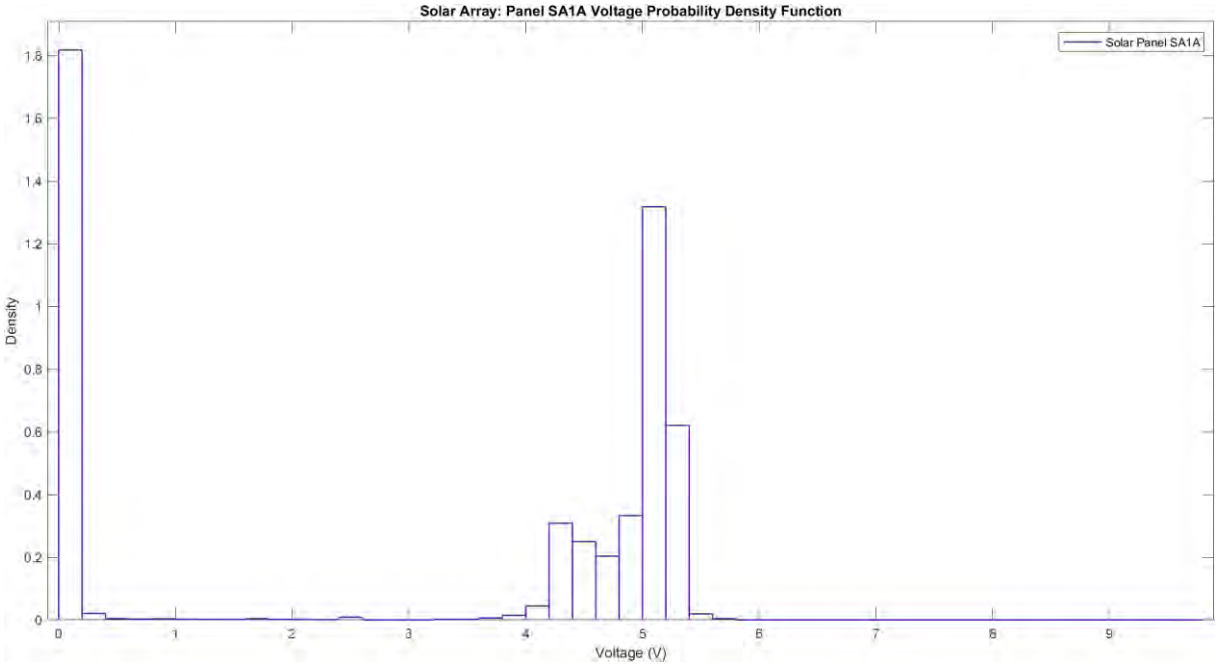

Figure 4.54: Solar Array Panels SA1A and SA1B Voltage Probability Density Function

4.7.1.2.3 Cumulative Density Function

The CDF for solar panel SA1A current and voltage is presented in Figure B.19 and Figure B.20 in Appendix B, respectively.

4.7.2 Solar Panels SA2A and SA2B

This section shows the raw telemetry data as well as data analysis process for solar panels SA2A and SA2B.

4.7.2.1 Current and Voltage Raw Telemetry

Figure 4.55 and Figure 4.56 show the current being generated from solar panels SA2A and SA2B, respectively.

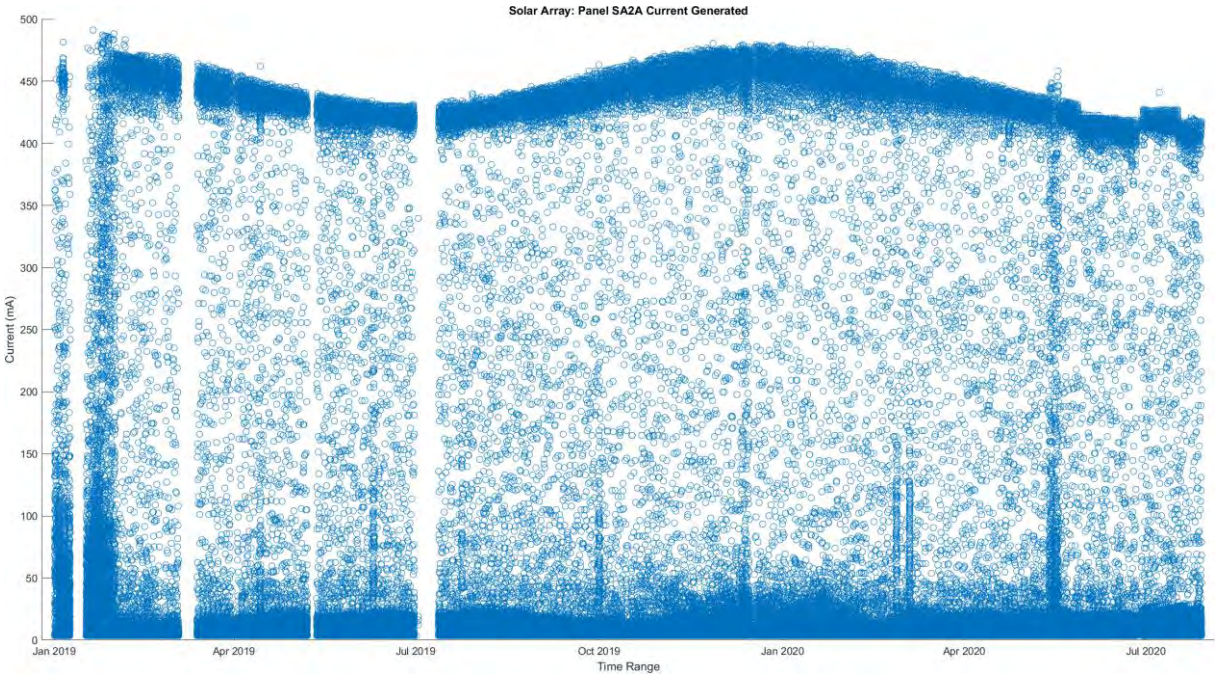

Figure 4.55: Solar Panel SA2A Current Generated

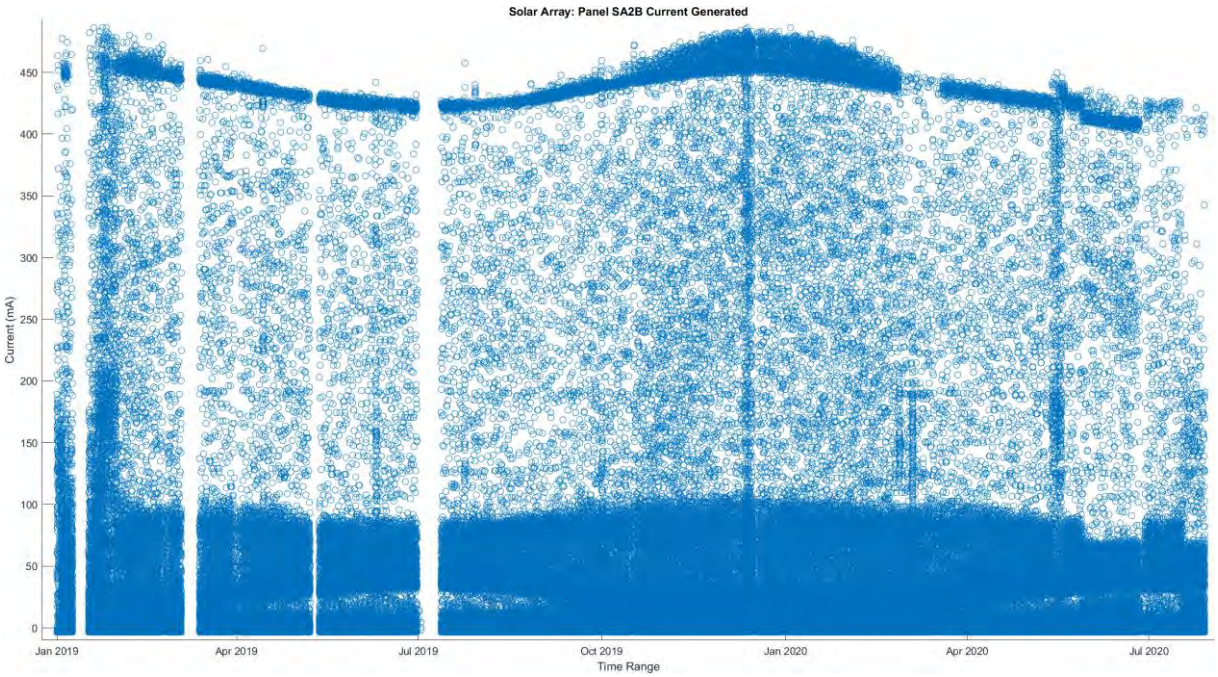

Figure 4.56: Solar Panel SA2B Current Generated

An interesting pattern, which can only be observed with this pair of solar panels, is that the current being generated appears to resemble a sine wave, with the maximum around January and the minimum around July.

Subsequently, the combined voltage being produced by the solar panel pair SA is presented in Figure 4.57.

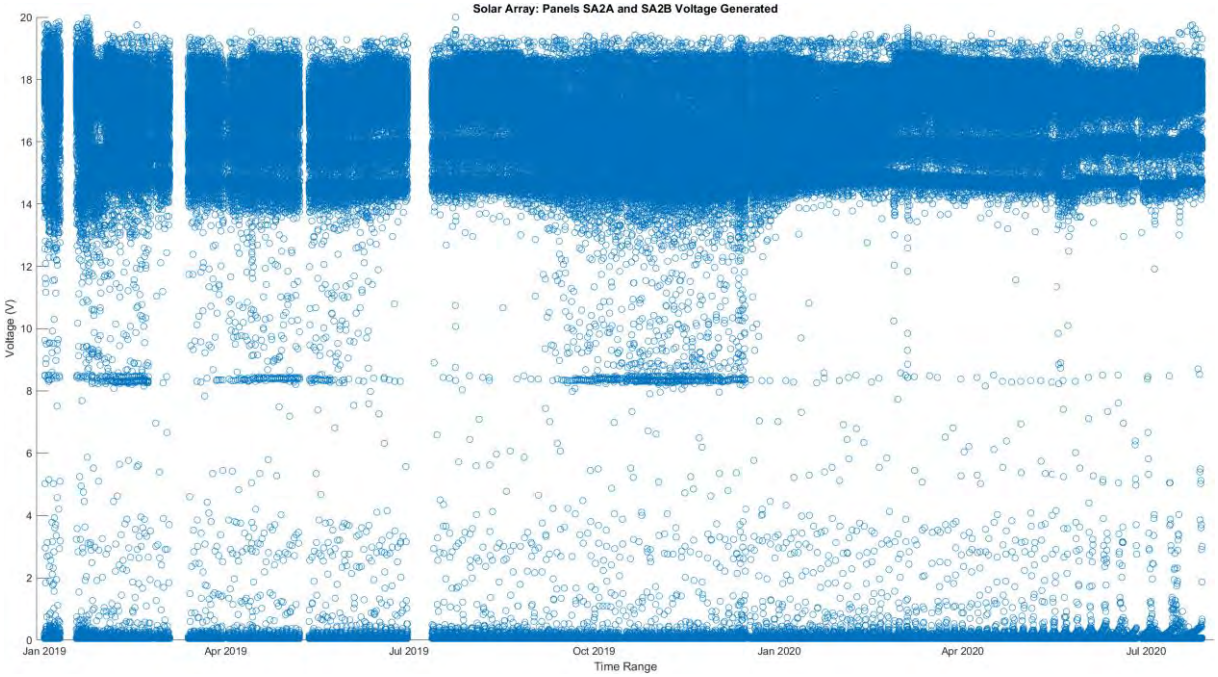

Figure 4.57: Solar Panel SA2A and SA2B Voltage Generated

4.7.2.2 Current and Voltage Data Analysis

The following section summarises the data analyses of the various telemetry channels for solar panels SA2A and SA2B.

4.7.2.2.1 Basic Statistics

The basic statistics for solar panels SA2A and SA2B current and voltage are summarised in Table 4.26 and Table 4.27, respectively.

Table 4.26: Solar Panels SA2A and SA2B Current Basic Statistics

Statistic	Current (A)
Mean	0.098
Median	0.022
Mode	0.002
Range	0.866
Minimum value	0.001
Maximum value	0.866
Variance	0.023
Standard deviation	0.152

Table 4.27: Solar Panels SA2A and SA2B Voltage Basic Statistics

Statistic	Voltage (V)
Mean	10.334
Median	15.023
Mode	0.073
Range	19.950
Minimum value	0.048
Maximum value	19.998
Variance	63.841
Standard deviation	7.990

4.7.2.2.2 Probability Density Function

The PDF for solar panels SA2A and SA2B current and voltage is presented in Figure 4.58 and Figure 4.59, respectively.

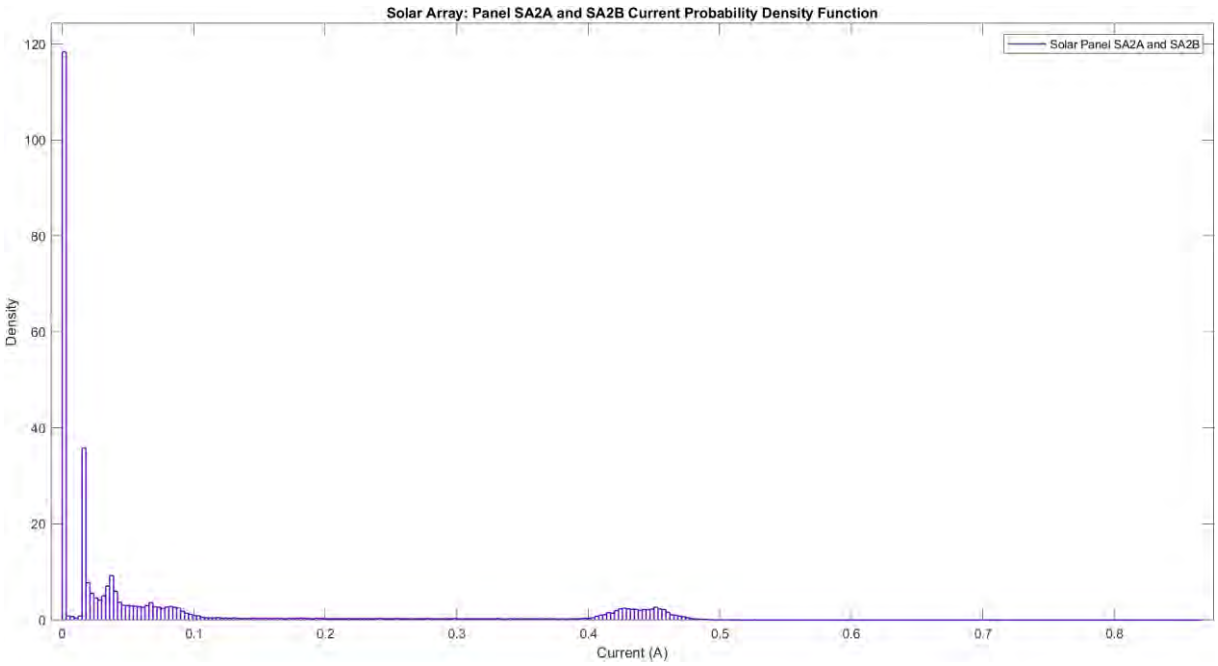

Figure 4.58: Solar Array Panels SA2A and SA2B Current Probability Density Function

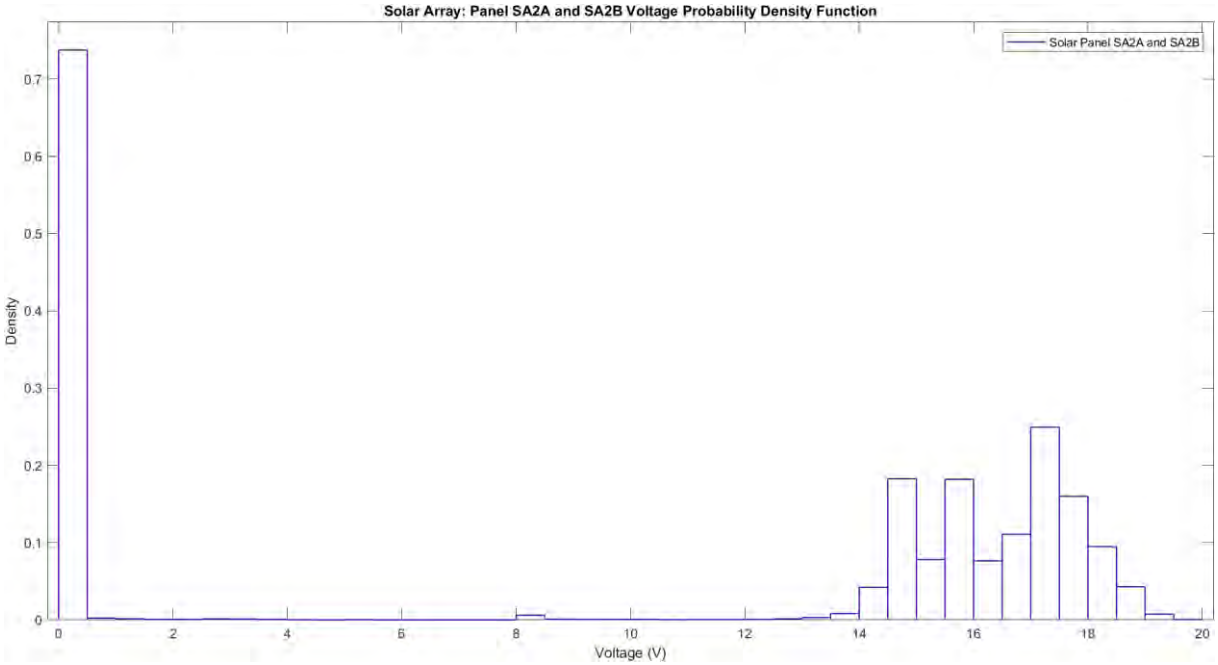

Figure 4.59: Solar Array Panels SA2A and SA2B Voltage Probability Density Function

4.7.2.2.3 Cumulative Density Function

The CDF for solar panels SA2A and SA2B current and voltage is presented in Figure B.21 and Figure B.22 in Appendix B.

4.7.3 Solar Panels SA3A and SA3B

This section shows the raw telemetry graphical data as well as the resulting the data analysis for solar panels SA3A and SA3B.

4.7.3.1 Current and Voltage Raw Telemetry

Figure 4.60 and Figure 4.61 show the current being generated from solar panels SA3A and SA3B, respectively.

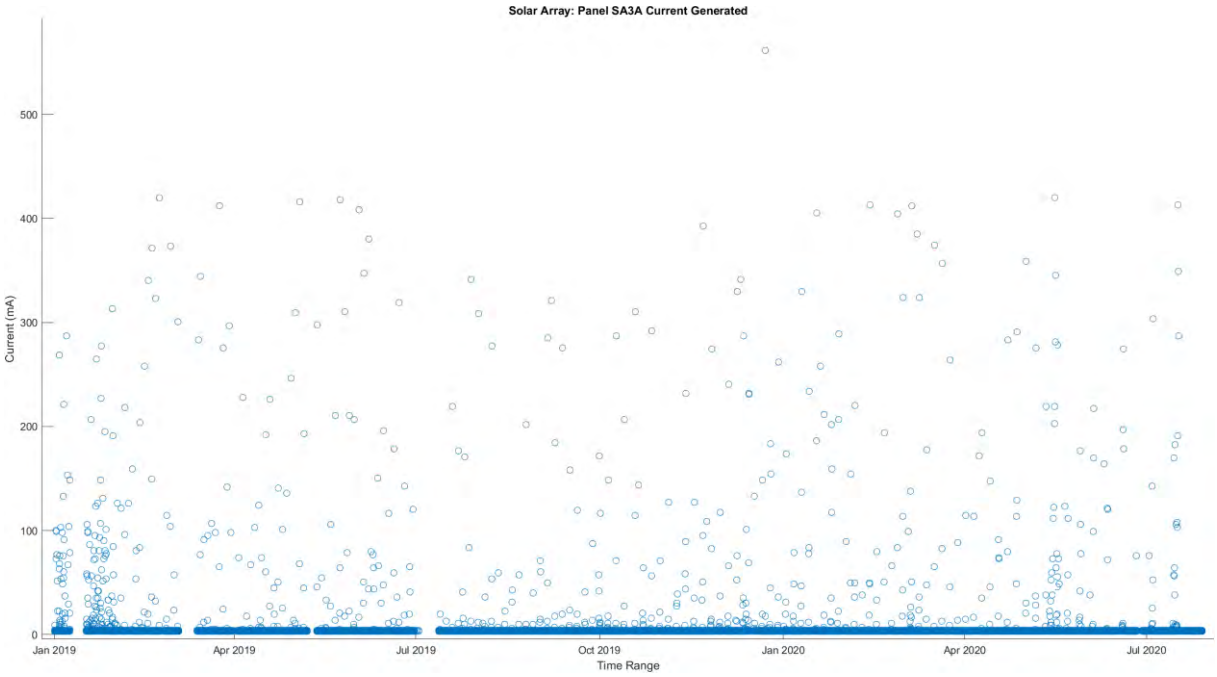

Figure 4.60: Solar Panel SA3A Current Generated

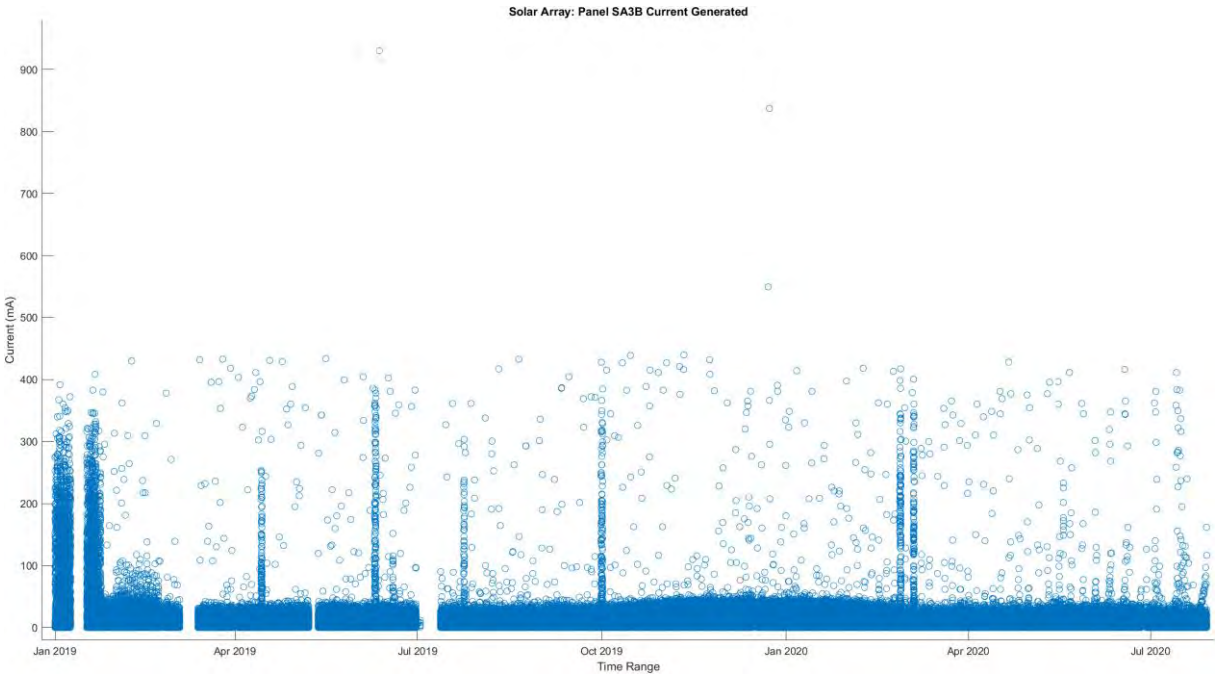

Figure 4.61: Solar Panel SA3B Current Generated

The combined voltage being generated by both solar panels SA3A and SA3B is shown in Figure 4.62.

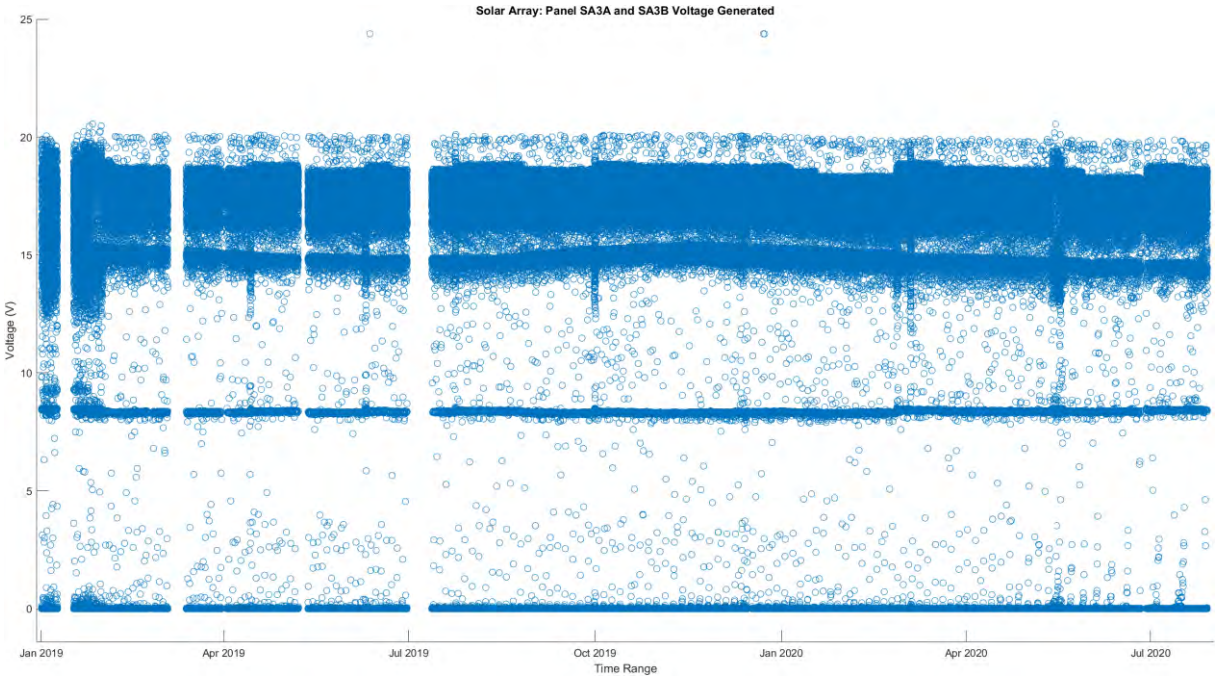

Figure 4.62: Solar Panel SA3A and SA3B Voltage Generated

4.7.3.2 Current and Voltage Data Analysis

The following section summarises the resulting data analyses of the various telemetry channels for solar panels SA3A and SA3B.

4.7.3.2.1 Basic Statistics

Table 4.27: Solar Panels SA3A and SA3B Current Basic Statistics

Statistic	Current (A)
Mean	0.013
Median	0.005
Mode	0.005
Range	1.435
Minimum value	0.003
Maximum value	1.438
Variance	0.001
Standard deviation	0.024

Table 4.28: Solar Panels SA3A and SA3B Voltage Basic Statistics

Statistic	Voltage (V)
Mean	10.187
Median	15.027
Mode	0.023
Range	24.382
Minimum value	-0.002
Maximum value	24.379
Variance	64.952
Standard deviation	8.059

4.7.3.2 Probability Density Function

The PDF for solar panels SA3A and SA3B current and voltage is presented in Figures 4.63 and 4.64, respectively.

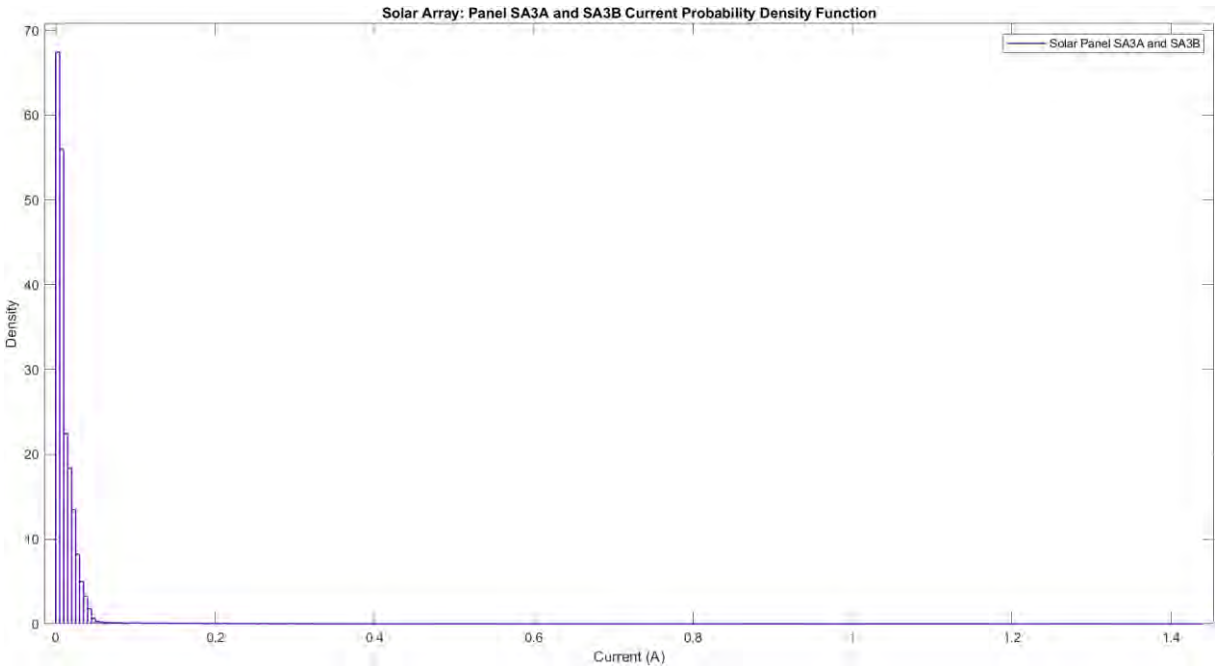

Figure 4.63: Solar Array Panels SA3A and SA3B Current Probability Density Function

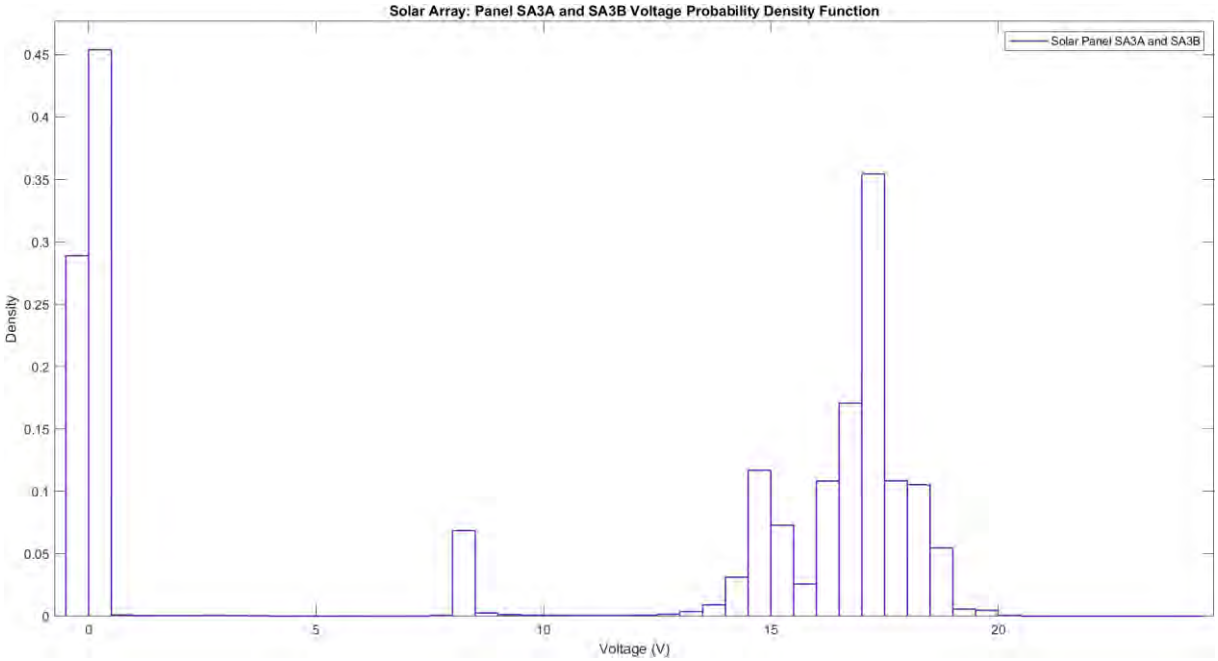

Figure 4.64: Solar Array Panels SA3A and SA3B Voltage Probability Density Function

4.7.3.3 Cumulative Density Function

The CDF of solar panels SA3A and SA3B current and voltage is presented in Figure B.23 and Figure B.24 in Appendix B, respectively.

4.7.4 Solar Panels Current and Voltage Telemetry Correlation

The current and voltage correlations between these five solar panel telemetry channels are summarised in Table 4.29 and Table 4.30, respectively.

Table 4.29: Solar Panel Current Telemetry Correlation

Solar Panel	SA1A	SA2A	SA2B	SA3A	SA3B
SA1A	1	-0.018	0.068	0.049	0.220
SA2A	-0.018	1	-0.143	0.015	-0.016
SA2B	0.068	-0.143	1	0.018	0.034
SA3A	0.049	0.015	0.018	1	0.115
SA3B	0.220	-0.016	0.034	0.115	1

Table 4.30: Solar Panel Voltage Telemetry Correlation

Solar Panels	SA1A and SA1B	SA2A and SA2B	SA3A and SA3B
SA1A and SA1B	1	0.978	0.990
SA2A and SA2B	0.978	1	0.975
SA3A and SA3B	0.990	0.975	1

4.7.5 Solar Array Combined Current and Voltage Generated

This section shows the raw telemetry data as well as the resulting data analysis for the combined current and voltage generated, respectively.

4.7.5.1 Combined Current and Voltage Generated Raw Telemetry

With the individual current and voltage known, the combined instantaneous current and voltage for the solar array can be calculated and graphs plotted, showing the behaviour over the course of the previously mentioned telemetry time span. Figure A.9 shows the combined current generated from the solar array from all five panels. The removal of outliers results in the graph presented in Figure 4.65.

Figure 4.65: Solar Array Total Current Generated with No Outliers

The combined voltage generated from all five panels of the solar array consists of the three voltage telemetry sets belonging to the three pairs of solar panels as seen in the figure below.

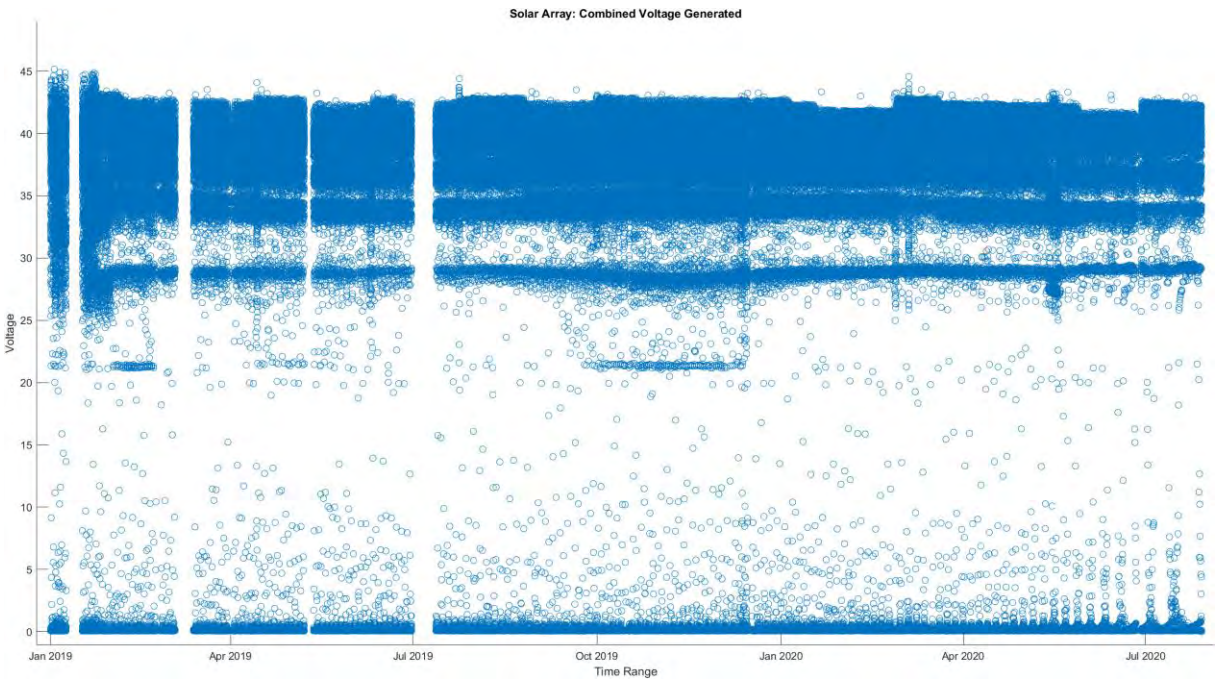

Figure 4.66: Solar Array Combined Voltage Generated

4.7.5.2 Combined Current and Voltage Generated Data Analysis

The following section presents the data analyses of the various telemetry channels for the combined current and voltage generation of the solar array.

4.7.5.2.1 Basic Statistics

The basic statistics for the solar array combined current and voltage are presented in Table 4.31 and Table 4.32, respectively.

Table 4.31: Solar Array Combined Current Basic Statistics

Statistic	Current (A)
Mean	0.250
Median	0.317
Mode	0.014
Range	1.282
Minimum value	0
Maximum value	1.282
Variance	0.042
Standard deviation	0.206

Table 4.32: Solar Array Combined Voltage Basic Statistics

Statistic	Voltage (V)
Mean	23.629
Median	34.731
Mode	0.112
Range	45.106
Minimum value	0.052
Maximum value	45.158
Variance	335.761
Standard deviation	18.324

4.7.5.2 Probability Density Function

The PDF for the solar array combined current and voltage is presented in Figure 4.67 and Figure 4.68, respectively.

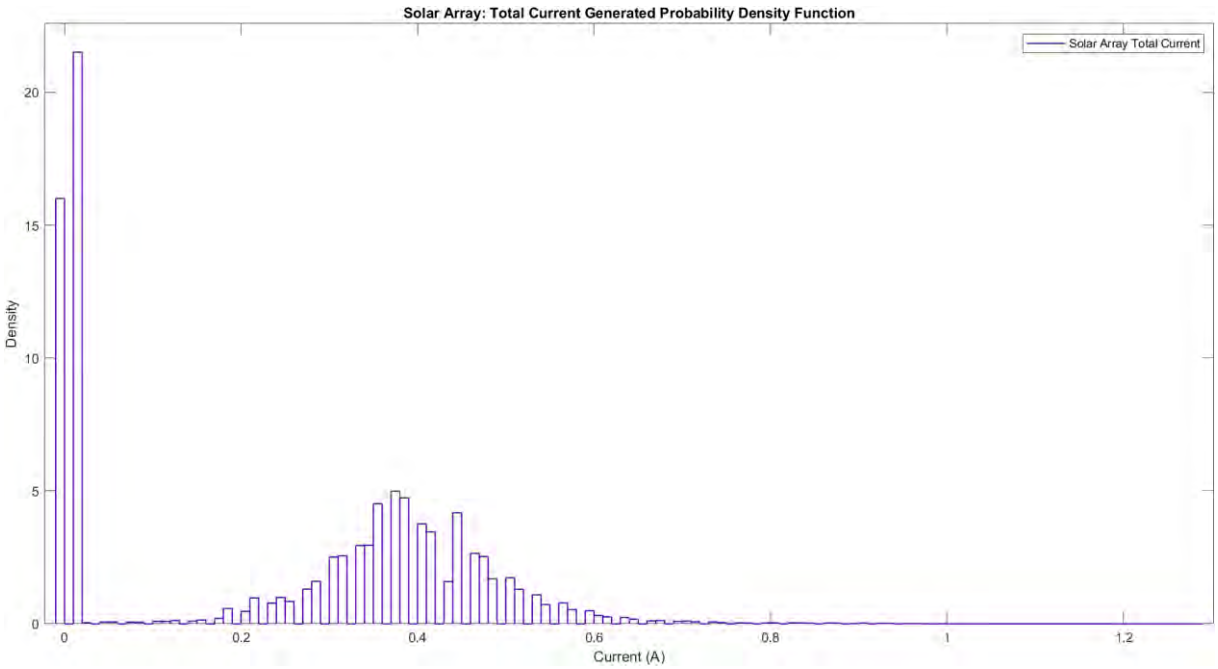

Figure 4.67: Solar Array Total Current Generated Probability Density Function

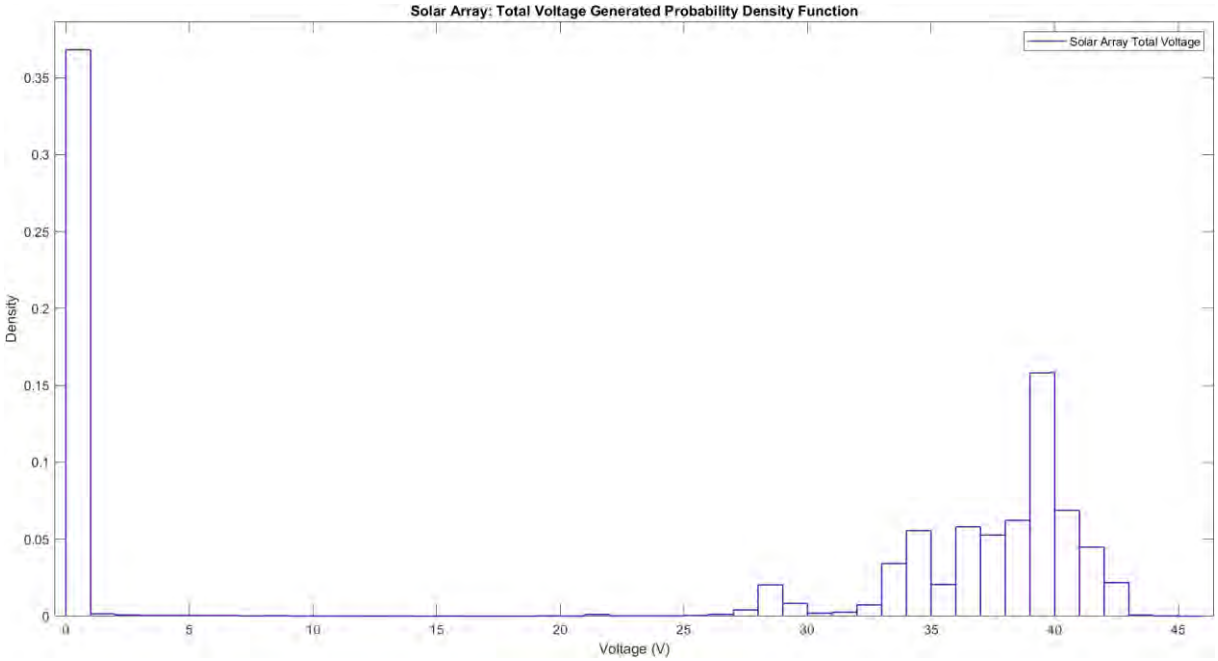

Figure 4.68: Solar Array Total Voltage Generated Probability Density Function

4.7.5.3 Cumulative Density Function

The CDF for the solar array combined current and voltage is presented in Figure B.25 and Figure B.26 in Appendix B, respectively.

4.7.6 Solar Array Power

Various power graphs were calculated by combining the currents for the respective pairs of solar panels and then multiplying that value with the associated generated voltage. This was done for all three pairs of solar panels with a total instantaneous power being generated by combining the power value of the three pairs of solar panels.

4.7.6.1 Solar Panels SA1A and SA1B Power Generated

This section shows the raw telemetry data as well as the resulting data analysis for the power generated by solar panels SA1A and SA1B.

4.7.6.1.1 Power Generated Raw Telemetry

The power generated from panels SA1A and SA1B was calculated and plotted in Figure 4.69.

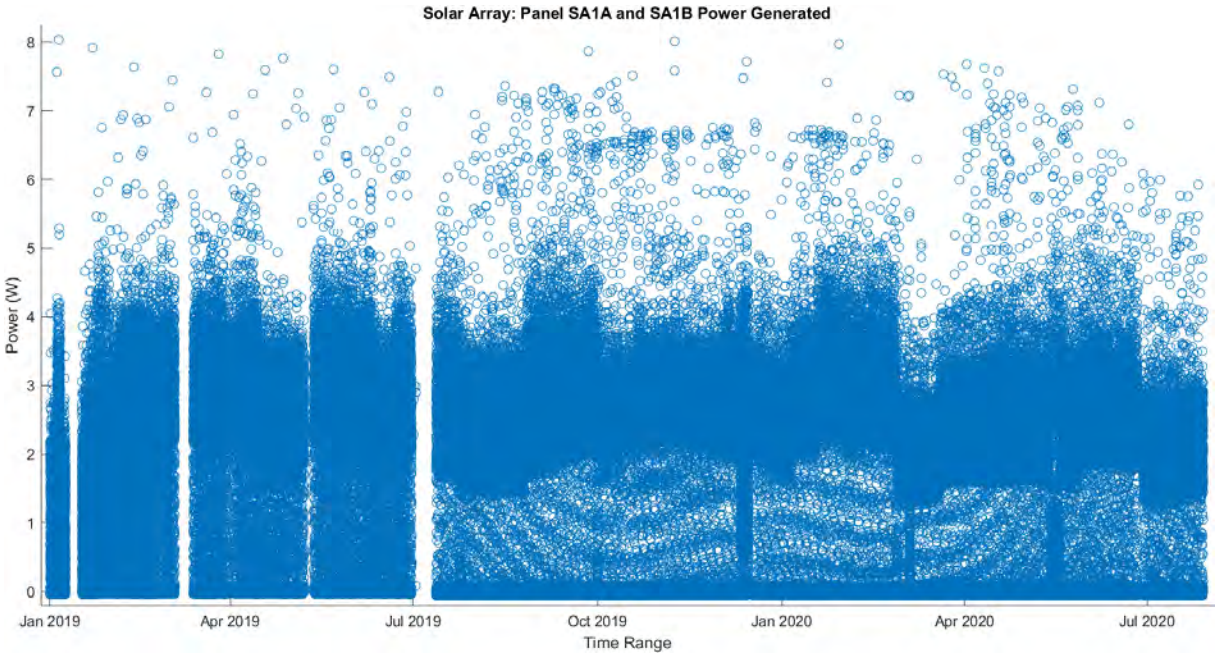

Figure 4.69: Solar Panels SA1A and SA1B Power Generated

4.7.6.1.2 Power Generated Data Analysis

The following section summarises the resulting data analysis of the power generated for solar panels SA1A.

4.7.6.1.2.1 Basic Statistics

The basic statistics for solar panel SA1A power generated is summarised in Table 4.33.

Table 4.33: Solar Panels SA1A and SA1B Power Basic Statistics

Statistic	Power (W)
Mean	0.965
Median	0.005
Mode	0
Range	8.102
Minimum value	-0.065
Maximum value	8.037
Variance	1.817
Standard deviation	1.348

4.7.6.1.2.2 Probability Density Function

The PDF for solar panel SA1A power generated is presented in in Figure 4.70.

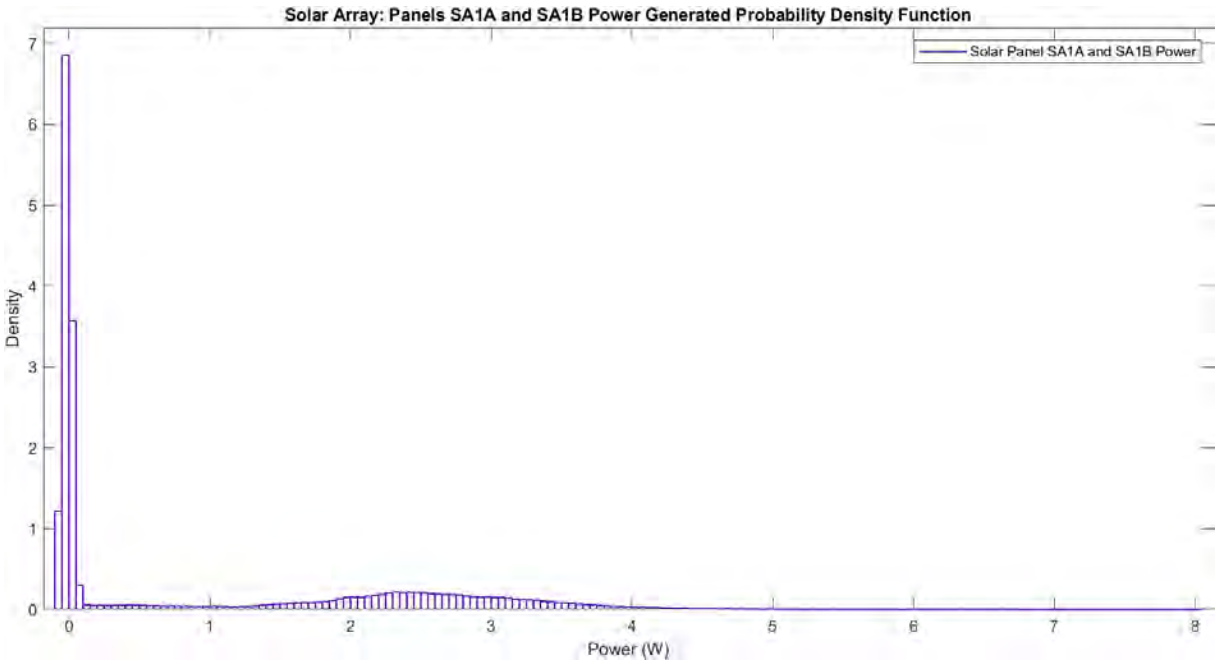

Figure 4.70: Solar Array Panels SA1A and SA1B Power Generated Probability Density Function

4.7.6.1.2.3 Cumulative Density Function

The CDF for solar panel SA1A power generated is presented in Figure B.27 in Appendix B.

4.7.6.2 Solar Panels SA2A and SA2B Power Generated

This section shows the raw telemetry data as well as the resulting data analysis for the power generated by solar panels SA2A and SA2B.

4.7.5.2.1 Power Generated Raw Telemetry

Power generated from panels SA2A and SA2B is presented in Figure 4.71.

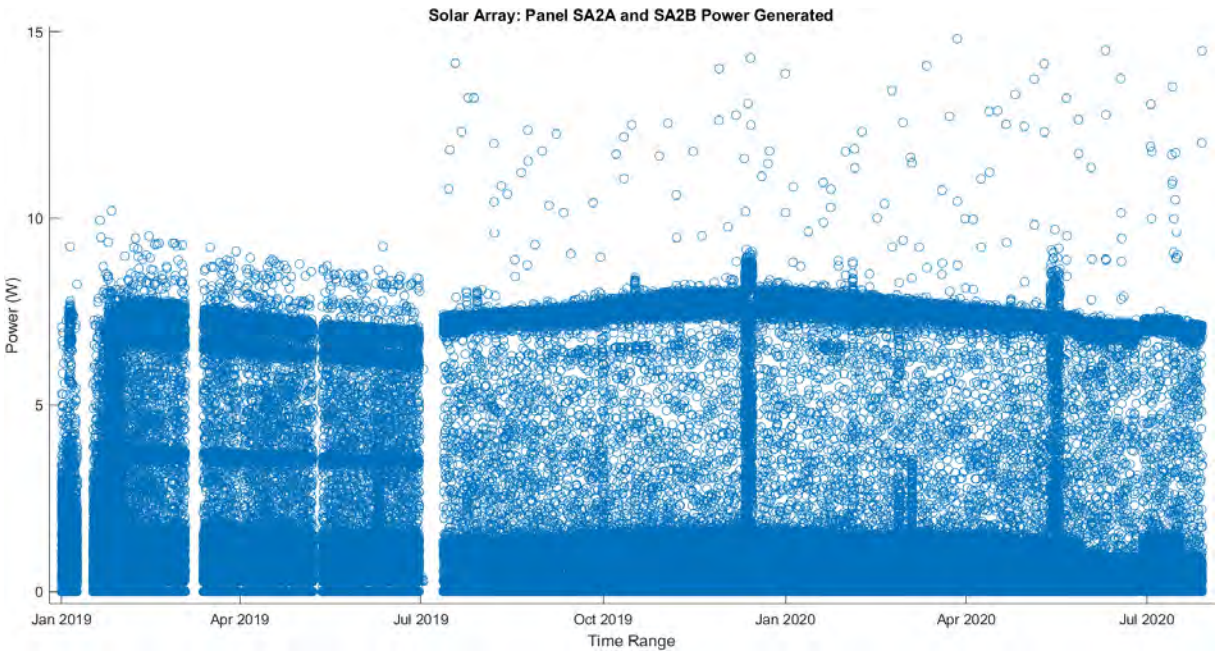

Figure 4.71: Solar Panels SA2A and SA2B Power Generated

4.7.6.2.2 Power Generated Data Analysis

The following section summarises the resulting data analysis of the power generated for solar panels SA2A and SA2B.

4.7.6.2.2.1 Basic Statistics

The basic statistics for solar panels SA2A and SA2B power generated are listed in Table 4.34.

Table 4.34: Solar Panels SA2A and SA2B Power Basic Statistics

Statistic	Power (W)

Mean	1.067
Median	0.034
Mode	0
Range	14.814
Minimum value	-0.002
Maximum value	14.812
Variance	4.692
Standard deviation	2.167

4.7.6.2.2.2 Probability Density Function

The PDF for solar panels SA2A and SA2B power generated is shown in Figure 4.72.

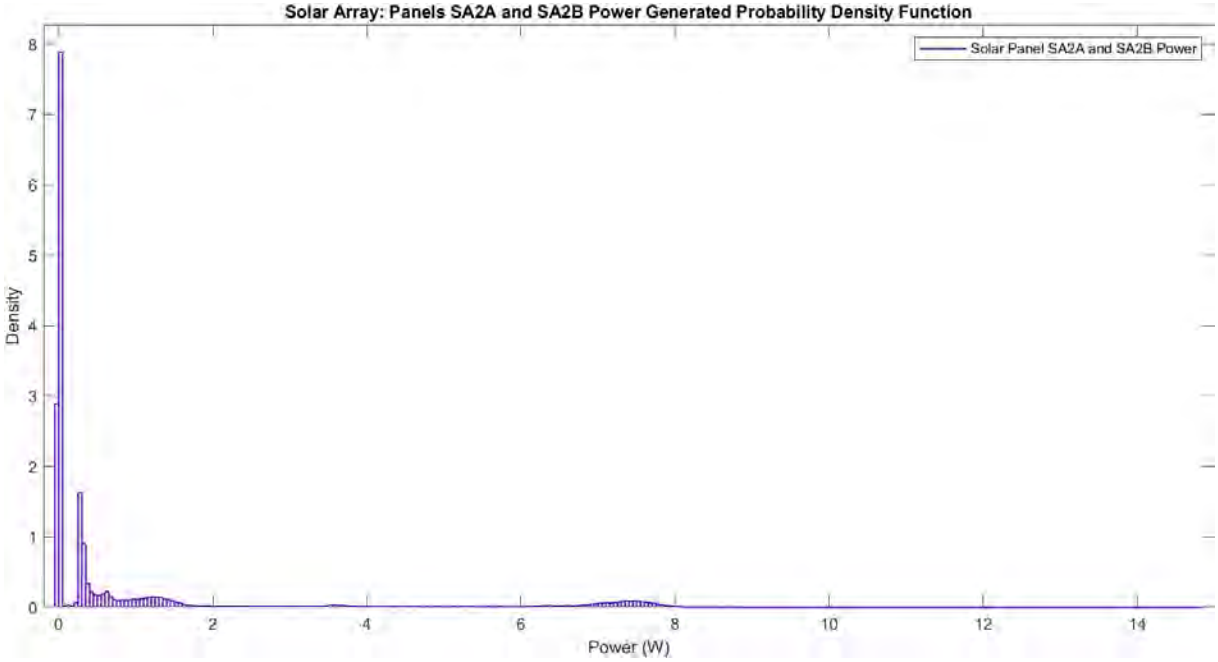

Figure 4.72: Solar Array Panels SA2A and SA2B Power Generated Probability Density Function

4.7.6.2.2.3 Cumulative Density Function

The CDF for solar panels SA2A and SA2B power generated is presented in in Figure B.28 in Appendix B.

4.7.6.3 Solar Panels SA3A and SA3B Power Generated

This section repeats the previous sections for the solar panels SA3A and SA3B.

4.7.6.3.1 Power Generated Raw Telemetry

Power generated from solar panels SA3A and SA3B is presented in Figure A.10. With outliers removed, the resulting data is presented in Figure 4.73

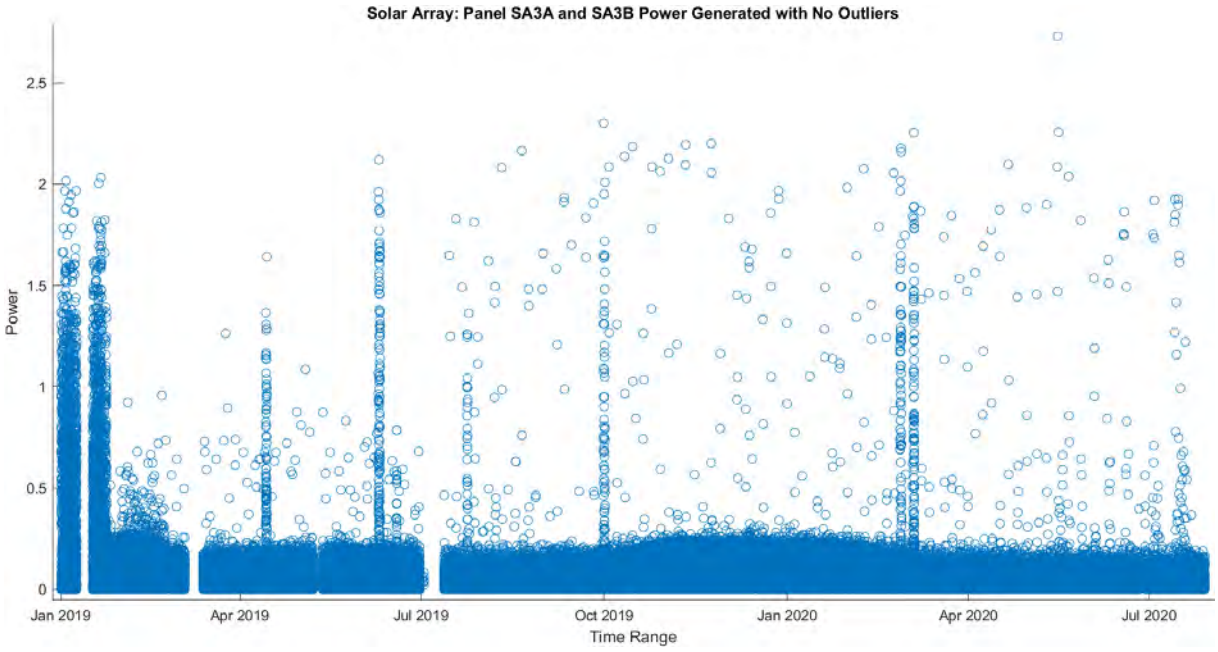

Figure 4.73: Solar Panels SA3A and SA3B Power Generated with No Outliers

4.7.6.3.2 Power Generated Data Analysis

This section gives details regarding the basic statistic, probability density function and cumulative density function for the power generated by solar panels SA3A and SA3B.

4.7.6.3.2.1 Basic Statistics

The basic statistics for solar panels SA3A and SA3B power generated is listed in Table 4.35.

Table 4.35: Solar Panels SA3A and SA3B Power Basic Statistics

Statistic	Power (W)
Mean	0.048
Median	0.021
Mode	0
Range	2.730
Minimum value	0
Maximum value	2.730
Variance	0.011
Standard deviation	0.104

4.7.6.3.2 Probability Density Function

The PDF for solar panels SA3A and SA3B power generated is presented in Figure 4.74.

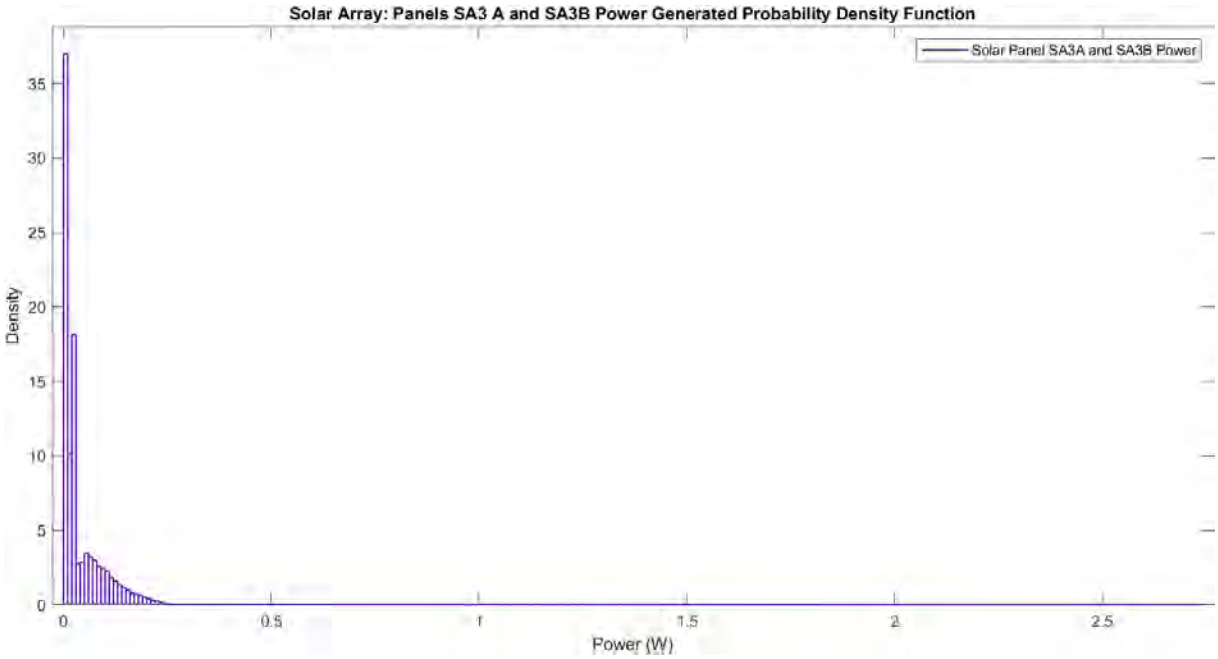

Figure 4.74: Solar Array Panels SA3 A and SA3B Power Generated Probability Density Function

4.7.6.3.3 Cumulative Density Function

The CDF for solar panels SA3A and SA3B power generated is shown in Figure B.29 in Appendix B.

4.7.6.4 Solar Panel Power Correlation

The power correlation between these three pairs of solar panel telemetry channels is summarised in Table 4.36.

Table 4.36: Solar Panel Power Telemetry Correlation

Solar Panels	SA1A and SA1B	SA2A and SA2B	SA3A and SA3B
SA1A and SA1B	1	0.159	0.331
SA2A and SA2B	0.159	1	0.092
SA3A and SA3B	0.331	0.092	1

4.7.6.5 Solar Array Combined Power Generated

This section shows the raw telemetry data as well as the resulting data analysis for the combined power generated by the entire solar array.

4.7.6.5.1 Combined Power Generated Raw Telemetry

The combined instantaneous power from all solar panels is plotted in Figure 4.75.

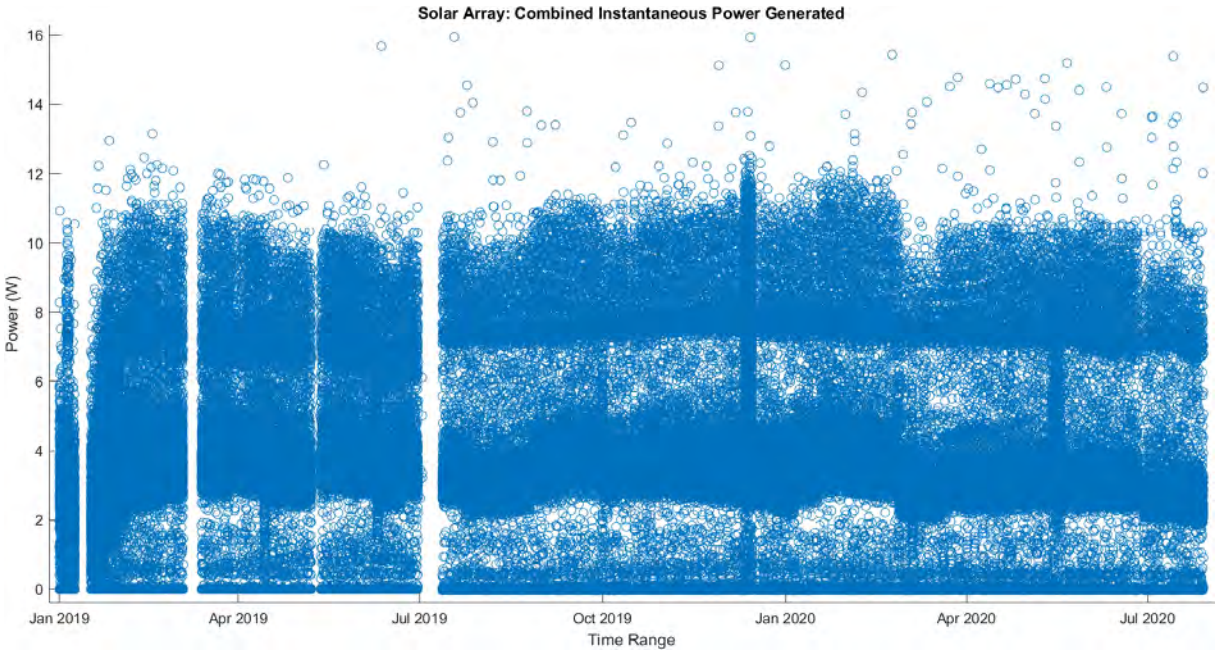

Figure 4.75: Solar Array Combined Instantaneous Power Generated

4.7.6.5.2 Combined Power Generated Data Analysis

This section gives details regarding the basic statistic, probability density function and cumulative density function for the combined power generated by the entire solar array.

4.7.6.5.2.1 Basic Statistics

The basic statistics for the solar array combined power generated is summarised in Table 4.37.

Table 4.37: Solar Array Combined Power Basic Statistics

Statistic	Power (W)

Mean	2.080
Median	0.016
Mode	0
Range	15.992
Minimum value	-0.047
Maximum value	15.945
Variance	7.588
Standard deviation	2.755

4.7.6.5.2.2 Probability Density Function

The PDF for the solar array combined power generated is shown in Figure 4.76.

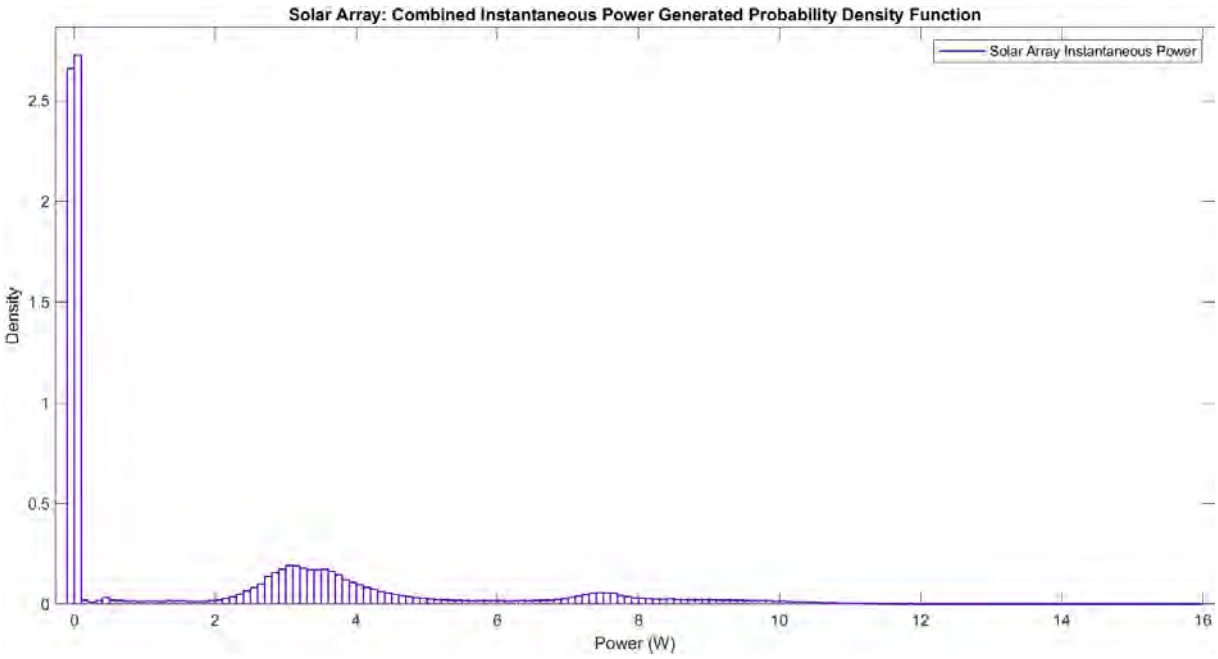

Figure 4.76: Solar Array Combined Instantaneous Power Generated Probability Density Function

4.7.6.5.2.3 Cumulative Density Function

The CDF for the solar array combined power generated is shown in Figure B.30 in Appendix B.

4.7.7.5 Solar Array Combined Power Generated in Comparison to Combined EPS Bus Power

This section presents the raw telemetry data as well as the resulting data analysis when comparing the power generated by the solar array in comparison to the EPS bus power.

4.7.7.5.1 Combined Power Generated in Comparison to Combined EPS Bus Power Raw Telemetry

As previously mentioned, power is an important design aspect of a satellite's operation, because there is no contingency plan if the satellite power generation does not meet the consumption rate.

Therefore, comparing the instantaneous combined solar array power generation to the EPS bus power consumption is vital to make sure that there is enough available electrical energy to ensure that all systems operate nominally.

Figure 4.77 shows this comparison where the telemetry spans from 12 May 2019 09:06:05 UTC to 28 July 2020 09:30:15 UTC with a timestep of every 3 minutes. Evidently there is a surplus of power being generated from the solar arrays with only a few occurrences where the EPS power consumption exceeds that of the power generation.

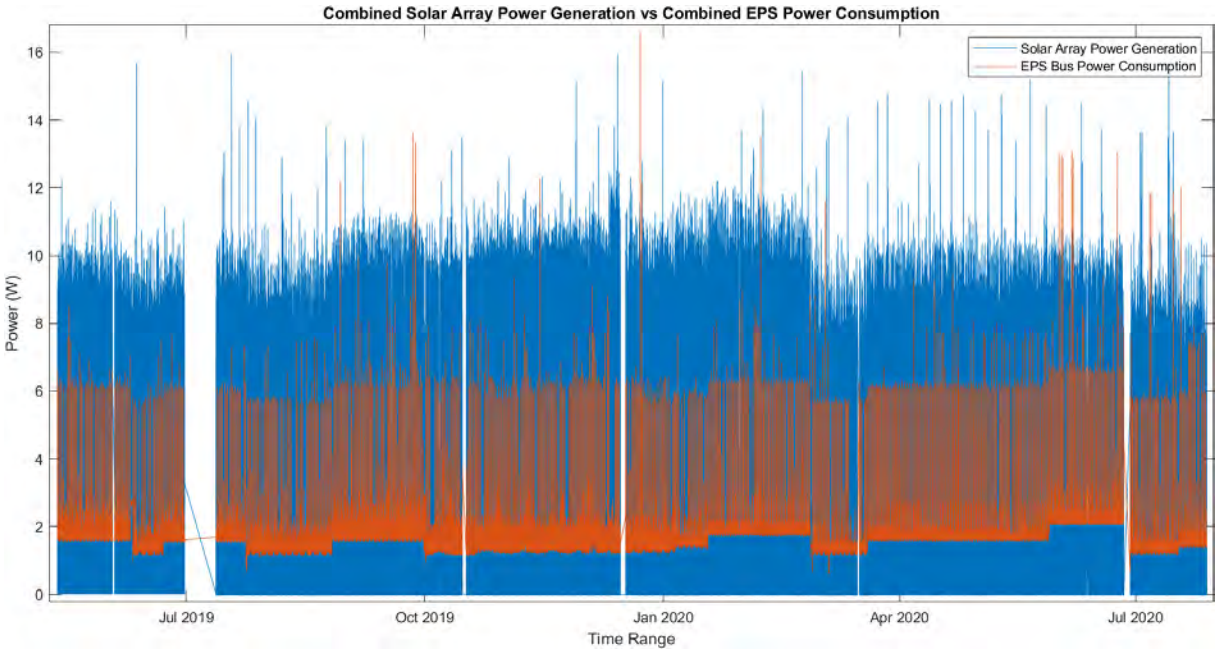

Figure 4.77: Combined Solar Array Power Generation vs Combined EPS Power Consumption

However, the excess power being generated by the solar arrays is stored in the battery, which then can be used by the EPS to meet that deficit, as seen in the graph below where the telemetry spans from 12 May 2019 09:06:05 UTC to 28 July 2020 09:30:15 UTC with a timestep of every 3 minutes. This is represented in Figure 4.78.

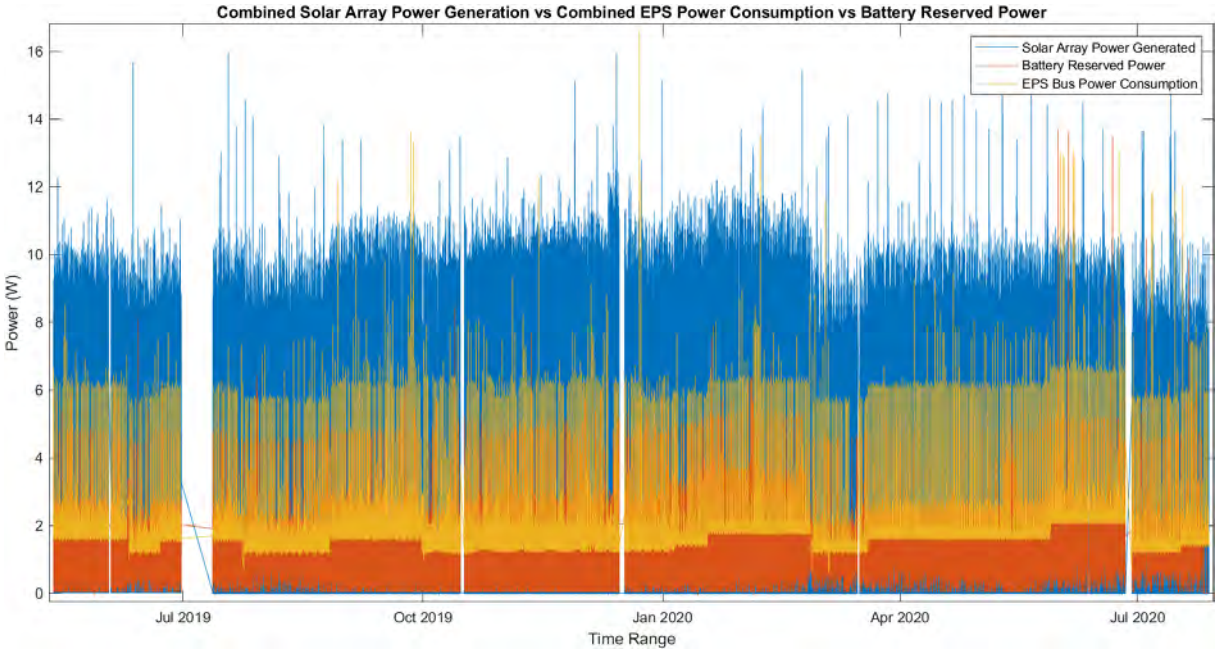

Figure 4.78: Combined Solar Array Power Generation vs Combined EPS Power Consumption vs Battery Reserved Power

4.8 UHF Transceiver (UTRXC)

One of the subsystems onboard ZACube-2 that was designed in-house, is the UTRX, a compact UHF transceiver used to downlink as well as uplink telemetry data to the satellite from the ground segment. The telemetry range for the UTRXC spans from 01 January 2019 00:02:39 UTC to 28 July 2020 23:57:15 UTC at a timestep of 3 minutes.

4.8.1 3.3V Regulated Bus

This section shows the raw telemetry data as well as the resulting of data analysis for the UTRXC 3V regulated bus current.

4.8.1.1 Raw Telemetry

The UTRXC is a transceiver that requires power from both the 3.3V and 5V regulated buses. For this subsection, the focus will be on the 3.3V regulated bus. Due to the voltage being regulated, the current will fluctuate. The graph generated from the captured current telemetry for the UTRXC 3.3V regulated bus can be seen in Figure A.11. Without outliers removed, the telemetry is presented in Figure 4.79.

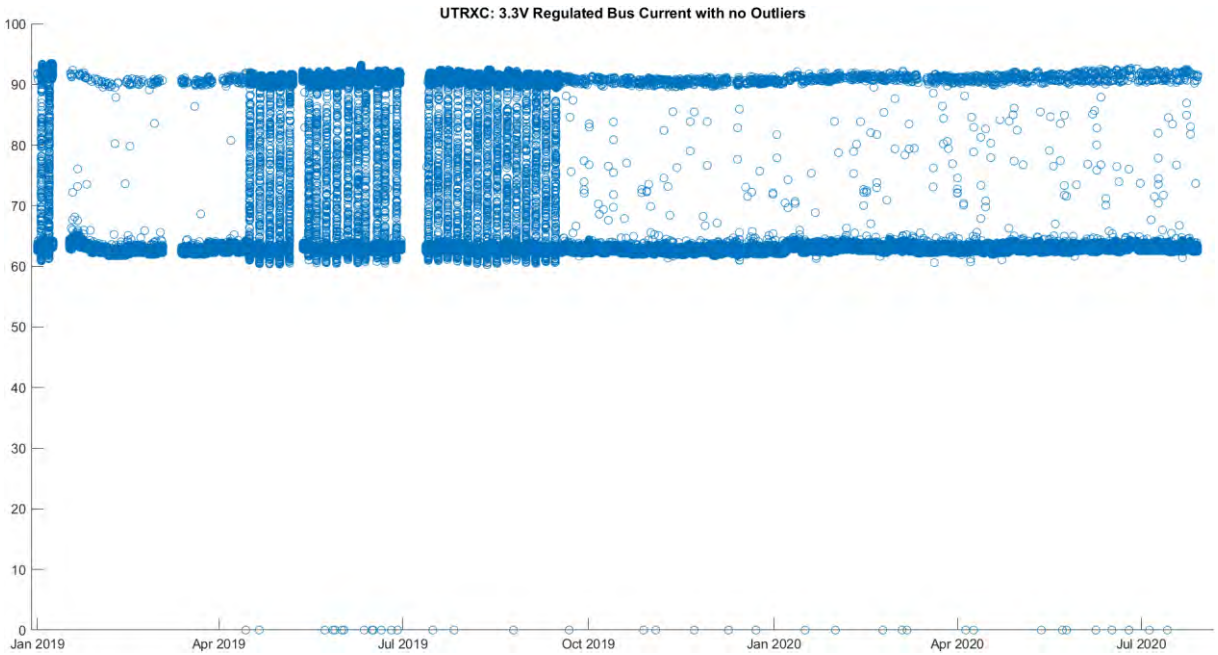

Figure 4.79: UTRXC 3.3V Regulated Bus Current with no Outliers

It can be seen that the majority of the current drawn is either at the lower end ± 62mA or ±92mA at the upper end, with cases of there being no current drawn.

4.8.1.2 Data Analysis

This section gives details regarding the basic statistic, probability density function and cumulative density function for the UTRXC 3.3V regulated bus current.

4.8.1.2.1 Basic Statistics

The basic statistics for the 3.3V regulated bus current is summarised in Table 4.38.

Table 4.38: UTRXC 3.3V Regulated Bus Current Basic Statistics

Statistic	Current (A)
Mean	0.066
Median	0.063
Mode	0.063
Range	0.094
Minimum value	0
Maximum value	0.094
Variance	0
Standard deviation	0.009

4.8.1.2.2 Probability Density Function

The PDF for the 3.3V regulated bus can be seen in the figure below.

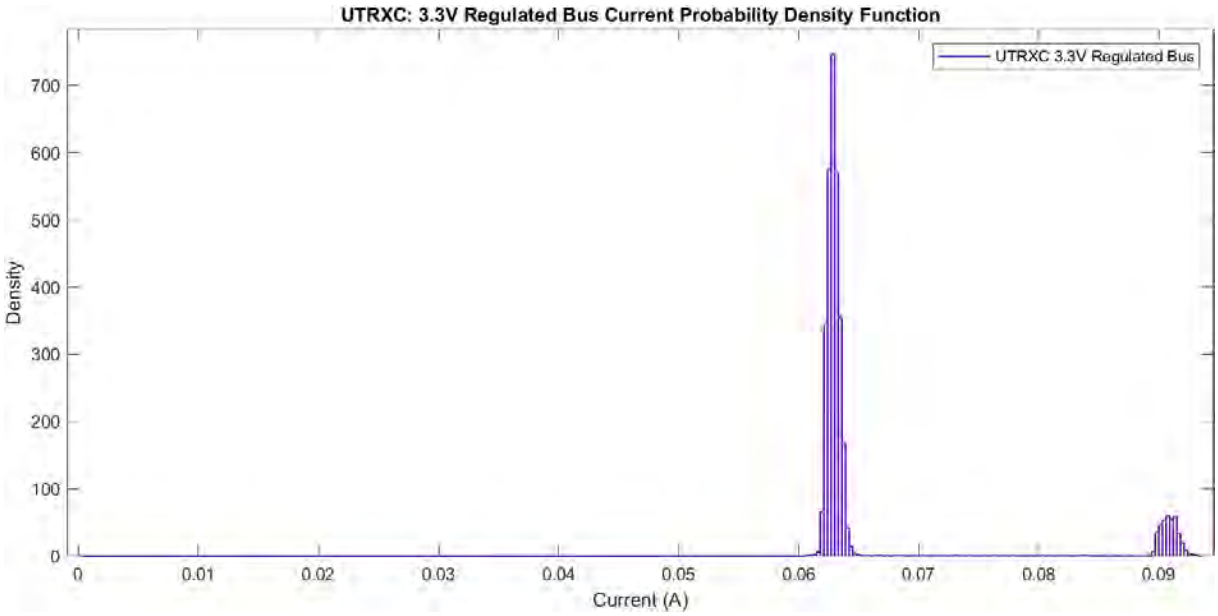

Figure 4.80: UTRXC 3.3V Regulated Bus Current Probability Density Function

4.8.1.2.3 Cumulative Density Function

The CDF for the 3.3V regulated bus current can be found in Figure B.31 in Appendix B.

4.8.2 5V Regulated Bus

This section repeats the previous sections for the UTRXC 5V regulated bus current.

4.8.2.1 Raw Telemetry

As mentioned previously, the UTRXC transceiver requires power from both the 3.3 and 5V regulated buses. For this subsection, the 5V regulated bus current will be the focus. Since the bus lines are regulated in nature, the current values will vary.

The telemetry current values from the regulated 5V are presented in Figure 4.81 (with outliers removed).

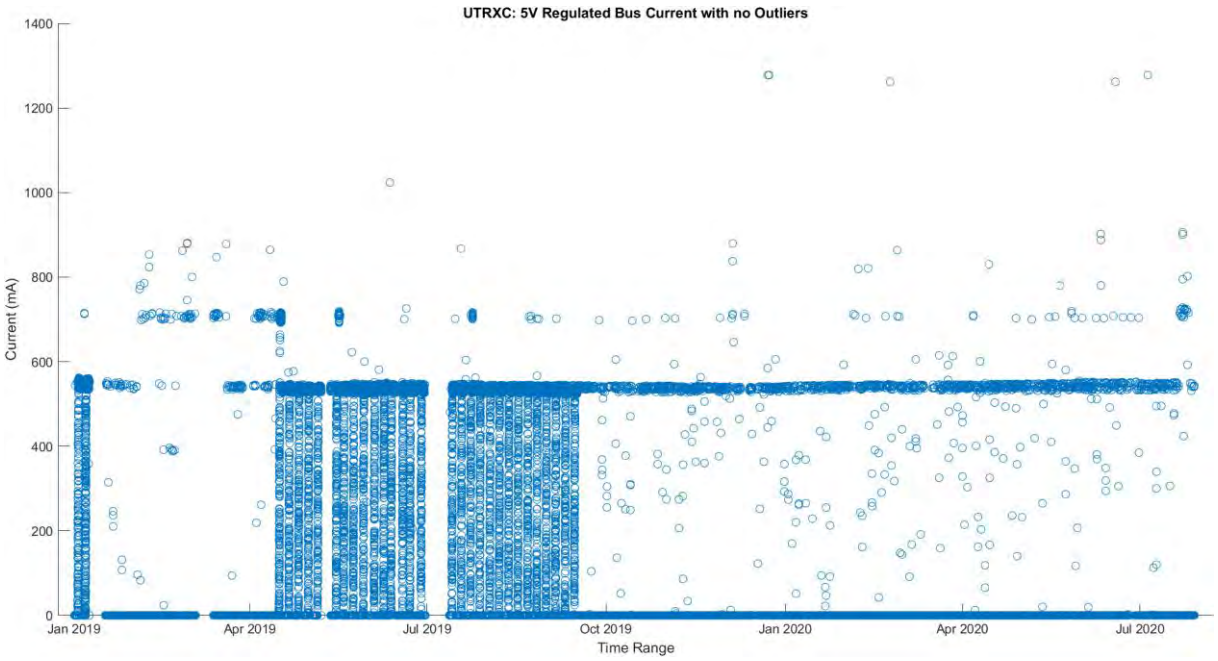

Figure 4.81: 5V Regulated Bus Current with no Outliers

It is evident that the majority of current consumed was just under 600mA with the transceiver being significantly utilised from mid-April 2019 until mid-September 2019. This is further demonstrated when the current telemetry data is plotted logarithmically, as presented in Figure 4.82.

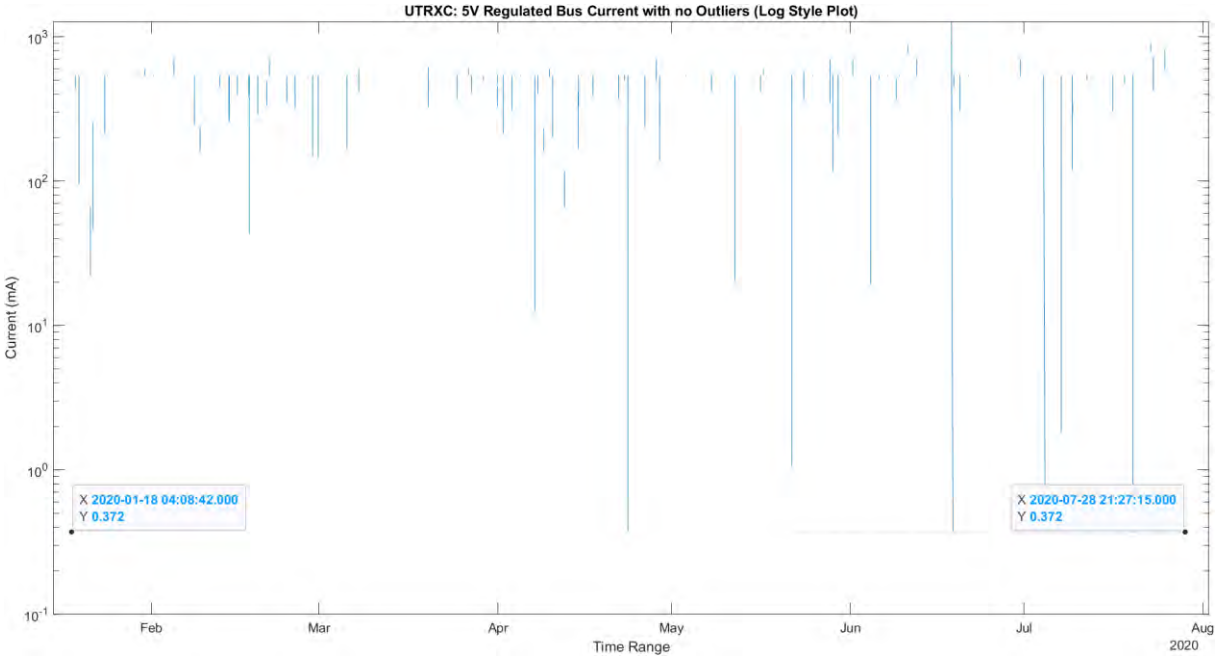

Figure 4.82: 5V Regulated Bus Current with no Outliers Logarithmic Plot

Additionally, from 18 January 2020 UTC to 28 July 2020 UTC there are micro fluctuations that did not exist before the aforementioned time range. However, since these variations are so minute, it was ignored.

4.8.2.2 Data Analysis

This section gives details regarding the basic statistic, probability density function and cumulative density function for the UTRXC 5V regulated bus current.

4.8.2.2.1 Basic Statistics

The basic statistics for the 5V regulated bus current is listed in Table 4.39.

Table 4.39: UTRXC 5V Regulated Bus Current Basic Statistics

Statistic	Current (A)
Mean	0.066
Median	0
Mode	0
Range	1.278
Minimum value	0
Maximum value	1.278
Variance	0.030
Standard deviation	0.174

4.8.2.2.2 Probability Density Function

The PDF for the 5V regulated bus current is presented in the figure below.

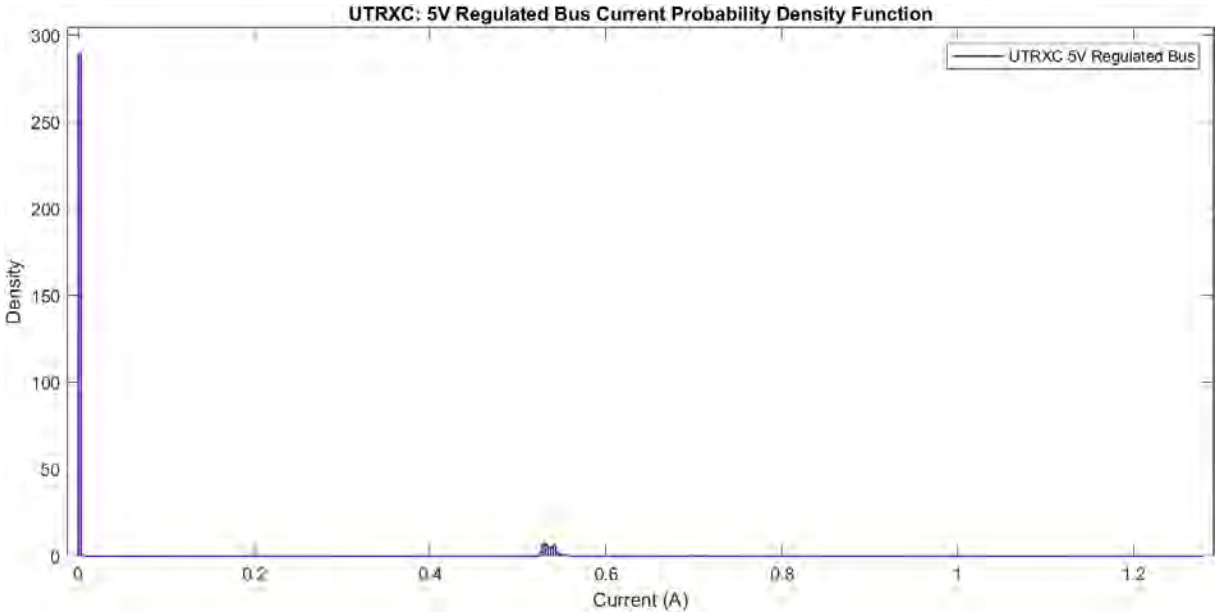

Figure 4.83: UTRXC 5V Regulated Bus Current Probability Density Function

4.8.2.2.3 Cumulative Density Function

The CDF for the 5V regulated bus current is presented in Figure B.32 in Appendix B.

4.8.3 Power Usage

With the current values known and the data sets being cleaned of the outliers, the respective power graphs can be generated for both the 3.3V and 5V regulated bus lines in addition to the overall power consumed.

4.8.3.1 3.3V Regulated Bus Power

This section shows the raw telemetry data as well as the resulting data analysis for the UTRXC 3.3V regulated bus power.

4.8.3.1.1 Power Raw Telemetry

Figure 4.84 is a representation of the power consumed for the 3.3V regulated bus line.

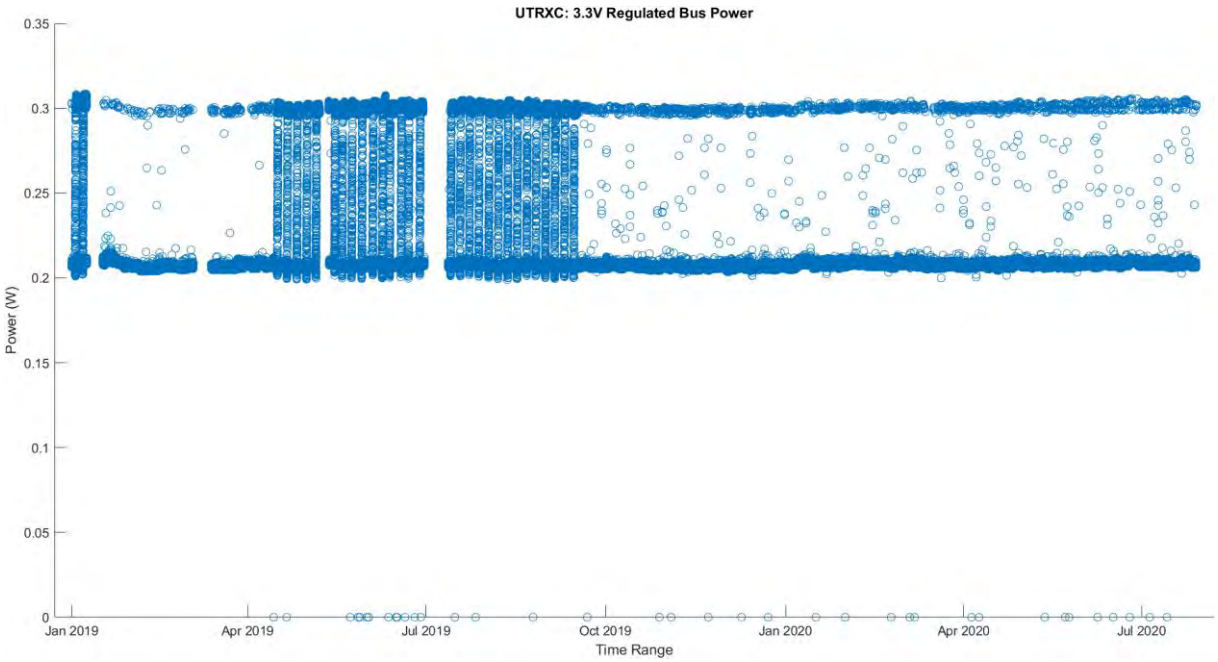

Figure 4.84: UTRXC 3.3V Regulated Bus Power

4.8.3.1.2 Data Analysis

This section gives details regarding the basic statistic, probability density function and cumulative density function for the UTRXC 3.3V regulated bus power.

4.8.2.1.2.1 Basic Statistics

The basic statistics for the 3.3V regulated bus power generated is summarised in Table 4.40

Table 4.40: UTRXC 3.3V Regulated Bus Power Basic Statistics

Statistic	Power (W)
Mean	0.219
Median	0.271
Mode	0.207
Range	0.309
Minimum value	0
Maximum value	0.309
Variance	0.001
Standard deviation	0.030

4.8.3.1.2.2 Probability Density Function

The PDF for the 3.3V regulated bus power can be seen in Figure 4.85

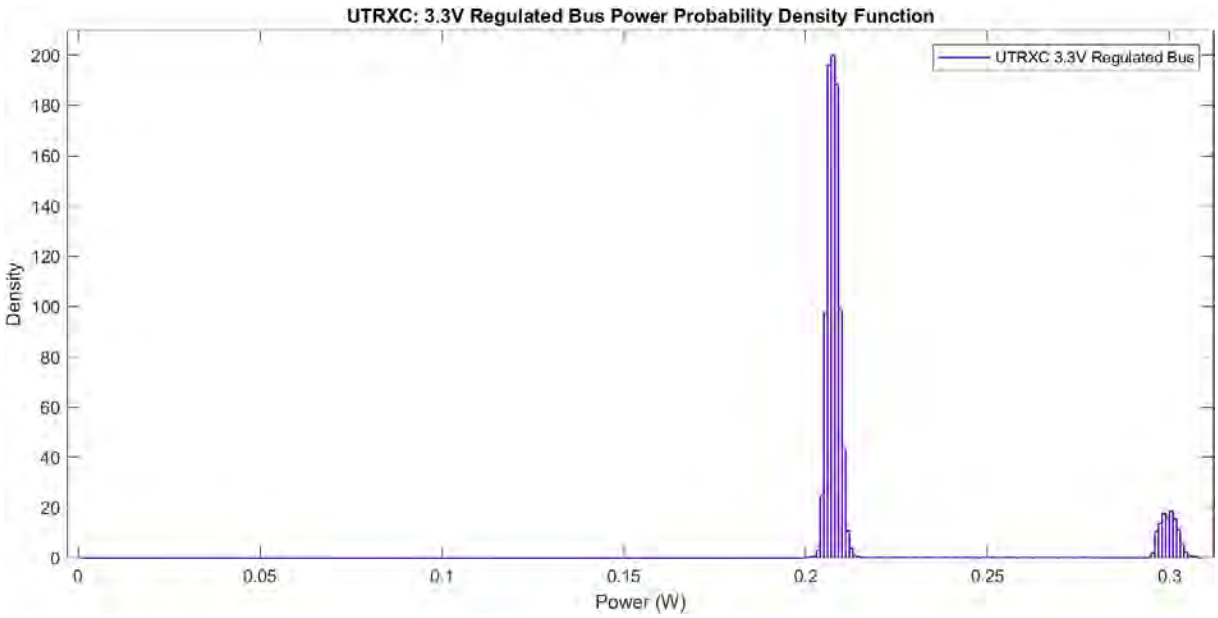

Figure 4.85: UTRXC 3.3V Regulated Bus Power Probability Density Function

4.8.3.1.2.3 Cumulative Density Function

The CDF for the 3.3V regulated bus power can be seen in Figure B.33 in Appendix B.

4.8.3.2 5V Regulated Bus Power

This section shows the raw telemetry data as well as the resulting data analysis of the 5V regulated by power.

4.8.3.2.1 Power Raw Telemetry

Figure 4.86 presents the power consumed for the 5V regulated bus line.

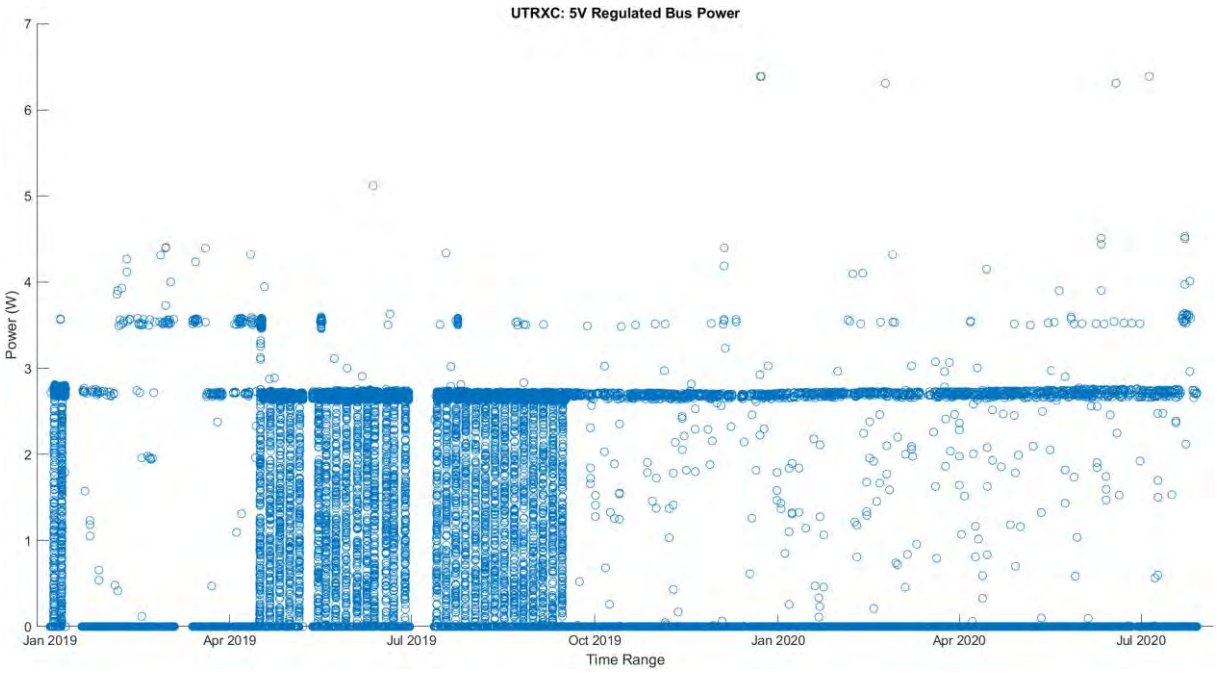

Figure 4.86: UTRXC 5 Regulated Bus Power

4.8.3.2.2 Power Data Analysis

This section gives details regarding the basic statistic, probability density function and cumulative density function for the UTRXC 5V regulated bus power.

4.8.3.2.2.1 Basic Statistic

The basic statistics for power consumed by the 5V regulated bus is listed in Table 4.41.

Table 4.41: UTRXC 5V Regulated Bus Power Basic Statistics

Statistic	Power (W)
Mean	0.328
Median	0
Mode	0
Range	6.388
Minimum value	0
Maximum value	6.388
Variance	0.757
Standard deviation	0.870

4.8.3.2.2.2 Probability Density Function

The PDF for the 5V regulated bus power can be seen in the figure below.

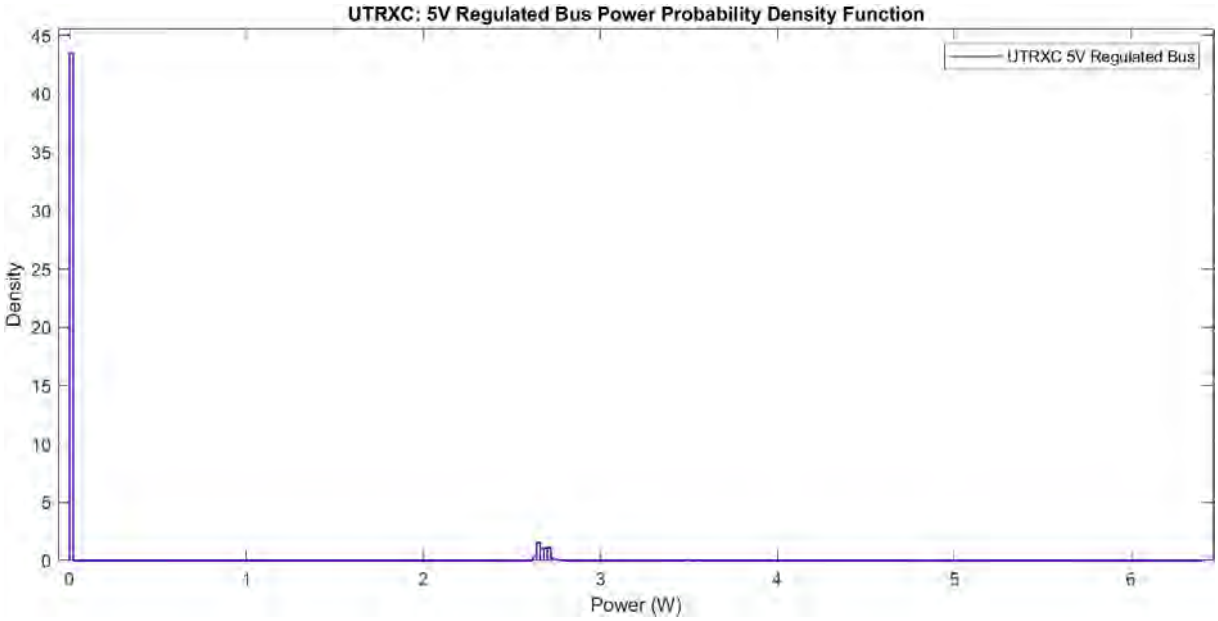

Figure 4.87: UTRXC 5V Regulated Bus Power Probability Density Function

4.8.3.2.2.3 Cumulative Density Function

The CDF for the 5V regulated bus power can be seen in Figure B.34 in Appendix B.

4.8.3.3 Combined Regulated Bus Power

This section shows the raw telemetry data as well as the resulting data analysis for the combined regulated bus power.

4.8.3.3.1 Combined Regulated Bus Power Raw Telemetry

With both regulated bus power values calculated, the combined regulated bus power can be calculated as presented in Figure 4.88.

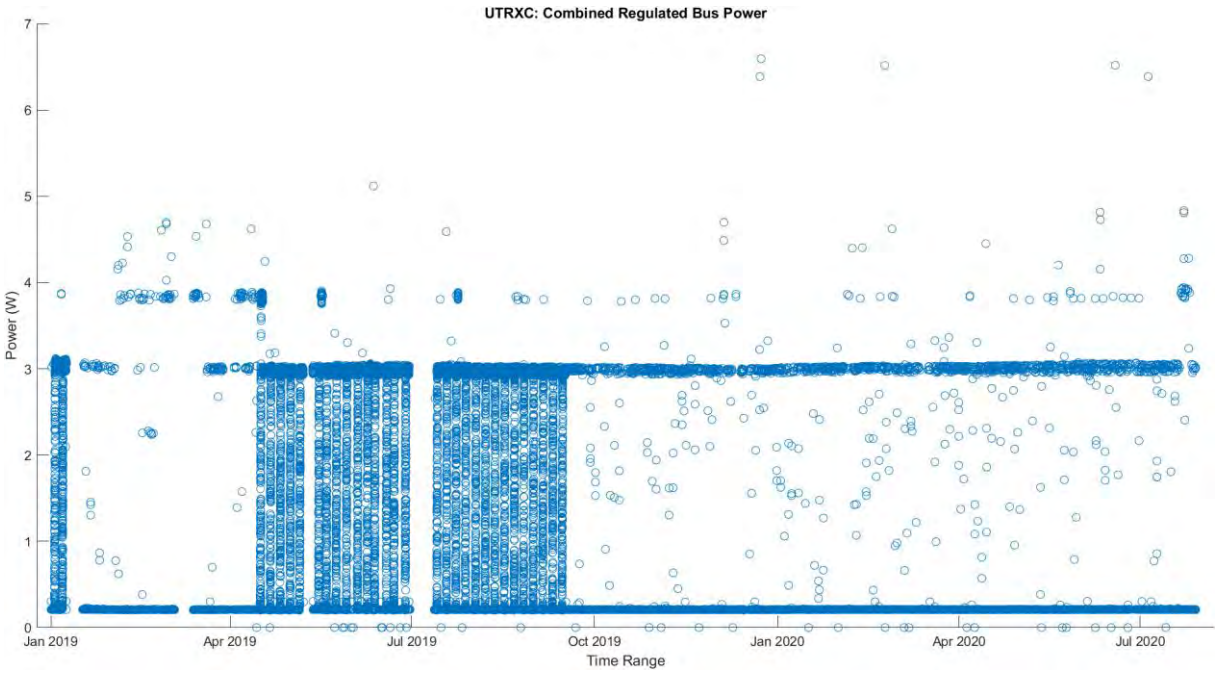

Figure 4.88: UTRXC Combined Regulated Bus Power

While it may seem that, through visual means, the 5V regulated bus power and the combined regulated power are the same, by superimposing these graphs the combined regulated bus power has a higher average low power value as seen in the figure below

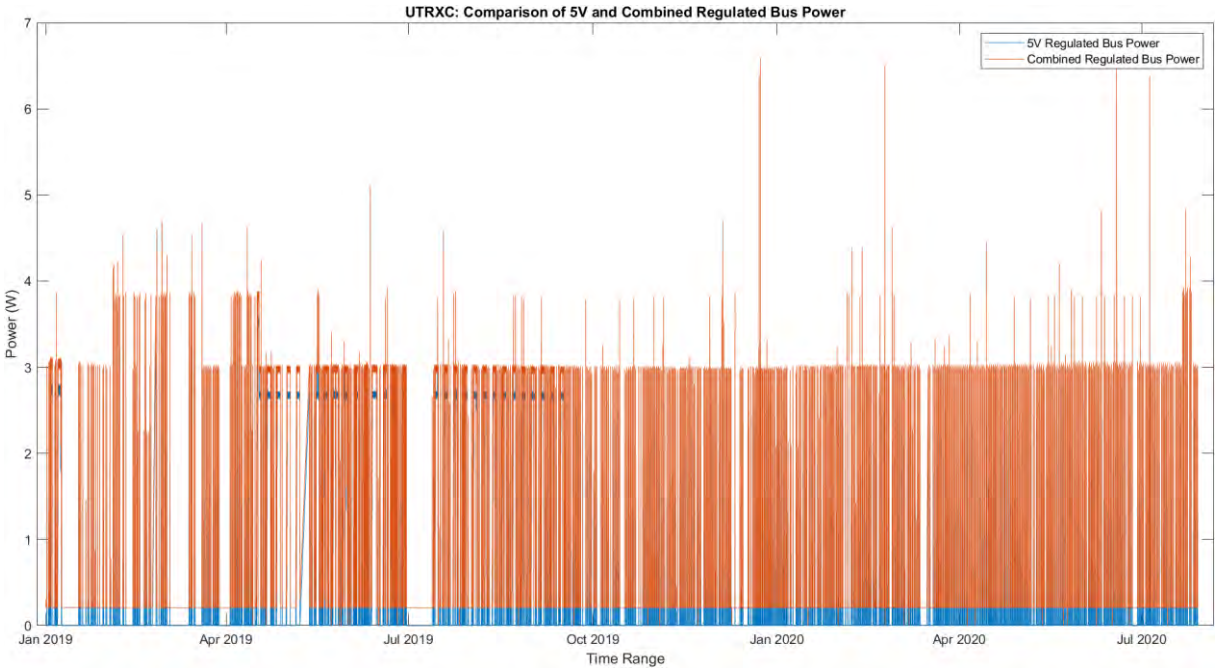

Figure 4.89: UTRXC Comparison of 5V and Combined Regulated Bus Power

4.8.3.3.2 Combined Regulated Bus Power Data Analysis

The following section presents the data analysis of the combined regulated bus power for the UTRXC.

4.8.3.3.2.1 Basic Statistics

The basic statistic for the combined regulated bus power is listed in Table 4.42.

Table 4.42: UTRXC Combined Regulated Bus Power Basic Statistics

Statistic	Power (W)
Mean	0.547
Median	0.208
Mode	0.207
Range	3.389
Minimum value	0
Maximum value	3.389
Variance	0.808
Standard deviation	0.899

4.8.3.3.2.2 Probability Density Function

The PDF for the combined regulated bus power can be referred to in Figure 4.90.

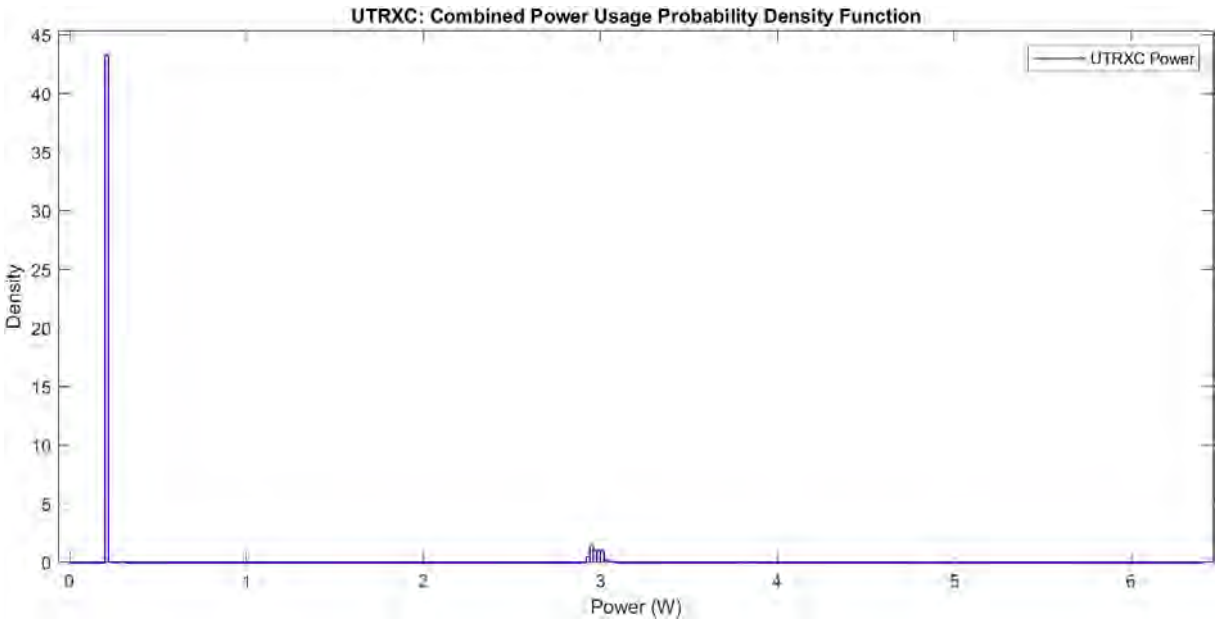

Figure 4.90: UTRXC Combined Power Probability Density Function

4.8.3.3.2.3Cumulative Density Function

The CDF for the combined regulated bus power is shown in Figure B.35 in Appendix B.

4.8.4 Power Amplifier (PA) Forward Power

The power amplifier amplifies the transmitted radio frequency (RF) signal. Forward power is the magnitude of the forward wave towards the antenna, which is one of the components of a standing wave. As the name implies, the forward wave moves towards the antenna(s), whilst the reflected wave returns from the antenna towards the power amplifier when the antenna is not matched to the amplifier's output.

The UTRXC was designed in-house and was designed to transmit at three different output powers, which can be seen in the table below along with whether it was behaving solely as a receiver or as a transceiver.

Table 4.43: UTRXC Basic RF Characteristics

RF Power	State of Operation	Signal Strength Power (dBm)
0.5W	Receiver ON, transmitter ON	27
1W	Receiver ON, transmitter ON	30
2W	Receiver ON, transmitter ON	33

The following sections presents the relevant raw telemetry data as well as the resulting data analysis.

4.8.4.1 Power Amplifier (PA) Forward Power Raw Telemetry

Figure A.13 shows the power amplifier's forward power. This is presented without outliers in Figure 4.91.

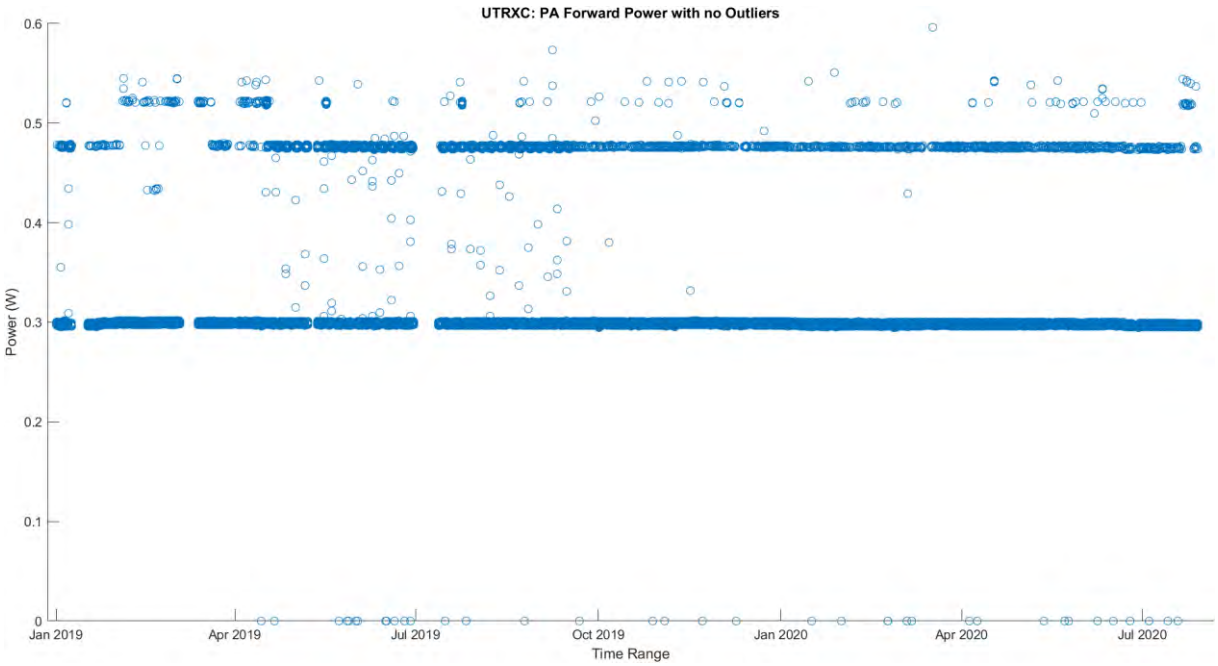

Figure 4.91: UTRXC PA Forward Power with no Outliers

The figure above shows that the UTRXC was at 0.5W transmit power for the majority of the time it was active. When cross-referenced with the table regarding the UTRXC basic RF characteristics, the lowest constant value was 0.3W, whilst the highest was 0.5W.

4.8.4.2 Power Amplifier (PA) Forward Power Data Analysis

The following section presents the data analysis of the PA forward power for the UTRXC.

4.8.4.2.1 Basic Statistics

The basic statistics for the UTRXC PA forward power are listed in Table 4.44.

Table 4.44: UTRXC PA Forward Power Basic Statistics

Statistic	Power (W)
Mean	0.316
Median	0.299
Mode	0.298
Range	0.596
Minimum value	0
Maximum value	0.596
Variance	0.003
Standard deviation	0.054

4.8.4.2.2 Probability Density Function

The PDF for the UTRXC PA forward power is shown in Figure 4.92.

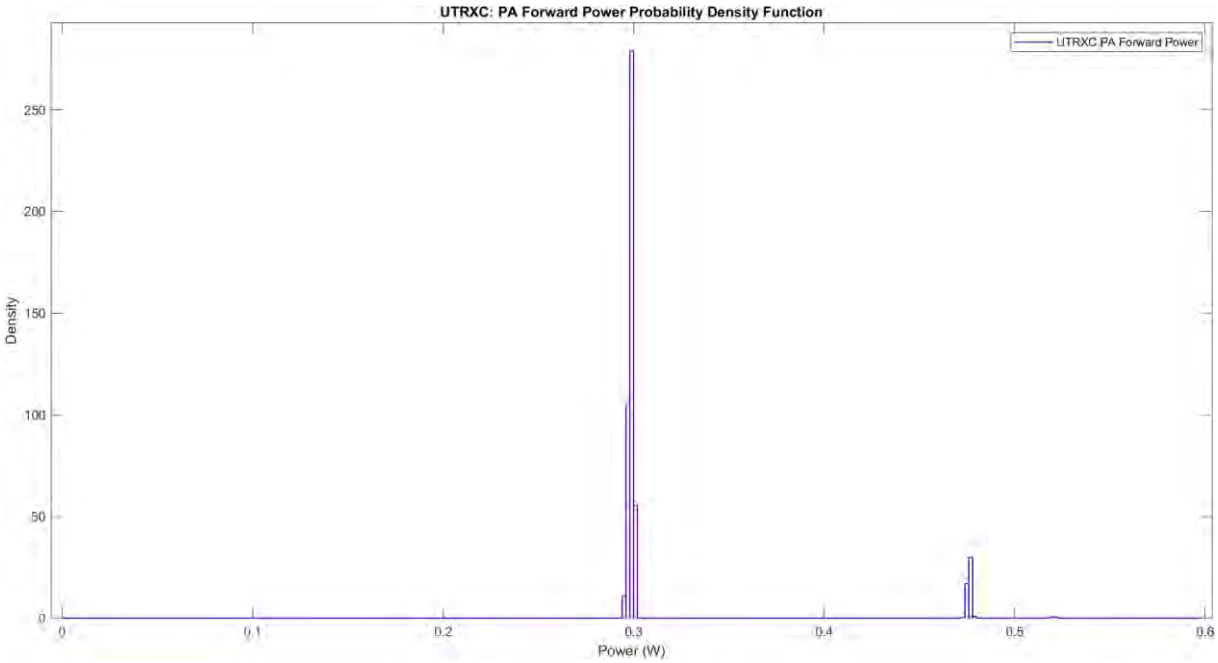

Figure 4.92: UTRXC PA Forward Power Probability Density Function

4.8.4.2.3 Cumulative Density Function

The CDF for the UTRXC PA forward power is shown in Figure B.36 in Appendix B.

4.8.5 Power Amplifier (PA) Reverse Power

This section repeats the previous sections for the PA reverse power

4.8.5.1 Raw Telemetry

The reverse or reflective power telemetry is plotted in Figure A.14, and without outliers, in Figure 4.93

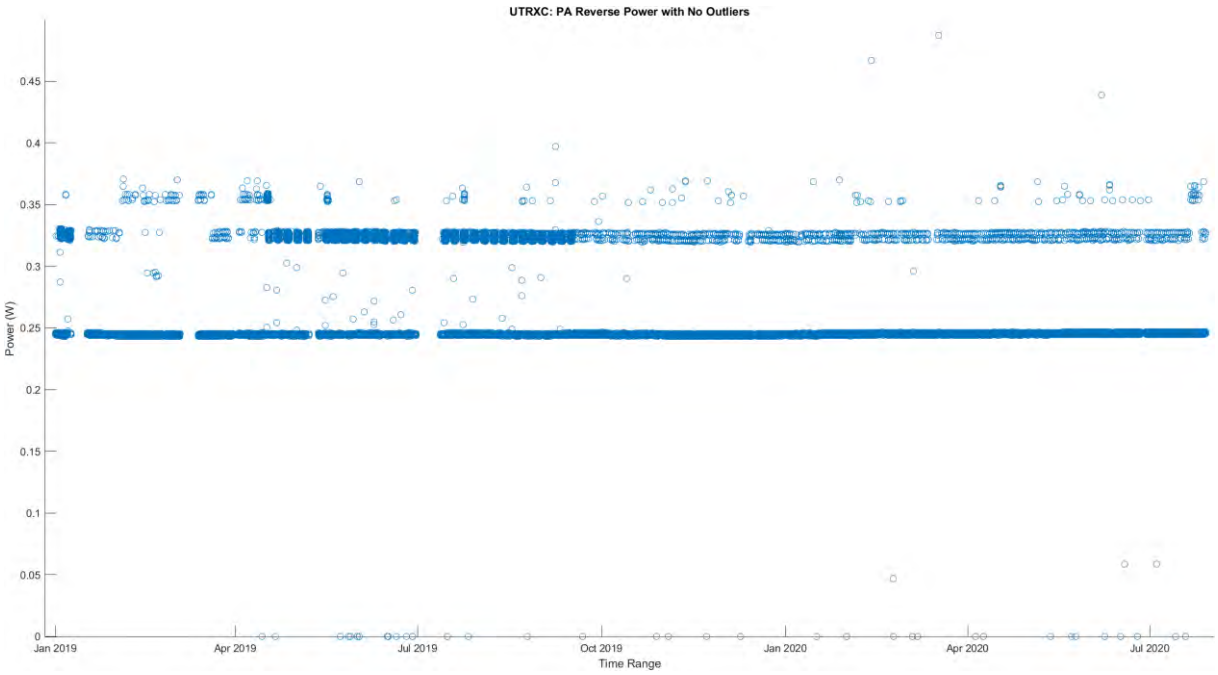

Figure 4.93: UTRXC PA Reverse Power with No Outliers

From Figure 4.93, the average reflective power was less than that of the forward or incident power as is expected.

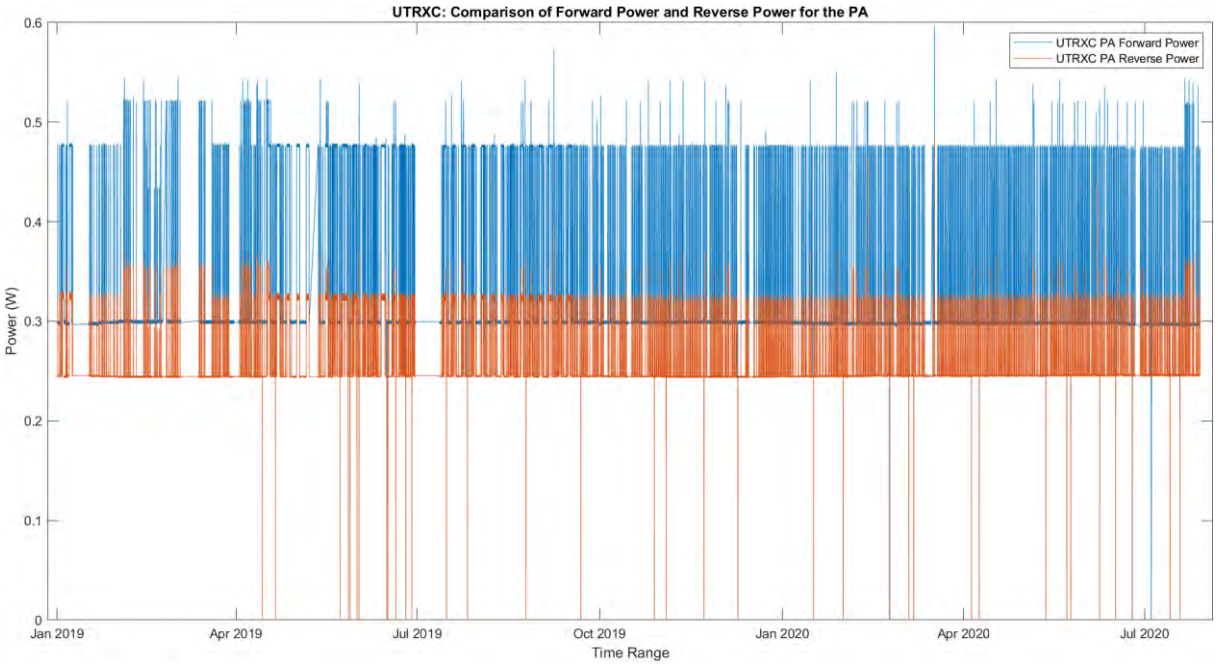

Figure 4.94: UTRXC Comparison of Forward Power and Reverse Power for the PA

4.8.5.2 Data Analysis

This section gives details regarding the basic statistic, probability density function and cumulative density function for the UTRXC PA reverse power.

4.8.5.2.1 Basic Statistics

The basic statistics for the UTRXC PA reverse power are summarised in Table 4.45.

Table 4.45: UTRXC PA Reverse Power Basic Statistics

Statistic	Power (W)
Mean	0.253
Median	0.245
Mode	0.245
Range	0.487
Minimum value	0
Maximum value	0.487
Variance	0
Standard deviation	0.024

4.8.5.2.2 Probability Density Function

The PDF for the UTRXC PA reverse power is shown in Figure 4.95.

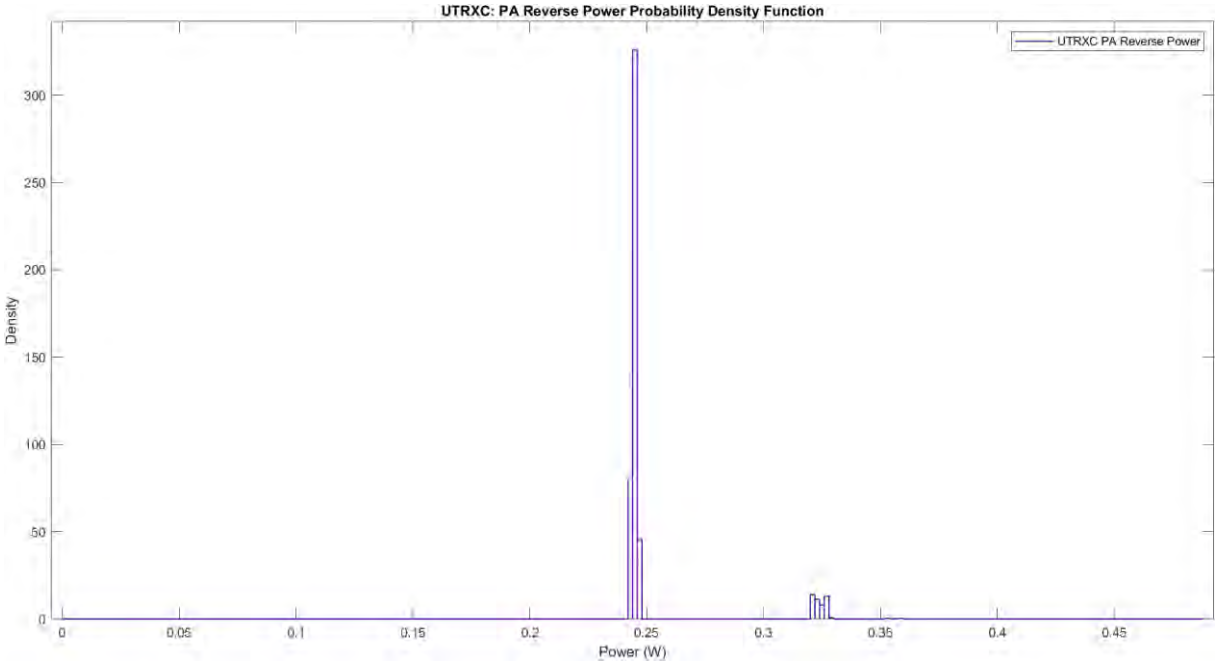

Figure 4.95: UTRXC PA Reverse Power Probability Density Function

4.8.5.2.3 Cumulative Density Function

The CDF for the UTRXC PA reverse power is shown in Figure B.37 in Appendix B.

4.8.6 Power Amplifier (PA) Temperature

This section presents the raw telemetry data as well as the data analysis of the PA temperature.

4.8.6.1 Raw Telemetry

The temperature of the PA is vital as it contributes a sizeable portion of the onboard heat generation. If operating too hot, or too cold, the amplifier will not work nominally and potentially leading to either packets lost or worst-case, device failure. Therefore, comparing the telemetry to the designed operating thermal limits is vital. The PA temperature is shown in Figure 4.96

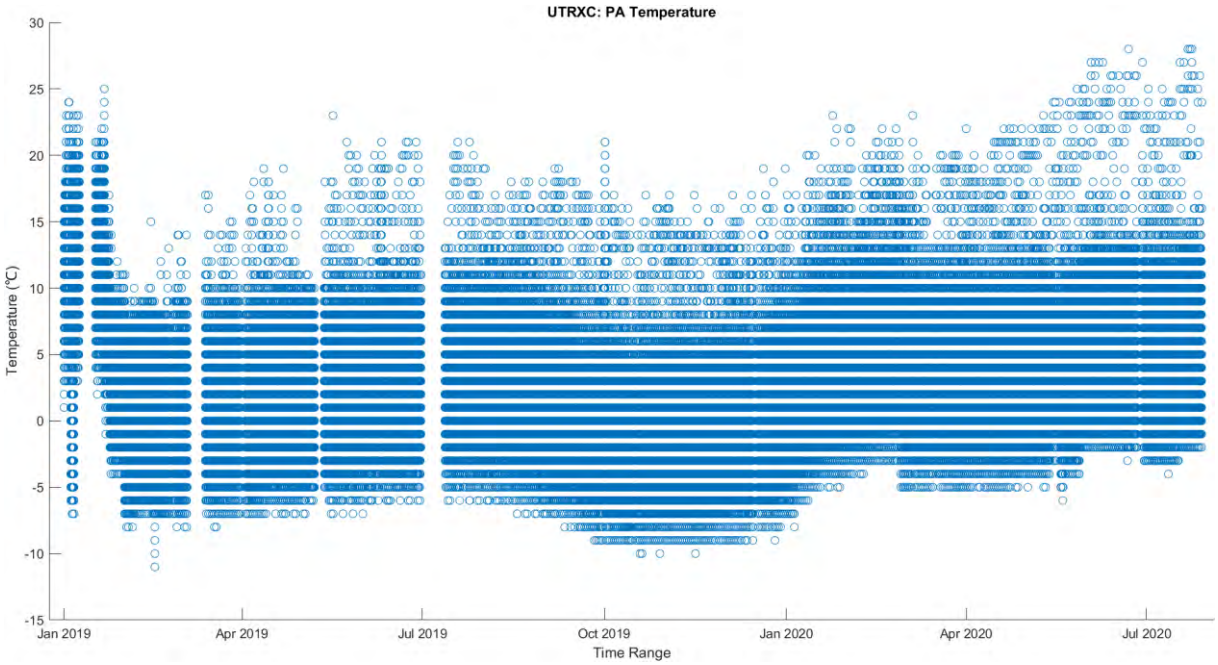

Figure 4.96: UTRXC PA Temperature

4.8.6.2 Data Analysis

This section gives details regarding the basic statistic, probability density function and cumulative density function for the UTRXC PA temperature.

4.8.6.2.1 Basic Statistics

The basic statistics for the UTRXC PA temperature are summarised in Table 4.46.

Table 4.46: UTRXC PA Temperature Basic Statistics

Statistic	Temperature (°C)
Mean	3.102
Median	3
Mode	6
Range	39
Minimum value	-11
Maximum value	28
Variance	31.060
Standard deviation	5.573

4.8.6.2.2 Probability Density Function

The PDF for the UTRXC PA temperature is shown in Figure 4.97.

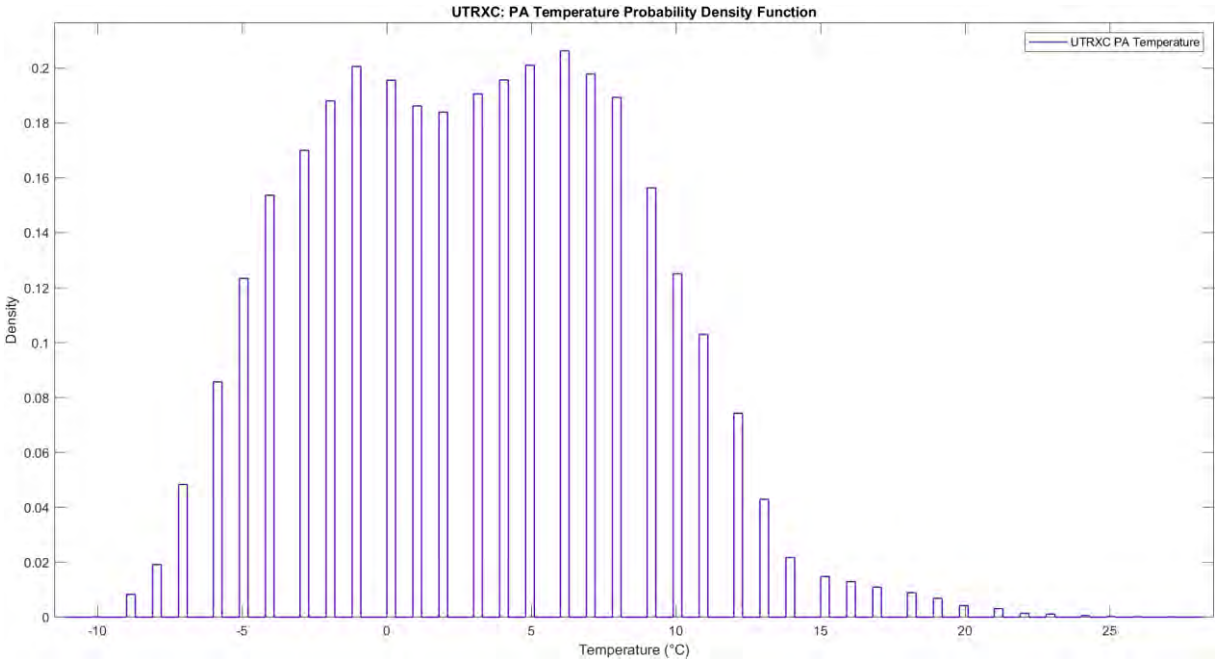

Figure 4.97: UTRXC PA Temperature Probability Density Function

4.8.6.2.3 Cumulative Density Function

The CDF for the UTRXC PA temperature is shown in Figure B.38 in Appendix B.

4.8.7 Rx Received Signal Strength Indicator (RSSI)

RSSI is a measurement of the received signal strength from a source where the source is the ground station in this case and varies with elevation. At a lower elevation, a decrease in the RSSI value can be observed, owing to a weaker signal strength due to the satellite being further away from the ground station. RSSI values can either be in decibels (dB) or decibels milli-Watt (dBm or dBmW). The RSSI telemetry value for the UTRXC is given in volts, equivalent to a specific received RF level, which was provided in the design documentation by the engineering team.

Table 4.47: RSSI Received Power

	Voltage (V)		
RF Level (dBm)	**Minimum**	**Typical**	**Maximum**
-118	N/A	0.3	0.8
-68	0.7	1.1	1.8
-23	1.2	1.8	2.5

The following section shows the raw telemetry data as well as the resulting data analysis process.

4.8.7.1 Raw Telemetry

From Figure 4.98, the approximate highest and lowest values are 1.3V and 0.5V, respectively

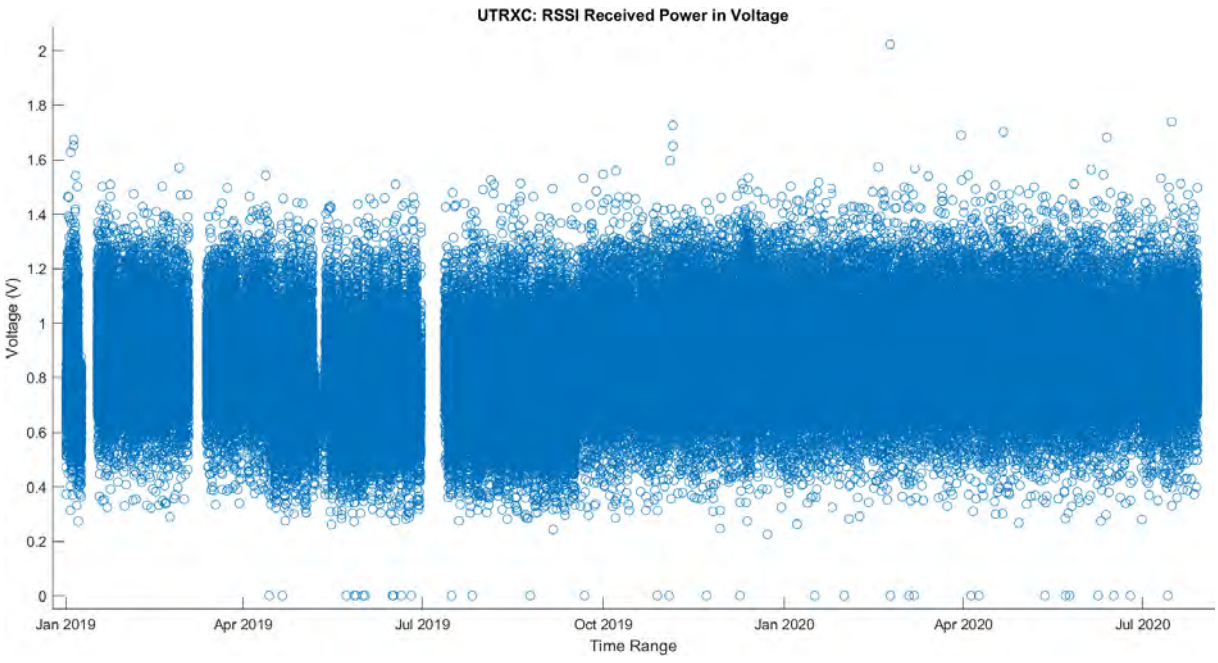

Figure 4.98: UTRXC RSSI Received Power in Voltage

4.8.7.2 Data Analysis

This section gives details regarding the basic statistic, probability density function and cumulative density function for the UTRXC Rx RSSI

4.8.7.2.1 Basic Statistics

The basic statistics for the UTRXC RSSI is listed in Table 4.48.

Table 4.48: UTRXC Rx RSSI Basic Statistics

Statistic	Voltage (V)
Mean	0.851
Median	0.853
Mode	0.877
Range	2.024
Minimum value	0
Maximum value	2.024
Variance	0.019
Standard deviation	0.138

4.8.7.2.2 Probability Density Function

The PDF for the UTRXC RSSI is shown in Figure 4.99.

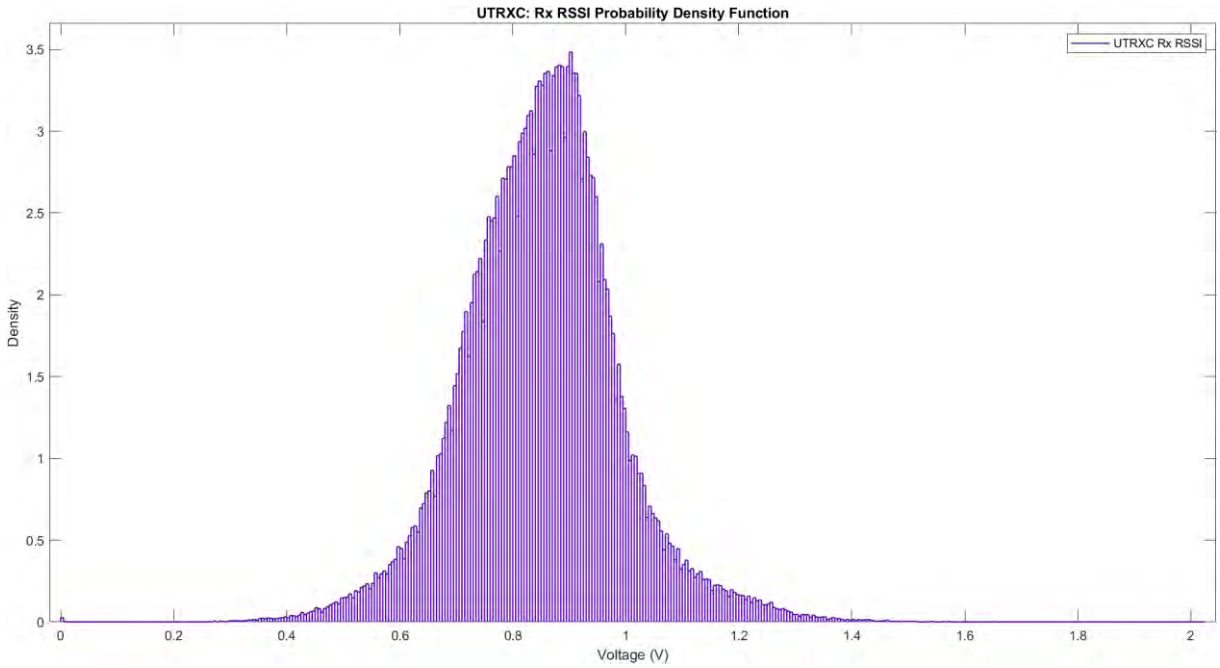

Figure 4.99: UTRXC Rx RSSI Probability Density Function

4.8.7.2.3 Cumulative Density Function

The CDF for the UTRXC RSSI is shown in Figure 4.100.

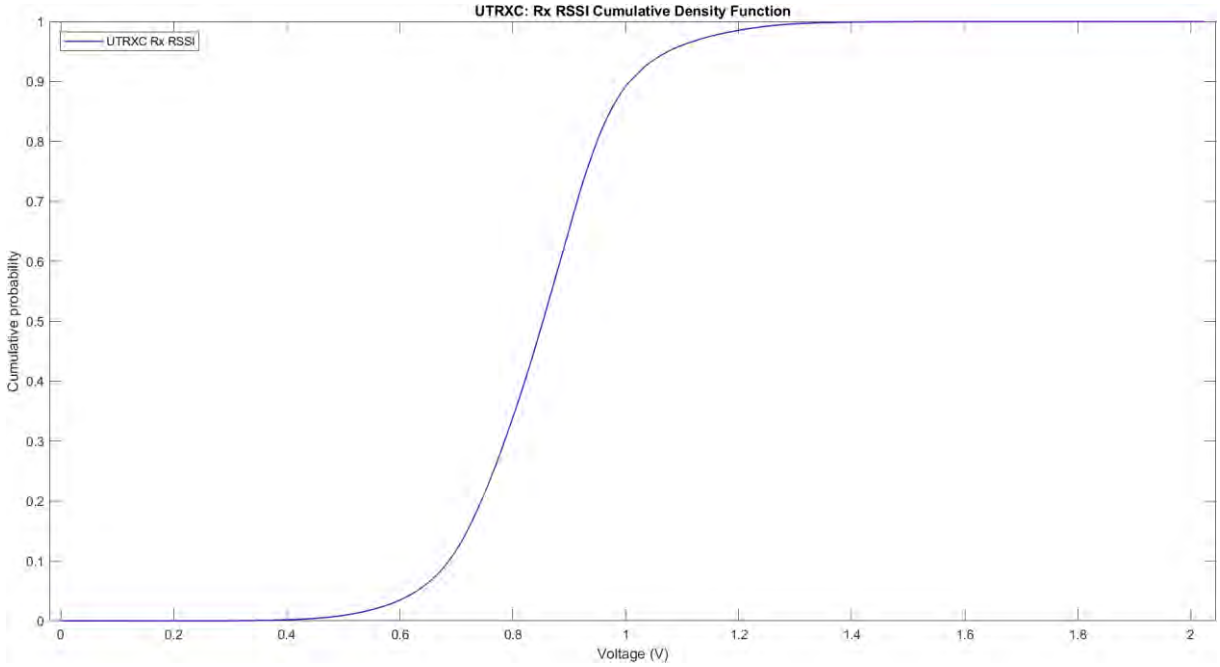

Figure 4.100: UTRXC Rx RSSI Cumulative Density Function

4.8.8 Switched-Mode Power Supply (SMPS) Temperature

There are two types of power supplies than can be used to generate power: a linear power supply and a switched-model power supply. Linear power supplies regulate voltage through the usage of power dissipation and in doing that can disperse heat.

However, with switched mode power supply, it uses transistors to meet the power supply demands, supplying just sufficient power to achieve the desired current and voltage levels. This means that SMPS are more efficient and to make sure that there is nominal operating efficiency, the operating temperatures must be nominal as well.

The following section shows the raw telemetry data as well as the data analysis of this telemetry.

4.8.8.1 Raw Telemetry

Figure 4.101 shows the SMPS operating temperature.

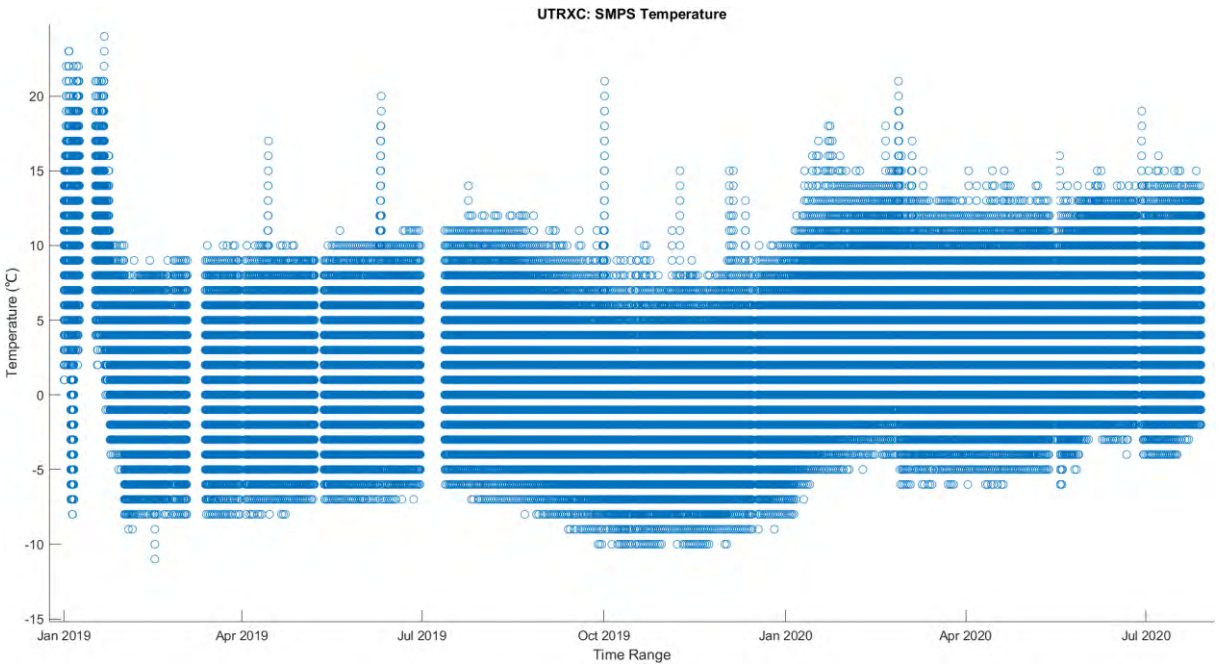

Figure 4.101: UTRXC SMPS Temperature

4.8.8.2 Data Analysis

This section gives details regarding the basic statistic, probability density function and cumulative density function for the UTRXC SMPS temperature.

4.8.8.2.1 Basic Statistics

The basic statistics for the temperature of the UTRXC SMPS are summarised Table 4.49.

Table 4.49: UTRXC SMPS Temperature Basic Statistics

Statistic	Temperature (°C)
Mean	2.281
Median	2
Mode	6
Range	35
Minimum value	-11
Maximum value	24
Variance	30.425
Standard deviation	5.516

4.8.8.2.2 Probability Density Function

The PDF for the temperature of the UTRXC SMPS is shown in Figure 4.102.

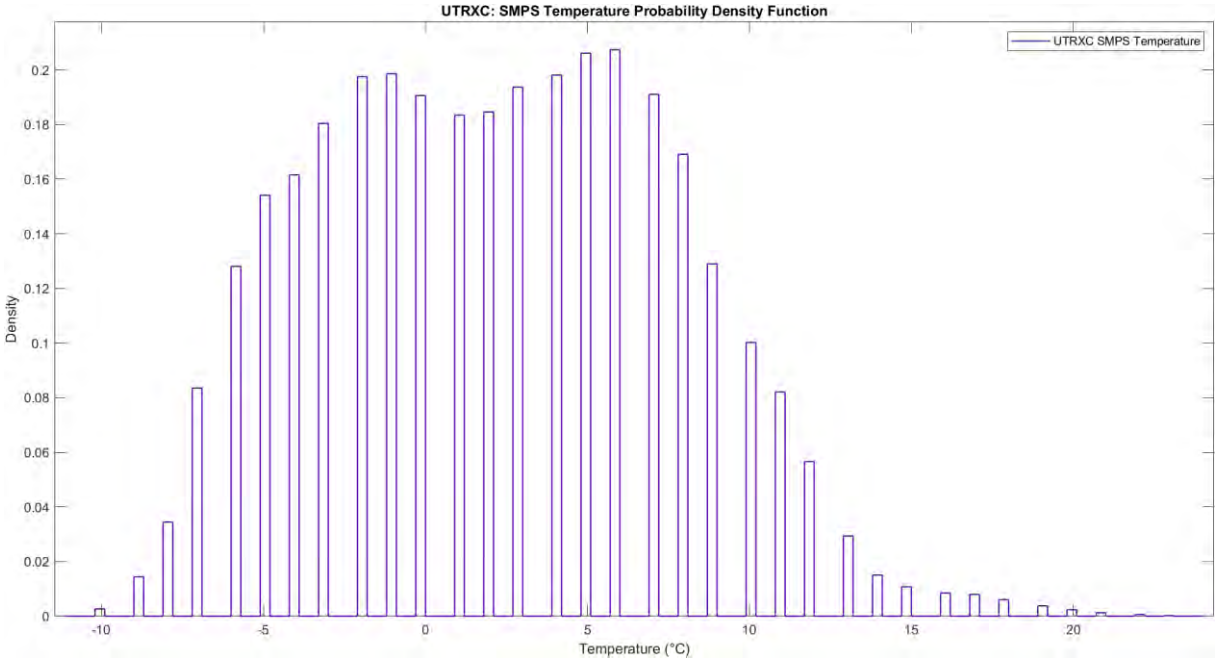

Figure 4.102: UTRXC SMPS Temperature Probability Density Function

4.8.8.2.3 Cumulative Density Function

The CDF for the temperature of the UTRXC SMPS is shown in Figure B.39 in Appendix B.

4.8.9 UHF Transceiver (UTRXC) Telemetry Correlation

The correlation of the six telemetry channels, all the presented telemetry sans the RSSI telemetry, can be found in the table below.

Table 4.50: UTRXC Telemetry Correlation

Telemetry Channel	3.3V Bus Current	5V Bus Current	PA Forward Power	PA Reverse Power	SMPS Temp	PA Temp
3.3V Bus Current	1	0,967	0,894	0,880	0,005	0,006
5V Bus Current	0,967	1	0,902	0,883	-0,002	-0,001
PA Forward Power	0,8934	0,902	1	0,983	-0,002	-0,003
PA Reverse Power	0,880	0,883	0,983	1	-0,002	-0,003
SMPS Temperature	0,005	-0,002	-0,002	-0,002	1	0,974
PA Temperature	0,006	-0,001	-0,003	-0,003	0,974	1

4.9 Orbital Decay

Orbital decay is the phenomenon through which, after the satellite has reached the design orbit altitude, there is a gradual decrease in the orbiting altitude. What this means, is that given a large enough time frame, the satellite will re-enter the Earth's atmosphere.

The Inter-Agency Space Debris Coordination Committee (IADC), which is an international organization made up of multiple national space agencies such as NASA and ESA, aims to monitor and the exchanging of information regarding space debris; both artificial and natural. Space debris is a constant problem as debris can damage satellites to the point where the satellite becomes inoperable. This problem is ever-growing as there is an increasing number of satellites being launched, especially in low Earth orbit (LEO)

To combat this problem, the IADC has guidelines that dictate that satellites that terminate or interfere within the LEO region must have a maximum orbital lifetime of 25 years with a 90% success rate of disposal (IADC Space Debris Mitigation Guidelines, 2020). In addition to ensuring that the satellite complies with this regulation, orbital decay gives an overview as to whether the satellite is operating as expected, e.g., a malfunction in the ADCS causes the satellite's orbit to decay faster than projected or space weather impacting the satellite's path.

To this end, orbital elements were needed. Instead of using TLEs, a JSON (JavaScript object notation) based format was used as the format lends itself to easy information extraction regarding ZACube-2's respective apoapsis (apogee), periapsis (perigee) and the average of the respective apsis in relation to the Earth being the central body.

The following section presents the raw telemetry data as well as the data analysis process.

4.9.1 Orbital Decay Raw Telemetry

The aforementioned orbital telemetry that was used to generate Figure 4.103, spans from 01 January 2019 UTC to 28 November 2021 UTC. It can be seen from the apoapsis, periapsis and the average of the apsis that there is a constant trend of orbital decay as the respective apsis values decrease.

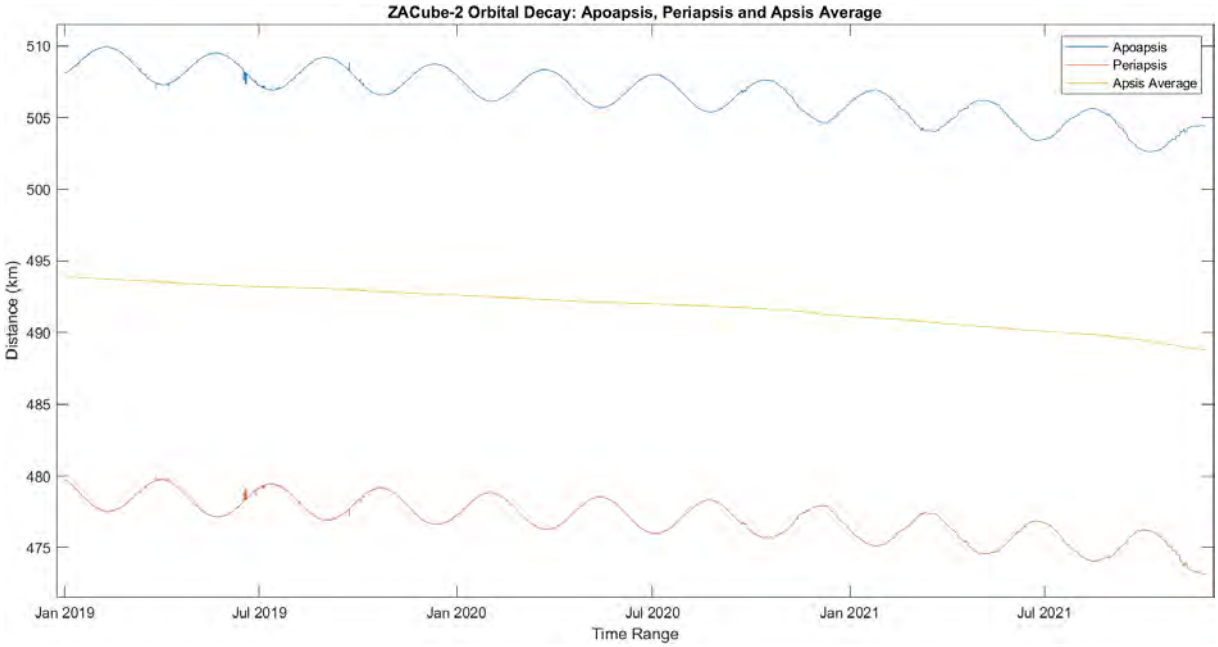

Figure 4.103: ZACube-2 Orbital Decay Apoapsis, Periapsis and Apsis Average

(Space-Track, 2019-2020)

An additional way to view the overall orbital decay is to plot and view the orbital period, which can be seen in the figure below.

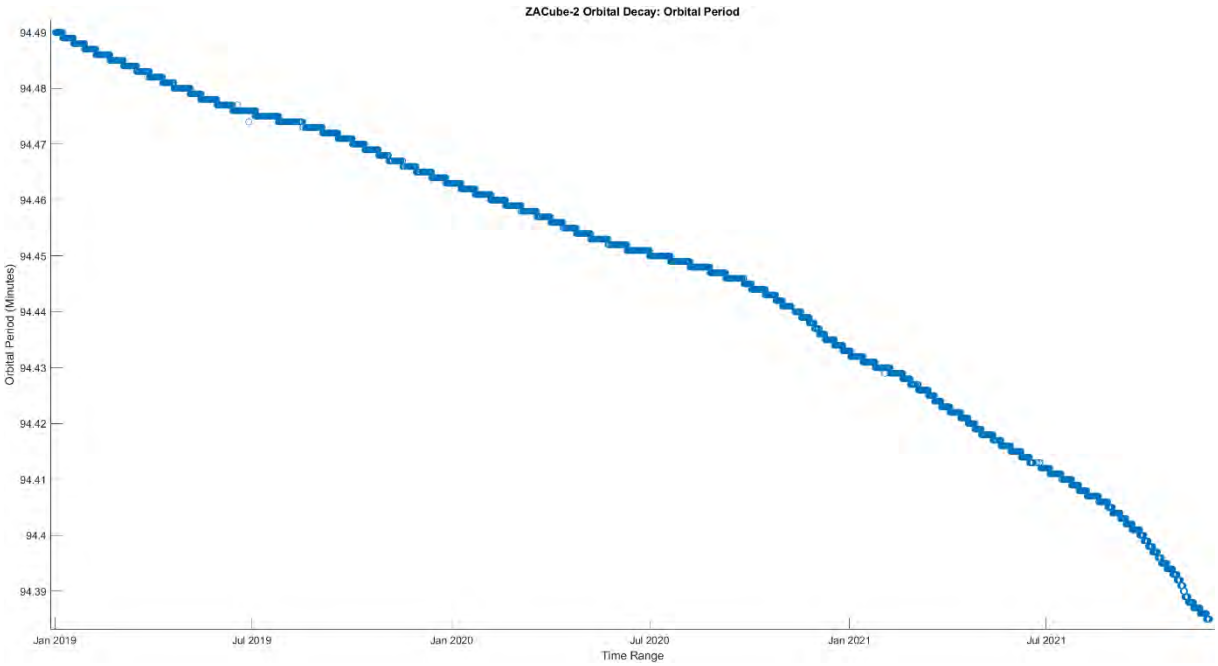

Figure 4.104: ZACube-2 Orbital Decay Orbital Period

(Space-Track, 2019-2020)

As demonstrated in the aforementioned figures, a steady decline can be observed. In this instance from the orbital period, the maximum and minimum value observed was 94.490 and 94.385 minutes, respectively, giving a difference of 6 minutes and 18 seconds over an approximate two-year span.

CHAPTER FIVE
DISCUSSION OF RESULTS

This section details the findings gleamed from *CHAPTER FOUR: RAW RESULTS AND DATA ANALYSIS* and how the telemetry performance compared to the expected performance of ZACube-2. Furthermore, results will be detailed when looking at how the individual performance of the telemetry channels affects the various resources budget however that will be elaborated in *CHAPTER SIX: RESOURCE BUDGET PROFILE COMPARISON*.

5.1 Telemetry

The following sections delve into the findings that were gained only from the raw telemetry as well as the data analysis.

5.1.1 Attitude Determination Control System (ADCS)

When the satellite is first launched, it is launched into a random tumbling state after being ejected from the P-POD, for ZACube-2 this tumbling period was from 01 January 2019 UTC to 18 January 2019 UTC, after which the ADCS controller will put the satellite in a Y-Thomson spin stabilising the satellite in two of the three axes with a controller putting the Y-axis in a constant spin with a full Y-Thomson spin enabled on the 23 January 2019 UTC.

Once this has been achieved, the controller fully stabilises the satellite as directed by the ADCS. The above sequence is a simplification of the process whilst the list below is the ADCS commissioning milestones as specified by the manufacturer (CubeSpace CubeADCS 3-Axis Commissioning Manual v7.1, 2020).

1. Determining the initial angular rates.
2. Initial detumbling.
3. The continued detumbling to a Y-Thomson.
4. Magnetometer deployment.
5. Magnetometer calibration.
6. Angular rate and pitch angle estimation.
7. Y-Wheel ramp-up test.
8. Initial Y-momentum activation.
9. Continued Y-momentum activation and magnetometer EKF.
10. CubeSense Sun/nadir commissioning.
11. EKF activation with Sun and nadir measurements included.

12. Star tracker commissioning.
13. EKF activation with star vector measurements.
14. Zero-bias 3-axis reaction wheel control.
15. EKF with rate gyro measurements, the inclusion of star tracker measurements.
16. Sun tracking 3-axis control.
17. Ground target tracking controller.
18. GPS receiver commissioning.

From the figures generated from the ADCS telemetry, namely the attitude angle for both the Y-axis and Z-axis but most prominent in the attitude angle for the Y-axis, after May 2019 UTC the attitude angle increases significantly in relation to the previously data logged. The figure below, which is the attitude angle for the Y-axis, visually demonstrates this.

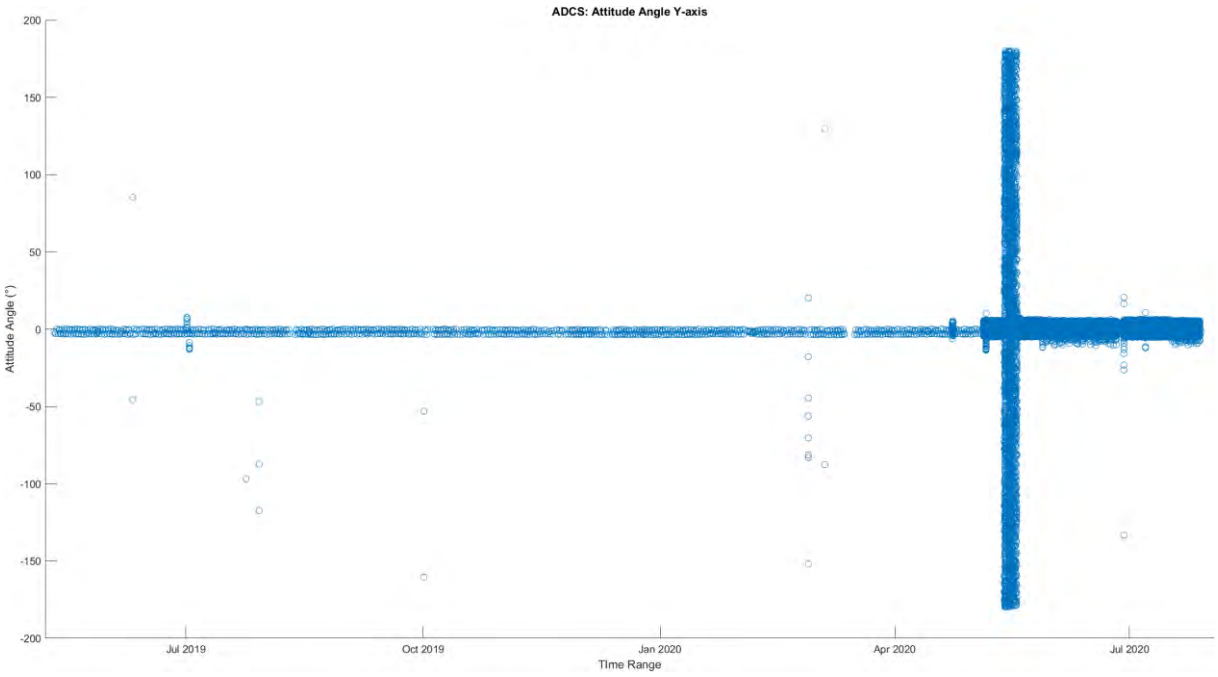

Figure 5.1: ADCS Attitude Angle Y-axis

This increase was due to the recalibration of the magnetometer, where a Y-Thomson spin was induced, that took place from 13 May 2019 UTC to 19 May 2019 UTC as prior to May 2019 UTC only the magnetometer readings were the main input for the ADCS as the sun sensors still needed to be calibrated. The sun sensors in question are the coarse and fine sun sensors.

Once the magnetometer has been successfully calibrated, the satellite was commanded back into nadir pointing mode. Calibrated suns sensors measurements are needed as it, in turn, give accurate estimates when subjected to an EKF (extended Kalman filter).

Liaising with Professor WH Steyn from the University of Stellenbosch who is an ADCS specialist, it was found that when calibrating the sun sensors, there were two instances when the readings for the Y-centroid were particularly high; the calibration graph can be seen in the figure below.

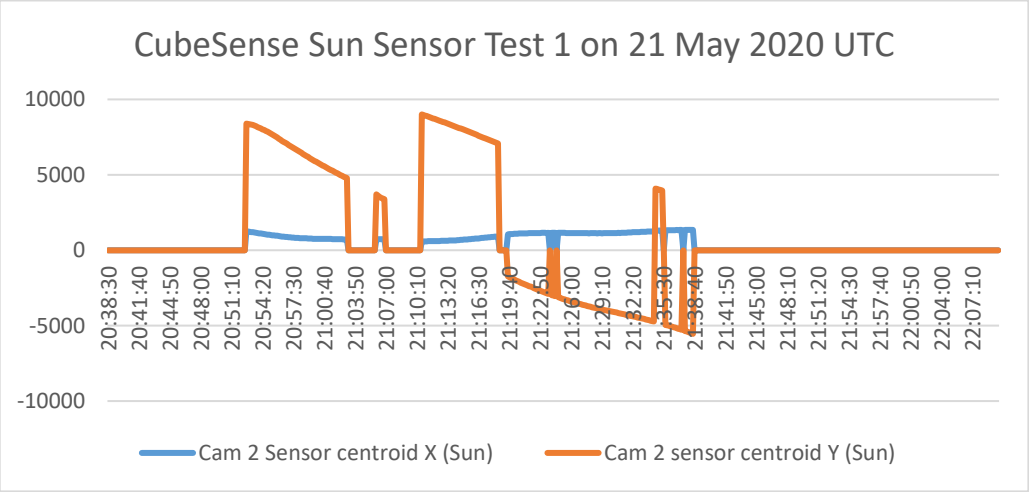

Figure 5.2: Sun Sensor Calibration Test 1 Readings on 21 May 2020 UTC

It was found that the ZACube-2 antenna was in the field of view of the solar sensor because the base of the antenna was close to the lens of the solar sensor. *This caused the solar sensor to view reflections made by the antenna as a false sun, causing the jumps that can be seen in the figure above*.

While the idea of a mask was supposed to be used to remove the antenna from the solar sensor field of vision, it was not available on the sun sensors and therefore it was decided to increase the fine sun sensors exposure, resulting in the graph below.

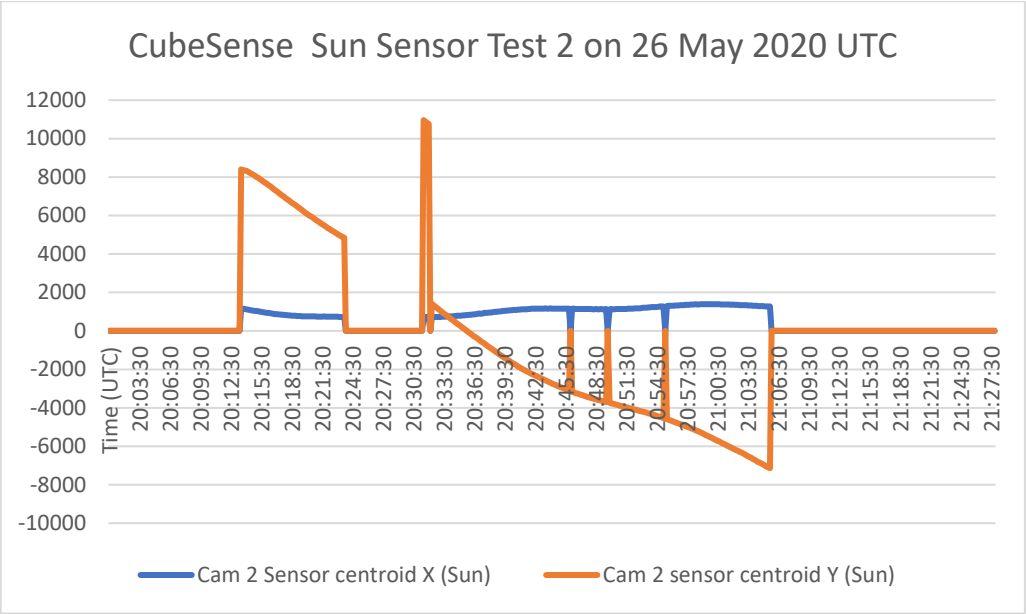

Figure 5.3: Sun Sensor Calibration Test 2 Readings on 26 May 2020 UTC

From the figure above, the second spike that was seen before has now disappeared. To confirm that the problem had been resolved, a comparison of the calibrated elements of the coarse sun sensor vectors and the fine sun sensor vectors was needed, which can be seen in the respective figures below.

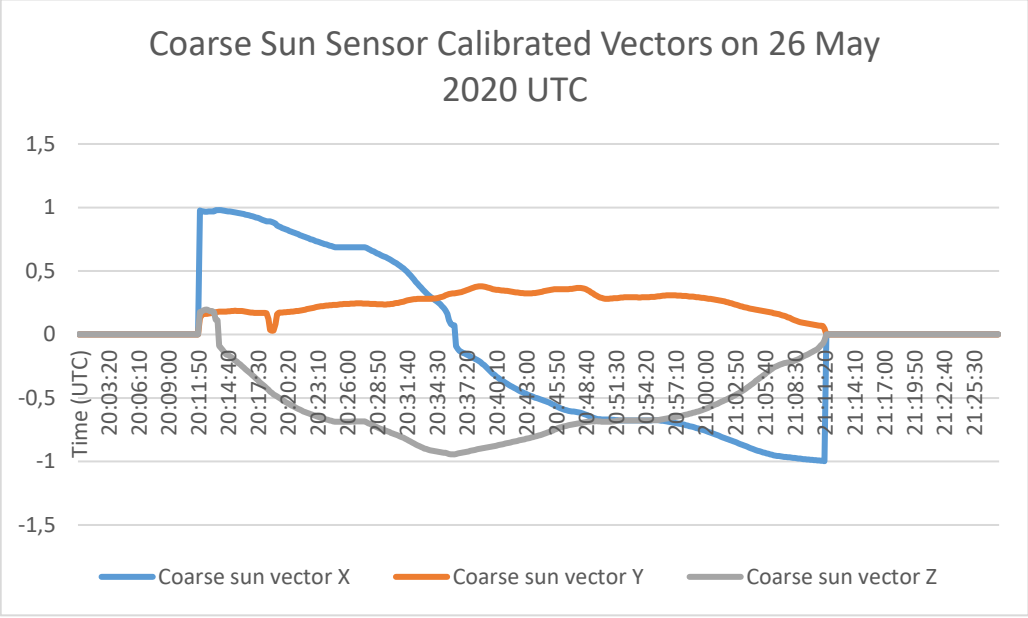

Figure 5.4: Coarse Sun Sensor Calibrated Vectors on 26 May 2020 UTC

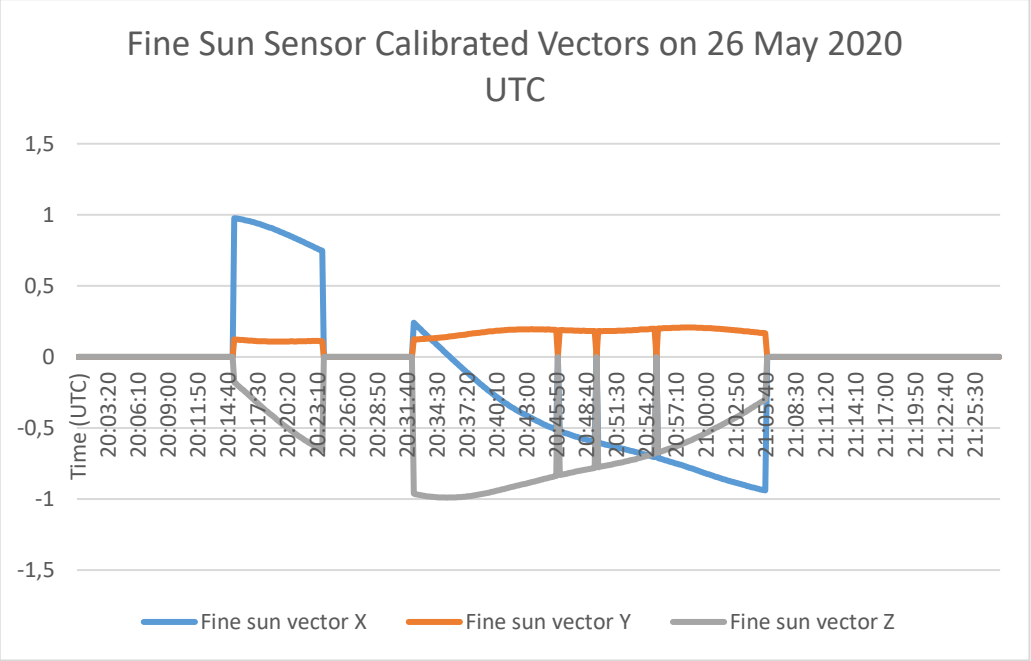

Figure 5.5: Fine Sun Sensor Calibrated Vectors on 26 May 2020 UTC

From these graphs, which show the coarse sun sensor calibrated vectors, a dip in the reading is present. This is from the shadow that was cast by the deployed antenna. In addition, from the figures the vector components are much smoother, indicating more accurate sun direction measurements.

After the calibration and subsequently the addition of the various sun sensor data to the EKF estimator, which as explained previously gives a more accurate indication of the spacecraft's attitude angles and angular rate, it can be seen that there is an increase in the angular rate and attitude angle for the Y-axis and attitude angle for the Z-axis. This translates into an increase pointing accuracy.

When the sun sensors were activated, there was a deviation of 5° where the fine sun sensor would activate at 3.5°. These large deviations caused problems, especially in relation to when the secondary payload would be used, i.e., the K-line imager. Having minor deviations at such a long distance means that the target area is not accurately captured.

5.1.2 Battery

As described in the power budget of ZACube-2, it was stated that the maximum DoD or depth of discharge for the battery was to be 20%. The battery used for ZACube-2 has a charge limit of 8.4V, therefore this equates to a minimum battery charge of 6.72V.

However, the maximum and minimum output voltage were found to be 8.4V and 7.7V, respectively, indicating that the maximum discharge voltage experienced is 0.7V, 8.42%, which is less than that of the maximum designed depth of discharge.

Having a low depth of discharge percentage implies that certain subsystems that utilize more power than others can be utilised more often without fear of overexerting the battery to a certain extent, as overexerting the battery can lead to a decrease in operating quality. Additionally, the inclusion of new subsystems or advanced versions of already used subsystems can be included, whilst still conforming to the CubeSat platform, in the next iteration of CubeSats launched as there is a large voltage/charge overhead.

The maximum battery current to the telemetry was 1.7A. According to the user manual, the maximum charge current, which is the same maximum rating as the discharge current, is 1.95A, therefore, the maximum current was only 87.5% of the maximum current rating.

5.1.3 Electrical Power System (EPS)

The EPS has four bus lines, which are the 3.3V, 5V, 12V and an unregulated battery bus that is directly connected to the battery, as listed in Table 5.1.

Table 5.1: EPS Powered Subsystem

EPS Power Bus	Subsystem Powered
3.3V regulated	Attitude determination control system (ADCS)
	UTRXC (UHF)
	Deployable antenna
5V regulated	K-line imager
	HSTXC (S-band)
	XTX (X-band)
	Onboard computer (OBC)
	UTRXC (UHF)
	Attitude determination control system (ADCS)
12V regulated	EPS motherboard
Unregulated	Software defined radio (SDR)

The SDR and HSTXC are two subsystems on ZACube-2 that utilise high amounts of currents, therefore, it is possible that these two subsystems, instead of operating asynchronously, could be operating concurrently. The calculations below show the steps that were taken to calculate how long the two subsystems could be operating concurrently:

$$Available\ Power = \ Capacity\ of\ Battery\ x\ Depth\ of\ Discharge$$

$$Available\ Power = \ 30Wh\ x\ 20\%$$
$$Available\ Power = \ 6Wh$$

The maximum current for the HSTXC and SDR were found to be 0.35A and 1.7A, respectively, and therefore, employing those values the operating time can be found. However, first the maximum power of the subsystems must be calculated as shown below.

$$HSTXC\ Maximum\ Power = Maximum\ Current\ x\ Voltage\ Input$$
$$HSTXC\ Maximum\ Power = 0.35\ x\ 5$$
$$HSTXC\ Maximum\ Power = 1.75W$$

This process was repeated for the SDR as well:

$$SDR\ Maximum\ Power = Maximum\ Current\ x\ Voltage\ Input$$
$$SDR\ Maximum\ Power = 1.7\ x\ 8$$
$$SDR\ Maximum\ Power = 13.6W$$

Therefore, the combined instant power usage would equate to 15.35W. With the available power and the combined power, the operating time can be calculated:

$$Operating\ Time = \frac{Power\ Available}{Combined\ Power\ Usage}$$
$$Operating\ Time = \frac{6}{15.35}$$
$$Operating\ Time = \ 0.391\ hours$$
$$Operating\ Time = 23.454\ minutes$$

From these results it can be seen that if both the HSTXC and the SDR were to operate concurrently, there would be enough power to run for approximately 23.454 minutes, which would prove useful as the SDR is integral to the purpose of the mission, i.e. AIS messaging, and with the HSTXC providing a high speed downlink to the ground station, both operations can take place.

However, the above calculation does not factor into account the power required from the other subsystems, which is vital to the functionality of the satellite, such as the ADCS and OBC subsystems; the operating duration calculated above would therefore be optimistic.

5.1.4 Orbital Decay

The orbital decay of ZACube-2 was plotted using telemetry attained from NORAD with the telemetry in question being the periapsis, apoapsis and apsis average, which is shown in Figure 5.6.

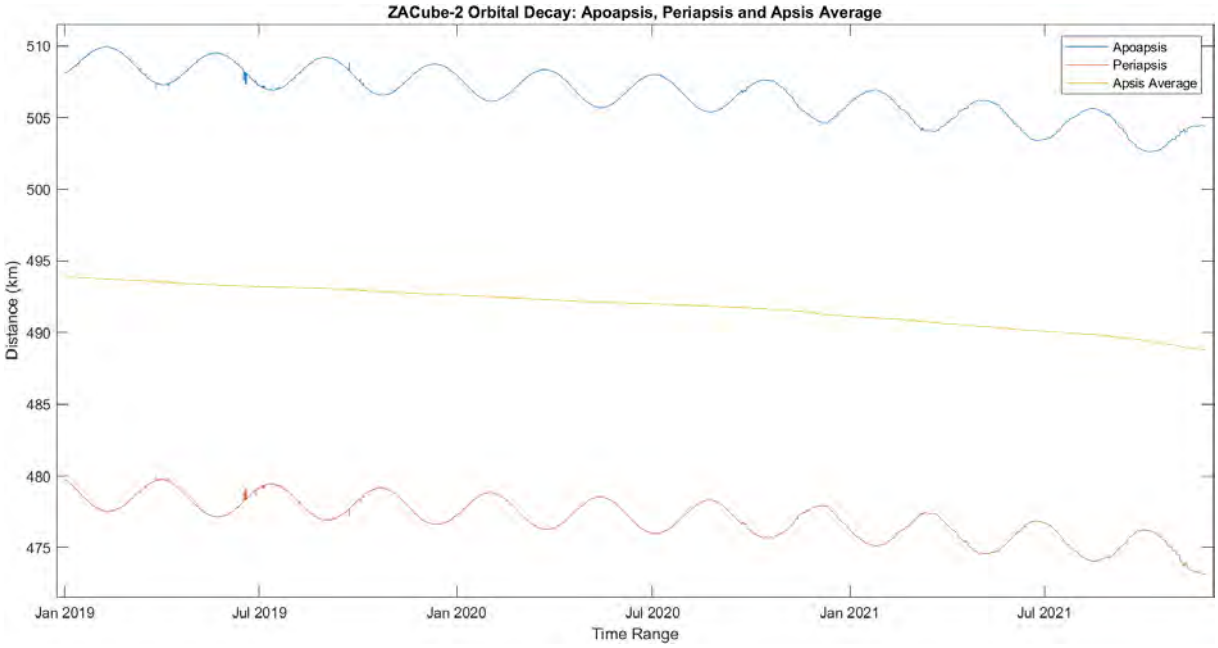

Figure 5.6: ZACube-2 Telemetry Orbital Decay Apoapsis, Periapsis and Apsis Average

(Historical Elset Search, 2021)

From the figure above it can be seen that there is a linear decline in the orbital decay as the respective apsis values decrease. Over the period from 01 January 2019 UTC to the 28 November 2021 UTC, the average apsis declined from 493.920km to 488.785km over a period of 1063 days, translating to 4.8m per day.

For spacecraft, in order to reduce the amount of space debris, the maximum orbital lifetime is defined as 25 years (Nagavarapu et al., 2021). Satellite altitude will not decrease linearly over time, and linear extrapolation of the results shown in Figure 5.6 cannot be applied to determine the orbital lifetime.

To confirm whether the rate of orbital decay is satisfactory, a simulation of the overall de-orbiting of the satellite is done. This assesses if the calculated decay to date is in line with the expected. To do this, the Semi-Analytic Tool for End-of-Life Analysis software (STELA) designed by the French Space Agency (CNES) is employed. Two variations of the simulation are done with the only changing factor being the type of solar activity. For the simulations the following parameters were used (it should be noted that for the orbital parameters were taken from TLE's):

Table 5.2: STELA Simulations Parameters

Parameter	**Simulation One**	**Simulation Two**
Mass (kg)	4	
Reflecting area (m^2)	0.03	
Reflectivity Co-efficient	1.5	
Drag area (m^2)	0.03	
Drag Co-efficient	Variable	
Atmospheric model	NRLMSISE-00	
Solar activity	Mean constant	Variable
Nature of initial state	Mean parameters	
Type of initial state	Perigee/Apogee	
Frame of initial state	CIRF	
Start data (UTC)	01 January 2019 06:52:17	
Perigee(km)	479.755	
Apogee (km)	507.085	
Inclination (°)	97.3	
Right ascension of ascending node (RAAN) (°)	270.902	
Argument of perigee (°)	222.943	
Mean anomaly (°)	137.02	
Re-entry altitude (km)	120	

The simulation outputs consist of a summary and subsequent perigee and apogee plot from simulation 1 (mean constant solar activity) and simulation 2 (variable solar activity):

Figure 5.7: Simulation One Orbital Parameters and Orbital Lifetime Results

Figure 5.8: Simulation One Perigee and Apogee Plot

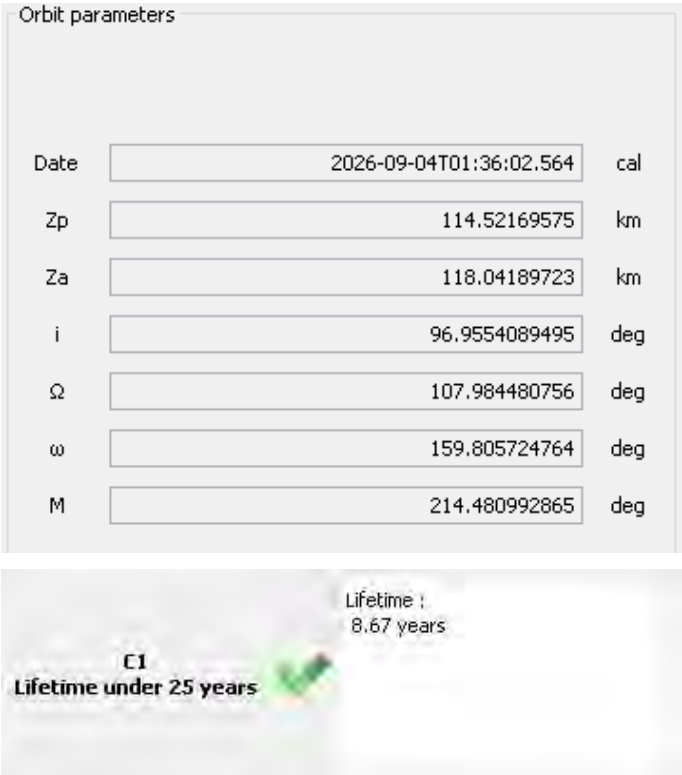

Figure 5.9: Simulation Two Orbital Parameters and Orbital Lifetime Results

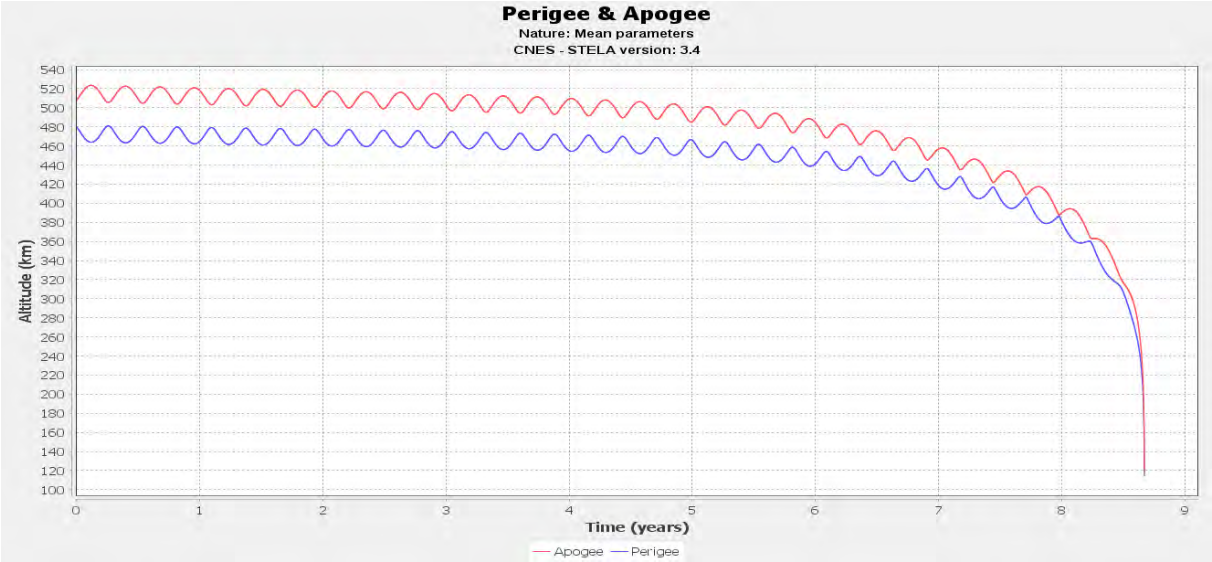

Figure 5.10: Simulation Two Perigee and Apogee Plot

From the figures above, a clear distinction can be seen in terms of how solar activity and the start date of the initial orbital parameters affect the drag experienced by the satellite and subsequently the lifetime, with both results complying with the maximum lifetime of a satellite in LEO. Comparing Figure 5.10 and Figure 5.6 shows that orbital decay of both the simulation completed in STELA and the TLE's are alike when compared side by side, as seen in Figure 5.11.

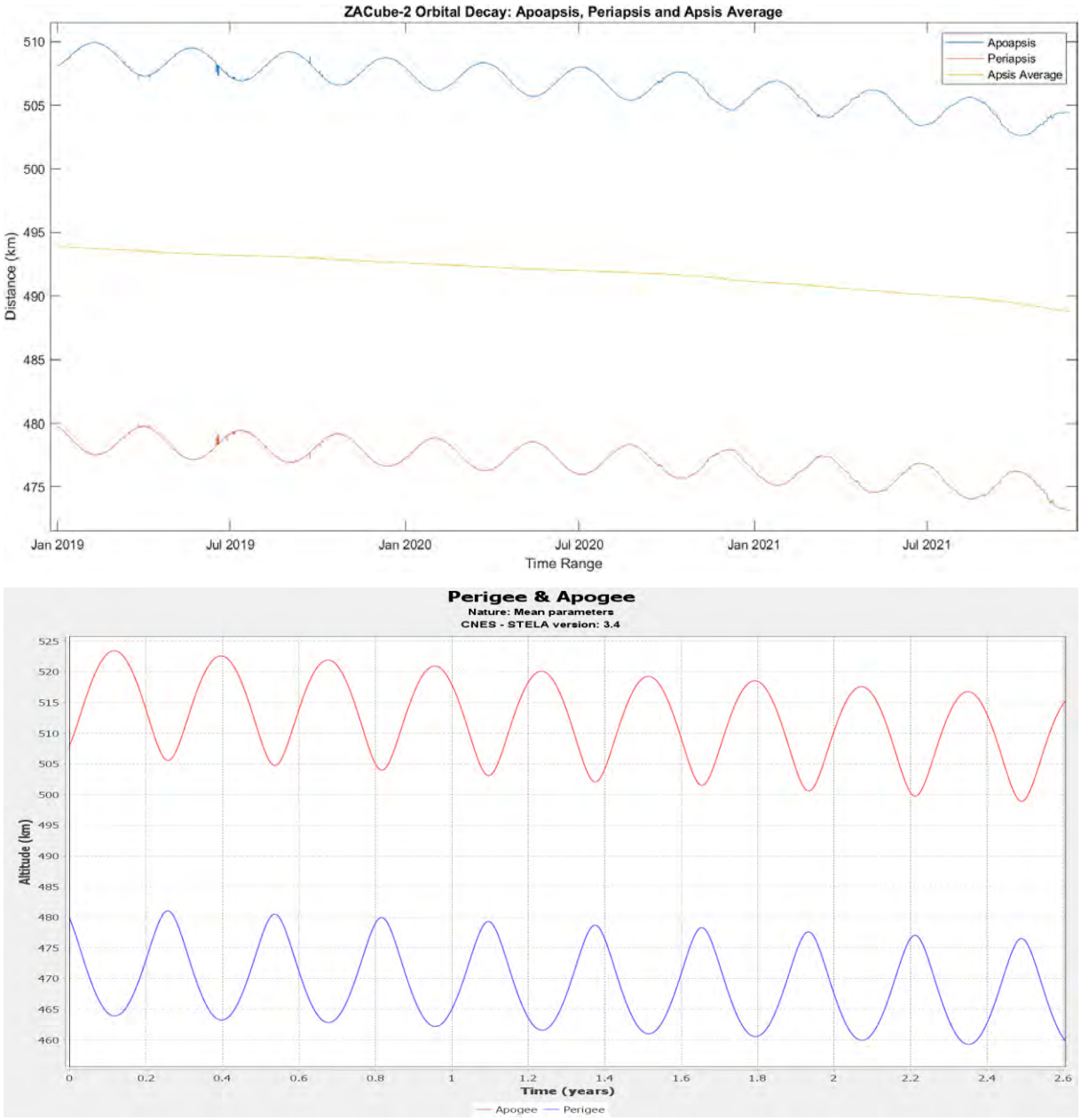

Figure 5.11: Comparison of Telemetry and Simulation Orbital Decay

An additional way to view the orbital decay is to plot and view the orbital period, which can be seen in the figure below.

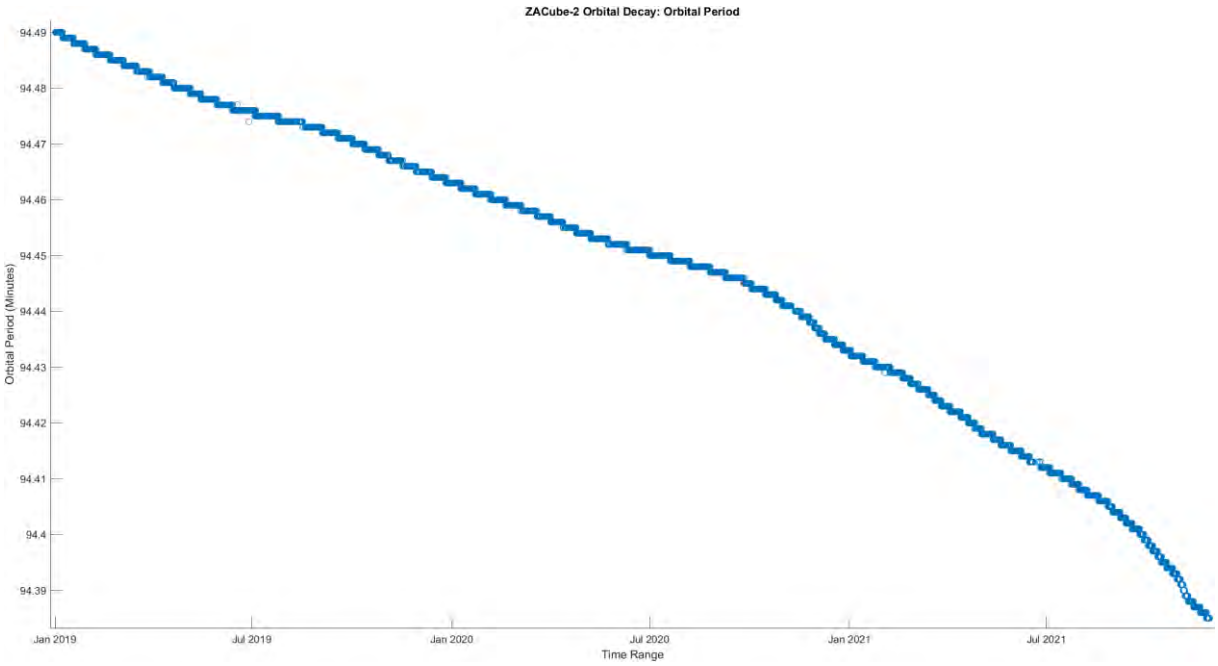

Figure 5.12: ZACube-2 Orbital Decay Orbital Period

Once again, a steady (non-linear) decline can be seen. With the period data known, a goodness-of-fit was done to see the relationship between the data and the model using a linear fit in MATLAB's Curve Fitting Tool. This process yielded a root mean square error (RMSE) of 0.004 and a R-square (R^2) value of 0.976 describing that the average deviation between the model and actual telemetry is 0.043 minutes with the model being able to explain 97.62% of the variation in the orbital period telemetry.

Consideration of how closely the actual orbit decay relates to the simulated orbit decay needs to be accounted for using the same period. A simulation was completed using AGI's STK (Systems Tool Kit). The figure shows results attained from the simulation with a telemetry based orbital period superimposed to show how the two data sets differ.

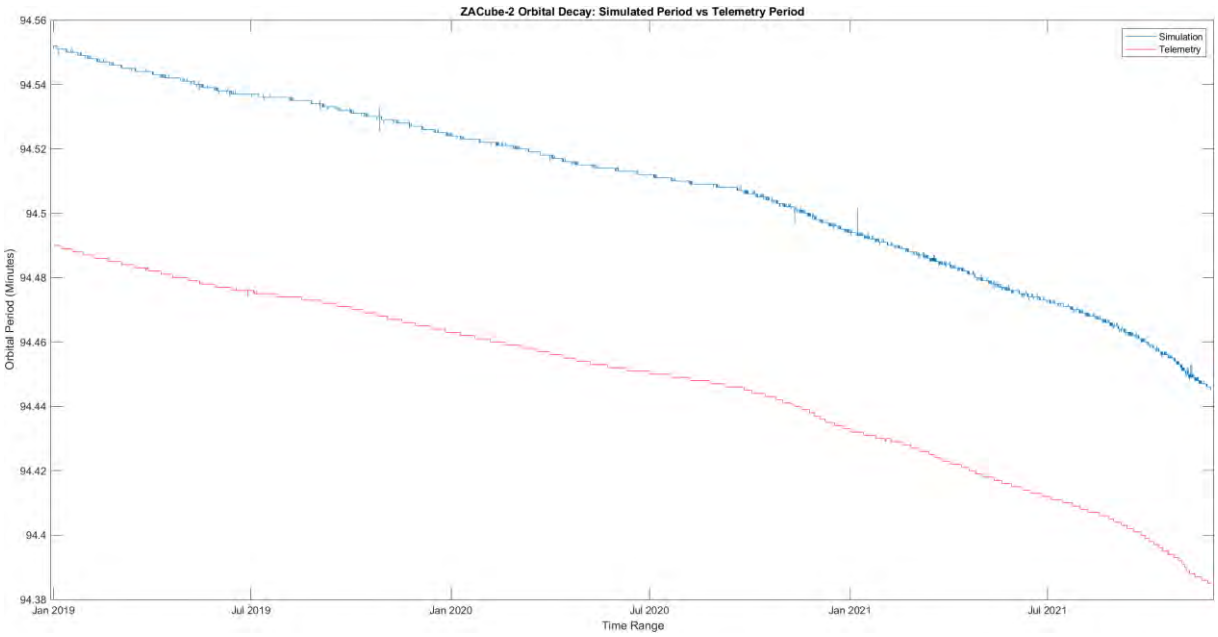

Figure 5.13: ZACube-2 Orbital Decay: Simulated Period vs Telemetry Period

From the figure above, there is a constant difference between the simulation results and the telemetry results of approximately 3.6 seconds, which is negligible.

5.1.5 Solar Array

The solar array consisted of six solar panels, but only five had a current output as one of the panels is nadir facing. The average power generated across the five solar panels varied due to not only the angle at which the solar panel faced the sun, but also the effective area that was illuminated, as a larger exposed area would yield more power generated.

Table 5.3 shows the average power generated by each respective pair of solar panels and the combined effective area of said solar panel. It should be noted that the average power values calculated were done in both instances of when ZACube-2 was in sunlit and eclipse conditions, i.e., the entire telemetry range.

Table 5.3: Solar Array Panels Average Power Generated

Solar Panel Pair	**Average Power Generated (W)**	**Combined Area(m^2)**
SA1A and SA1B	0.965	0.03
SA2A and SA2B	1.067	0.06
SA3A and SA3B	0.048	0.02
Total	2.080	0.11

It can be seen that the panels SA2A and SA2B having the largest area also have the highest average power generated; however, another interesting observation is that while the panel pair SA1 has half of the combined area of panel pair SA2, it produced 90.5% of the power generated by both SA2A and SA2B. This is in addition to SA1B producing no current as it was nadir pointing.

What can be gleaned from this is that solar panel SA1A produces the most power per panel, indicating that either the panel spends the least amount of time in eclipse or the angle at which the sun hits the solar panel is different than the angle for the solar panel pair SA2.

5.1.6 System Performance

Most of the telemetry channels had data logged at an interval of 2 or 3 minutes, dependent on the respective subsystem, with only the ADCS subsystem having a shorter data logging interval due to the frequently changing parameters. Other less vital subsystems logged telemetry data only when the respective subsystem was active, or if there was a change in value.

When going through the telemetry data, there were many instances where there was either no data logged, or data was logged with outliers. This phenomenon was not isolated to a single subsystem level, but across multiple subsystems, suggesting that it was on a system level.

The table below shows in chronological order lapses in data logged from 01 January 2019 00:02:39 UTC to 28 July 2020 09:30:15 UTC. It should be noted that in some telemetry channels the intervals described below can be a singular outlier, rather than a period.

Table 5.4: Temporal Lapses in Telemetry Channel Data Logging

	Datetime (UTC)	
Instances	**Start**	**End**
1	08 January 2019 21:20:29	16 January 2019 21:20:29
2	23 February 2019 03:42:35	24 February 2019 21:00:14
3	04 March 2019 08:27:14	13 March 2019 08:57:18
4	31 March 2019 01:24:18	02 April 2019 09:33:18
5	07 May 2019 19:20:58	12 May 2019 09:06:05
6	02 June 2019 13:48:10	03 June 2019 09:00:10
7	11 June 2019 22:12:18	
8	30 June 2019 10:00:15	12 July 2019 10:29:28
9	07 August 2019 10:26:49	
10	16 August 2019 08:05:51	16 August 2019 10:11:51
11	17 September 2019 03:29:59	17 September 2019 09:33:00
12	18 September 2019 00:42:00	18 September 2019 07:27:00
13	23 September 2019 01:18:00	23 September 2019 08:03:00
14	06 October 2019 10:51:03	06 October 2019 17:36:03
15	15 October 2019 10:27:07	16 October 2019 21:59:08

16	05 December 2019 14:59:18	05 December 2019 20:56:20
17	15 December 2019 08:40:33	17 December 2019 09:08:33
18	23 December 2019 00:34:52	
19	23 December 2019 00:36:03	
	23 December 2019 08:50:36	
	23 December 2019 08:56:36	
20	23 December 2019 15:04:38	
	23 December 2019 23:26:36	
21	30 January 2020 02:44:46	30 January 2020 02:44:46
22	23 February 2020 18:07:47	23 February 2020 21:19:47
23	15 March 2020 16:22:19	16 March 2020 10:34:21
24	11 June 2020 23:34:47	12 June 2020 09:28:48
25	18 June 2020 10:31:49	18 June 2020 16:58:49
26	23 June 2020 06:34:51	23 June 2020 10:04:51
27	26 June 2020 09:01:51	28 June 2020 20:16:56
28	04 July 2020 09:14:56	04 July 2020 15:47:56
29	05 July 2020 00:38:56	

There are several instances where the data present in the telemetry channel was either an extreme outlier or there was no data recorded. These lapses also affect the interval at which the data is logged; specifically, for some telemetry sets the data is logged every 2 minutes.

With no consistent interval at which these lapses occur, an external factor, such as space weather and in particular solar flares, could be the cause for the lapses. Using space weather data from the NOAA space weather prediction centre, solar activity was at a minimum partially due to the sun being in a solar minimum cycle with the zenith of solar maximum projected to be in July 2025.

With the sun being in a solar minimum cycle, other factors such as geomagnetic activity was at a minimum with the highest Kp-index rating of Kp 6 or in the G-scale equivalent of G2 indicating a moderate geomagnetic storm. Geomagnetic storms that have a rating of G2 affect spacecraft by influencing the drag effect in orbit predictions, possibly changing it and restorative actions in relation to the spacecraft's orientation may be required by ground control (NOAA Space Weather Scales, 2011).

5.1.7 UHF Transceiver (UTRXC)

The UTRXC subsystem operated within the design specifications as expected with the temperature range from the telemetry having a maximum of 28°C and a minimum of -11°C, which falls within the temperature range specified by the manufacturer of -25°C to 61°C. This leaves enough thermal headroom to either reorganise the stack position of the UTRXC if an additional subsystem is included in the next iteration of CubeSats.

Using both the 3.3V and 5V regulated bus lines from the EPS, the UTRXC transmits at varying DC power values, which have equivalent decibels per milliwatt ratings that can be seen in the table below.

Table 5.5: UTRXC RF Characteristics

State of Operation	RF Transmit Power	Signal Strength Power (dBm)	DC Power
Receiver ON, transmitter OFF	Idle	Idle	220mW
Receiver ON, transmitter ON	0.5 W	27	2.8
Receiver ON, transmitter ON	1 W	30	3.8
Receiver ON, transmitter ON	2 W	33	5.1

Comparing these values to the figure below, which is the combined regulated bus power of the 3.3V and 5V bus lines, the most consistent high-power rating is approximately 3.2W. This translates to over 27 dBm, or roughly 28.6 dBm if linear interpolation is used. Once again, using linear interpolation, it is found that the RF transmit power is 0.7W.

Figure 5.14: UTRXC Combined Regulated Bus Power

Another important facet of the UTRXC telemetry was the RSSI values, which described the strength of the received signal. Using the table below, which provides the RF level given a certain voltage output, in conjunction with a figure showing the cumulative density function of the RSSI values, an indication of the performance can be deduced.

Table 5.6: RSS Received Power

	Voltage (V)		
RF Level (dBm)	**Minimum**	**Typical**	**Maximum**
-118	N/A	0.3	0.8
-68	0.7	1.1	1.8
-23	1.2	1.8	2.5

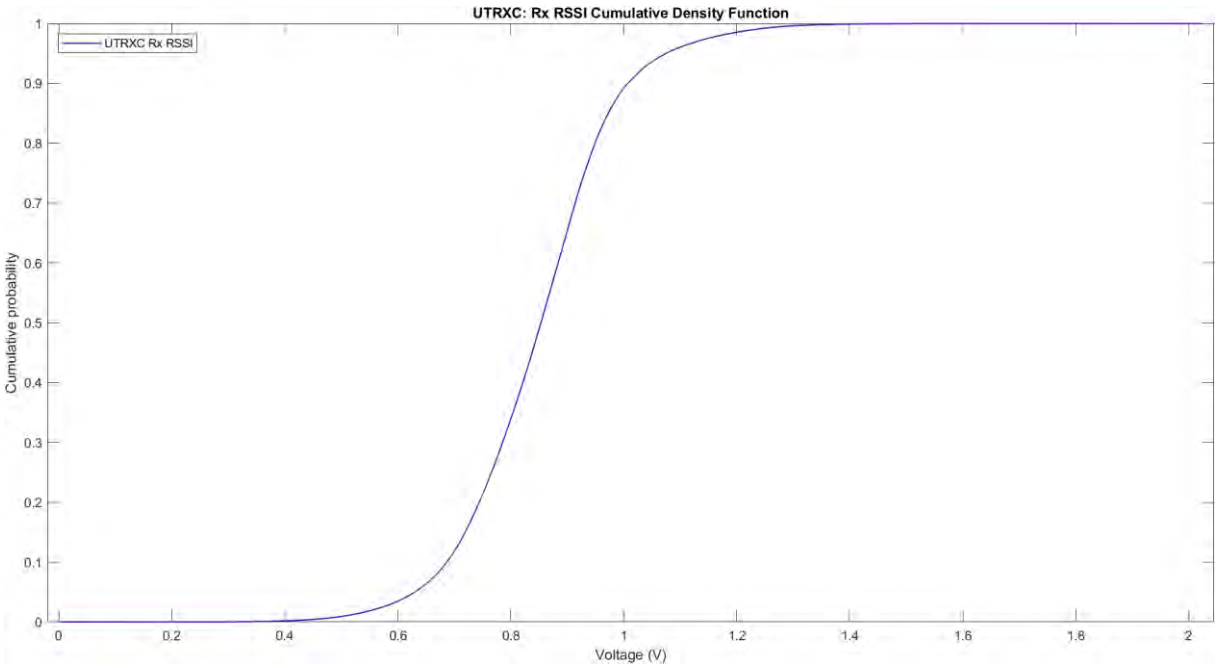

Figure 5.15: UTRXC Rx RSSI Cumulative Density Function

Using the table and the figure above, the signal range that the subsystem can detect, encompasses the entire range of values that are within the CDF plot, indicating that during an overpass it is expected that the signal being transmitted can be received for the entire overpass. This implies that the link budgets are calculated accurately, if not conservatively.

5.2 Resource Budgets

The following details the findings and compares the telemetry-based calculations in relation to the as-designed resource budgets.

5.2.1 Power Budget

The power budget consists of ten parts, making it the most comprehensive resource budget that had to be verified. Of the ten parameters, the latter eight are power profiles, which had to be calculated and compared:

- Orbital period, sunlit minimum, and eclipse maximum.
- Minimum power generated by the solar array.
- Safe sun
- Safe eclipse
- Safe TT&C sun
- Safe TT&C eclipse
- Downlink sun
- Downlink eclipse
- Payload sun
- Payload eclipse

The tables below define and compares the telemetry-based values that were calculated to the values presented in the power budget, which were produced by the in-house engineering team based on a predetermined set of mission orientated specifications.

Table 5.7 shows the comparison of the orbital period, sunlit minimum, and eclipse maximum.

Table 5.7: Comparison of Orbital Period, Sunlit Minimum and Eclipse Maximum

	Period (Seconds)		
Orbital Parameter	**Telemetry**	**Power Budget**	**Difference**
Sunlit minimum	3375	3531.753	156.753
Eclipse maximum	2205	2145.225	-59.775
Orbital period	5580	5676.978	96.776

The sunlit minimum parameter that was calculated using telemetry was 157 seconds, or 2 minutes and 37 seconds, longer than the value calculated in the power budget. In contrast, the eclipse maximum period stated in the power budget was found to be 59.8 seconds longer. This translates to a longer telemetry calculated orbital period of 97 seconds.

However, the deviations between the telemetry value and the power budget value can be attributed to the interval at which the data is logged. The interval, also referred to as a time step, is 3 minutes and this means that the discrepancies calculated fit within that margin. It is possible that if the telemetry were recorded at a higher resolution, the variance between the two values could be negligible.

Table 5.8 shows the comparison of the calculation for the average power generated by the solar array. Samples 1 and 2 refer to the two telemetry samples that were calculated, which were 15 March 2019 UTC and 17 February 2020 UTC.

Table 5.8: Comparison of Solar Array Power Generation

	Sample One		Sample Two	
	Power (Wh)	**Time (Hour)**	**Power (Wh)**	**Time (Hour)**
Parameter	4.417	0.959	3.387	0.677
Minimum power generated	6.472	0.981	6.472	0.981
Difference	-2.055	-0.022	-3.085	-0.304

It can be seen that the total power generated from sample one is only 68.3% of the minimum power generated, as described in the power budget, while the sample 2 value is only 52.3% of the minimum required power stated in the power budget value. Two pieces of information can be extracted from these sample calculations.

The first piece of information is that from the two sample calculations, the power being generated by the solar array does not meet the minimum required power in the power budget and as such the battery's voltage depth of discharge should be greater than the 20% value specified in the power budget.

However, the calculated depth of discharge was found to be 8.42%, which is well within the 20% margin. The discrepancy may be attributed to either the interval at which the values were recorded, in this case data was logged at an interval of 3 minutes, or an incorrect combination of which current and/or voltage readings belong to a specific pair of solar panels.

The second piece of information is that sample values vary at 1.030Wh. This difference can be accredited to the combination of two factors; the first one is solar declination and/or whether the sun is in solar minimum or maximum. Due to the solar systems barycentre, the common centre of mass being the Sun. As the Earth orbits the Sun, the declination angle changes over the course of the year. This affects the angle at which the solar rays hit the solar panels and subsequently the power produced. The figure below gives a visual representation of this phenomenon.

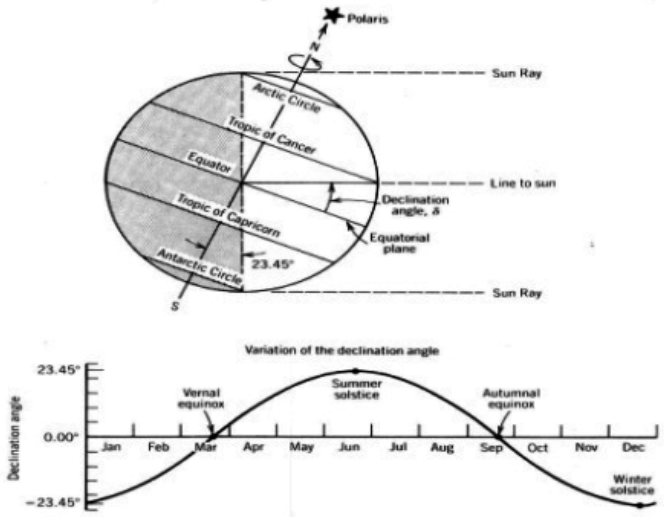

Figure 5.16: Solar Declination

(Ismail, Anis and Fathy, 2016)

The second factor is the solar cycle. A cycle is experienced by the sun, where approximately every 11 years the frequency of sunspots increases or decreases, respectively. This results in periods of more intense and less intense solar activity in the telemetry range that is used to calculate the sample values. The number of sunspots is directly proportional the strength of the UV radiation. The figure below shows the current solar cycle with the trend towards the 25th solar cycle, which is expected to peak in July 2025.

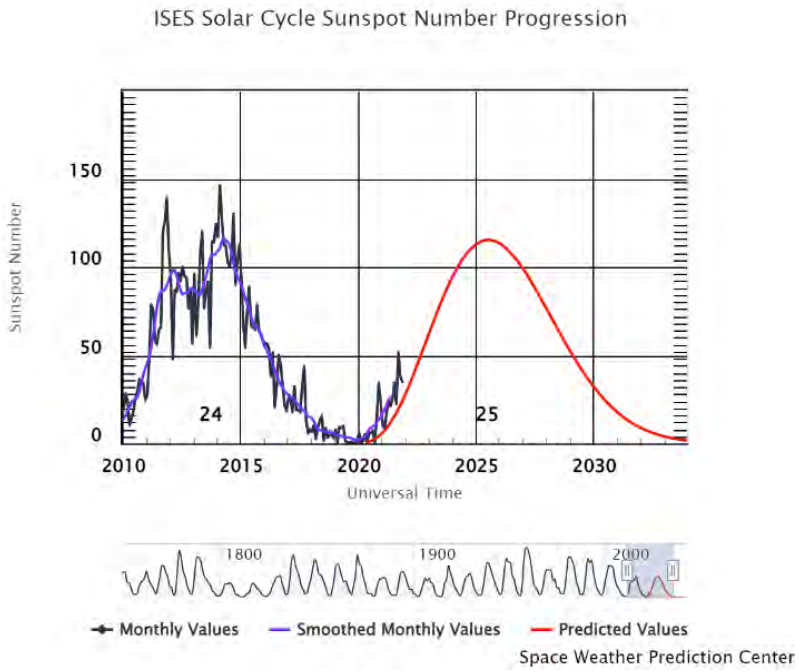

Figure 5.17: Solar Cycle Progression

(Solar Cycle Progression | NOAA / NWS Space Weather Prediction Center, 2021)

The third and final table is the comparison of the telemetry calculated power profile values in relation to the values specified in the power budget. The table below specifies the values from the telemetry (actual), the power budget and the difference between the two.

Table 5.9: Comparison of Power Profiles

	Power Consumed (Wh)		
Profile Name	**Power Budget**	**Telemetry**	**Difference**
Safe sun	1.759	1.705	0.054
Safe eclipse	1.068	1.049	0.019
Safe TT&C sun	2,576	2.101	0,354
Safe TT&C eclipse	1,885	1,583	0,274
Downlink sun	3.576	2.848	0.728
Downlink eclipse	1,432	1,408	0,024
Payload sun	4,976	2,297	2,679
Payload eclipse	4,285	N/A*	N/A

*Payload not operated when ZACube-2 is in eclipse

It can be clearly seen that overall, the power budget values are higher than the ones calculated using the respective telemetry, and within a 1 Wh margin. The largest difference between the telemetry derived values and the power budget is when the payload sun is active where only 46.2% of the power specified in the power budget was used.

The reason behind the significantly lower power value was that during the calculation stage, the telemetry from the different subsystems did not have the same time interval at which data was logged. This caused instances where either no power values were recorded, or one subsystem recorded a power value, but the other subsystem did not. While linear interpolation can be used to replace missing values, it is not an accurate representation of the data recorded.

5.2.2 Link Budget

To verify the integrity of the uplink, the UHF Rx RSSI was used. The RSSI is a tool that provides valuable information as to the performance of communication between the ground station and ZACube-2. The graph below is a cumulative density function (CDF) of the UTRXC RSSI, where the values are in volts, with the table below the graph showing what the signal strength is at a certain voltage.

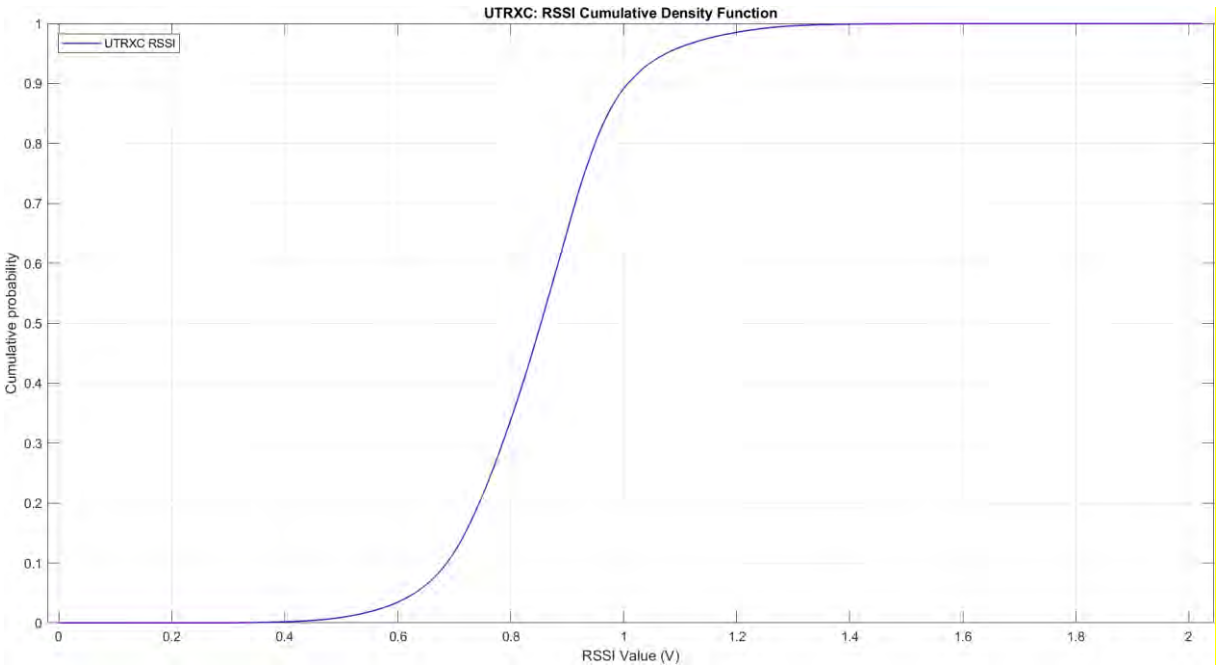

Figure 5.18: UTRXC RSSI Cumulative Density Function

Table 5.10 shows the conversion from the RSSI value (volt) to an equivalent signal strength (dBm).

Table 5.10: UTRXC RSSI Value to Signal Strength Conversion

	Voltage (V)		
RF Level (dBm)	**Minimum**	**Typical**	**Maximum**
-118	N/A	0.3	0.8
-68	0.7	1.1	1.8
-23	1.2	1.8	2.5

Comparing the table above and the X-axis range in Figure 5.13, it can be seen that, when looking at typical voltage values for an RF level of -118 dBm which equates to 0.3V, approximately less than 1% of the UTRXC received signals would be considered noise, or alternatively, the link is not closed for about 1 % of the overpass time.

5.2.3 Thermal Budget

From the thermal related telemetry in relation to both iterations of the hand calculations done and subsequentially the subsystem thermal operating specifications, the thermal performance of ZACube-2 performed well within the margins. The manual calculations were conservative.

Table 5.11 summarises the telemetry and calculations of maximum and minimum temperatures. It should be noted that in the table, Fortescue and Gilmore refer to the two methods that were used for the thermal equilibrium manual calculations.

Table 5.11: Comparison of Telemetry and Calculated Temperature Limits

	Temperature (°C)		
Parameter	**Maximum**	**Minimum**	**Difference**
Battery	31.987	-8.473	40.460
K-line imager	29.150	-15.125	44.275
HSTXC	37.231	13.867	23.364
UTRXC	28	-11	35
Fortescue	49.213	-21.452	80.664
Gilmore	43.329	-21.094	64.423

The method that employs calculation techniques from Fortescue (2011) has a larger thermal range when compared to the method that employs calculation techniques from Gilmore (2002), suggesting that while both are valid approaches, Fortescue (2002) is more conservative in nature than Gilmore (2002).

Telemetry from the battery, UTRXC and HSTXC show that the subsystems thermally performed within the manufacturer's specifications, with additional headroom meaning that the passive thermal control techniques employed on ZACube-2 work as designed. The three tables, one for each of the mentioned subsystems, below show the maximum and minimum temperature for both the telemetry (actual) and the manufacturer's specifications, and with the difference between the two sets.

Table 5.12: Comparison of Battery Thermal Telemetry and Manufacturer Specifications
(AAC_DataSheet_Optimus, n.d.)

	Temperature (°C)		
Parameter	**Telemetry**	**Manufacturer**	**Difference**
Maximum	31.987	50	18.014
Minimum	-8.473	-10	1.527

Table 5.13: Comparison of UTRXC Thermal Telemetry and Manufacturer Specifications
(CubeSat VHF/UHF Transceiver, n.d.)

	Temperature (°C)		
Parameter	**Telemetry**	**Manufacturer**	**Difference**
Maximum	28	61	33
Minimum	-11	-25	14

Table 5.14: Comparison of HSTXC Thermal Telemetry and Manufacturer Specifications

(CubeSat S-Band TX, n.d.)

	Temperature (°C)		
Parameter	**Telemetry**	**Manufacturer**	**Difference**
Maximum	37.231	61	23.769
Minimum	13.867	-25	11.133

The averaged thermal performance of the respective subsystem is well within the limits specified by the manufacturer. with there being more thermal headroom when the respective subsystems are experiencing maximum temperature in comparison to the minimum temperature thermal headroom.

Two approaches were taken to manually calculate the thermal range that would be experienced by ZACube-2. And compared to the temperature telemetry. The table below shows the comparison of the maximum and minimum temperatures calculated or gained from the telemetry (actual).

Table 5.15: Comparison of Thermal Hand Calculation Techniques in Relation to Temperature Telemetry

	Thermal Hand Calculation Temperatures (°C)			
	Fortescue		Gilmore	
	Minimum	**Maximum**	**Minimum**	**Maximum**
Thermal Telemetry (°C)	-21.451	49.213	-21.094	43.329
Minimum	-15.125		-15.125	
Maximum		37.231		37.231
Difference	6.327	11.981	5.969	6.098

In relation to the thermal telemetry from ZACube-2, the hand calculation that employs the Gilmore (2002) method is more in line with the thermal telemetry, compared to the method described by Fortescue (2011).

5.3 Effects of Space Weather on Subsystem Performance

As previously mentioned, space weather has a considerable influence on space segments, with a multitude of different phenomena from solar flares to coronal holes that emit highly charged particles, such as gamma photons and protons. These particles, when interacting with the various electronics on the aforementioned segments, can cause soft errors or a disruption in the logic state of the memory, e.g., changing the logic from “1” to “0”.

Therefore, investigation of historic space weather events in comparison to the telemetry (especially outliers) is informative. The Kp-index is an averaged planetary magnetic activity

index taken from thirteen geomagnetic observatories, where eight samples are recorded over the day at a 3-hour interval, with a rating of 0 being quiet to a rating of 9 being extreme. Below is a table of the effects experienced at various spectrums on the Kp-index.

Table 5.16: Kp Index and Subsequent Effects
(NOAA Space Weather Scales, 2021)
(National Geophysical Data Center, 2010)
(The KP-index | help | spaceweatherlive.com, 2022)
(Helmholtz Centre Potsdam GFZ German Research Centre for Geosciences, n.d.)

Kp Index Value	Kp Index Value in Decimals	Severity	Effect	Average Frequency (1 cycle = 11 years)
5-	4.67	Minor	• Minimal impact on satellite operation.	1700 per cycle (900 days per cycle)
5o	5.00			
5+	5.33			
6-	5.67	Moderate	• Potential changes in orbital drag. • Restorative actions to orientation might be required by the ground segment.	600 per cycle (360 days per cycle)
6o	6.00			
6+	6.33			
7-	6.67	Strong	• Modifications may be needed for problems with orientating spacecraft. Drag. • Potential increase of drag with satellites in LEO. • Surface charging of the satellite's components may occur.	200 per cycle (130 days per cycle)
7o	7.00			
7+	7.33			
8-	7.67	Severe	• Potential surface charging • Problems with satellite tracking • Possible corrections due to orientation complications	100 per cycle (60 days per cycle)
8o	8.00			
8+	8.33			
9-	8.67	Extreme	• Likely extensive surface charging can be present • Orientation problems • Difficulties with uplink and/or downlink • Troubles with tracking the satellite	4 per cycle (4 days per cycle)
9o	9.00			

With the scale, known relative data can be captured and transformed. The Kp index data will be used to locate any anomalies in the various telemetry sets with recorded space weather events. The figure below is the Kp indexed data, which has the same temporal range of the telemetry from the 01 January 2019 UTC to 31 July 2022.

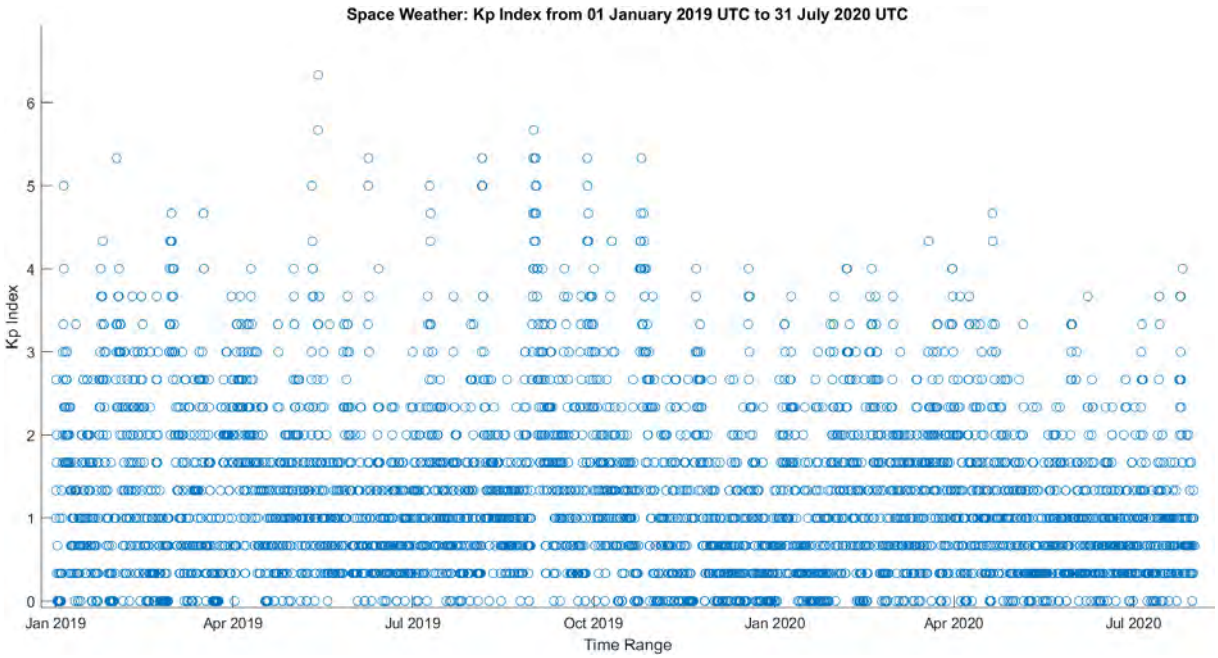

Figure 5.19: Kp Index from 01 January 2019 UTC to 31 July 2020 UTC

(Helmholtz Centre Potsdam GFZ German Research Centre for Geosciences, 2019-2022)

From the figure above, there was only a moderate geomagnetic storm with a decimal Kp index rating of 6.33. While there were several minor storms during this period, this is to be expected as this was during the solar transition phase from cycle 24 to cycle 25, going from solar minimum to solar maximum. The occurrence and spread of recorded storms are illustrated in the probability density function below.

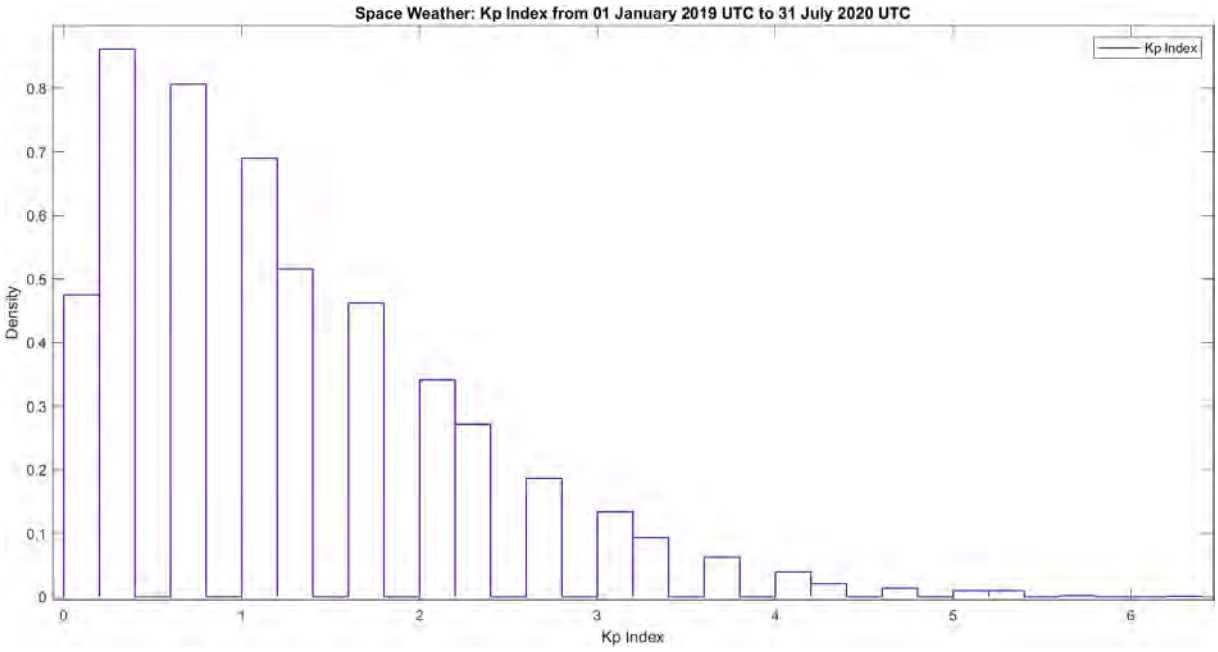

Figure 5.20: Kp Index Probability Density Function

(Helmholtz Centre Potsdam GFZ German Research Centre for Geosciences, 2019-2022)

Figure 5.16 and Figure 5.17 is an expansion of areas of interest where a moderate storm was recorded.

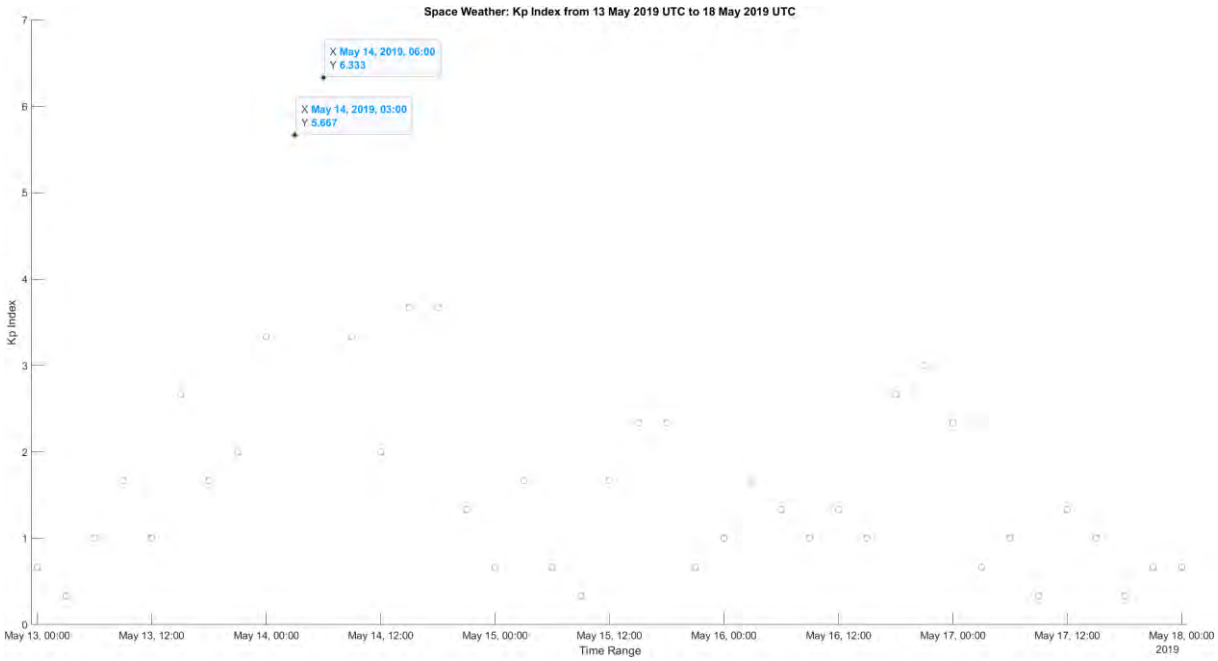

Figure 5.21: Kp Index from 13 May 2019 UTC to 18 May 2019 UTC

(Helmholtz Centre Potsdam GFZ German Research Centre for Geosciences, 2019-2022)

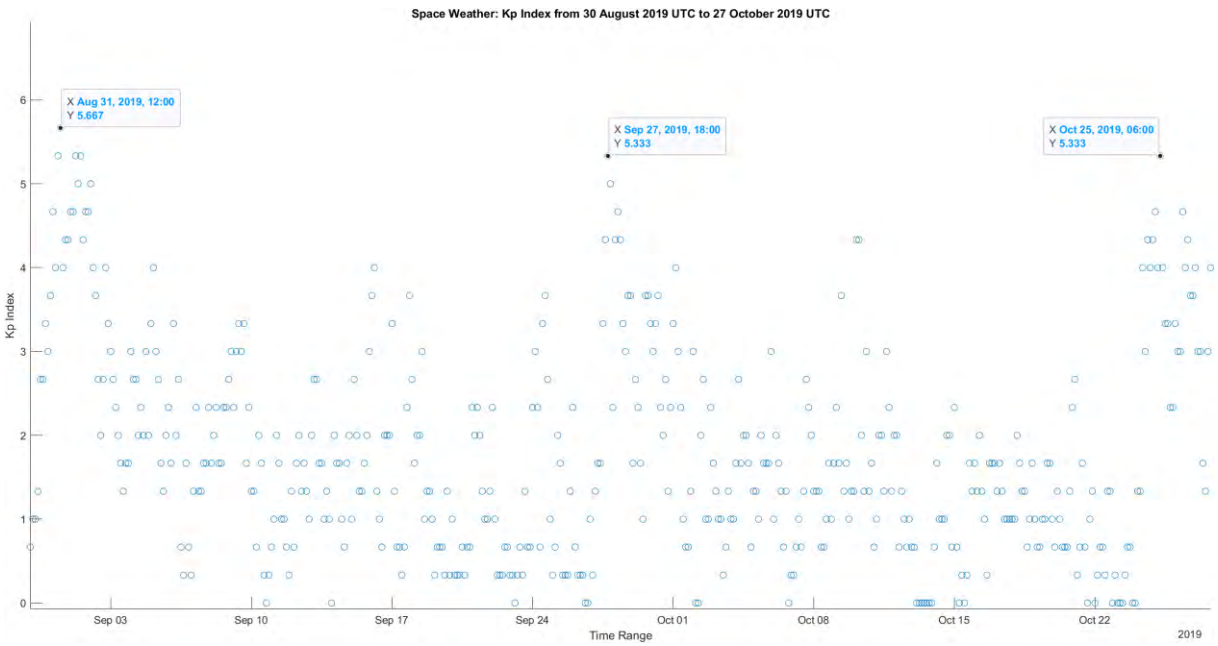

Figure 5.22: Kp Index from 30 August 2019 UTC to 27 October 2019 UTC

(Helmholtz Centre Potsdam GFZ German Research Centre for Geosciences, 2019-2022)

Figure 5.16 is of interest not only because there was a minor and moderate storm recorded in the span of 3 hours, but additionally, in the same period there were issues regarding the ADCS where the attitude and angular rate for the X-axis and Y-axis started acting abnormally in relation to previous behaviour

Another potential aspect that these geomagnetic storms can affect, is on-board memory. In section *5.1.6 System Performance* it was discussed that there were lapses in the telemetry channel data logging, leaving gaps. These lapses were cross-referenced with recorded Kp index values, which can be seen in the table below. Refer to Table 5.16 for explanations on the various Kp index values.

Table 5.17: Telemetry Channel Data Logging Temporal Lapses in Comparison to Historical Kp Index Values
(SpaceWeatherLive, 2019-2020)

	Datetime (UTC)		
Instances	**Start**	**End**	**Maximum Kp Index Value**
1	08 January 2019 21:20:29	16 January 2019 21:20:29	3+
2	23 February 2019 03:42:35	24 February 2019 21:00:14	1o
3	04 March 2019 08:27:14	13 March 2019 08:57:18	3-
4	31 March 2019 01:24:18	02 April 2019 09:33:18	4-
5	07 May 2019 19:20:58	12 May 2019 09:06:05	3o
6	02 June 2019 13:48:10	03 June 2019 09:00:10	2o
7	11 June 2019 22:12:18		1-
8	30 June 2019 10:00:15	12 July 2019 10:29:28	4-
9	07 August 2019 10:26:49		2+
10	16 August 2019 08:05:51	16 August 2019 10:11:51	2o
11	17 September 2019 03:29:59	17 September 2019 09:33:00	4-
12	18 September 2019 00:42:00	18 September 2019 07:27:00	3o
13	23 September 2019 01:18:00	23 September 2019 08:03:00	1+
14	06 October 2019 10:51:03	06 October 2019 17:36:03	2o
15	15 October 2019 10:27:07	16 October 2019 21:59:08	2+
16	05 December 2019 14:59:18	05 December 2019 20:56:20	1-
17	15 December 2019 08:40:33	17 December 2019 09:08:33	2+
18	23 December 2019 00:34:52		1+
19	23 December 2019 00:36:03		1+
	23 December 2019 08:50:36		
	23 December 2019 08:56:36		
20	23 December 2019 15:04:38		1+
	23 December 2019 23:26:36		1+
21	30 January 2020 02:44:46	30 January 2020 02:44:46	3+
22	23 February 2020 18:07:47	23 February 2020 21:19:47	2+

23	15 March 2020 16:22:19	16 March 2020 10:34:21	2o
24	11 June 2020 23:34:47	12 June 2020 09:28:48	2-
25	18 June 2020 10:31:49	18 June 2020 16:58:49	2-
26	23 June 2020 06:34:51	23 June 2020 10:04:51	1+
27	26 June 2020 09:01:51	28 June 2020 20:16:56	3-
28	04 July 2020 09:14:56	04 July 2020 15:47:56	3o
29	05 July 2020 00:38:56		3+

From the table there were several geomagnetic storms occurring during these periods. None of said storms were potent enough to classify on the Kp index as a “minor” and could not be the cause for the lapses in the data logging for the various telemetry channels.

CHAPTER SIX
RESOURCE BUDGET PROFILE COMPARISON

The purpose of this analysis is to validate the various budgets that were used during the design ZACube-2. These budgets are the power, thermal, mass and link budgets, with the mass budget not requiring a verification through telemetry.

Validation of the various budgets is important as it guides the development of the next iteration of CubeSats relaying information on areas of improvement. A prime example would be the comparison of different power profile versions with one being calculated or simulated and the other being calculated directly from the telemetry.

This section details the comparison of values taken from the three aforementioned budgets (power, link and thermal) in relation to the profile constructed using telemetry values.

6.1 Power Budget

ZACube-2 has four modes in which it operates, specified by either the schedule file or activated by meeting a prescribed location or altitude parameter. Each profile has a sunlit and eclipse variant as power consumed will be different when the CubeSat is in either the sun or eclipse. The four power profiles, including the sunlit and eclipse variants, are as follows:

Table 6.1: ZACube-2 Power Profiles

Power Profile	Description
Safe sun	Basic sunlit "safe mode" with most of the bus idle and payload off.
Safe eclipse	Basic eclipse "safe mode" with most of the bus idle and payload off.
Safe TT&C sun	Basic sunlit "safe mode" with TT&C session and most of the bus in idle and payload off.
Safe TT&C eclipse	Basic eclipse "safe mode" with TT&C session and most of the bus in idle and payload off.
Downlink sun	Sunlit "downlink mode" with TT&C session, data downlink and most of the bus in idle and payload off
Downlink eclipse	Eclipse "downlink mode" with TT&C session, data downlink and most of the bus in idle and payload off.
Payload sun	Sunlit payload operations with TT&C session, data downlink and most of the bus in idle and payload on for one pass.
Payload eclipse	Eclipse payload operations with TT&C session, data downlink and most of the bus in idle and payload on for one pass.

However, prior to calculating and comparing telemetry derived values and values described in the power budget, confirmation of the orbital period, and likewise the sunlit and eclipse period, needs to be done.

6.1.1 Confirmation of Orbital Period Parameters

In the power budget, ZACube-2 is described as having a circular sun-synchronous orbit at an inclination of 98° and with an altitude of 500 km, giving the following orbital parameters

Table 6.2: ZACube-2 Power Budget Orbital Period

	Period	
Orbital Parameter	**Seconds**	**Hours**
Sunlit minimum (seconds)	3531.753	0.981
Eclipse maximum (seconds)	2145.225	0.596
Orbital period (seconds)	5676.978	1.577

To confirm these values, the orbital period must be calculated from the telemetry in the most efficient way by looking at the battery voltage behaviour. It is known that when in an eclipse, the battery discharges to power vital systems and, likewise, charges when the satellite is in view of the sun.

Looking at any day and taking note of when the battery voltage starts to decrease gives an estimated eclipse maximum period. Noting when the voltage starts to increase will give an approximation of the sunlit minimum period. An example of this can be seen below where the voltage starts to decline, indicating the satellite is in eclipse with the remaining times being that the satellite is in sunlit minimum.

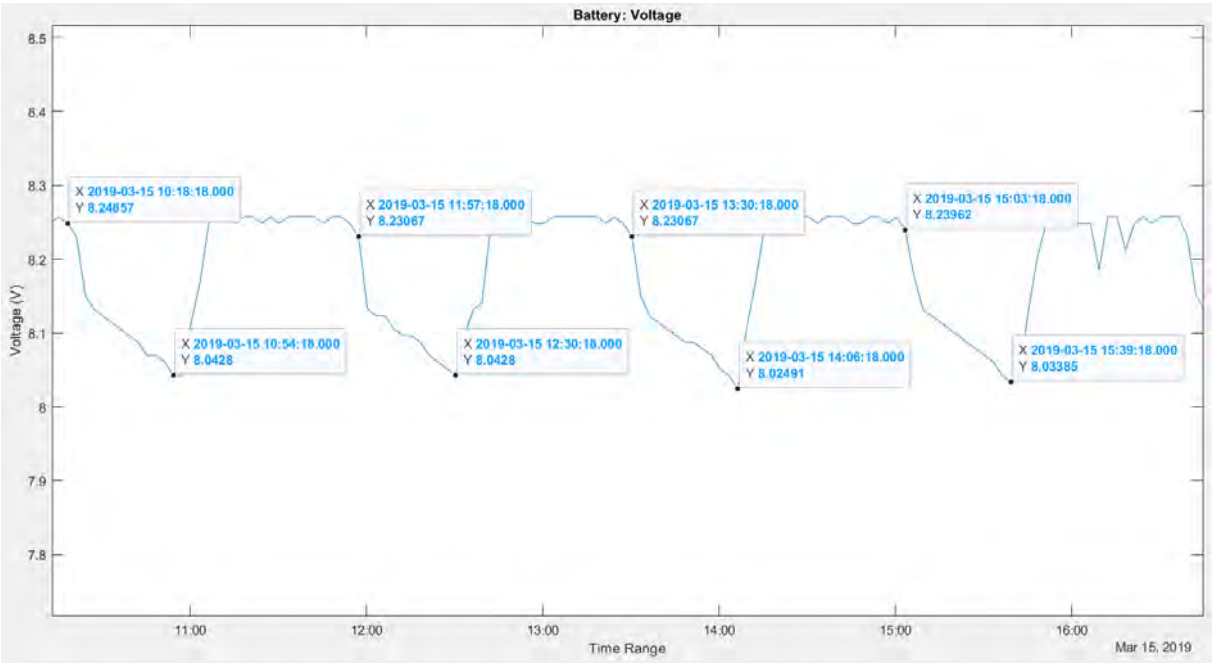

Figure 6.1: Example of Calculating Eclipse Max and Sunlit Min Period

The respective times were averaged and then compared to the calculated power budget values, which can be seen in the table below.

Table 6.3: Telemetry Orbital Parameters Comparison

	Period (seconds)		
Orbital Parameters	**Telemetry**	**Power Budget**	**Difference**
Sunlit minimum (seconds)	3375	3531.753	156.753
Eclipse maximum (seconds)	2205	2145.225	-59.775
Orbital period (seconds)	5580	5676.978	96.776

There are some discrepancies; however, an error of ± 3 minutes will be present in the calculated data due to the battery voltage times being recorded at an interval or timestep of every 3 minutes.

6.1.2 Solar Panel Configuration

Prior to the calculation of the various profiles, the minimum power generated by the solar panels when the satellite is in a sunlit minimum phase needs to be calculated. To do this, a singular instance of when ZACube-2 was in sunlit minimum was chosen where there was a value recorded, i.e., the solar array is generating power. A day was chosen instead of a singular event as there would be multiple occurrences when the satellite is in view of the sun. The period in question is 17 February 2020 00:01:44 UTC to 17 February 2020 23:58:44 UTC, where a value was recorded at an interval of 3 minutes. The power generated by the combined solar array for the period described can be seen in the figure below.

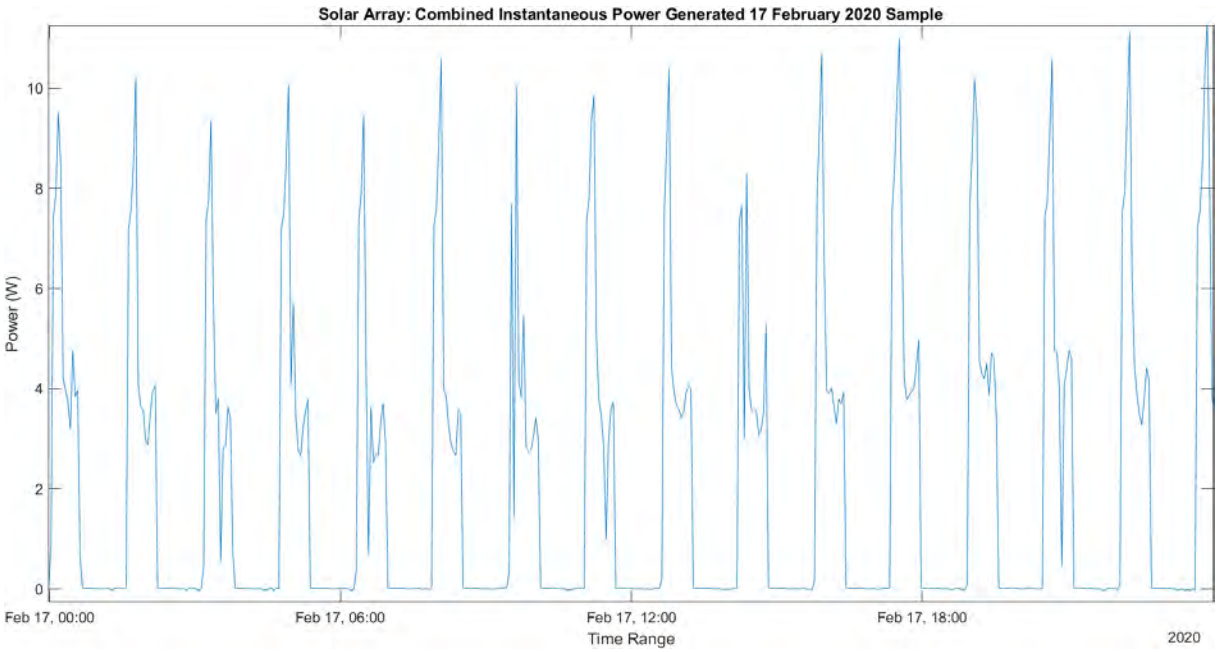

Figure 6.2: Solar Array Combined Instantaneous Power Generated 17 February 2020 Sample

The peak instantaneous power generated is approximately between 8W and 8.5W. Therefore, by using the graph and extrapolating the values during these “peaks”, the average solar array power generated per hour can be found. A sample of the calculation done, is given in the table below, where the cells highlighted in yellow is when the solar array generates power.

Table 6.4: Sample Calculation of Solar Array Power Generation

Time	Instant Power (W)	Ave Power (W)	Time (Hr)	Power (Wh)
2020-02-17 00:01:44	0			
2020-02-17 00:04:44	-0.028			
2020-02-17 00:07:44	0.014			
2020-02-17 00:10:44	0.020			
2020-02-17 00:13:44	-0.013			
2020-02-17 00:16:44	0.018			
2020-02-17 00:19:44	0			
2020-02-17 00:22:44	-0.017			
2020-02-17 00:25:44	0.863			
2020-02-17 00:28:44	7.448	5.134	0.600	3.080
2020-02-17 00:31:44	7.874			
2020-02-17 00:34:44	9.514			
2020-02-17 00:37:44	8.475			
2020-02-17 00:40:44	4.193			
2020-02-17 00:43:44	3.982			
2020-02-17 00:46:44	3.723			
2020-02-17 00:49:44	3.196			
2020-02-17 00:52:44	4.766			
2020-02-17 00:55:44	3.832			
2020-02-17 00:58:44	3.965			
2020-02-17 01:01:44	0.643			

Results from this process can be seen in the table below, which is compared to the solar panel configuration that yields the least amount of power.

Table 6.5: Solar Array Configuration Calculation Results

Profile Name	Power (Wh)
Calculated value from sample	3.387
Sun on 3U	6.472
Difference	-3.085

It can be seen that the value calculated from the sample is roughly only half of what was calculated. Additionally, the sunlit minimum period was calculated as 0.981 hours, while the time calculated in which the solar array generated power is 0.677 hours. From the sample calculation, it can be seen that the solar array generated power for only a fraction of the sunlit min period, specifically for 18.3 minutes.

However, the same process was replicated using the same time period in which the sunlit minimum and the eclipse maximum period were calculated, e.g., telemetry sample calculation on 15 May 2019 UTC. Both the period in which the combined solar array generated power and the average power generated differ as can be seen in the table below

Table 6.6: Difference in Solar Array Telemetry Configuration Calculation

Sample Number	Date of Telemetry Sample (UTC)	Power (Wh)	Time (hr)
1	15 March 2019	4.417	0.960
2	17 February 2020	3.387	0.677
	Difference	1.030	0.283

From the table above, the sample calculation is done on 17 February 2019 UTC and generated only 76.68% of the power calculated on 15 March 2020 UTC, with the initial sample having a period in which the solar array generated power of 70.53% of the latter sample.

Additionally, the difference between the power generation period for the second sample and the telemetry calculated sunlit minimum period (1.3 minutes) is less than the timestep at which the telemetry was logged.

6.1.3 Safe Sun and Safe Eclipse

Safe sun and safe eclipse are modes that use the least amount of power per orbit, since only essential subsystems, such as the UTRX, EPS, battery, OBC and ADCS, are in usage. To calculate both the safe sun and safe eclipse, the same method to calculate the orbital parameters was used in conjunction with the EPS combined power generated.

A day when neither the HSTXC, SDR or K-line imager was activated, nor when the satellite was over the ground station, which was from 10:00 to 12:00 UTC and 22:00 to 00:00 UTC - as the UTRX would be transmitting over the ground station - was chosen.

The EPS datetime-dependent EPS combined power values were cross-referenced with the battery voltage to determine if ZACube-2 was in eclipse or not, with a total of four passes being used. Averages of the combined EPS power were taken for each sunlit minimum and eclipse period, with each respective period being multiplied by the previously calculated sunlit minimum and eclipse period, transforming the values from Watt-to-Watt hour. In turn, the respective sunlit minimum and eclipse maximum values were then averaged.

The table below contains the data for a single orbit and shows how the data was used to calculate the respective safe sun and safe eclipse values.

Table 6.7: Sample Calculation of Safe Sun and Safe Eclipse Power Profiles

Time (UTC)	Z2 in Sun	EPS Comb. Power (W)	Average Power (W)	Average Power (Wh)
2019-05-12 13:42:05	1	1.700	1.876	1.759
2019-05-12 13:45:05,	1	1.700		
2019-05-12 13:48:05	1	1.970		
2019-05-12 13:51:05	1	2.022		
2019-05-12 13:54:05	1	1,996		
2019-05-12 13:57:05	1	1,996		
2019-05-12 14:00:05	1	1.953		
2019-05-12 14:03:05	1	1.935		
2019-05-12 14:06:05	1	1.969		
2019-05-12 14:09:05	1	2.004		
2019-05-12 14:12:05	1	1.978		
2019-05-12 14:15:05	1	1.794		
2019-05-12 14:18:05	1	1.742		
2019-05-12 14:21:05	1	1.742		
2019-05-12 14:24:05	1	1.759		
2019-05-12 14:27:05	1	1.759		
2019-05-12 14:30:05	0	1.742	1.753	1.074
2019-05-12 14:33:05	0	1.760		
2019-05-12 14:36:05	0	1.700		
2019-05-12 14:39:05	0	1.743		
2019-05-12 14:42:05	0	1.761		
2019-05-12 14:45:05	0	1.752		
2019-05-12 14:48:05	0	1.743		
2019-05-12 14:51:05	0	1.726		
2019-05-12 14:54:05	0	1.760		
2019-05-12 14:57:05	0	1.700		
2019-05-12 15:00:05	0	1.717		
2019-05-12 15:03:05	0	1.934		

Repeating the process as depicted above for four orbits from 12 May 2019 13:42:05 UTC to 12 May 2019 19:51:05 UTC, results in the average values that is summarised in Table 6.8.

Table 6.8: Comparison of Calculated and Telemetry Derived Safe Sun and Safe Eclipse Power Profile Values

	Total Power Consumed (Wh)		
Profile Name	**Power Budget**	**Telemetry**	**Difference**
Safe sun	1.759	1.705	0.054
Safe eclipse	1.068	1.049	0.019

6.1.4 Safe TT&C Sun and Safe TT&C Eclipse

As the profile designation implies, this is when the satellite interfaces with the ground segment to downlink telemetry information and uplink of an operational schedule. This mode also acts as a redundant means to downlink data with the HSTXC being the primary method. Using the UHF TT&C link, however, does mean a reduced downlink rate.

The safe TT&C and the standard safe profile mirror each other in terms of subsystems being active, with the only difference being that the UTRXC is now being powered to transmit data when the satellite is in range of the ground station.

To calculate the power usage for when this power profile is active, it is necessary to look at the UTRX's electrical characteristics as defined by the in-house engineering team who designed this subsystem.

Table 6.9: UTRXC Electrical Characteristics

DC Power	Description	Typical Power Rating (W)
Idle power	Receiver ON, transmitter OFF	0.220
Transmit 0.5W RF	Receiver ON, transmitter ON	2.800
Transmit 1W RF	Receiver ON, transmitter ON	3.800
Transmit 2W RF	Receiver ON, transmitter ON	5.100

Therefore, to calculate the power profile safe TT&C sun and eclipse, a number of conditions have to be first met:

- Transmission times are from 10:00 to 12:00 UTC and from 22:00 to 00:00 UTC.
- UTRXC PA forward power reading must be approximately 0.5 W showing that both the receiver and transmitter are in the ON state.

- The combined power reading from both the 3.3V and 5V regulated bus is approximately 2.8W in accordance with the subsystem transmitting.
- Both the SDR and imager are in the OFF state as the safe TT&C profile is for when the HSTXC and UTRXC are active.

Using the same methodology that was used with the calculation of the safe sun and safe eclipse in conjunction with the above criteria, the EPS combined power reading for when the UTRXC was active, was averaged and then multiplied by the time it was active for with the remaining EPS combined power values for that phase. The summation of these values, which are now in Watt hour, depicts the power consumption for the safe TT&C.

The table below is a demonstration of the process applied. The cells highlighted in green correspond to the UTRXC and blue to the respective EPS values.

Table 6.10: Sample Calculation of Safe TT&C Power Profile Value

Time (UTC)	UTRXC PA Power (W)	UTRXC Power (W)	EPS Comb Power (W)	UTRXC Average Power (W)	UTRXC Average Power (Wh)	EPS Average Power (W)	EPS Average Power (Wh)	Total Power Consumed (Wh)
2019-05-13 10:03:05	0.300	0.209	1.881	6.235	0.623	1.738	1.477	2.101
2019-05-13 10:06:05	0.300	0.208	1.639					
2019-05-13 10:09:05	0.300	0.208	1.639					
2019-05-13 10:12:05	0.300	0.208	1.613					
2019-05-13 10:15:05	0.300	0.208	1.639					
2019-05-13 10:18:05	0.543	2.973	6.108					
2019-05-13 10:21:05	0.543	2.958	6.225					
2019-05-13 10:24:05	0.478	2.999	6.371					
2019-05-13 10:27:05	0.300	0.208	1.873					
2019-05-13 10:30:05	0.300	0.208	1.917					
2019-05-13 10:33:05	0.299	0.208	1.899					
2019-05-13 10:36:05	0.299	0.209	1.874					
2019-05-13 10:39:05	0.299	0.209	1.664					
2019-05-13 10:42:05	0.299	0.209	1.664					
2019-05-13 10:45:05	0.298	0.209	1.655					
2019-05-13 10:48:05	0.298	0.210	1.733					
2019-05-13 10:51:05	0.298	0.210	1.742					
2019-05-13 10:54:05	0.298	0.210	1.768					
2019-05-13 10:57:05	0.298	0.210	1.655					

Once the respective safe TT&C power profile values have been calculated, a comparison between the telemetry calculated and the power budget values can be made. The table below is a comparison of these values.

Table 6.11: Comparison of Calculated and Telemetry Derived Safe TT&C Sun and Safe TT&C Eclipse Power Profile Values

	Total Power Consumed (Wh)		
Profile Name	**Power Budget**	**Telemetry**	**Difference**
Safe TT&C sun	2.576	2.101	0.354
Safe TT&C eclipse	1.885	1.583	0.274

The values calculated from the telemetry are lower than that of the values taken from the power budget, because for the power budget, the duration during which the UTRXC was active was set at 10 minutes, whilst it can be seen in the demonstrative calculation that the active time was in fact 9 minutes.

6.1.5 Downlink Sun and Downlink Eclipse

This profile is used for the downlink of both TT&C and payload data. As mentioned previously, the HSTXC or S-band are the primary channels in which to downlink payload data when initiated via a telecommand by the ground station. Payload data consists of real-time messages or logs that contain the ships' positions, metadata and telemetry regarding the state and health of the payload.

The downlink profile is similar to the safe TT&C profile, with the exception of the HSTXC or S-band being enabled. To calculate the downlink power profile when the CubeSat is the sun and eclipse, respectively, several criteria need to be met for an accurate value to be calculated:

- Downlink times are from 10:00 to 12:00 UTC and from 22:00 to 00:00 UTC.
- HTSX is enabled during downlink times
- UTRXC PA forward power reading must be approximately 0.5 W showing that both the receiver and transmitter are in the ON state.
- The combined power reading from both the 3.3V and 5V regulated bus is approximately 2.8W in accordance with the subsystem transmitting.
- Both the SDR and imager are in the OFF state as the safe TT&C profile is for when the HSTXC and UTRXC are active.

Once those criteria have been met, the respective values can be calculated. The EPS combined power value is averaged and multiplied by the active time when the UTRXC is transmitting with the remaining EPS values in that phase, be it when the satellite is in sunlit min or eclipse max condition, being averaged with the respective value being multiplied by the remaining time within in that period. These two values, now in Watt hour, are added together and subsequently compared to the power budget.

The table below demonstrates this process by calculating the downlink sun value. This is when a downlink is occurring as ZACube-2 is in the sun. For ease of reading, the blue cells are related to the EPS, while the green cells relate to the criteria of the profile, namely when the HSTXC is enabled and when the UTRXC is transmitting.

Table 6.12: Sample Calculation of Downlink Power Profile Value

Time	UTRXC Power Drawn (W)	UTRXC PA Power (W)	HSTXC Enabled	EPS Power Comb. (W)	Average UTRXC Power (W)	Average UTRXC Power (Wh)	Average EPS Power (W)	Average EPS Power (Wh)	Total Power Consumed
2019-08-12 09:47:48,000	2,9924561	0,476074219	0	1,158828627	4,735361	0,078891	2,914655	2,768921	2.848
2019-08-12 09:50:48,000	2,9864108	0,476074219	0	1,472754015					
2019-08-12 09:53:48,000	2,9859356	0,476806641	0	1,36569721					
2019-08-12 09:56:48,000	2,9625204	0,477539063	0	1,305918637					
2019-08-12 09:59:48,000	2,9565939	0,476074219	0	1,305882965					
2019-08-12 10:02:48,000	2,9614611	0,477539063	0	1,201024991					
2019-08-12 10:04:54,420	NaN	NaN	0	NaN					
2019-08-12 10:05:07,927	NaN	NaN	1	NaN					
2019-08-12 10:05:51,000	2,9601951	0,476806641	1	2,197203188					
2019-08-12 10:06:26,920	NaN	NaN	1	NaN					
2019-08-12 10:06:32,930	NaN	NaN	NaN	7,345258784					
2019-08-12 10:06:57,933	NaN	NaN	NaN	7,280127172					
2019-08-12 10:07:21,923	NaN	NaN	NaN	7,298896868					
2019-08-12 10:07:44,423	NaN	NaN	NaN	7,41076754					
2019-08-12 10:08:10,433	NaN	NaN	NaN	7,37408534					
2019-08-12 10:08:35,433	NaN	NaN	NaN	7,421549101					
2019-08-12 10:08:51,000	2,9766715	0,477539063	1	7,273518092					

2019-08-12 10:09:08,423	NaN	NaN	NaN	7,452299057					
2019-08-12 10:09:53,933	NaN	NaN	0	NaN					
2019-08-12 10:09:57,433	NaN	NaN	0	NaN					
2019-08-12 10:11:51,000'	2,9660492	0,477539063	0	1,236827851					
2019-08-12 10:14:51,000	2,962758	0,476806641	0	1,262645721					
2019-08-12 10:17:51,000	2,9593944	0,476806641	0	1,228149124					
2019-08-12 10:20:51,000	2,959632	0,476806641	0	1,288925004					
2019-08-12 10:23:51,000	2,9618385	0,476806641	0	1,306703424					
2019-08-12 10:26:51,000	2,9641737	0,476806641	0	1,245290654					
2019-08-12 10:29:51,000	2,9679401	0,476806641	0	1,271487311					
2019-08-12 10:32:51,000	2,9703842	0,476074219	0	1,245290654					
2019-08-12 10:35:51,000	2,9741506	0,476074219	0	1,262645721					
2019-08-12 10:38:51,000	2,9802058	0,475341797	0	1,245515472					
2019-08-12 10:41:51,000	2,9822211	0,475341797	0	1,245194423					
2019-08-12 10:44:51,000	2,9844375	0,475341797	0	1,244133894					
2019-08-12 10:47:51,000	2,9957627	0,475341797	0	1,30512331					

This process was repeated once again when the UTRXC and HSTXC were in the ON state when the satellite was in an eclipse. As apparent in the table above, there were multiple instances when there were no values recorded, shown as NaN (not a number), for the equivalent datetime across the different telemetry sets when combined. With values missing, an accurate representation of the explicit power consumed cannot be calculated.

The table below shows the values calculated from the telemetry with respect to the values calculated from the power budget.

Table 6.13: Comparison of Calculated and Telemetry Derived Downlink Sun and Downlink Eclipse Power Profile Values

	Total Power Consumed (Wh)		
Profile Name	**Power Budget**	**Telemetry**	**Difference**
Download sun	3.576	2.848	0.728
Download eclipse	1,432	1,408	0,024

For both the sun and eclipse profiles the values calculated from the respective telemetry sets are lower than those determined in the power budget. As previously explained, with missing equivalent values across the different telemetry, the final calculated telemetry value was only done using known values, leading to a plausible reason as to why the telemetry value is lower than that of the power budget equivalent.

6.1.6 Payload Sun and Payload Eclipse

This power profile defines the power consumption when the payloads aboard, namely the software defined radio (SDR) and K-line imager, are operated, with the SDR being the primary payload and the K-line imager the hosted payload.

Both the primary and hosted payloads are controlled by the satellite bus on either time-based scheduling or when a particular location has been reached. Because the two payloads do not necessarily operate simultaneously, finding an instance in the telemetry when both of these payloads were active, yield maximum power usage.

To calculate the payload power profile when the CubeSat is in the sun and eclipse, respectively, several criteria need to be met in order for an accurate value to be calculated:

- HSTXC needs to be active
- SDR needs to be active

- K-line Imager needs to be active

Once the aforementioned criteria have been met, the payload power can be determined. For a particular phase, be it when the satellite is in sunlit minimum or eclipse maximum, the average EPS power consumed when both the K-line imager and SDR are active, is multiplied by the time it was active. The remainder of the EPS values in that particular phase is averaged and multiplied by the remaining time in the phase. The addition of these two values gives the maximum power consumed for the respective payload profiles.

The table below demonstrates this process by calculating the payload sun value, when both payloads are active as ZACube-2 is in the sun. For ease of reading, the blue cells relate to the EPS, while the green cells indicate the EPS values when the primary and hosted payload are active.

Table 6.14: Sample Calculation of Payload Power Profile Value

Time	HSTXC Enabled	SDR Enabled	K-line Imager Enabled	EPS Comb Power Value (W)	Average Payload EPS Value (W)	Average Payload EPS Value (Wh)	Average EPS Value (W)	Average EPS Value (Wh)	Total Power Consumed (Wh)
2019-12-23 00:08:36,000	0	0	0	1,210938637	15,23452653	0,761726326	1,729790859	1,535189387	2,297
2019-12-23 00:11:36,000	0	0	0	1,289185494					
2019-12-23 00:14:36,000	0	0	0	1,769060939					
2019-12-23 00:17:36,000	0	0	0	1,725769705					
2019-12-23 00:20:36,000	0	0	0	1,830556334					
2019-12-23 00:23:36,000	0	0	0	2,004830856					
2019-12-23 00:26:36,000	0	0	0	1,944101929					
2019-12-23 00:29:36,000	0	0	0	2,238745951					
2019-12-23 00:32:36,000	0	0	0	2,195090369					
2019-12-23 00:34:52,000	1	1	1	13,85063125					
2019-12-23 00:35:36,000	0	0	0	2,212528062					
2019-12-23 00:36:03,000	1	1	1	16,61842181					
2019-12-23 00:38:36,000	0	0	0	2,004830856					
2019-12-23 00:41:36,000	0	0	0	2,022656229					
2019-12-23 00:44:36,000	0	0	0	1,803931612					
2019-12-23 00:47:36,000	0	0	0	1,488582538					
2019-12-23 00:50:36,000	0	0	0	1,532051636					

2019-12-23 00:53:36,000	0	0	0	1,278761402					
2019-12-23 00:56:36,000	0	0	0	1,279820103					
2019-12-23 00:59:36,000	0	0	0	1,304792808					

Unlike the previous profiles where the above methodology was followed for when the satellite was in the eclipse max phase, it was found that there were no instances when either the K-line imager or SDR was active when the satellite was in eclipse max.

The table below shows the values calculated from the telemetry with respect to the values calculated from the power budget.

Table 6.15: Comparison of Calculated and Telemetry Derived Payload Sun Power Profile Value

	Total Power Consumed (Wh)		
Profile Name	**Power Budget**	**Telemetry**	**Difference**
Payload sun	4,976	2,297	2,679
Payload eclipse	4,285	Not operated	N/A

6.2 Link Budget

The link budget is a set of calculations aimed at considering whether the satellite makes an acceptable link with the ground station at various elevation angles, ensuring no packet loss. In addition to power being an important aspect in the satellite's survival, guaranteeing that the satellite can communicate viably with the ground station is as important - there is an uplink and downlink of data pertaining not only to the platform such as tracking, telemetry and control but ultimately the motive for the mission is the payload.

The link budget comprises a TT&C uplink and downlink section, respectively, of which the focus will be shifted onto the downlink proportion. A link budget is an interactive tool that contains all pertinent parameters that determine the link performance, all of which are entered by the user and are dependent on whether the uplink or downlink is being calculated. Said parameters for the uplink and downlink are given in Table 6.16.

Table 6.16: Link Budget Tool User Input Parameters

Parameters			
Uplink	**Unit**	**Downlink**	**Unit**
Orbit height	km	Orbit	km
Uplink frequency	MHz	Downlink frequency	MHz
Ground station Tx power	W	Satellite TX power	W
GS Tx antenna gain	dBi	TX SNR	dB
Tx SNR	dB	Tx gain at boresight	dB
Feedline and antenna mismatch losses [dB]	dB	Feedline and antenna mismatch losses	dB
Random losses [dB]	dB	Random losses	dB
Antenna gain uncertainty	dB	Antenna gain uncertainty	dB
Polarization loss - satellite and GS antenna	dB	Polarization loss - satellite and GS antenna	dB

Pointing/tracking errors at satellite	dB	Pointing/tracking errors at satellite	dB
Pointing/tracking errors at GS	dB	Pointing/tracking errors at GS	dB
Rain attenuation	dB	Rain attenuation	dB
Demodulator implementation losses	dB	Demodulator implementation losses	dB
Diverse losses	dB	Diverse losses	dB
Modulation Type	BPSK, QPSK, GMSK and 8PSK	Modulation type	BPSK, QPSK, GMSK and 8PSK
Transmission rate	Mbit/s	Transmission rate	Mbit/s
Receiver antenna noise temperature	K	Receiver antenna noise temperature	K
Receiver noise figure	dB	Receiver noise figure	dBi
Satellite Rx antenna gain	dB	GS RX antenna gain	dB

With the user requirements in the link budget tool, a link margin is automatically calculated for each angle spanning from the horizon to the zenith. For ZACube-2, the designed minimum link margin is 3 dB and for each link margin lower than the minimum link, the cell is highlighted red. The figure below is a screenshot of the in-house link budget tool when calculating the downlink portion.

Parameter	Notes	Questions	Symbol														
Orbit [km]				500,00													
Downlink frequency [MHz]				410,00	400-420MHz Tx (Commercial band)												
Satellite TX power [W]				2,00													
TX SNR [dB]				19,00	Imperfect transmitter												
Tx gain at boresight [dB]				-10,00													
Orbital parameters																	
Elevation [degrees]				0,00	1,00	2,00	3,00	4,00	5,00	6,00	7,00	8,00	9,00	10,00	11,00	12,00	13,00
Slantrange [km]				2573,13	2464,34	2360,37	2261,21	2166,81	2077,09	1991,96	1911,29	1834,94	1762,76	1694,57	1630,19	1569,45	1512,16
Satellite angle [degrees]				68,01	67,99	67,92	67,81	67,66	67,47	67,24	66,97	66,67	66,32	65,94	65,53	65,09	64,62
Transmit power																	
Satellite TX power [dBm]				33,01													
Losses																	
Feedline and antenna mismatch losses [dB]				1,00	PA to antenna port + antenna port to antenna												
Radome losses [dB]				0,00													
Antenna gain uncertainty [dB]				0,50													
Polarization loss - satellite and GS antenna [dB]				3,00	4dB axial ratio gives 0.4dB loss												
Pointing / tracking errors at satellite [dB]				0,50													
Pointing / tracking errors at GS [dB]				0,30													
Rain attenuation [dB]				0,00													
Demodulator implementation losses [dB]	Accounted for by the "real world" figures for spectral efficiency in E38			0,00													
Diverse losses [dB]				2,00		Ageing & Back-off provision											
Total extra losses [dB]				7,30													
Gains																	
Satellite TX antenna gain [dBic] at this angle				-10,00	-10,00	-10,00	-10,00	-10,00	-10,00	-10,00	-10,00	-10,00	-10,00	-10,00	-10,00	-10,00	-10,00
EIRP [dBm]				15,71	15,71	15,71	15,71	15,71	15,71	15,71	15,71	15,71	15,71	15,71	15,71	15,71	15,71
EIRP [dBW]				-14,29	-14,29	-14,29	-14,29	-14,29	-14,29	-14,29	-14,29	-14,29	-14,29	-14,29	-14,29	-14,29	-14,29
Pathloss [dB]				152,91	152,53	152,16	151,78	151,41	151,05	150,68	150,32	149,97	149,62	149,28	148,94	148,61	148,29
Ground station parameters																	
Modulation	Choose between BPSK,QPSK, GMSK and 8PSK (Default BPSK)			GMSK													
Spectral Efficiency [bits/s/Hz]				0,38													
Transmission rate [Mbit/s]	Air rate		B	0,0096	Doesn't need to be fast for TT&C												
Receiver IF bandwidth [MHz]			B	0,025													
Boltzmann constant [dBm / Hz-K]			k	1,4E-23													
Receiver antenna noise temperature [K]			T	100,00													
Receiver noise figure [dB]	Noise figure gives an indication of receiver noise temperatur		T	1,00													
Receiver noise temperature [K]			T	75,09													
Receiver system noise temperature [K]			T	175,09	[1]												
Receiver system noise temperature [dB]				22,43													
Receiver IF bandwidth [dB]				43,98													
Receiver noise floor [dBm] (kTB)			N	-132,19													
GS RX antenna gain [dBi]				18,90													
Received signal power [dBm]				-118,30	-117,92	-117,55	-117,17	-116,80	-116,44	-116,07	-115,71	-115,36	-115,01	-114,67	-114,33	-114,00	-113,68
Power FluxDensity [dBW/m2/4kHz]				-158,44	-158,06	-157,69	-157,32	-156,95	-156,58	-156,22	-155,86	-155,50	-155,15	-154,81	-154,48	-154,15	-153,82
Results																	
Noise after antenna due to TX [dBm]				-137,30	-136,92	-136,55	-136,17	-135,80	-135,44	-135,07	-134,71	-134,36	-134,01	-133,67	-133,33	-133,00	-132,68
Received SNR due to H/W noise [dB]				19,00	19,00	19,00	19,00	19,00	19,00	19,00	19,00	19,00	19,00	19,00	19,00	19,00	19,00
Noise power due to receiver system temperature [dBm]				-132,19													
Receiver SNR due to environmental noise [dB]				13,89	14,27	14,64	15,01	15,38	15,75	16,11	16,47	16,83	17,18	17,52	17,86	18,19	18,51
Total system noise power [dBm]				-131,02	-130,93	-130,83	-130,73	-130,62	-130,50	-130,38	-130,26	-130,13	-129,99	-129,85	-129,71	-129,57	-129,42
Eb/No (dB) required for BER < 10e-6 for normal BPSK	SHANNON, CODING AND THE RADIO AMATEUR, James Miller			10,50													
Signal power needed for required Eb/No [dBm]				-120,52	-120,43	-120,33	-120,23	-120,12	-120,00	-119,88	-119,76	-119,63	-119,49	-119,35	-119,21	-119,07	-118,92
Eb/No (dB) @ GS (Best measured Eb/No available @ demod)	[dB]			18,05	18,42	18,80	19,17	19,54	19,91	20,27	20,63	20,98	21,33	21,68	22,01	22,34	22,66
Actual system Eb/No [dB]				12,72	13,01	13,28	13,55	13,82	14,07	14,31	14,55	14,77	14,98	15,19	15,38	15,56	15,74
Link margin [dB]	Must be better than 3 dB			2,22	2,51	2,78	3,05	3,32	3,57	3,81	4,05	4,27	4,48	4,69	4,88	5,06	5,24

Figure 6.3: Link Budget Tool Screenshot

6.2.1 UHF Transceiver (UTRXC) Received Signal Strength Indicator (RSSI)

One means of measuring the link integrity is to analyse the RSSI. As previously explained, RSSI is a measurement of the received signal strength from a source with the source being the ground station located at the CPUT Bellville campus.

One indication for performance is to look at a cumulative density function (CDF) graph of the RSSI that relays the information of how the UTRXC operated and the quality of the signal. The RSSI telemetry that was used in the CDF graph are in Volt, where each voltage has a corresponding signal strength value in dBm, as found in the user manual compiled by the engineering team. The table below displays the RSSI values with the corresponding signal strength.

Table 6.17: UTRXC RSSI Voltage to Signal Strength

	Voltage (V)		
RF Level (dBm)	**Minimum**	**Typical**	**Maximum**
-118	N/A	0.3	0.8
-68	0.7	1.1	1.8
-23	1.2	1.8	2.5

With the respective RF level and corresponding RSSI values known, the graph for the CDF can be generated and found below. The UTRXC RSSI telemetry used spans from 01 January 2019 00:02:39 UTC to 28 July 2020 23:57:15 UTC.

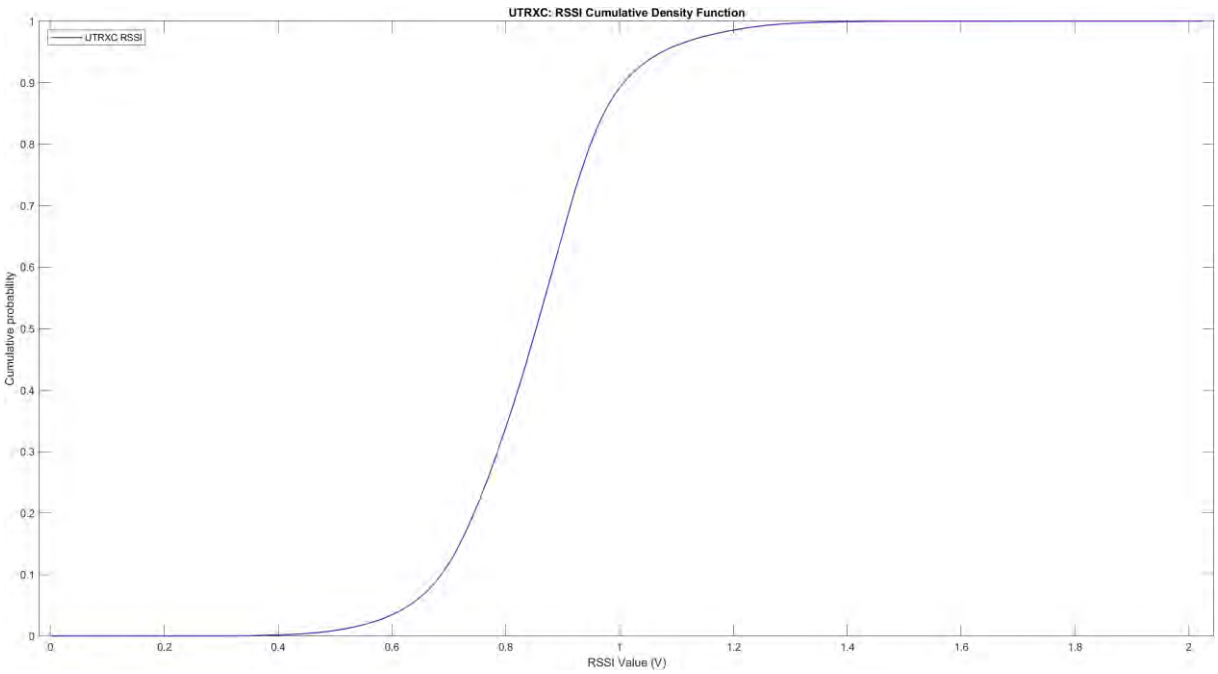

Figure 6.4: UTRXC RSSI Cumulative Density Function

From the figure above and using the provided guidelines, the value range in the CDF plot fits within the values described in Table 6.16, and therefore, it is expected that the signal is received for the entirety of the overpass.

6.2.2 Ground Station RSSI

As previously mentioned, one means of verifying link integrity is by evaluating the UTRXC RSSI values. However, the inherent problem with using the RSSI from ZACube-2 is that data is logged at an interval 3 minutes, while an average overpass lasts on average 8 to 11 minutes, giving only approximately three data points.

Having such a limited number of data points does not give an accurate representation of the performance and could be interpreted as the satellite barely made no contact with the ground station.

An alternative way to show that the link did in fact close, is by looking at the RSSI downlink for the ground station and see whether it conforms to the counterpart as described in the link budget. This is a better method as the ground station has data recorded at a higher temporal resolution, equating to a truer depiction of link performance. In the link budget, a graph was generated that illustrates the link margin in relation to the elevation for the design of ZACube-2. The required and designed link margin is 3 dB at which the satellite is at an elevation of 3°.

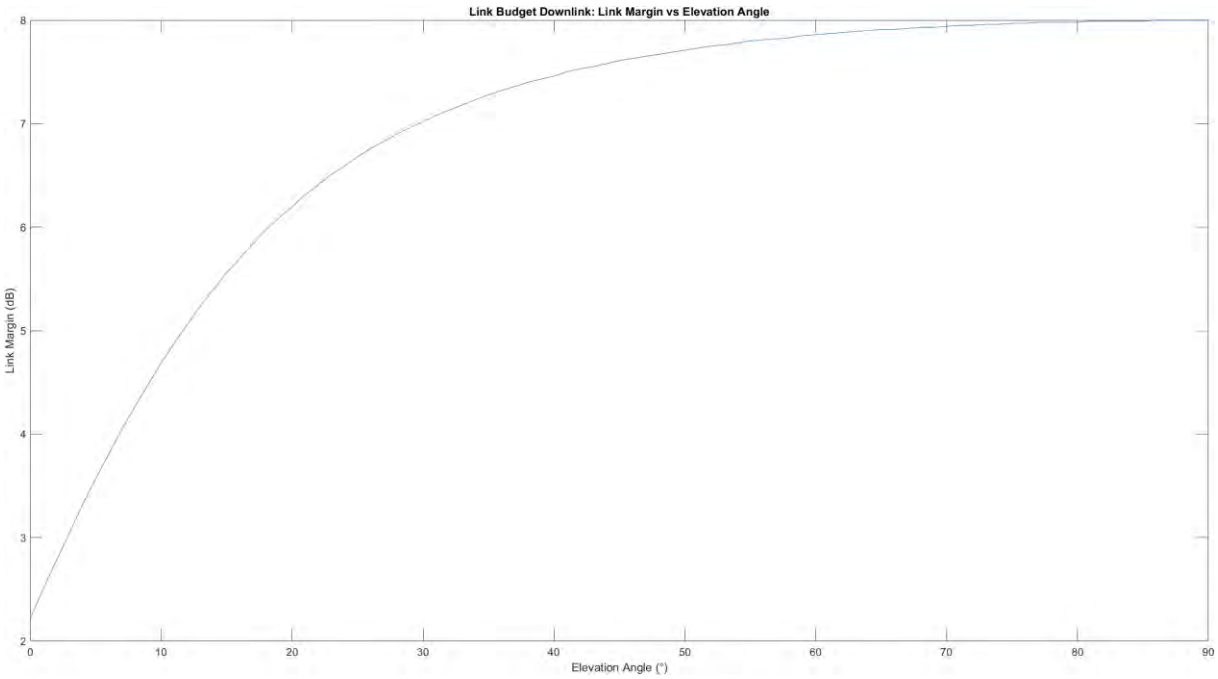

Figure 6.5: Link Budget Downlink Link Margin vs Elevation Angle

To satisfy the link margin at various elevation angles, a minimum signal power is required. This relationship between the minimum signal power required at various elevation angles was described in the downlink portion of the link budget compiled by the engineering team and can also be seen in Figure 6.6.

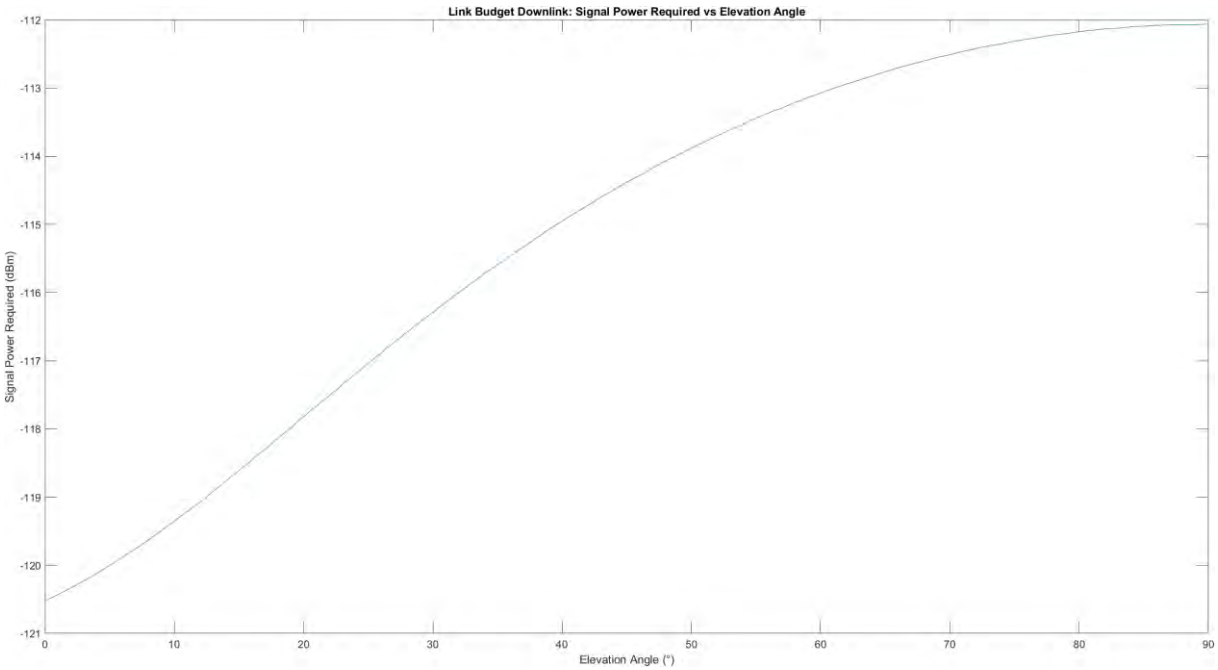

Figure 6.6: Link Budget Downlink Signal Power Required vs Elevation Angle

With the threshold known, it was a matter of collecting and compiling the UHF RSSI and elevation angle from the ground station and comparing the values to see if the link closes. An overpass with a high elevation of 84.5° was chosen. The overpass in question was on 06 April 2019 from 21:39:08 to 21:50:24 UTC from which a graph depicting elevation angle and UHF RSSI was generated.

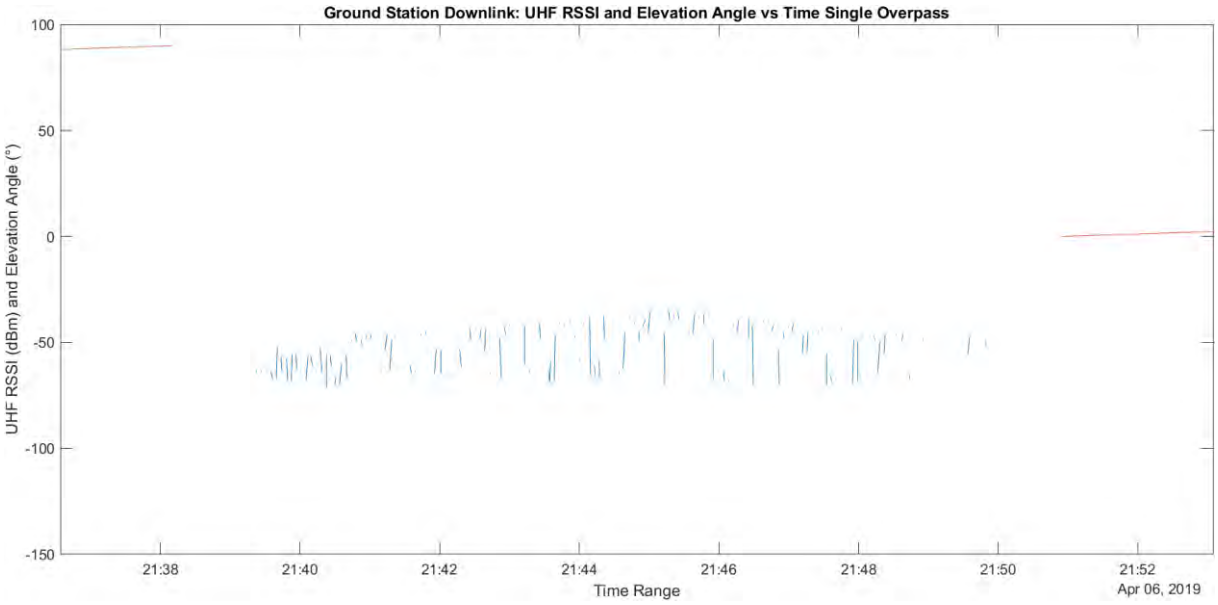

Figure 6.7: Ground Station Downlink UHF RSSI and Elevation Angle vs Time Single Overpass

In the data set and as apparent from the figure above, the elevation angle and RSSI had varying time intervals. To combat this, both time-based data sets were synchronized and linearly interpolated, resulting in the figure below.

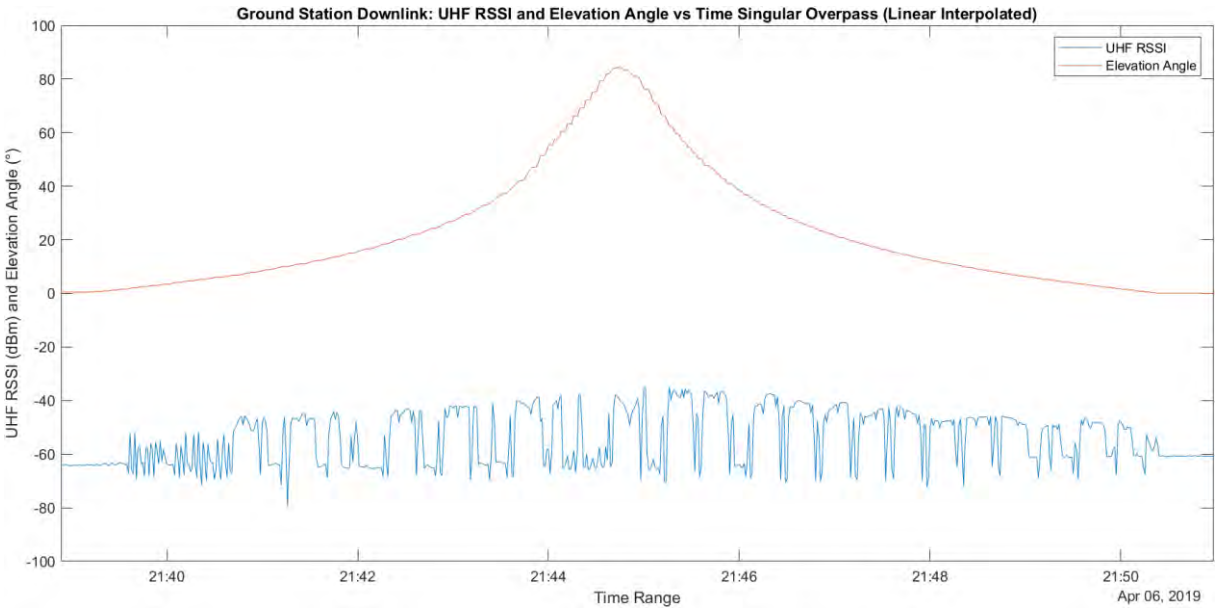

Figure 6.8: Ground Station Downlink UHF RSSI and Elevation Angle vs Time Single Overpass (Linear Interpolated)

As demonstrated in Figure 6.8, the trend of the RSSI approximately follows that of the satellite elevation; as the elevation peaks so does the RSSI, which imitates the same trend seen in Figure 6.7. Communication from ZACube-2 to the ground station can be seen from the elevated RSSI values with every successful instance of a downlink.

Comparing the overpass behaviour from Figure 6.7 in relation to Figure 6.5, the downlink signal power required vs elevation angle, the received signal power is significantly larger than the required downlink signal power by approximately 50 dB.

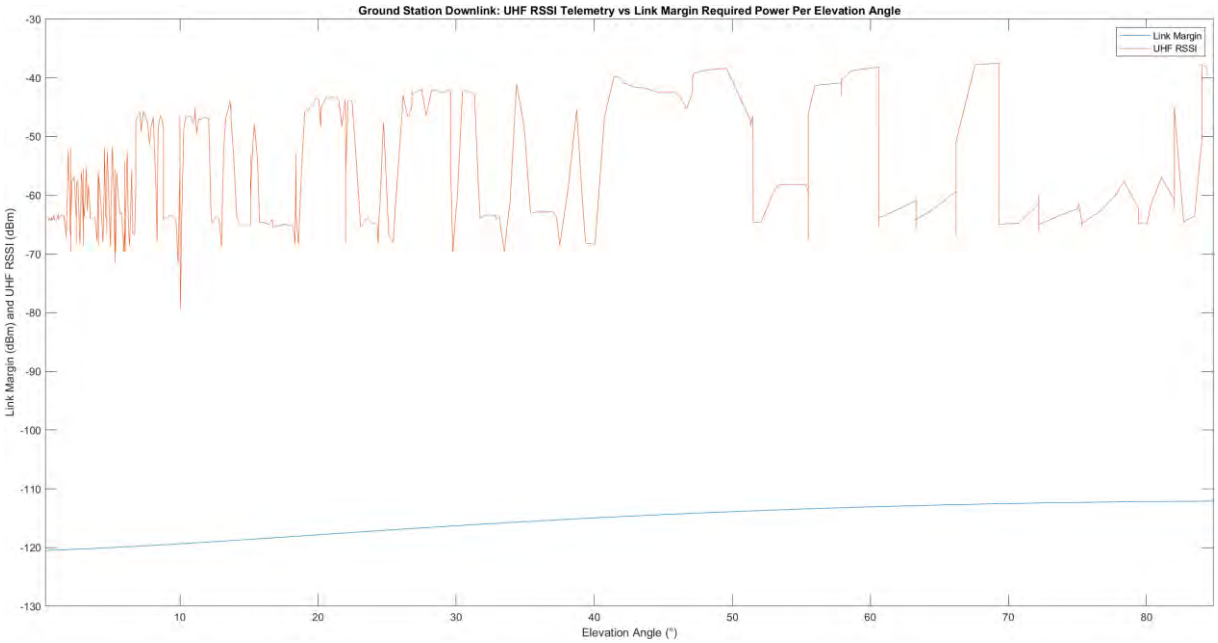

Figure 6.9: Ground Station Downlink UHF RSSI Telemetry vs Link Budget Required Power Per Elevation Angle

While, as demonstrated in the graph above, the RSSI values do follow the trend of the expected required signal power to satisfy the signal-to-noise ratio at each elevation angle, the disparity between these two graphs is large, but consistent. This is due to an artificial calibration offset in the MCS software, which can be re-calibrated for future missions.

6.3 Thermal Budget

With analysis of both the power and link budget, the third crucial budget in designing a space craft is the thermal design. As the various subsystem operate, there is a thermal output which, if left unmanaged, can lead to components onboard exceeding both their operational minimum and maximum thermal limits.

By managing the thermal output through a thermal budget, the chances of a subsystem or component exceeding its respective thermal operating limits, decreases. By comparing telemetry with simulation values, any discrepancies can be accounted for in future satellite design phases.

6.3.1 Battery

As previously mentioned, the battery unit that is used on ZACube-2 has an operating temperature range of -10°C to 50°C, with built in autonomous heaters that are designed to maximise the capacity of the battery by keeping the battery temperature above 0°C (at 5°C it switches off). There are two temperature sensors within the battery, providing an average readout of temperatures as well as having a contingent sensor in case the other sensor experiences a failure.

The graphs for the two respective temperature sensors can be seen below, with the upper and lower operating temperatures.

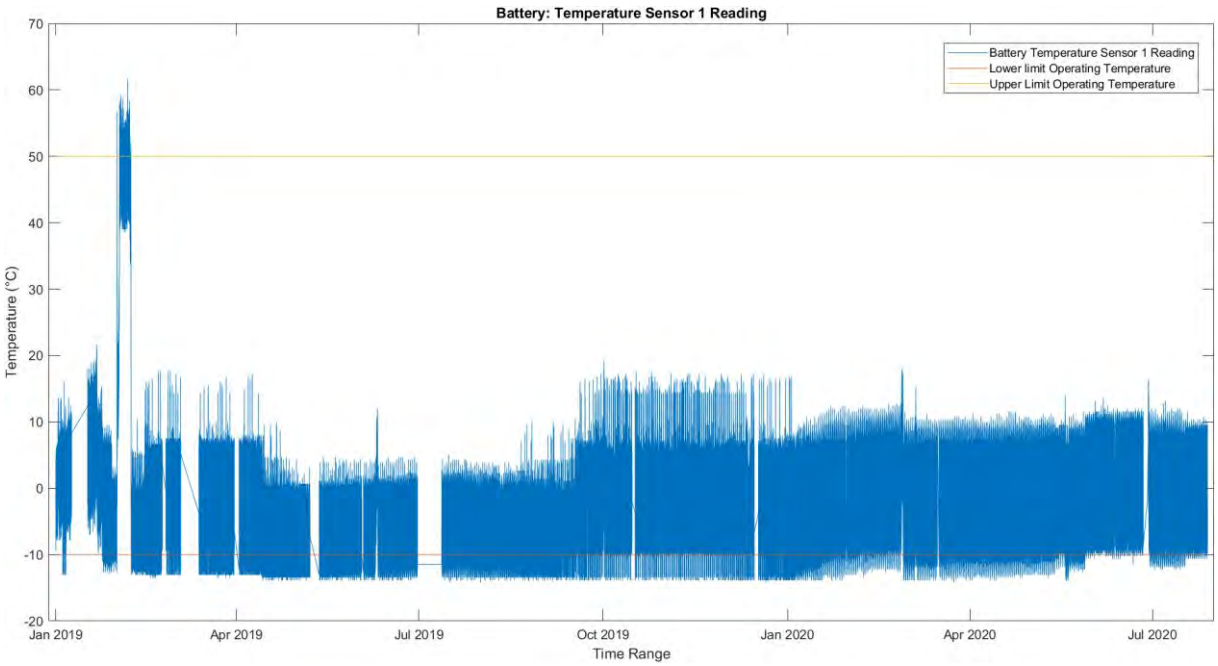

Figure 6.10: Battery Temperature Sensor 1 Reading

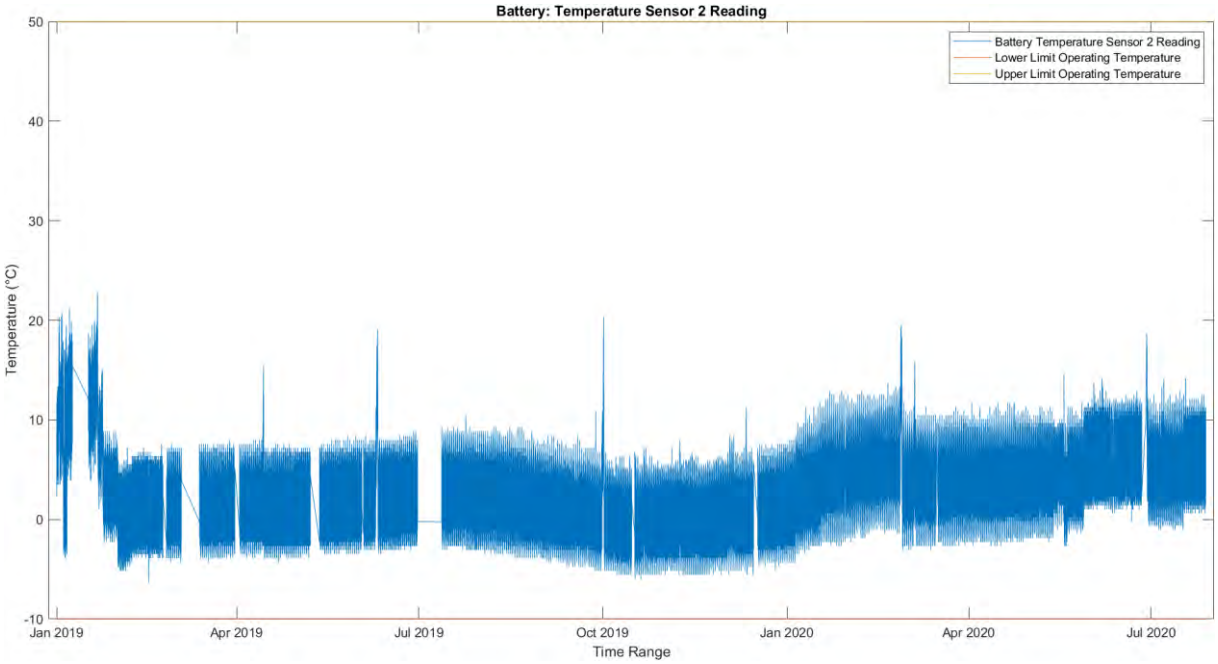

Figure 6.11: Battery Temperature Sensor 2 Reading

If these temperature readings, which have the same datetime interval, are plotted on the same graph, the difference between the two readings can be seen in Figure 6.12.

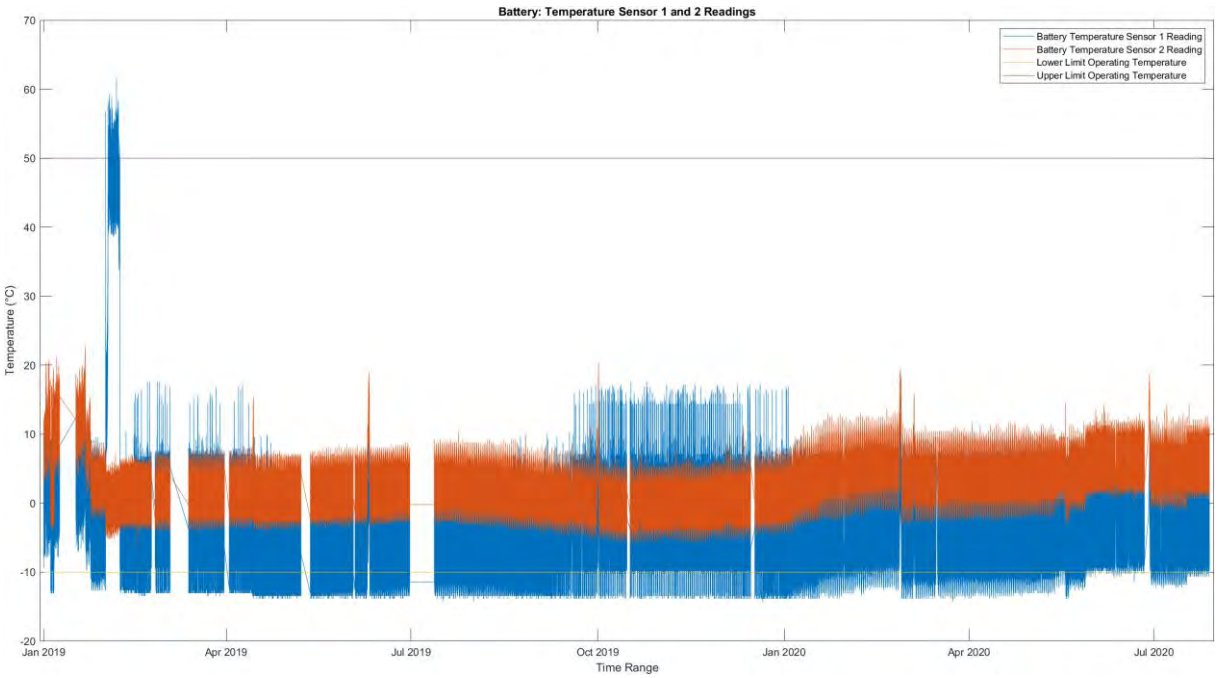

Figure 6.12: Battery Temperature Sensor 1 and 2 Readings

If the temperature values from the respective sensors are averaged and plotted against the same time-axis, the following graph is generated. From Figure 6.13 it can be seen that the battery operates well within the manufacturer's temperature limits, with only readings from sensor one exceeding both the upper and lower limits.

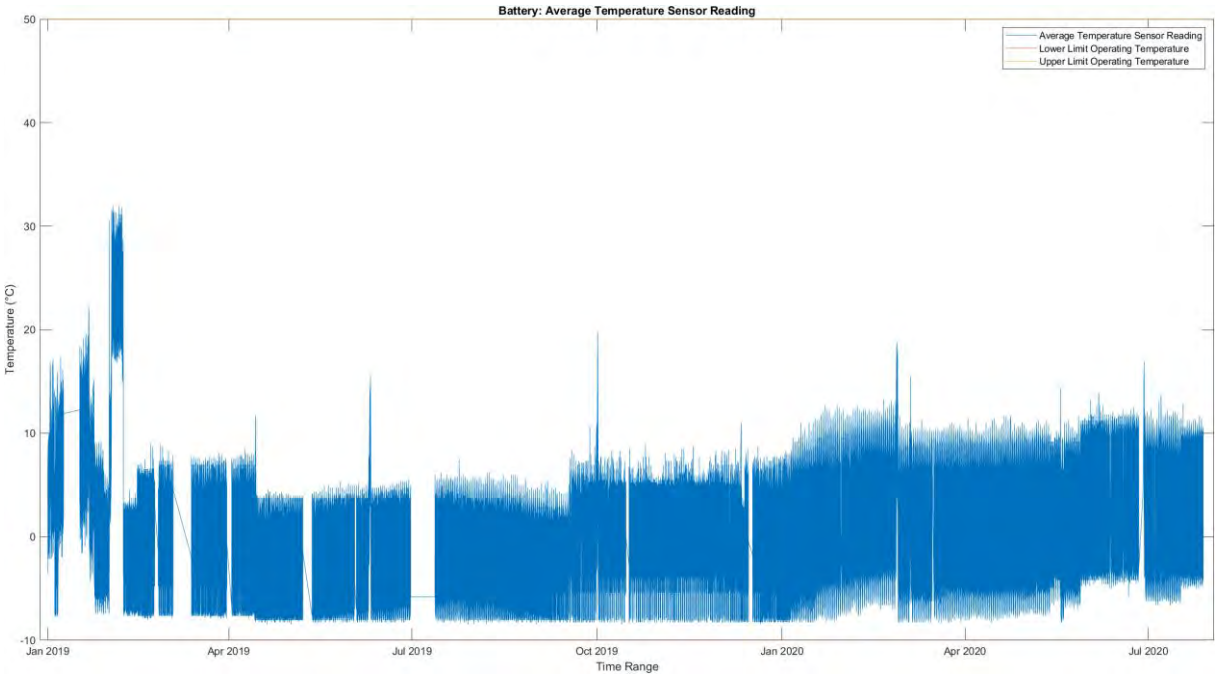

Figure 6.13: Battery Average Temperature Sensor Reading

6.3.2 K-Line Imager

This being one of the payloads aboard ZACube-2, it is vital that the temperature is monitored and likewise analysed to see if the temperature when the payload was operating, adheres to its lower and upper thermal limits. On the imager's processing unit there was a total of nine temperature sensors from various locations:

- CPU
- Top of the imager
- Bottom of the imager
- Module
- Accompaniment of five additional sensors

To observe a representative temperature variation of the payload, sample telemetry readings from the aforementioned sensors were logged from 29 October 2020 20:21:36 UTC to 29 October 2020 21:19:36 UTC. The telemetry that was logged, is presented in Figure 6.14.

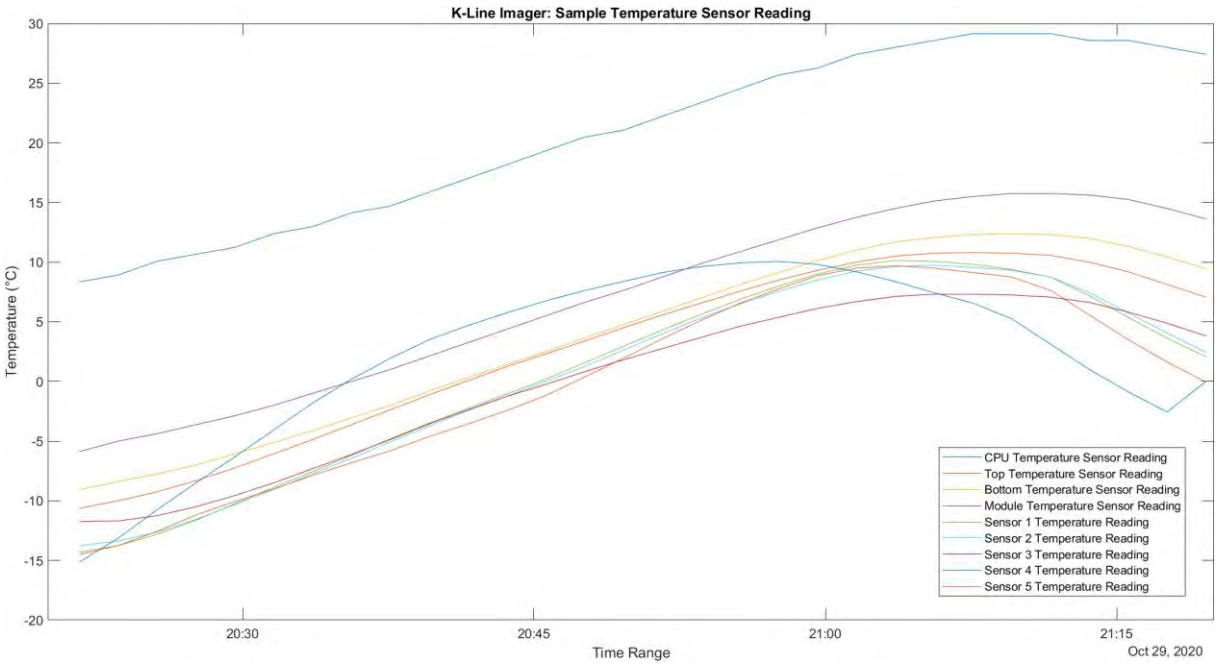

Figure 6.14: K-Line Imager Sample Temperature Sensor Readings

From the figure above, the CPU experiences the highest temperature of 29.15°C, with sensor 4 having the lowest temperature recorded of -15.125°C. However, these temperatures cannot be compared to the specifications as non were provided.

6.3.3 S-Band Transmitter (HSTXC)

The S-band transmitter is expected to yield elevated temperatures. Therefore, by looking at the recorded PA temperature telemetry, it can be determined whether additional thermal management techniques should be employed. The graph below is a depiction of the recorded PA temperatures in relation to the upper and lower limit operating temperatures, which are -25°C and +60°C, respectively

Figure 6.15: HSTXC PA Temperature Sensor Reading

Evidently, the temperature of the PA operates well within both the upper and lower operating temperature limits

6.3.4 UHF Transceiver (UTRXC)

The UTRXC is the primary method of downlink used for the satellite's tracking, telemetry and control in addition to being a contingent method of downlink payload data. Therefore, an inspection of the UTRXC's PA temperature telemetry needs to be investigated in regard to whether the operating temperature exceeds that of the designed operating temperature limits of between -25°C and +61°C. The graph below shows the PA temperature telemetry in relation to the operating temperature limits.

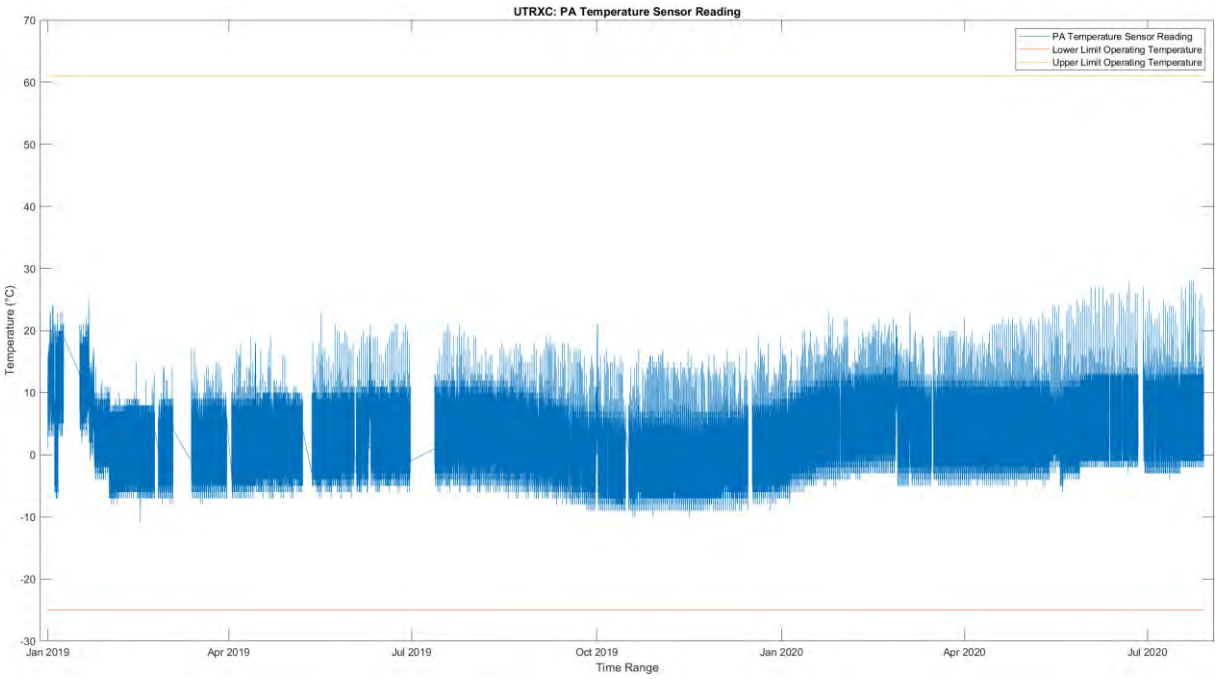

Figure 6.16: UTRXC PA Temperature Sensor Reading

What can be surmised from the figure above is that the thermal behaviour of the UTRXC PA is within the designed operating limits

With the UTRXC in frequent use and therefore using more power on average, being power efficient is of the utmost importance. This problem is addressed by the integration of an SMPS or a switched mode power supply which, unlike a linear mode power supply, is more efficient. The SMPS' operational thermal profile is shown in Figure 6.17.

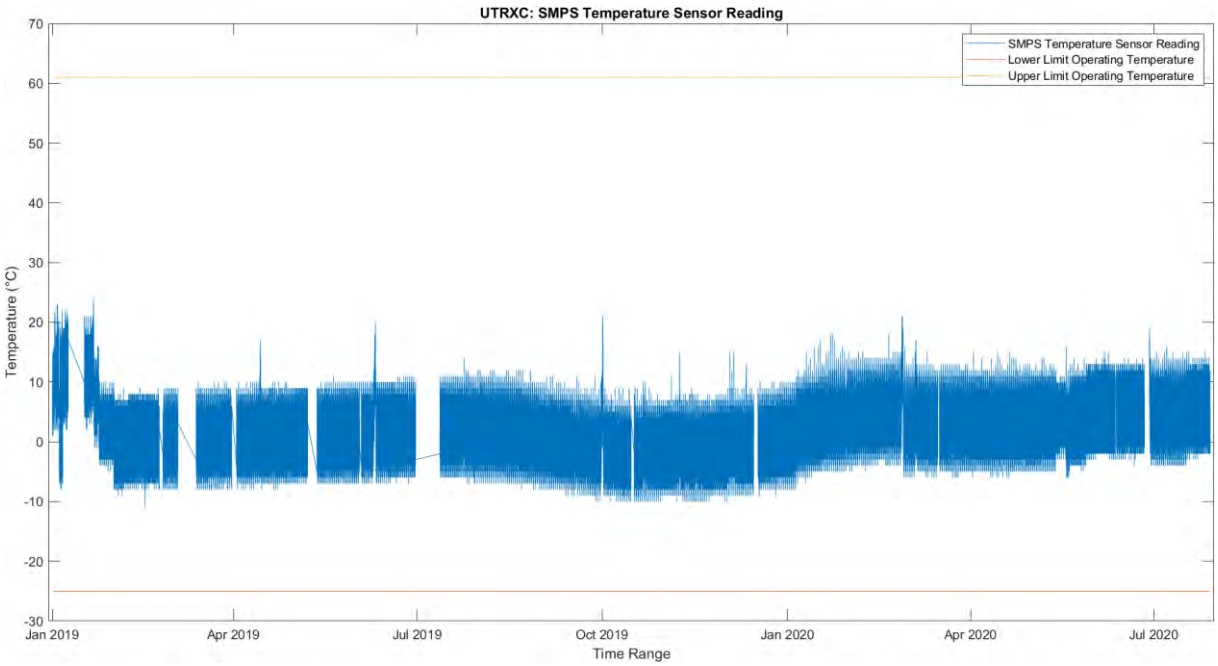

Figure 6.17: UTRXC SMPS Temperature Sensor Reading

As with the PA temperature results, the SMPS temperature stayed within the thermal operating limits as specified in the manufacturer's manual.

6.3.5 Thermal Control Design Hand Calculations

Whilst looking at the individual thermal performance of subsystems is beneficial for pinpointing temperatures that do not fall within a specific subsystem thermal operating limit, looking at a system overview is just as vital. With a system overview, a broader spectrum can be defined in terms of thermal performance. A rudimentary method of defining the thermal performance is by doing manual calculations that incorporate the multitude of factors that influence a satellite's thermal characteristic, be it in a sunlit minimum or eclipse maximum period. These factors are:

- Solar radiation
- Planetary albedo
- Planetary radiation
- Energy absorbed in the visible
- Energy emitted in the IR

These factors culminate into a formula that describes the satellite's thermal equilibrium when heat received equates to the heat emitted. This thermal equilibrium can also be represented by the formula below.

$$\sum\left(A_{surface}\sigma T^4\varepsilon\right) = \sum(A_{solar}J_s\alpha) + (\sum(A_{albedo}J_a\alpha) + \sum(A_{planetary}J_p\varepsilon)) + \sum Dissipated \quad \textbf{(Equation 6.1)}$$

Where:

- $A_{surface}$ is the total area of the spacecraft for which a 3U is being used therefore a total area of 0.151m^2 is for a standard 3U CubeSat in accordance with (CubeSat Design Specification Rev. 13, 2015).
- σ is the Stefan-Boltzmann constant which is equal to 5.67 x 10^{-8} W/(m^2.K^4)
- T^4 is the equilibrium temperature.
- ε is the infrared emittance factor.

- A_{solar} is the total area receiving solar radiation.
- J_s is the solar intensity radiation.
- α is the solar absorptance factor.
- A_{albedo} is the area which is receiving albedo radiation.
- J_a is the intensity of the albedo radiation.
- α is the solar absorptance factor.
- $A_{planetary}$ is the total area receiving planetary radiation.
- J_p is the planetary intensity radiation.
- ε is the infrared emittance factor.
- $Dissipated$ is the Internal heat dissipated by all the components.

A simplified way of showing the formula above is by making the equilibrium temperature, T^4, the subject of the formula resulting in:

$$T^4 = \frac{A_{planetary}J_p}{A_{surface}\sigma} + \frac{Dissipated}{A_{surface}\sigma\varepsilon} + \frac{A_{solar}J_s + A_{albedo}J_a}{A_{surface}\sigma}(\frac{\alpha}{\varepsilon}) \quad \textbf{(Equation 6.2)}$$

If the fraction of the orbit which is sunlit, denoted as *f*, is factored into the equation with the resulting albedo value equating to zero, the equilibrium temperature formula now modifies to the one below for a maximum eclipse value:

$$T^4 = \frac{A_{planetary}J_p}{A_{surface}\sigma} + \frac{Dissipated}{A_{surface}\sigma\varepsilon} + \frac{A_{solar}J_s}{A_{surface}\sigma}(\frac{\alpha}{\varepsilon})f \quad \textbf{(Equation 6.3)}$$

However, whilst using Fortescue, Swinerd and Stark (2011) based values, the albedo component is not included in the maximum eclipse formula. Gilmore (2002) includes these, resulting in a modified version of Equation 6.3:

$$T^4 = \frac{A_{planetary}J_p}{A_{surface}\sigma} + \frac{Dissipated}{A_{surface}\sigma\varepsilon} + \frac{A_{solar}J_s + A_{albedo}J_a}{A_{surface}\sigma}(\frac{\alpha}{\varepsilon})f \quad \textbf{(Equation 6.4)}$$

6.3.5.1 Thermal Calculation Based on Fortescue, Swinerd and Stark (2011)

With the terms known, the respective values for these terms need to be calculated such that the thermal equilibrium under varying conditions can be determined. These values can be easily calculated using the formulas described by Fortescue, Swinerd and Stark (2011), which can be seen as theoretical values as it is equation based. The subsequent calculated values are summarised in Table 6.18.

Table 6.18: Thermal Equilibrium Values Based on Fortescue, Swinerd and Stark (2011)

Term	Symbol	Value
Total area planetary radiation	$A_{planetary}$	0.03275
Planetary intensity radiation	J_p	203.7622
Total area of the satellite	$A_{surface}$	0.151
Stefan-Boltzmann constant	σ	$5.67 \text{ x } 10^{-8}$
Internal heat dissipated	$Dissipated$	Varies with each power profile
Infrared emittance factor	ε	0.82
Total area of solar radiation	A_{solar}	0.03275
Solar intensity radiation	J_s	1371.12
Area of albedo radiation	A_{albedo}	0.03275
Albedo intensity radiation	J_a	Varies with beta angle and albedo
Solar absorptance factor	α	0.75
Sunlit portion of orbit	f	0.6221

From the table, both the albedo intensity radiation, J_a, and the internal heat dissipated have multiple values to allow for a more comprehensive understanding of the expected thermal behaviour prior to simulation. The tables below summarise the aforementioned values at an altitude of 500km.

Table 6.19: Thermal Equilibrium Albedo Intensity Radiation J_a Values

Beta Angle (°)	Visibility Factor	Albedo Intensity @ 0.31	Albedo Intensity @ 0.39
0	1,5	637,515	802,035
30	0,9	382,509	481,221
60	0,6	255,006	320,814
70	0,5	212,505	267,345
80	0,298	126,653	159,3376
90	0,15	63,7515	80,2035
100	0,04	17,0004	21,3876
110	0,004	1,70004	2,13876

From the table above, as the beta angle increases, the albedo intensity decreases, which is logical as the satellite is further away from the sun vector.

To ensure that the results include both ends of the thermal spectrum, the minimum and maximum internal heat dissipated by the various subsystems onboard ZACube-2 need to be calculated. During the process of calculating the power profile values the instantaneous power values are computed. Using these values gives a rough understanding of the thermal profile that ZACube-2 would experience. The results of this endeavour can be seen in the table below.

Table 6.20: Thermal Equilibrium Internal Heat Dissipated by Components

	Power Profile	Heat Dissipated (W)
Minimum Heat Dissipated	Safe eclipse	1.753
Maximum Heat Dissipated	Payload sun	16.964

With the beta angles known in addition to the minimum and maximum internal heat dissipated by the component, substitution of these values can be done by developing a scenario for the various temperatures that the satellite will experience. The results of this can be seen in the following tables.

Table 6.21: Thermal Equilibrium of ZACube-2 in No Eclipse at Minimum Orbital Average Albedo

	Temperature (°C)	Beta Angle (°)
Maximum Heat Dissipation	41,8	0
	38,6	30
	33,8	60
	32,5	70
	29,9	80
	27,9	90
Minimum Heat Dissipation	26,4	0
	17,7	30
	13,1	60
	11,5	70
	8,2	80
	5,7	90

Substituting the minimum orbital average albedo (0.31) with the maximum orbital average albedo (0.39), results in the table below.

Table 6.22: Thermal Equilibrium of ZACube-2 in No Eclipse at Maximum Orbital Average Albedo

	Temperature (°C)	Beta Angle (°)
Maximum Heat Dissipation	49,2	0
	40,4	30
	35,8	60
	34,2	70
	30,9	80
	28,4	90

Minimum Heat Dissipation	31,6	0
	21,2	30
	15,5	60
	13,6	70
	9,5	80
	6,3	90

The fraction in which the satellite is in sunlit condition, which for ZACube-2 was calculated as 62,2% using the orbital period parameters that were previously calculated using the telemetry, is now substituted and the formula modified appropriately. The results from the application of this formula can be seen in the table below. It should be noted that in this form of the equation that both the area of albedo radiation (A_{albedo}) and albedo intensity radiation (J_a) are not considered and, as such, the beta angle has no influence. This yields a singular value for the minimum and maximum heat dissipation, respectively.

Table 6.23: Thermal Equilibrium of ZACube-2 in Maximum Eclipse

	Temperature (°C)
Maximum Heat Dissipation	7,2
Minimum Heat Dissipation	-21,4

From the tables above, the minimum temperature calculated for ZACube-2 is -20.4°C. This is when the satellite is in maximum eclipse and operating in a safe eclipse power profile. The maximum temperature is 50.2°C, experienced in no eclipse at a maximum orbital albedo average when the satellite was operating in the payload sun power profile.

6.3.5.2 Thermal Calculations Based on Gilmore (2002)

As mentioned earlier, the values that were calculated and presented in *Table 6.18: Thermal Equilibrium Values* were done using methods described in Fortescue, Swinerd and Stark (2011), which were theoretically based, taking into consideration only the altitude at which the spacecraft.

However, the values described in Gilmore (2002) are telemetry based and more widely used in industry. In addition to being altitude dependent, the values are inclination dependent as well. Therefore, the following work incorporates values mentioned in Gilmore (2002), with an addition of specific tables containing data that is used in the calculation of both “hot” and “cold” situations where the satellite is in sunlight and in eclipse conditions, respectively.

Table 6.24: Thermal Equilibrium Values Based on Gilmore (2002)

Term	Symbol	Value
Total area planetary radiation	$A_{planetary}$	0.03275
Planetary intensity radiation	J_p	232
Total area of the satellite	$A_{surface}$	0.151
Stefan-Boltzmann constant	σ	5.67×10^{-8}
Internal heat dissipated	$Dissipated$	Same as the previous calculation
Infrared emittance factor	ε	0.82
Total area of solar radiation	A_{solar}	0.03275
Solar intensity radiation	J_s (Cold case)	1332
	J_s (Hot case)	1414
Area of albedo radiation	A_{albedo}	0.03275
Albedo intensity radiation	J_a	Varies with beta angle and albedo
Solar absorptance factor	α	0.75
Sunlit portion of orbit	f	0.6221

The albedo intensity radiation, J_a, and the internal heat dissipated have multiple values as to allow for a more comprehensive understanding of the expected thermal behaviour. In addition, the solar intensity radiation, J_s, has two values: one for a “cold” case and a “hot” case.

At a certain inclination angle, there is both an albedo and IR surface sensitivity. For ZACube-2 having an inclination angle of 97.4°, this results in a surface sensitivity value of 0.23 for a hot case and 0.20 for a cold case. However, at various beta angles, there is an orbit-average albedo correction value that needs to be accounted for, resulting in a corrected orbital average albedo. The table below shows this process of incorporating the correction factor. It should be noted that in the table “albedo cold” and “albedo hot” refer to the cold and hot scenarios, respectively.

Table 6.25: Corrected Orbital Average Albedo

Beta Angle (°)	Correction Value	Albedo Hot	Albedo Cold	Corrected Albedo Hot	Corrected Albedo Cold
0	0,04	0,23	0,2	0,27	0,24
30	0,06	0,23	0,2	0,29	0,26
40	0,07	0,23	0,2	0,3	0,27
50	0,09	0,23	0,2	0,32	0,29
60	0,12	0,23	0,2	0,35	0,32
70	0,16	0,23	0,2	0,39	0,36
80	0,22	0,23	0,2	0,45	0,42
90	0,31	0,23	0,2	0,54	0,51

With the new orbital average albedo values, the subsequent albedo intensity radiation (J_a) can be calculated. The table below is the resultant showing the new albedo intensity radiation (J_a) values.

Table 6.26: Corrected Thermal Equilibrium Albedo Intensity Radiation Values the Hot and Cold Scenario's

Beta Angle (°)	Visibility Factor	Albedo Intensity (Cold Scenario)	Albedo Intensity (Hot Scenario)
0	1,5	479.520	509.040
30	0,9	311.688	330.876
60	0,6	255.744	271.488
70	0,5	239.760	254.520
80	0,298	166.713	176.976
90	0,15	101.898	108.171

Substituting the new values into the respective terms, a new range of values is calculated for each power dissipation in a hot and cold case scenario, or when the solar intensity radiation is either at a maximum or minimum, which is 1411 W/m^2 and 1332 W/m^2, respectively. This is summarised in Table 6.27.

Table 6.27: Thermal Equilibrium of ZACube-2 Hot Scenario in No Eclipse

	Temperature (°C)	Beta Angle (°)
Maximum Heat Dissipation	43,329	0
	38,294	30
	36,560	60
	36,059	70
	33,739	80
	31,636	90
Minimum Heat Dissipation	24,652	0
	18,567	30
	16,452	60
	15,839	70
	12,987	80
	10,383	90

With the hot scenario values known, the cold scenario can now also be calculated, as summarised in Table 6.28.

Table 6.28: Thermal Equilibrium of ZACube-2 Cold Scenario in No Eclipse

	Temperature (°C)	Beta Angle (°)
Maximum Heat Dissipation	40,206	0
	35,322	30
	33,641	60
	33,156	70
	30,908	80
	28,871	90
Minimum Heat Dissipation	23,669	0

	17,889	30
	15,883	60
	15,303	70
	12,603	80
	10,142	90

The last part of replicating the first method of calculating the thermal equilibrium is to calculate the temperature that the spacecraft experiences at the different power dissipation values, which were only two values in the previous methodology. The resultant for the hot scenario calculation is given in Table 6.29.

Table 6.29: Thermal Equilibrium of ZACube-2 Hot Scenario in Maximum Eclipse

	Temperature (°C)
Maximum Heat Dissipation	9.488
Minimum Heat Dissipation	-18,353

In addition to the hot scenario for the maximum eclipse, the cold scenario in the maximum eclipse can be calculated with the result given in the table below.

Table 6.30: Thermal Equilibrium of ZACube-2 Cold Scenario in Maximum Eclipse

	Temperature (°C)
Maximum Heat Dissipation	7,491
Minimum Heat Dissipation	-21,094

With all the respective values calculated, graphs for each thermal parameter can be generated to compare how these two techniques - Fortescue (denoted by the blue line) and Gilmore (denoted by the red line) - differ from each other. The graph below shows a hot scenario for ZACube-2 in no eclipse when the satellite is undergoing maximum heat dissipation from

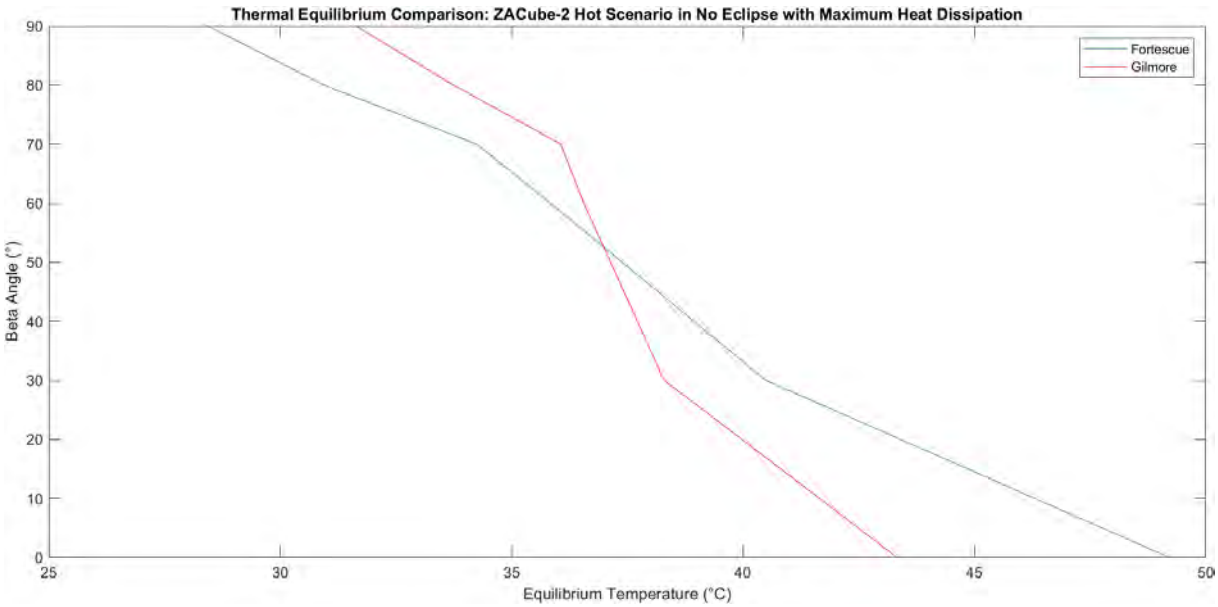

Figure 6.18: Thermal Equilibrium Comparison of ZACube-2 Hot Scenario of No Eclipse with Maximum Heat Dissipation

The graph below shows a hot scenario for ZACube-2 in no eclipse when the satellite is undergoing minimum heat dissipation.

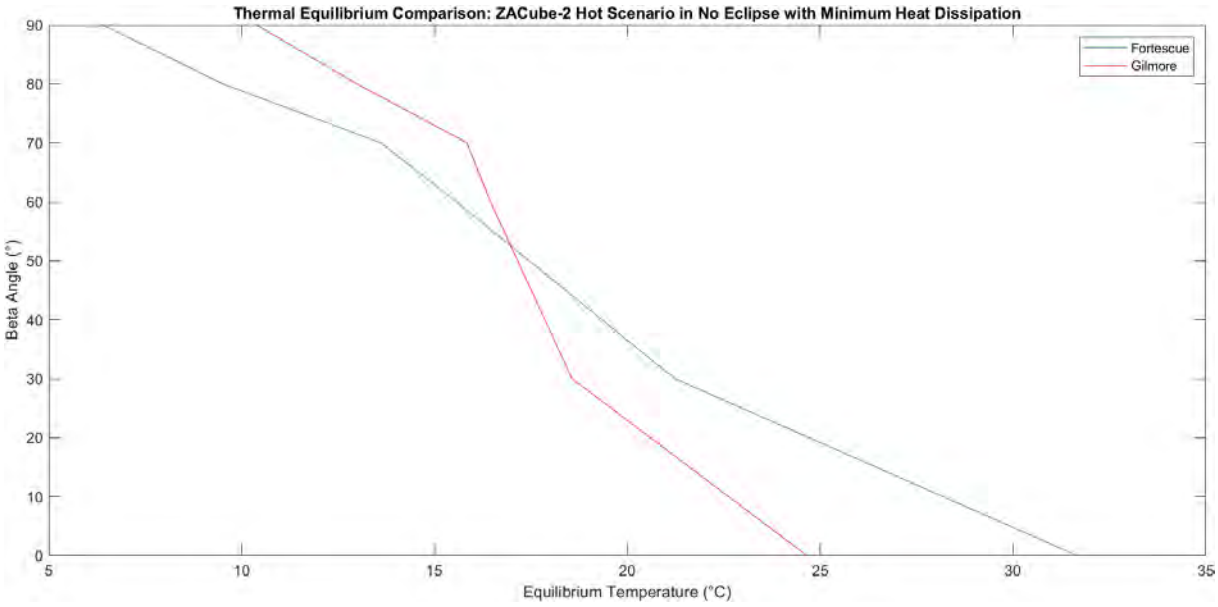

Figure 6.19: Thermal Equilibrium Comparison: of ZACube-2 Hot Scenario in No Eclipse with Minimum Heat Dissipation

The graph below shows a cold scenario for ZACube-2 in no eclipse when the satellite is undergoing maximum heat dissipation.

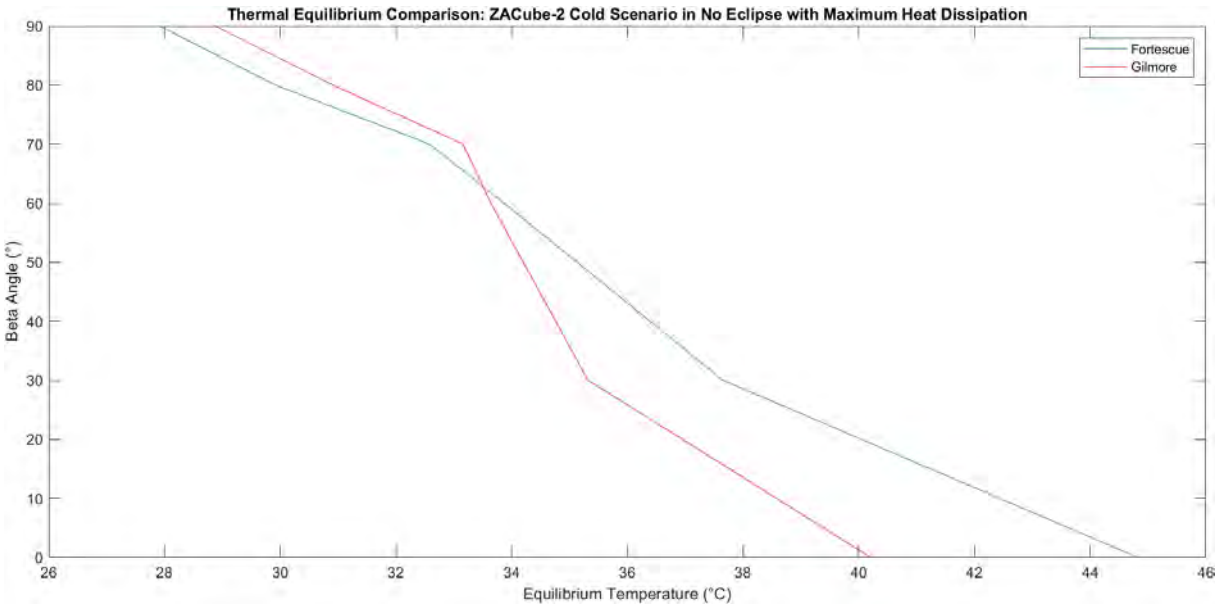

Figure 6.20: Thermal Equilibrium Comparison of ZACube-2 Cold Scenario of No Eclipse with Maximum Heat Dissipation

The graph below shows a cold scenario for ZACube-2 in no eclipse when the satellite is undergoing minimum heat dissipation.

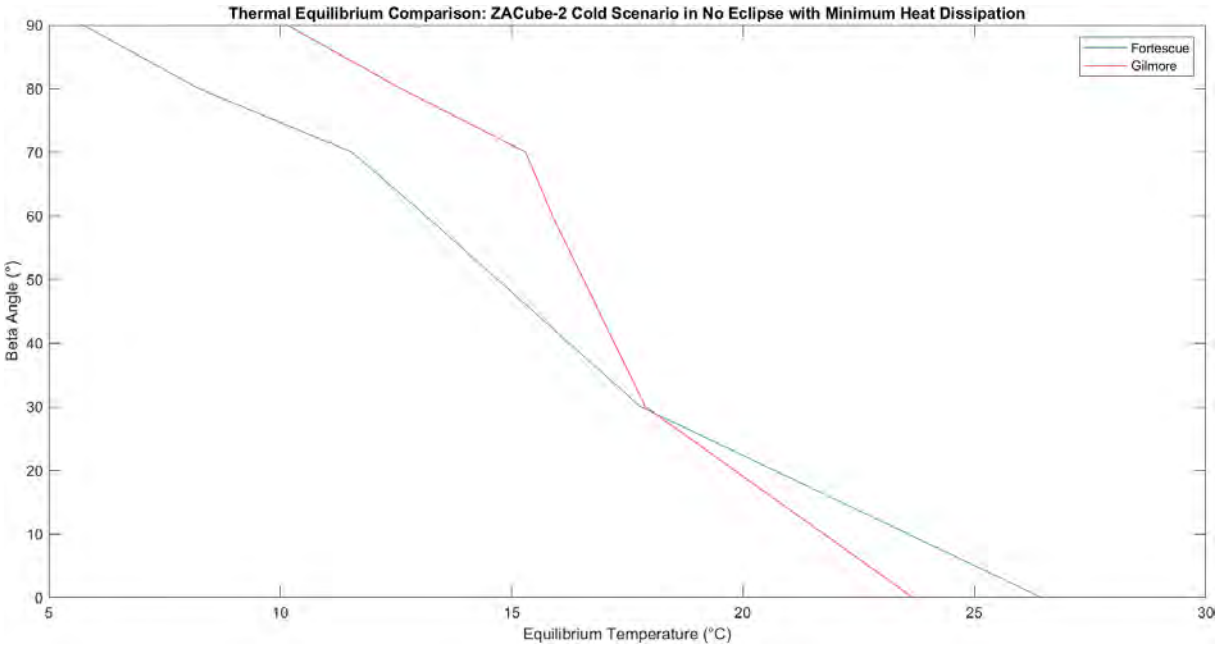

Figure 6.21: Thermal Equilibrium Comparison of ZACube-2 Cold Scenario in No Eclipse with Minimum Heat Dissipation

From the graphs above, there is a visual difference between the two methods. There is a clear distinction as to which method is conservative in relation to the thermal telemetry obtained,

namely the method that Gilmore (2001) describes. Additionally, from the graphs, there are points where the values calculated from the two methods intersect at various beta angles.

A similar process was repeated when ZACube-2 was in maximum eclipse with the only difference being that there are no varying temperatures as the beta angle changes. Instead, there is a constant value for each power dissipated. Each hot and cold scenario graph contains two data points per method, where one data point is the value calculated at maximum heat dissipation and the other at minimum heat dissipation.

The graph below shows a hot scenario for ZACube-2 in a maximum eclipse when the satellite is undergoing both maximum and minimum heat dissipation.

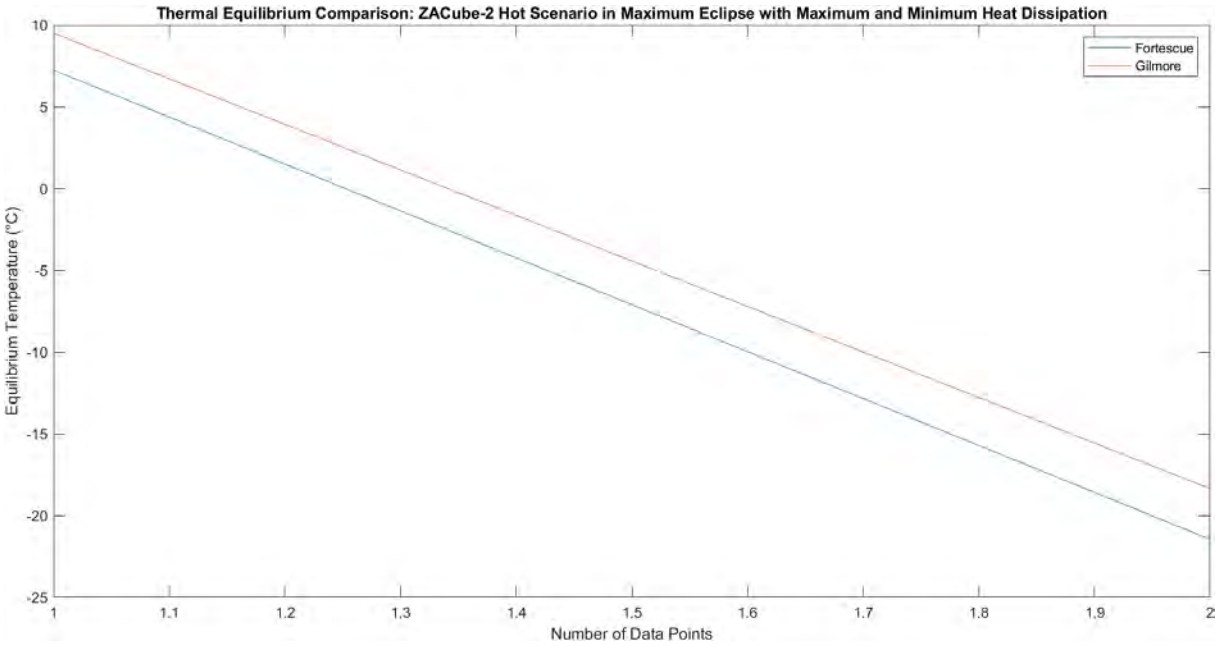

Figure 6.22: Thermal Equilibrium Comparison of ZACube-2 Hot Scenario in Maximum Eclipse with Maximum and Minimum Heat Dissipation

The graph below shows a cold scenario for ZACube-2 in a maximum eclipse when the satellite is undergoing both maximum and minimum heat dissipation.

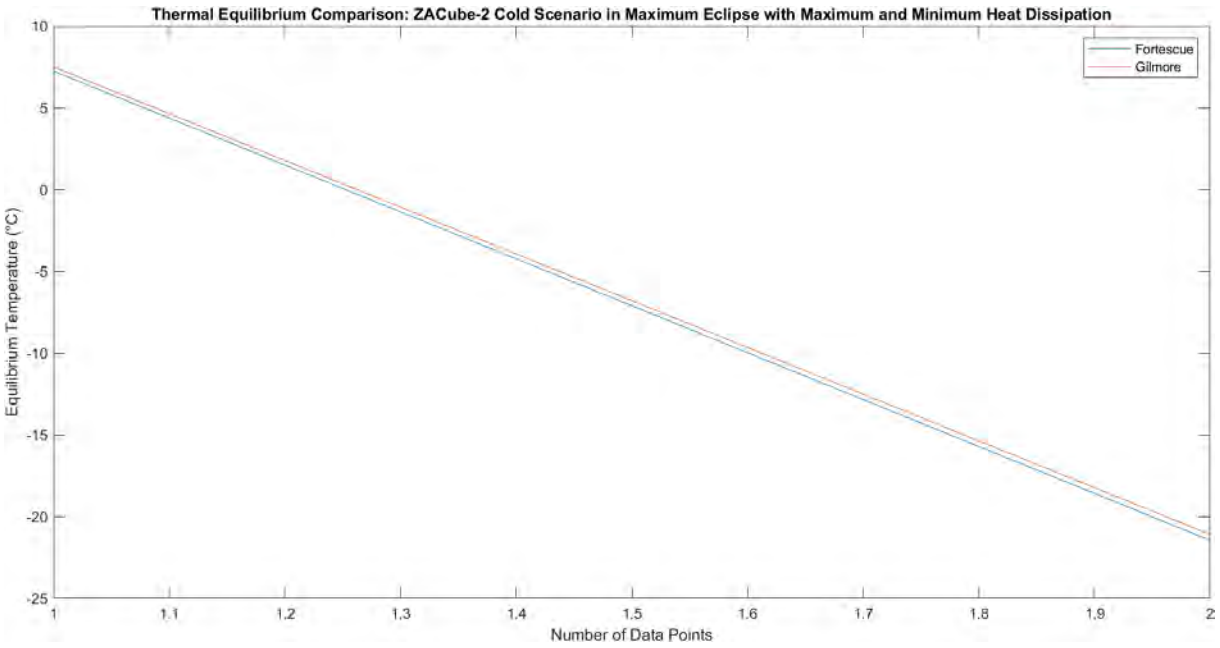

Figure 6.23: Thermal Equilibrium Comparison of ZACube-2 Cold Scenario in Maximum Eclipse with Maximum and Minimum Heat Dissipation

From the graphs, between the two methods, there is very little variance between the results generated with there being a greater difference between Fortescue's and Gilmore's method in relation to when the satellite is in a hot scenario. In the case of the cold scenario, the results generated are almost identical with a maximum difference of 2°C occurring in a hot scenario when the satellite is in maximum eclipse.

CHAPTER SEVEN
CONCLUSION AND RECOMMENDATIONS

This thesis presents an analysis of the ZACube-2 mission operations, in particular on-orbit operations, and analysed data obtained from the analyses to compare against the various designed resource budgets. The importance of analysing mission operations is to validate, objectively, the design calculations done by the in-house engineering team and to determine to what degree the resource budgets correspond to the actual telemetry data.

Using the output of this assessment, design improvements can be recommended for incorporation in the design cycle of future missions. This will translate into improving the satellite regarding how effective and efficient mission operations are executed and improving the satellite design as well as expertise of the engineering team.

7.1 Power Budget

All six of the power profile values, apart from the payload eclipse as the imager was not operated in eclipse, were lower than the values calculated in the power budget. This suggests that the power budget was conservative.

As for the conservative metric, on the lowest end of the spectrum, the safe eclipse telemetry-based value was only 1.7% lower, whist on the highest end of the spectrum, the payload sun telemetry-based value was 53.8% lower than the power budget value. The reason there was such a drastic difference in power level is that there was no common interval at which the telemetry data was logged, causing missing corresponding values across the respective subsystems.

The orbital period including the time in which the satellite was in sunlit minimum and eclipse maximum phase, was well within the range of the values assumed in the power budget. The largest deviation was 156 seconds, which was due to the 3-minute interval at which the data was logged.

The minimum power generated by the solar array proved to be somewhat problematic, as even though two separate telemetry-based samples were calculated, each sample not only gave a power value smaller than the one determined in the power budget, but in addition, the two samples did not output the same power value.

This dissimilarity was accredited to the varying solar declination that is experienced throughout the year, as the samples was calculated on 15 March 2019 UTC and 17 February 2020 UTC, respectively. Furthermore, the difference could be a trait of the solar cycle progression, as the range of telemetry value that was used in the calculation occurred at solar minimum, i.e., the transition phase between solar cycle twenty-four and solar cycle twenty-five.

With both telemetry sample calculations conveying that not enough power was being generated to sustain the requirements of the satellite, there should be substantial discharge from the battery. However, battery discharge was minimal at 8.42%, conveying that either the method in which the power values were calculated, is incorrect, or the problem lies within the telemetry values.

7.2 Link Budget

Knowing that the UTRXC makes successful contact with the ground station during an entire pass for elevations above 3 degrees (from first-hand experience of operating the satellite), it was a matter of verifying how well the UTRXC link works. Using the cumulative probability function, the receive RSSI of ZACube-2 UTRXC was plotted and converted to a power level. That showed that the range of the values within the CDF plot was within the stipulated values in the user manual, therefore, concluding that signals were above the receive level threshold for entire overpasses.

An additional method of gauging the link budget was using values gained from comparing the ground station downlink UHF RSSI in relation to the link margin as applied in the link budget. It was found that the RSSI values have an inherent offset due to the values recorded by the mission control software (MCS) not being absolute, but relative to the ADC's full scale. To standardize to an absolute value, calibration of the ground station's UHF receiver with a signal generator, both at the receiver and along the downlink path to the antenna, would be required.

7.3 Thermal Budget

Analysis of ZACube-2's thermal performance was done using two methods, which are the analysis of available thermal telemetry from various subsystems and the hand calculation of the thermal range using two techniques. From the telemetry, the largest thermal range experienced by a single subsystem was the K-line imager of 44.2°C, with a maximum of 29.1°C and a minimum of -15.1°C, respectively.

The HSTXC had the maximum overall temperature from any subsystem at 37.2°C, with the K-line imager having the lowest temperature logged from any subsystem at -15.1°C. All the subsystems performed well within the thermal limits specified by the manufacturer, implying that passive thermal management techniques employed on ZACube-2 worked as desired and leaving thermal headroom. This allows for operating subsystems for longer, or stacking the subsystems differently, if needed.

Telemetry-based thermal values were compared to the two methods; the first method described by Fortescue (2011) and the second method described by Gilmore (2002). The first method had the largest thermal range of 80.6°C, with the second method having a thermal range of 64.4°C. This directly translated to the method employed by Gilmore (2002) having a difference in maximum and minimum values of 6.098°C and 5.969°C, respectively whereas Fortescue (2011) method had differences in the maximum and minimum temperature values of 11.981°C and 6.327°C, respectfully.

These values give an indication of the average and/or expected temperature that the satellite should experience prior to a computer simulation. Additionally, the method described by Gilmore (2002) should be used as an initial thermal calculation prior computer simulation as it employs values that are based on actual telemetry. This makes it more aligned to real-world values than the method employed by Fortescue (2011), which is purely theoretically based.

7.4 Attitude Determination Control System

The ADCS operated as expected, but problems were encountered with the ADCS, such as the calibration of the sun sensors where said sensors interpreted the reflection from the antenna as a second sun. This caused navigation inaccuracy as seen in ADCS raw telemetry figures from 13 May 2020 UTC to 18 May 2020 UTC.

By adjusting the exposure threshold of the fine sun sensor, the reflections were not detected as sun reflections and the output of the data from the fine sun sensors were added to the EKF estimator, giving a more accurate indication of ZACube-2 attitude angles and angular in relation to the motion of the satellite.

7.5 Battery

Maximum depth of discharge (DoD) is prescribed as 20% in the power budget; however, it was found that the maximum discharge was only 8.4%. With a low depth of discharge experienced,

this means that some subsystems can be utilised more for extended periods for the various power profiles.

7.6 Orbital Decay

The orbital decay was compared using three methods with data gained from using TLEs, and two of which were simulation based. The first method was using the average apsis of the apoapsis and periapsis, and the second approach was to use the orbital period.

Regarding the simulations, the first simulation was performed using STELA, designed by CNES, in which the orbital decays of the apoapsis and the periapsis were simulated at both a mean constant and a variable solar activity. A mean constant for the solar activity gave an orbital lifetime of 3.08 years, satisfying the specified re-entry altitude condition, whilst the variable solar activity gave an orbital lifetime of 8.67 years, also satisfying the specified re-entry altitude condition.

The latter solar activity option was compared to TLE's of the same period as to evaluate the discrepancy between the simulated and actual apoapsis and periapsis. This comparison yielded that the simulated vs actual parameters were similar, with a difference of 10km to 12km for both the apoapsis and periapsis.

This means that the simulated orbital decay is consistent to the actual orbital decay.

The second simulation of the orbital period was done in STK using the same period as the telemetry data. The output of the simulation was compared to the telemetry-based period data and a difference of 3.6 seconds was found. This means that the telemetry-based period is consistent to what was simulated.

7.7 System Performance and the Effects of Space Weather on Subsystems

During the analysis period, there were many occasions in which multiple telemetry channels recorded no data over the same time period, or where there were outliers present in the data sets, or the recording of data was sporadic in nature. These instances were cross-referenced with documented space weather events, such as geomagnetic events. While there were several events with a maximum Kp index value of 4- occurring, none of these have enough potency to register as a "minor storm" as described in Table 5.17. Therefore, these events are mutually exclusive, leading to the possibility that the root cause of the missing instances of telemetry data are internal in nature, rather than external.

As with the comparison of space weather in relation to the lapses in telemetry data logging, there was no discernible space weather events that influenced subsystem performance to a point where a noticeable trend occurred or should have occurred.

This statement holds true regarding the ADCS attitude and angular rates for the X-axis and Y-axis. During the period where the aforementioned telemetry channels recorded values, there were problems where abnormal behaviour was experienced, such as attitude angle for the Y-axis varying from +180° to -180°, when a geomagnetic storm with a Kp index of 6.33 occurred.

A Kp index storm of this magnitude registers as a “moderate” storm and can cause potential changes in orbital drag and/or requiring of restorative actions to the satellite’s orientation. An investigation was done to see if any effects were experienced in terms of orbital drag by looking at both the orbital period and average apsis. There was no evidence of the storm influencing either the orbital period or the average apsis.

A similar investigation was done with the aforementioned telemetry channels, and even these two events appeared within the same time period and could be seen as mutually inclusive, these two events are uncorrelated as the moderate geomagnetic storm occurred during the period in which the said telemetry channels started behaving unusually. Therefore, this rules out the possibility of space weather being the cause for the abnormal performance.

7.8 Recommendations for Future Work

While objectively it can be said that ZACube-2 operates within its design envelop as the system did produce enough power to still be operational throughout, communicated with the ground station and never experienced any difficulties that are associated with poor thermal management, there were points of interest that could be implemented that would make it easier for future telemetry analysis on future missions.

- Recalculation of solar array results, as the information relayed by the telemetry does not accurately depict the actual performance.
- Examination of a broader spectrum of space weather events that could possibly cause the same events of no telemetry or outlier data to be present in multiple telemetry channels.
- Synchronizing the interval at which telemetry across multiple channels is logged and increasing the resolution of the telemetry data.
- Pre-set exposure threshold to account for antenna reflections or consider either relocating the ADCS to mitigate issues related to reflection from the sun.

- Complete a computer simulation of ZACube-2's thermal performance to confirm that all thermal parameters are met and to confirm that the method described by Gilmore (2002) is a good basis prior to simulation.
- RSSI calibration of the ground station UHF receiver with a signal generator and along the downlink path to the antenna.

BIBLIOGRAPHY

2011. *NOAA Space Weather Scales*. [ebook] Boulder, Colorado: National Oceanic and Atmospheric Administration, p.1. Available at: <https://www.swpc.noaa.gov/sites/default/files/images/NOAAscales.pdf> [Accessed 15 December 2021].

2015. *Cubesat Design Specification* 13th ed. [ebook] California: California Polytechnic State University, p.All. Available at: <https://static1.squarespace.com/static/5418c831e4b0fa4ecac1bacd/t/56e9b62337013b6c063a655a/1458157095454/cds_rev13_final2.pdf> [Accessed 24 August 2020].

2018. *State Of The Art Small Spacecraft Technology*. [ebook] California: National Aeronautics and Space Administration, p.All. Available at: <https://www.nasa.gov/sites/default/files/atoms/files/soa2018_final_doc-6.pdf> [Accessed 16 September 2020].

2019. *Command & Data Handling*. [ebook] Bern, Switzerland: RUAG, p.All. Available at: <https://www.ruag.com/system/files/media_document/2019-06/Command_Data_Handling_May%202019.indd_.pdf> [Accessed 5 October 2020].

2020. *Cubesat Design Specification*. 14th ed. [ebook] California: California Polytechnic State University, p.All. Available at: <https://static1.squarespace.com/static/5418c831e4b0fa4ecac1bacd/t/5f24997b6deea10cc52bb016/1596234122437/CDS+REV14+2020-07-31+DRAFT.pdf> [Accessed 24 August 2020].

2020. *IADC Space Debris Mitigation Guidelines*. 2nd ed. [ebook] Inter-Agency Space Debris Coordination Committee, pp.5-14. Available at: <https://orbitaldebris.jsc.nasa.gov/library/iadc-space-debris-guidelines-revision-2.pdf> [Accessed 29 November 2021].

2021. *AAC_DataSheet_Optimus*. [ebook] AAC Clyde Space, p.2. Available at: <https://www.aac-clyde.space/wp-content/uploads/2021/10/AAC_DataSheet_Optimus.pdf> [Accessed 6 December 2021].

Addaim, A., Kherras, A. and Bachir, E., 2010. Design of Low-cost Telecommunications CubeSat-class Spacecraft. *Aerospace Technologies Advancements*, [online] p.All. Available at: <https://www.intechopen.com/books/aerospace-technologies-advancements/design-of-low-cost-telecommunications-cubesat-class-spacecraft> [Accessed 12 September 2020].

AllAboutCircuits. 2021. *Understanding Reflections and Standing Waves in RF Circuit Design*. [online] Available at: <https://www.allaboutcircuits.com/textbook/radio-frequency-analysis-design/real-life-rf-signals/understanding-reflections-and-standing-waves-rf-circuit-design/> [Accessed 1 September 2021].

Braeunig.us. n.d. *Rocket And Space Technology*. [online] Available at: <http://www.braeunig.us/space/index.htm> [Accessed 12 September 2020].

Castet, J. and Saleh, J., 2009. Satellite and satellite subsystems reliability: Statistical data analysis and modeling. *Reliability Engineering & System Safety*, [online] 94(11), pp.1718-1728. Available at: <https://www.sciencedirect.com/science/article/abs/pii/S0951832009001094?via%3Dihub> [Accessed 22 October 2020].

Chemeurope.com. 2020. *Radiation Hardening*. [online] Available at: <https://www.chemeurope.com/en/encyclopedia/Radiation_hardening.html#Radiation-hardening_techniques> [Accessed 8 October 2020].

CEOS EO HANDBOOK – MISSION SUMMARY - ZACube-2 (2022) *The CEOS database: Mission summary - zacube-2*. Committee on Earth Observation Satellites (CEOS). Available at: http://database.eohandbook.com/database/missionsummary.aspx?missionID=911 (Accessed: December 7, 2022).

Clyde Space, n.d. *EPS System Diagram*. [image].

Coster, A. (n.d.) *Goodness-of-fit statistics*, *UNSW Mathematics and Statistics*. University of New South Wales. Available at: https://web.maths.unsw.edu.au/~adelle/Garvan/Assays/GoodnessOfFit.html (Accessed: November 16, 2022).

Dachwald, B., 2010. *Spacecraft Attitude Determination And Control V1.0*. [online] Available at: < https://www.slideshare.net/abi3/bsf08-spacecraft-attitude-determination-and-control-v1-0**>** [Accessed 8 October 2020].

DeCook, R., 2020. *Chapter 3 Discrete Random Variables and Probability Distributions*. [ebook] Iowa City: University of Iowa, pp.12-16. Available at: <https://homepage.divms.uiowa.edu/~rdecook/stat2020/notes/ch3_pt1.pdf> [Accessed 5 September 2021].

Fortescue, P., Swinerd, G. and Stark, J., 2011. *Spacecraft systems engineering*. 4th ed. Chichester: Wiley

Gilmore, D., 2002. Spacecraft Thermal Control Handbook, Volume I: Fundamental Technologies. *Spacecraft Thermal Control Handbook*, [online] 1. Available at: <https://arc.aiaa.org/doi/book/10.2514/4.989117> [Accessed 15 November 2021].

Gov.za. 2020. National Development Plan 2030 | South African Government. [online] Available at: <https://www.gov.za/issues/national-development-plan-2030> [Accessed 10 September 2020].

Hatfield, M., 2018. *Dellingr: The Little Cubesat That Could*. [online] NASA. Available at: <https://www.nasa.gov/feature/goddard/2018/dellingr-the-little-cubesat-that-could> [Accessed 24 August 2020].

Helmholtz Centre Potsdam GFZ German Research Centre for Geosciences (2019). Available at: https://kp.gfz-potsdam.de/app/json/?start=2019-01-01T00%3A00%3A00Z&end=2020-07-31T23%3A59%3A59Z&index=Kp#kpdatadownload-143 (Accessed: November 11, 2022).

Hill, S., n.d. *Space Weather Phenomena*. [image] Available at: <https://www.swpc.noaa.gov/phenomena> [Accessed 4 October 2020].

Howell, E., 2018. *What Is A Satellite?*. [online] Space.com. Available at: <https://www.space.com/24839-satellites.html> [Accessed 25 August 2020].

Ismail, M., Anis, W. and Fathy, R., 2016. Comparative Study Between Silicon & Gallium Arsenide ON Grid PV System. *International Journal of Advanced Research*, [online] 4(3), p.4. Available at: <https://www.journalijar.com/article/8644/comparative-study-between-silicon-&-gallium-arsenide-on-grid-pv-system/> [Accessed 7 December 2021].

Kaminskiy, M. and Kashem, N., 2015. *CubeSat Data Analysis Revision - Revision 2015*. [ebook] Maryland: National Aeronautics and Space Administration, pp.1-21. Available at:

<https://sma.nasa.gov/docs/default-source/News-Documents/cubesat-data-analysis.pdf?sfvrsn=0> [Accessed 31 July 2021].

Kaminskiy, M., 2015. *Cubesat Data Analysis Revision*. [ebook] Greenbelt, Maryland: National Aeronautics and Space Administration, pp.5-19. Available at: <https://sma.nasa.gov/docs/default-source/News-Documents/cubesat-data-analysis.pdf?sfvrsn=b106e4f8_0> [Accessed 23 October 2020].

Kulu, E., 2020. *What Is A Cubesat?* | *Nanosats Database*. [online] Nanosats Database. Available at: <https://www.nanosats.eu/cubesat> [Accessed 18 August 2020].

Langer, M. and Bouwmeester, J., 2016. Reliability of CubeSats – Statistical Data, Developers' Beliefs and the Way Forward. In: *Small Satellite Conference: Pioneering an Industry*. [online] Utah: Hosted by Utah State University Libraries, pp.1-12. Available at: <https://digitalcommons.usu.edu/cgi/viewcontent.cgi?article=3397&context=smallsat> [Accessed 23 October 2020].

Mathworks.com. 2020. *Normal Distribution- MATLAB & Simulink*. [online] Available at: <https://www.mathworks.com/help/stats/normal-distribution.html#bt5fmwo> [Accessed 31 October 2020].

Mathworks.com. 2021. *Read Spreadsheet Data Using Import Tool- MATLAB & Simulink*. [online] Available at: <https://www.mathworks.com/help/matlab/import_export/select-spreadsheet-data-interactively.html> [Accessed 26 February 2021].

Mathworks.com. 2021. *Remove missing entries - MATLAB rmmissing*. [online] Available at: <https://www.mathworks.com/help/matlab/ref/rmmissing.html?searchHighlight=rmmissing&s_tid=srchtitle> [Accessed 27 February 2021].

Mathworks.com. 2021. *Resample or aggregate data in timetable, and resolve duplicate or irregulartimes - MATLAB retime*. [online] Available at: <https://www.mathworks.com/help/matlab/ref/timetable.retime.html?searchHighlight=retime&s_tid=srchtitle#bvdhiwr-2> [Accessed 1 March 2021].

Mathworks.com. 2021. *Synchronize timetables to common time vector, and resample or aggregate datafrom input timetables - MATLAB synchronize*. [online] Available at: <https://www.mathworks.com/help/matlab/ref/timetable.synchronize.html?searchHighlight=synchronize&s_tid=srchtitle#bvdhiyk-2> [Accessed 1 March 2021].

Miller, David W., and John Keesee. "Spacecraft Power Systems." 2003. Presentation. Available at: **<**https://ocw.mit.edu/courses/aeronautics-and-astronautics/16-851-satellite-engineering-fall-2003/lecture-notes/l3_scpowersys_dm_done2.pdf> [Accessed 31 October 2020].

n.d. *Introduction to Switch Mode Power Supplies (SMPS)*. [ebook] Microchip Technology Inc, pp.3-5. Available at: <https://www.microchip.com/stellent/groups/SiteComm_sg/documents/Training_Tutorials/en528010.pdf> [Accessed 12 September 2021].

n.d. *Mission Control Datasheet*. [ebook] Bright Ascension, p.All. Available at: <https://www.brightascension.com/new_website/wp-content/uploads/2018/07/Mission-Control-Software-Datasheet.pdf> [Accessed 18 October 2020].

n.d. *CubeSat S-Band TX*. [ebook] Cape Peninsula University of Technology, p.1. Available at: <https://blogs.cput.ac.za/fsati/files/2016/07/BR-01-00017-STX-Brochure-Rev-B-Website.pdf> [Accessed 6 December 2021].

n.d. *CubeSat VHF/UHF Transceiver*. [ebook] Cape Peninsula University of Technology, p.1. Available at: <https://blogs.cput.ac.za/fsati/files/2020/07/BR-01-00045-Rev-D.pdf> [Accessed 6 December 2021].

Nagavarapu, S.C., Chandran, A. and Hastings, D.E. (2021) "Orbital Decay Analysis for Debris Deorbiting CubeSats in LEO: A Case Study for the VELOX-II Deorbit Mission," *8th European Conference on Space Debris*, 8(1), pp. 1–2. Available at: https://conference.sdo.esoc.esa.int/proceedings/sdc8/paper/297 (Accessed: November 12, 2022).

NASA, 2018. *Dellingr Cubesat*. [image] Available at: <https://www.nasa.gov/feature/goddard/2018/dellingr-the-little-cubesat-that-could> [Accessed 24 August 2020].

Nasa.github.io. n.d. *Open MCT - Open Source Mission Control Software — Open MCT*. [online] Available at: <https://nasa.github.io/openmct/> [Accessed 18 October 2020].

National Geophysical Data Center (2010) *Solar and terrestrial physics*, *NCEI*. U.S. Department of Commerce. Available at: https://www.ngdc.noaa.gov/stp/geomag/kp_ap.html (Accessed: November 11, 2022).

NOAA Space Weather Scales (2021) *NOAA Space Weather Scales | NOAA / NWS Space Weather Prediction Center*. National Oceanic and Atmospheric Administration (NOAA). Available at: https://www.swpc.noaa.gov/noaa-scales-explanation (Accessed: November 10, 2022).

Operationphakisa.gov.za. n.d. *Operation Phakisa*. [online] Available at: <https://www.operationphakisa.gov.za/Pages/Home.aspx> [Accessed 9 October 2020].

Orlof, J. and Bloom, J., 2014. *Covariance And Correlation*. Available at: < https://ocw.mit.edu/courses/mathematics/18-05-introduction-to-probability-and-statistics-spring-2014/readings/MIT18_05S14_Reading7b.pdf> [Accessed 27 August 2020]

Ruag.com. 2020. *Command And Data Handling Systems | RUAG*. [online] Available at: <https://www.ruag.com/en/products-services/space/electronics/satellite-and-launcher-computers/command-and-data-handling-systems> [Accessed 5 October 2020].

Schenkelberg, F., 2020. *Intro To Fault Tree Analysis — Accendo Reliability*. [online] Accendo Reliability. Available at: <https://accendoreliability.com/intro-to-fault-tree-analysis/> [Accessed 26 October 2020].

Scholl, R., 2020. *Forward and Reflected Powers. What Do They Mean?*. [ebook] Advanced Energy Industries Inc., pp.1-4. Available at: <https://www.advancedenergy.com/globalassets/resources-root/white-papers/en-srv-forward-reflected-powers-white-paper.pdf> [Accessed 1 September 2021].

Solar and Heliospheric Administration. 2020. *Space Weather*. [online] Available at: <https://soho.nascom.nasa.gov/spaceweather/> [Accessed 3 October 2020].

Spaceteq.co.za. 2018. *SPACETEQ MCS MISSION CONTROL SYSTEM*. [online] Available at: <https://www.spaceteq.co.za/mcs> [Accessed 18 October 2020].

Space-Track (2019) "HISTORICAL ELSET SEARCH." Available at: https://www.space-track.org/basicspacedata/query/class/gp_history/NORAD_CAT_ID/43907/orderby/TLE_LINE1%20ASC/EPOCH/2019-01-01--2020-07-31/format/json (Accessed: November 11, 2022).

Space-Track. 2021. *Historical Elset Search*. [online] Available at: <https://www.space-track.org/basicspacedata/query/class/gp_history/NORAD_CAT_ID/43907/orderby/TLE_LINE1%20ASC/EPOCH/2019-01-01--2021-11-28/format/json> [Accessed 20 December 2021].

Spaceweatherlive (no date) *Space weather archive | spaceweatherlive.com*, *SpaceWeatherLive*. Available at: https://www.spaceweatherlive.com/en/archive.html (Accessed: November 11, 2022).

spaceweatherlive.com (2022) *The KP-index | help | spaceweatherlive.com*, *SpaceWeatherLive*. SpaceWeatherLive. Available at: https://www.spaceweatherlive.com/en/help/the-kp-index.html (Accessed: November 11, 2022).

Stevenson, M., 2007. *An Introduction To Survival Analysis*. [online] Available at: < http://www.biecek.pl/statystykaMedyczna/Stevenson_survival_analysis_195.721.pdf> [Accessed 26 October 2020].

Swpc.noaa.gov. 2020. *Ionospheric Scintillation | NOAA / NWS Space Weather Prediction Center*. [online] Available at: <https://www.swpc.noaa.gov/phenomena/ionospheric-scintillation> [Accessed 3 October 2020].

Swpc.noaa.gov. 2020. *Satellite Communications | NOAA / NWS Space Weather Prediction Center*. [online] Available at: <https://www.swpc.noaa.gov/impacts/satellite-communications> [Accessed 3 October 2020].

Swpc.noaa.gov. 2020. *Space Weather Phenomena | NOAA / NWS Space Weather Prediction Center*. [online] Available at: <https://www.swpc.noaa.gov/phenomena> [Accessed 6 October 2020].

Swpc.noaa.gov. 2021. *Solar Cycle Progression | NOAA / NWS Space Weather Prediction Center*. [online] Available at: <https://www.swpc.noaa.gov/products/solar-cycle-progression> [Accessed 7 December 2021].

tutorialspoint, 2020. *Data Analysis - Process*. [image] Available at: <https://www.tutorialspoint.com/excel_data_analysis/data_analysis_process.htm> [Accessed 15 October 2020].

van Vuuren, G. (2020) “CubeSpace CubeADCS 3-Axis Commissioning Manual v7.1.” Stellenbosch: CubeSpace.

Wagner, R., 2006. *Battery Fuel Gauges: Accurately Measuring Charge Level*. [ebook] San Jose: Maximum Integrated, pp.1-8. Available at: <https://pdfserv.maximintegrated.com/en/an/AN3958.pdf> [Accessed 28 September 2020].

Weibull.com. 2020. *Nonparametric Analysis, This Issue's Reliability Basic*. [online] Available at: <https://www.weibull.com/hotwire/issue11/relbasics11.htm> [Accessed 30 October 2020].

Wertz, J. and Larson, W., 1999. *Space Mission Analysis And Design*. 3rd ed. Torrance, California: Microcosm.

APPENDICES

APPENDIX A: RAW RESULTS

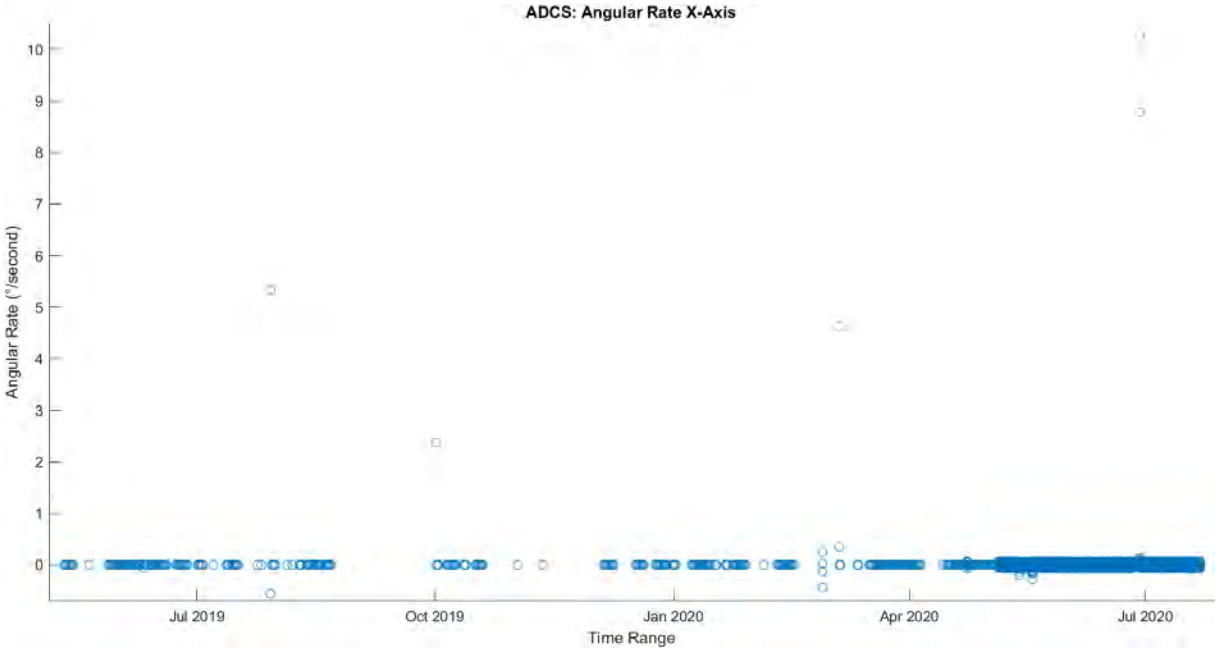

Figure A.1: ADCS Angular Rate X-Axis

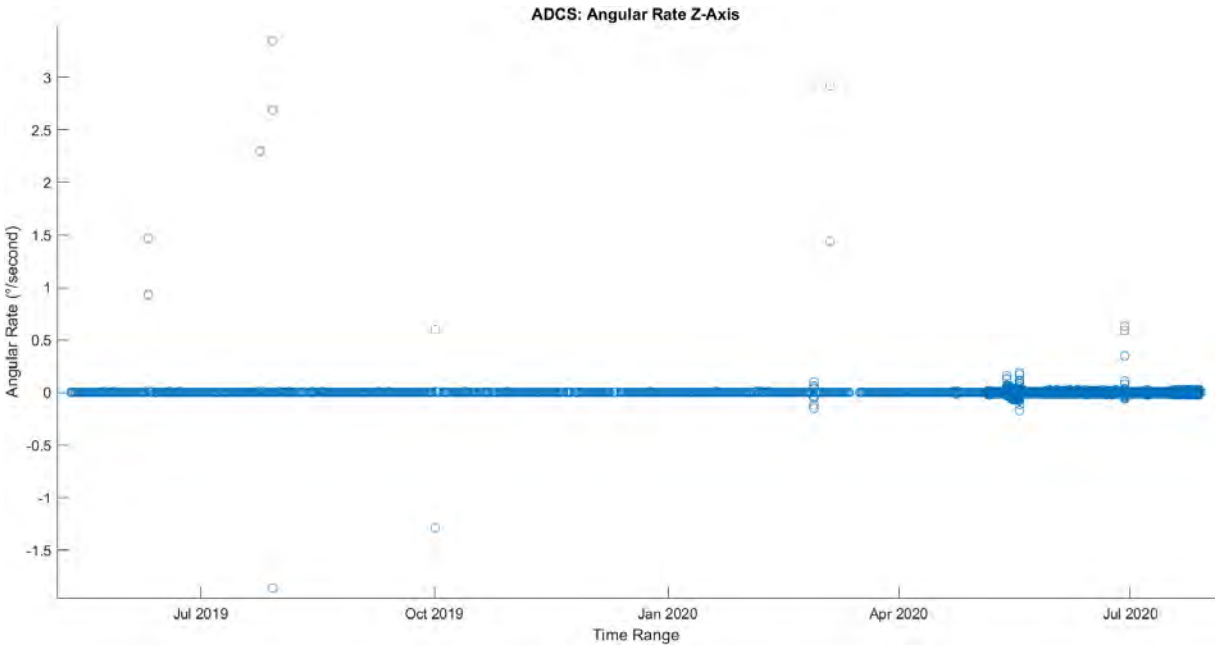

Figure A.2: ADCS Angular Rate Z-Axis

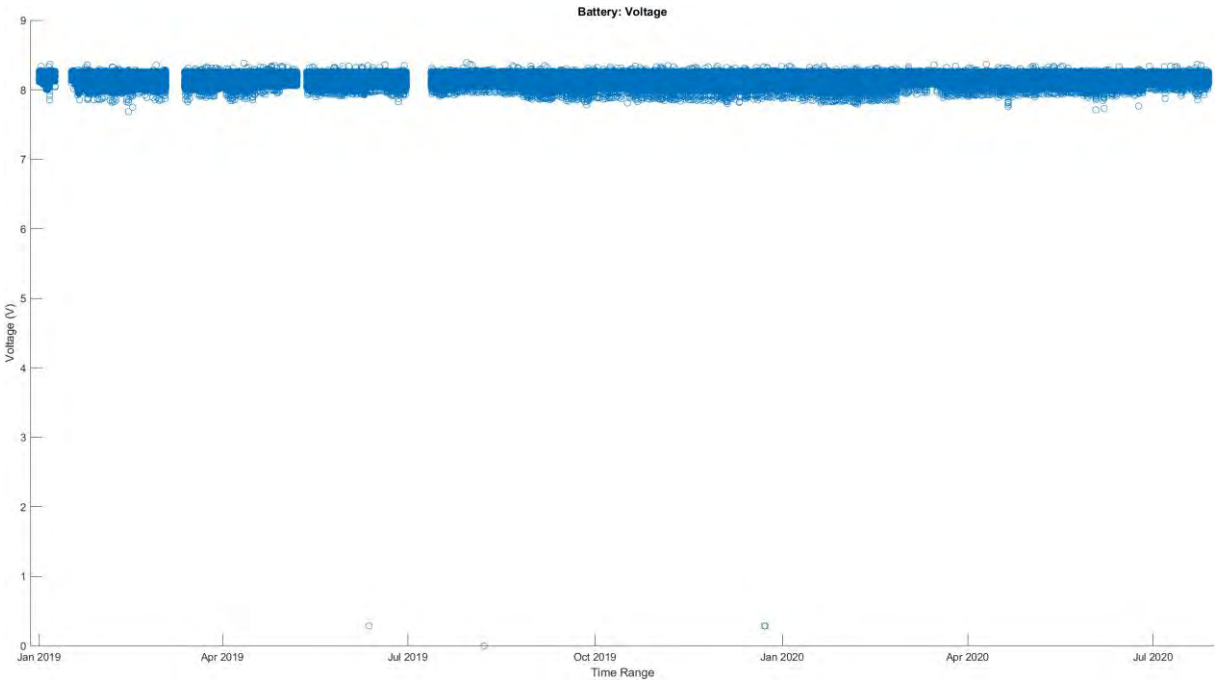

Figure A.3: Battery Voltage

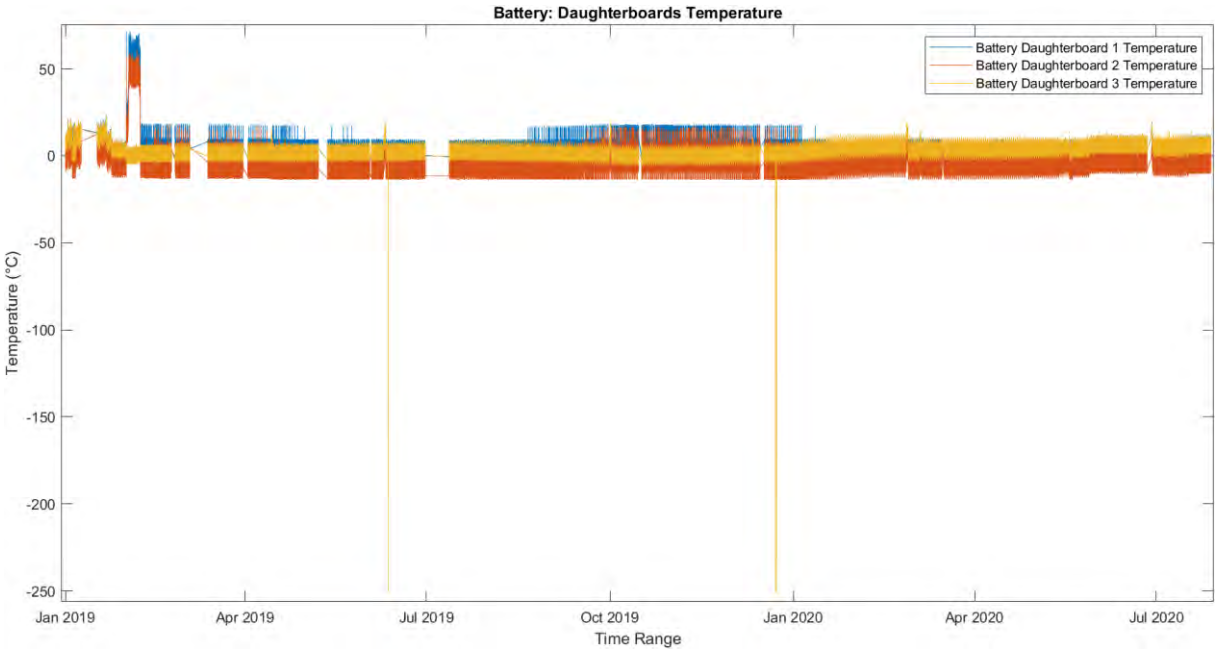

Figure A.4: Battery Daughterboards Temperatures

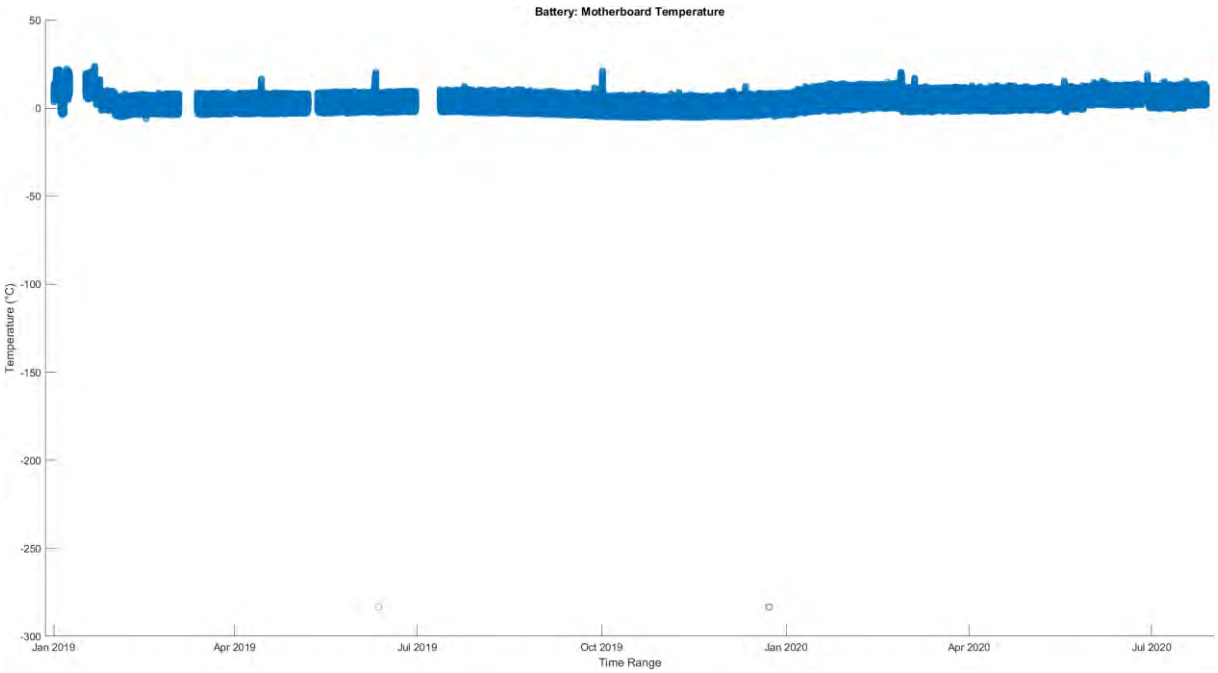

Figure A.5: Battery Motherboard Temperature

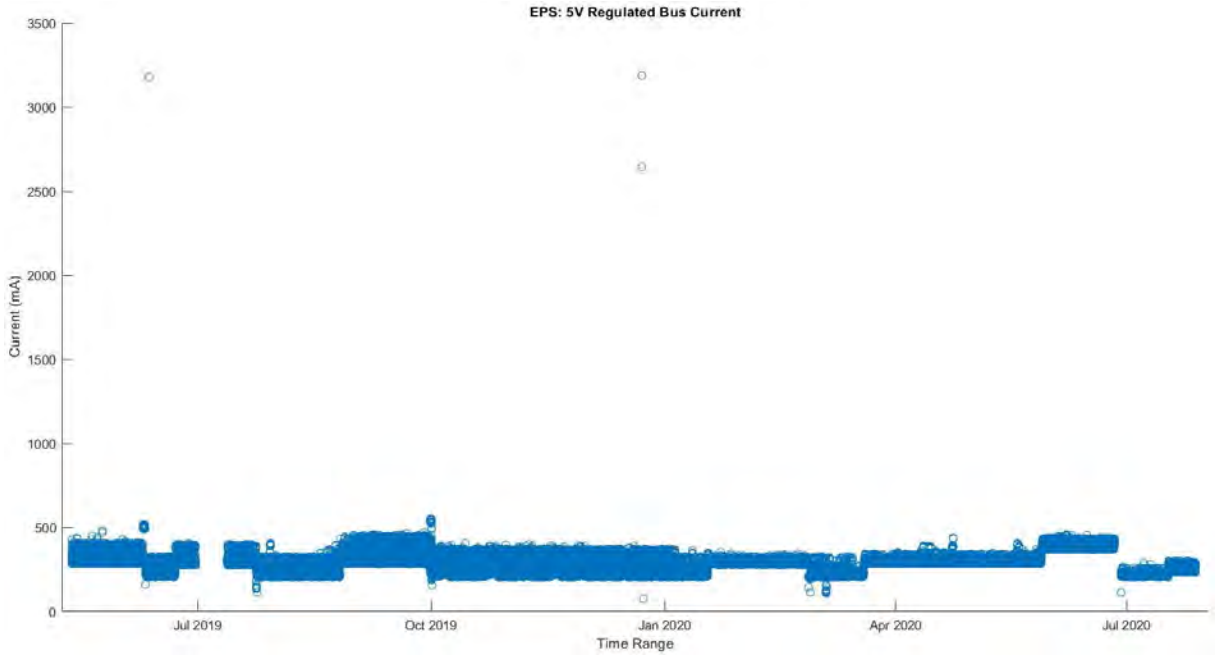

Figure A.6: EPS 5V Regulated Bus Current

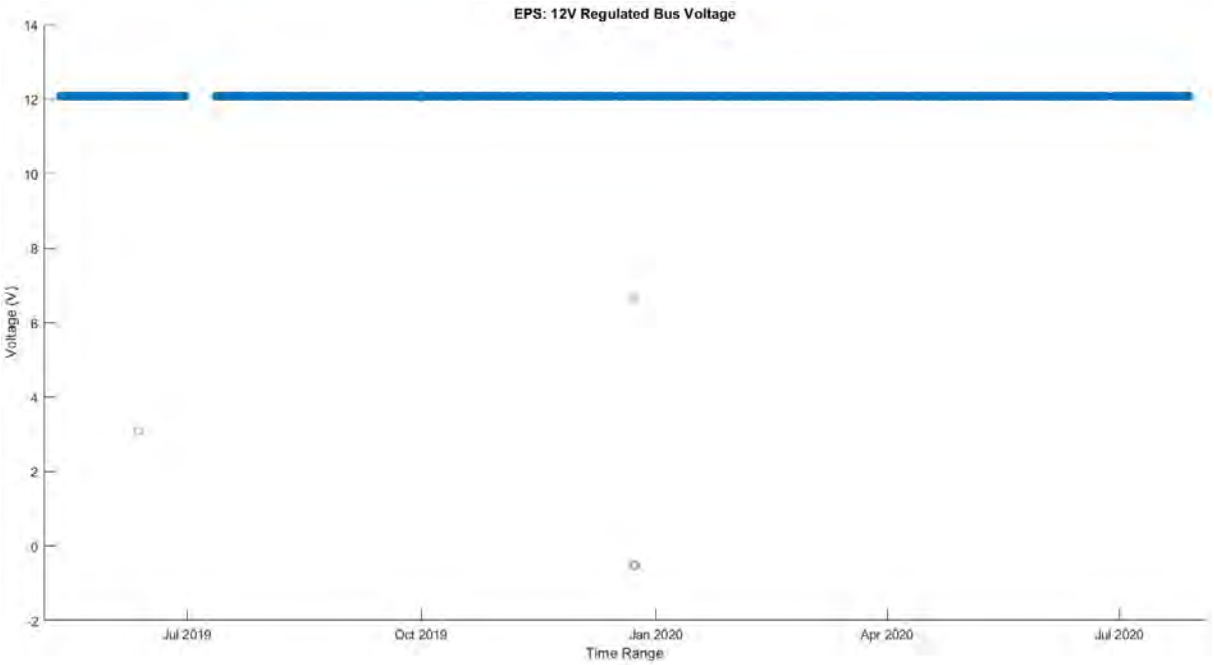

Figure A.7: EPS 12V Regulated Bus Voltage

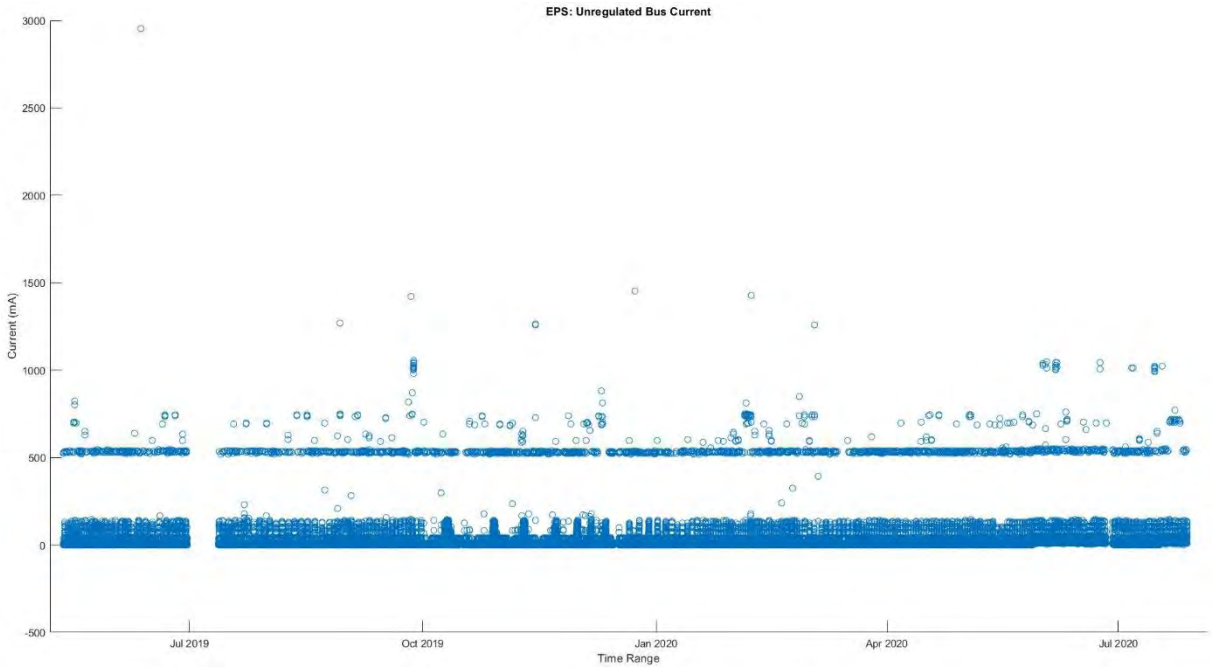

Figure A.8: EPS Unregulated Battery Bus Current

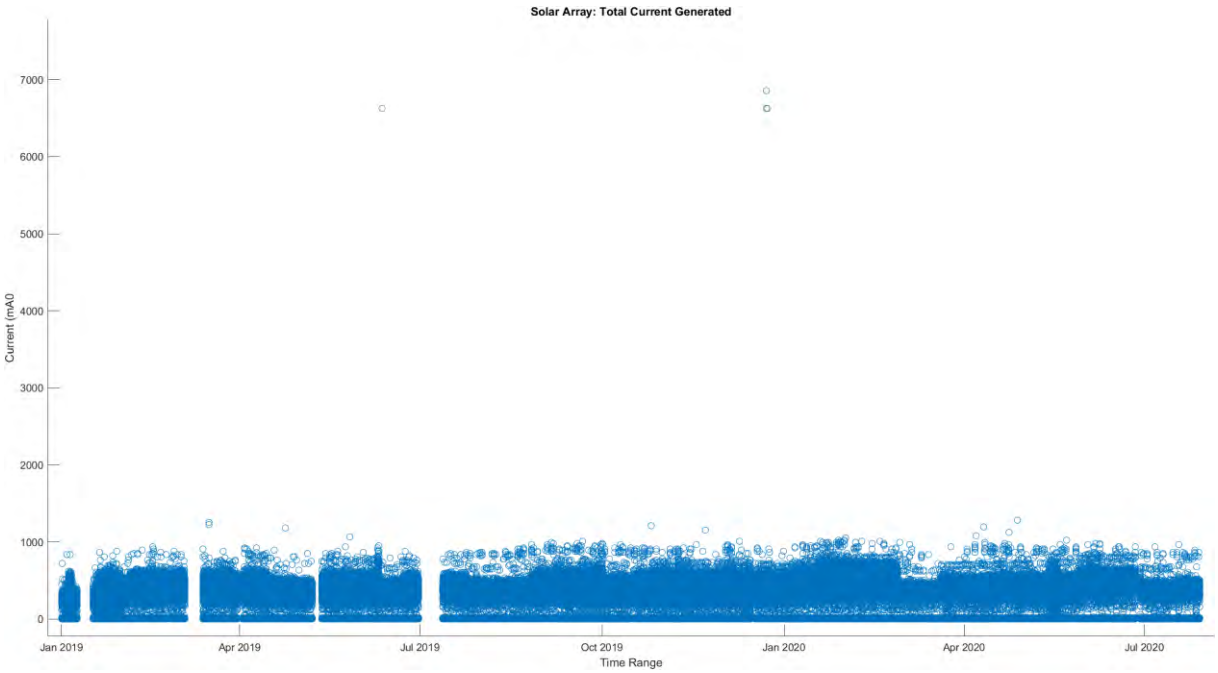

Figure A.9: Solar Array Total Current Generated

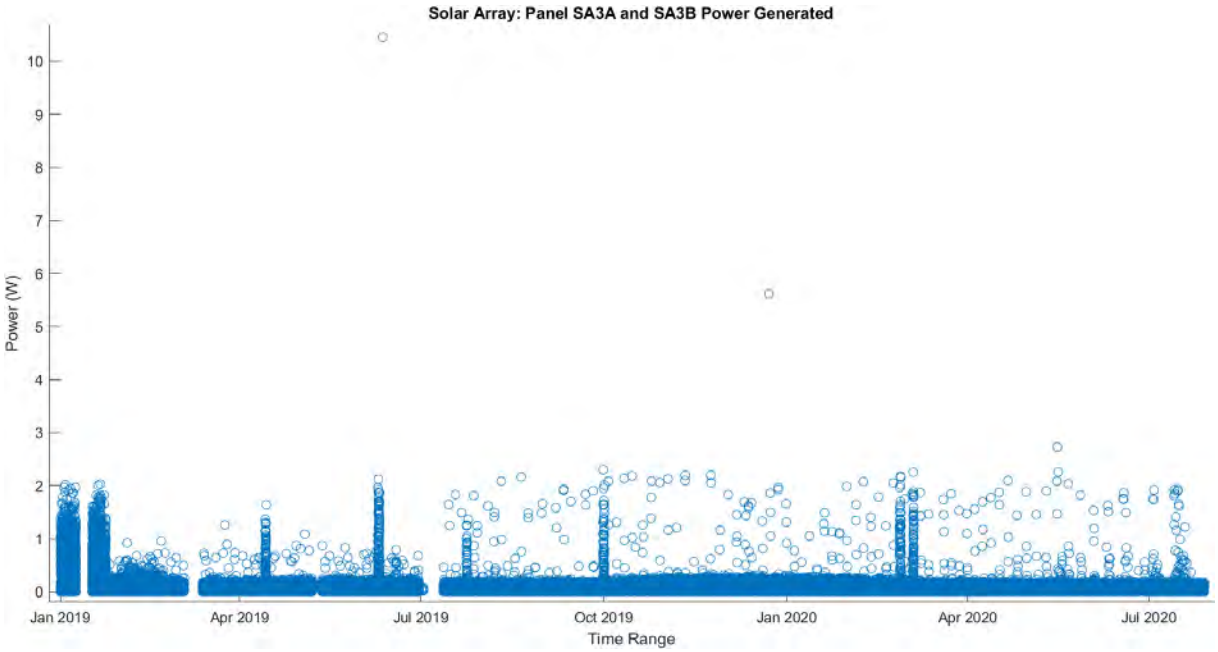

Figure A.10: Solar Panels SA3A and SA3B Power Generated

Figure A.11: UTRXC 3.3V Regulated Bus Current

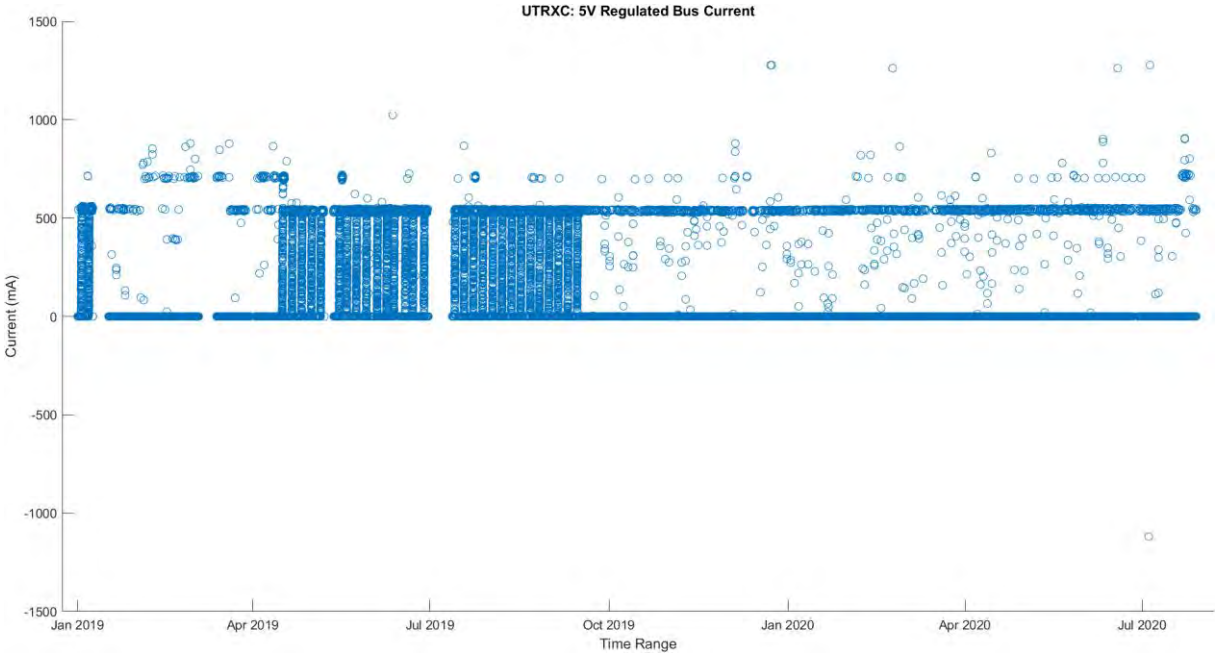

Figure A.12: 5V Regulated Bus Current

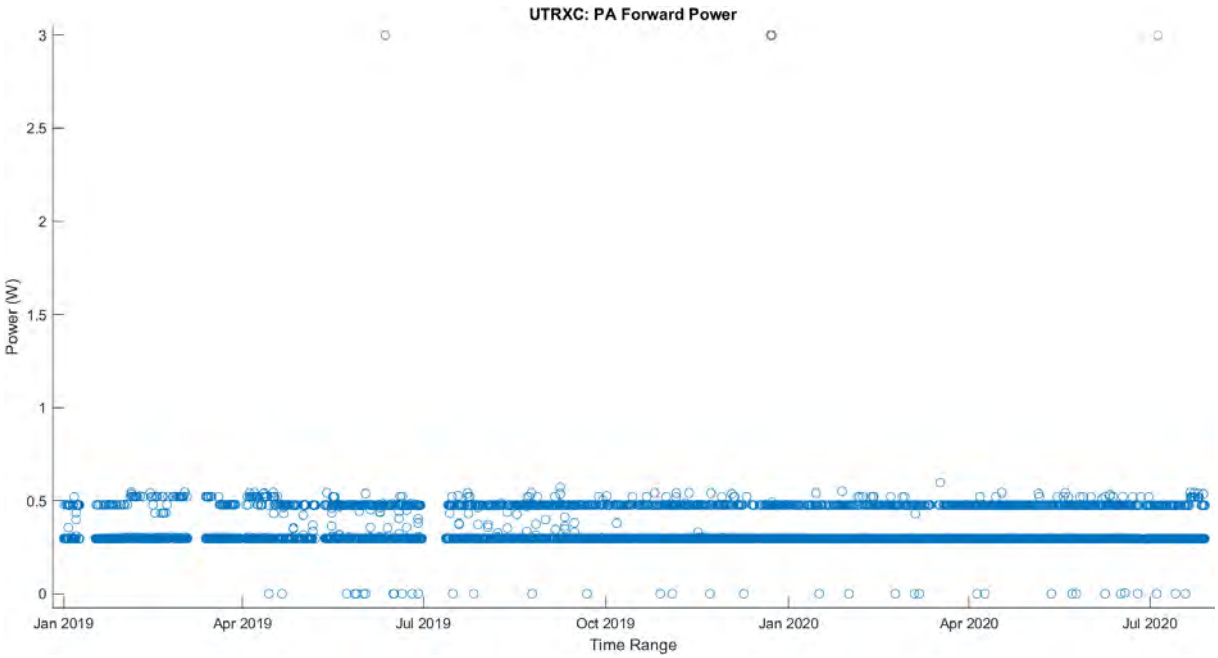

Figure A.13: UTRXC PA Forward Power

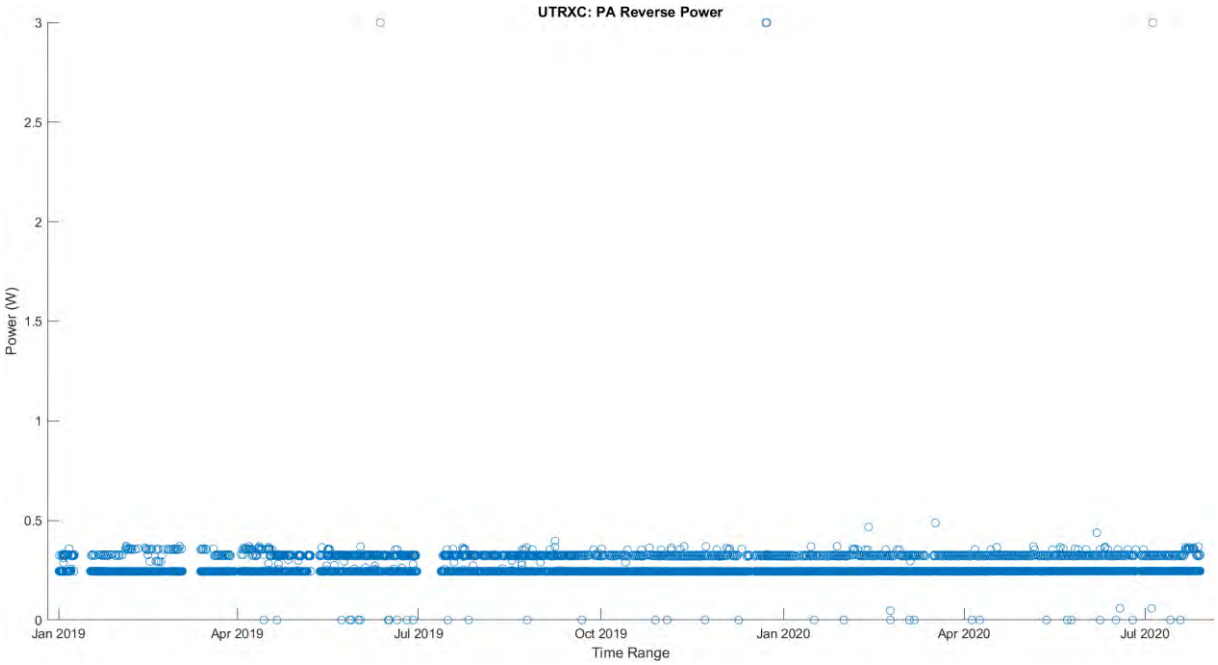

Figure A.14: UTRXC PA Reverse Power

APPENDIX B: DATA ANALYSIS CUMULATIVE DENSITY FUNCTION

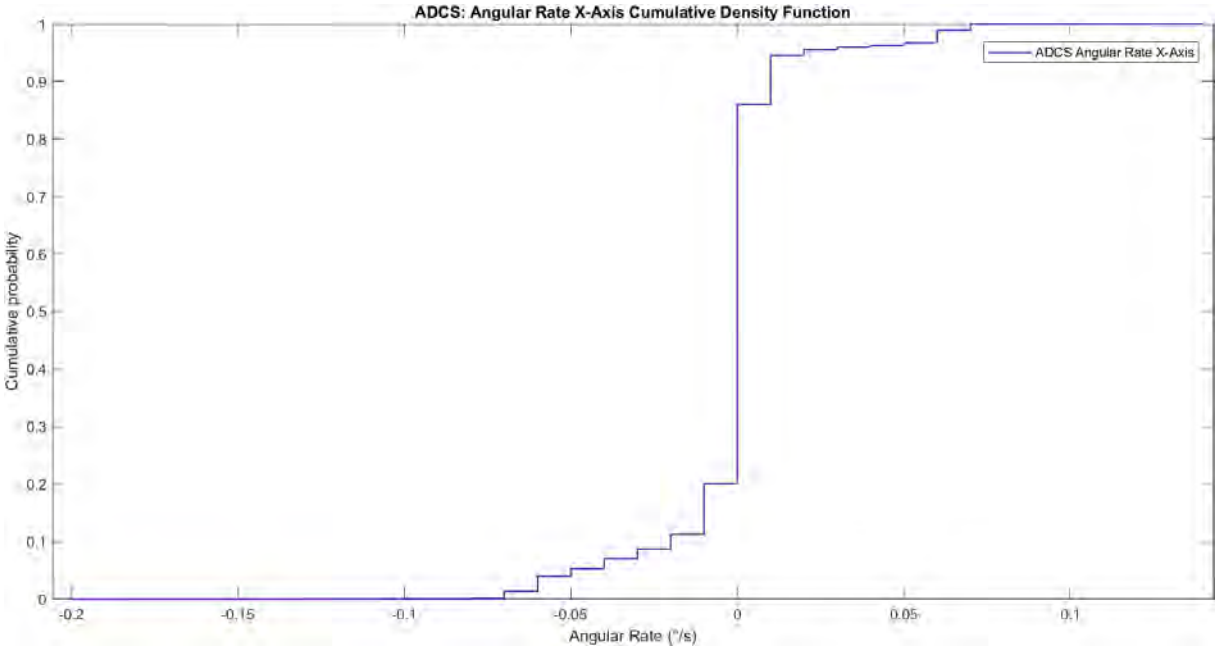

Figure B.1: ADCS Angular Rate X-Axis Cumulative Density Function

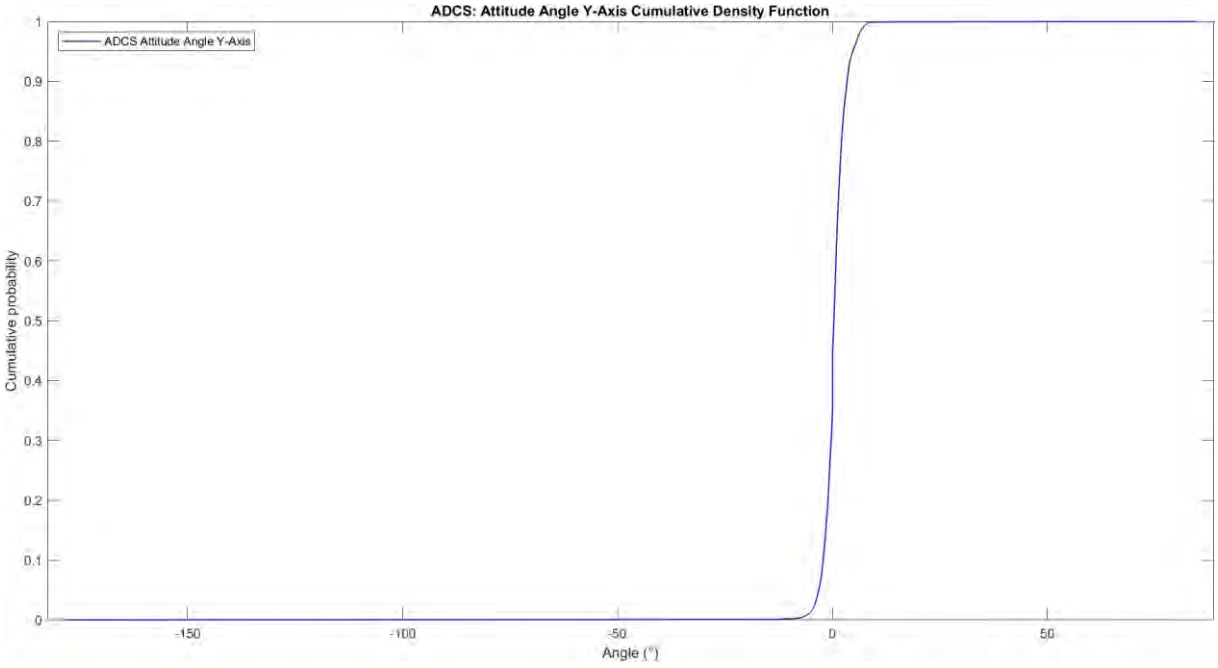

Figure B.2: ADCS Attitude Angle Y-Axis Cumulative Density Function

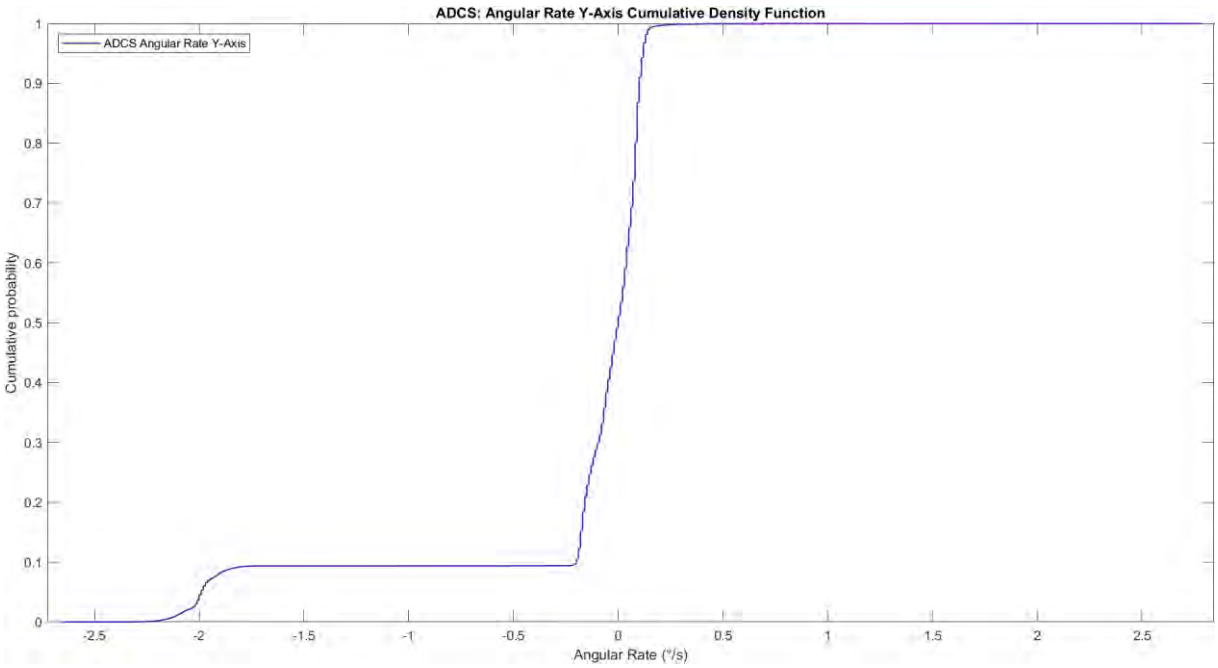

Figure B.3: ADCS Angular Rate Y-Axis Cumulative Density Function

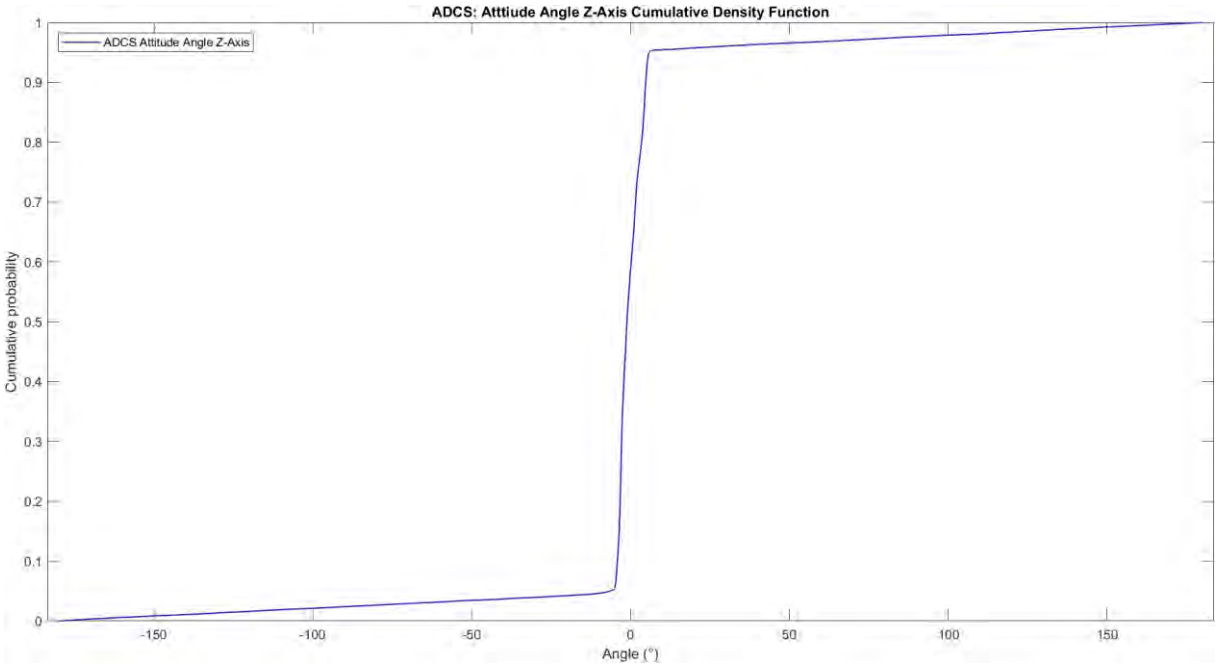

Figure B.4: ADCS Attitude Angle Z-Axis Cumulative Density Function

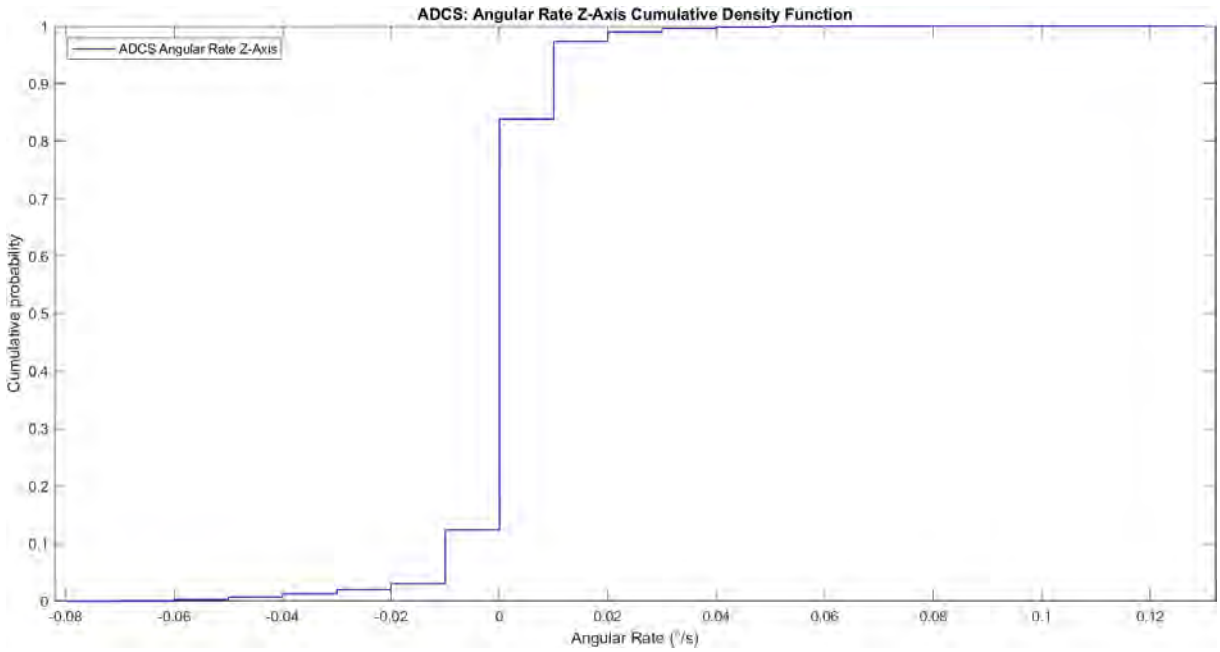

Figure B.5: ADCS Angular Rate Z-Axis Cumulative Density Function

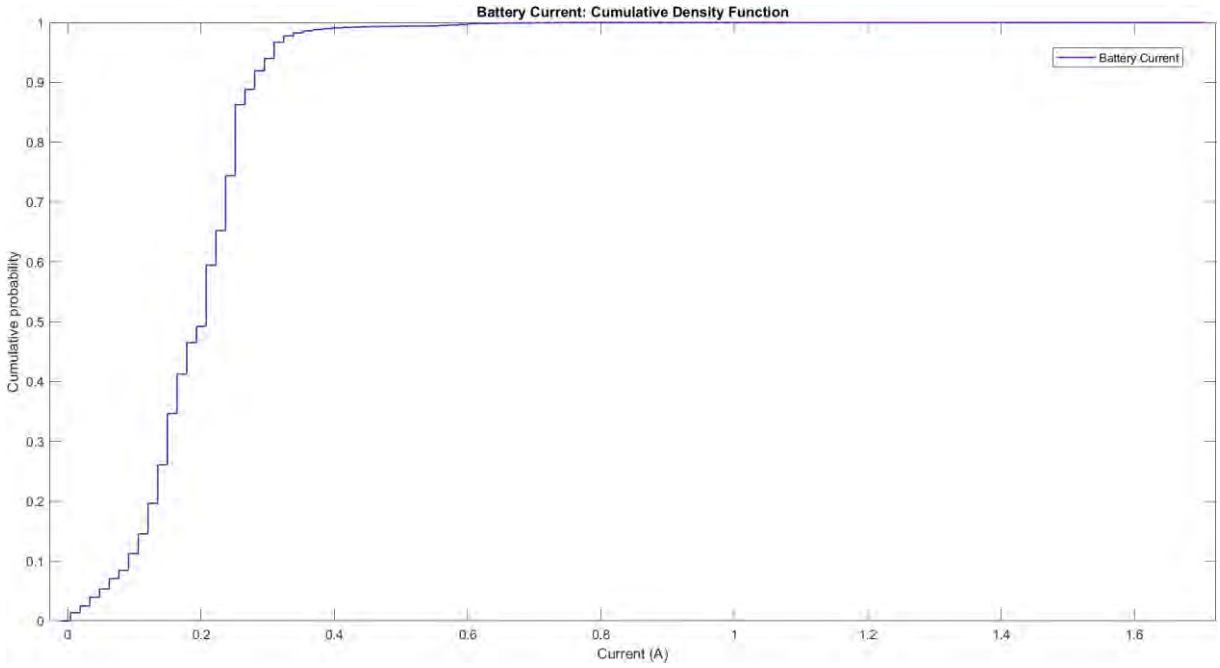

Figure B.6: Battery Current Cumulative Density Function

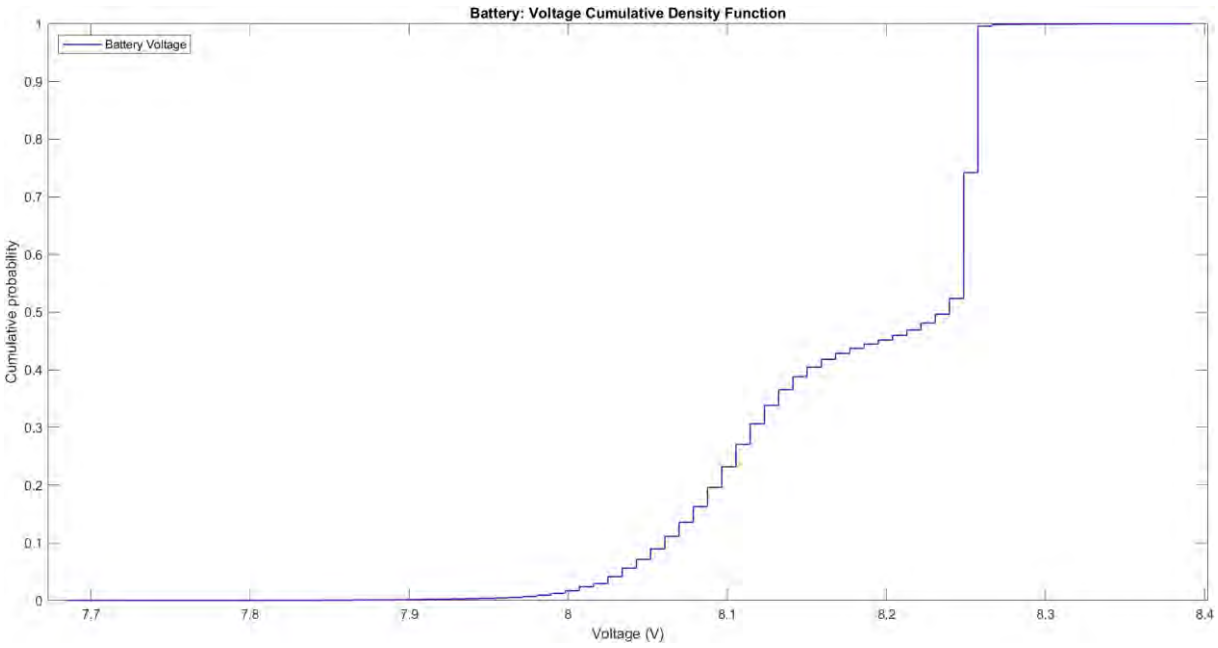

Figure B.7: Battery Voltage Cumulative Density Function

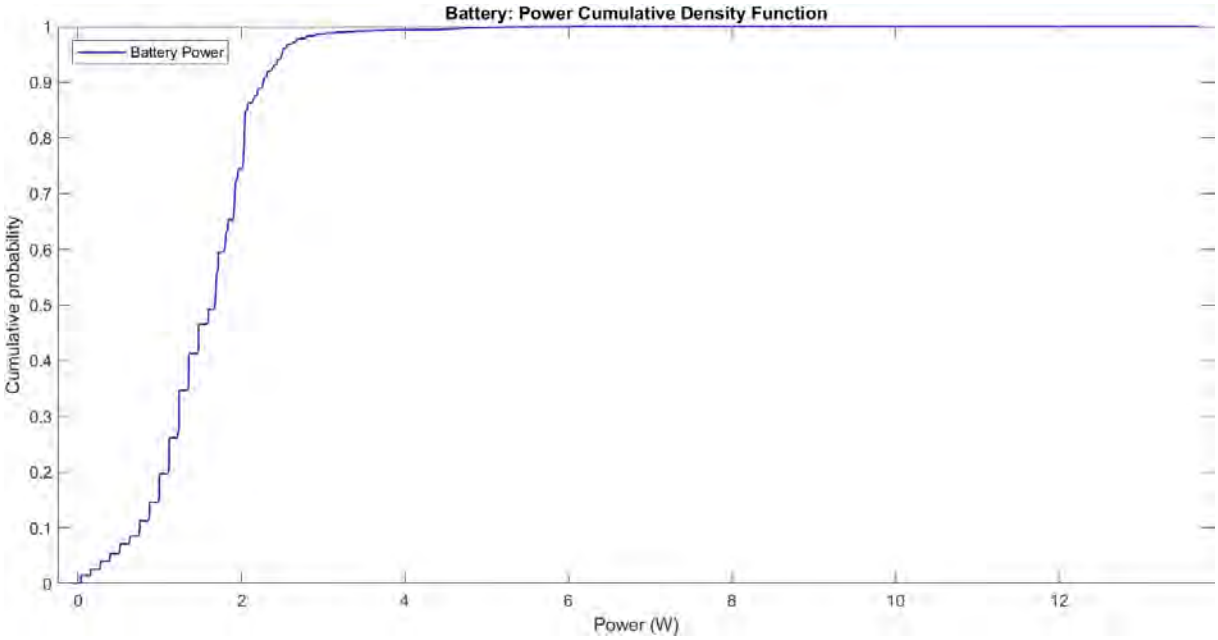

Figure B.8: Battery Power Cumulative Density Function

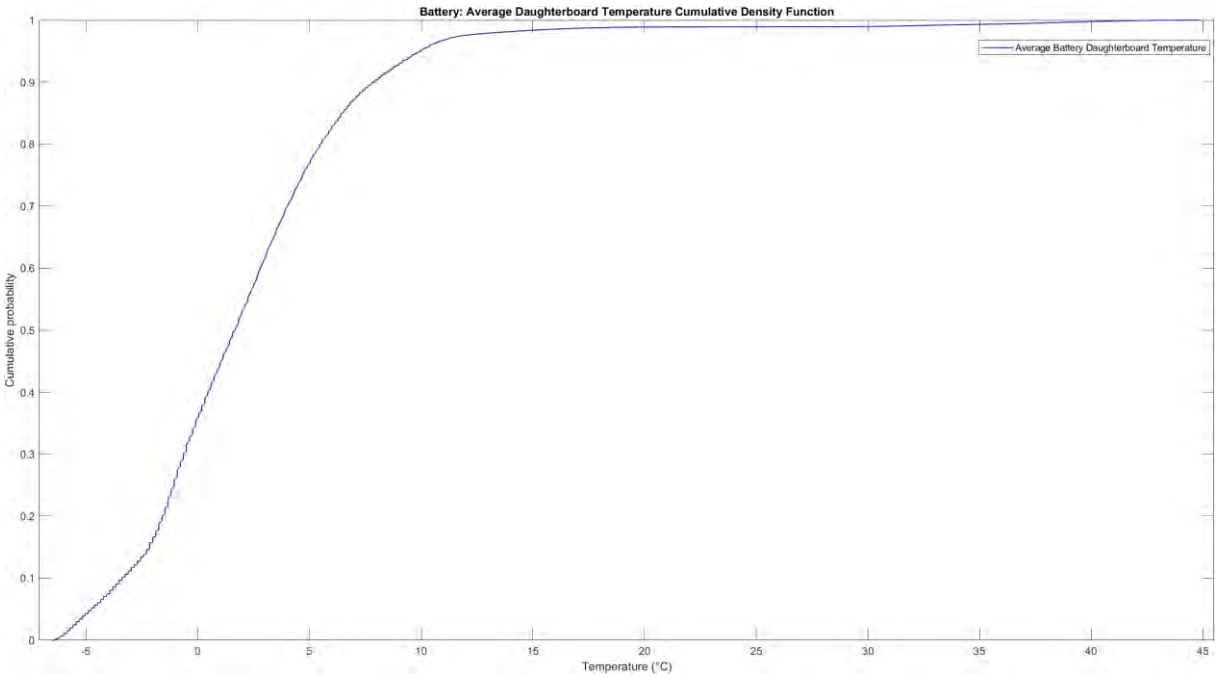

Figure B.9: Battery Average Daughterboard Temperature Cumulative Density Function

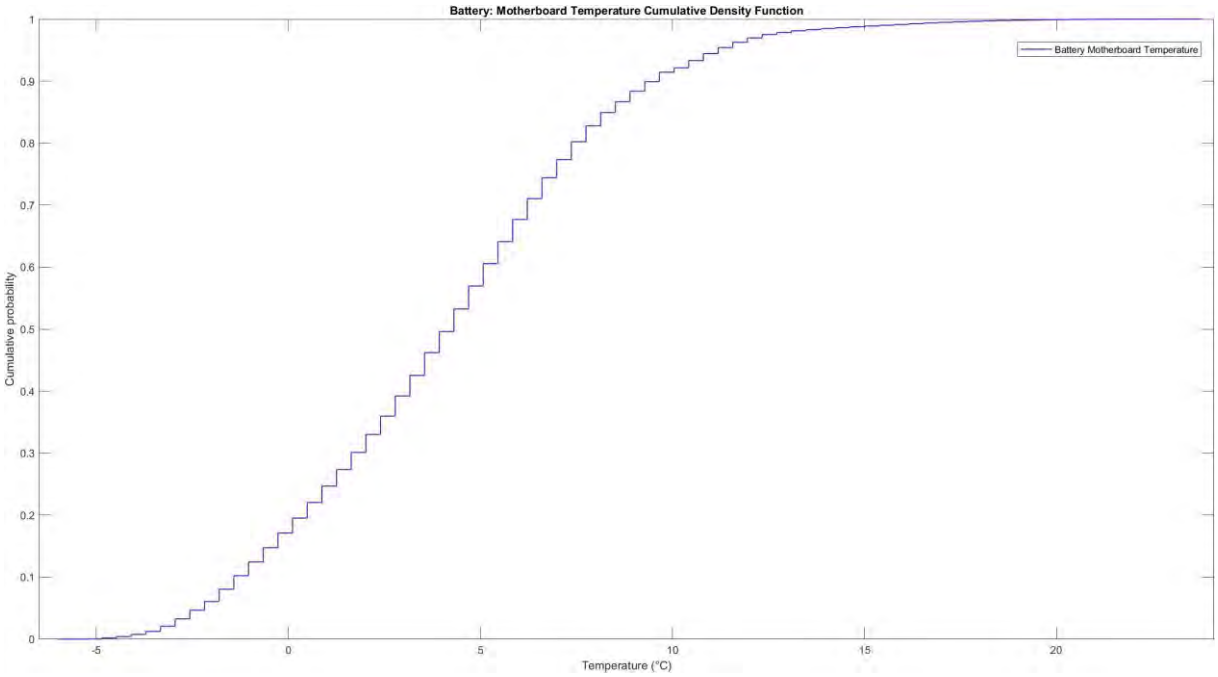

Figure B.10: Battery Motherboard Temperature Cumulative Density Function

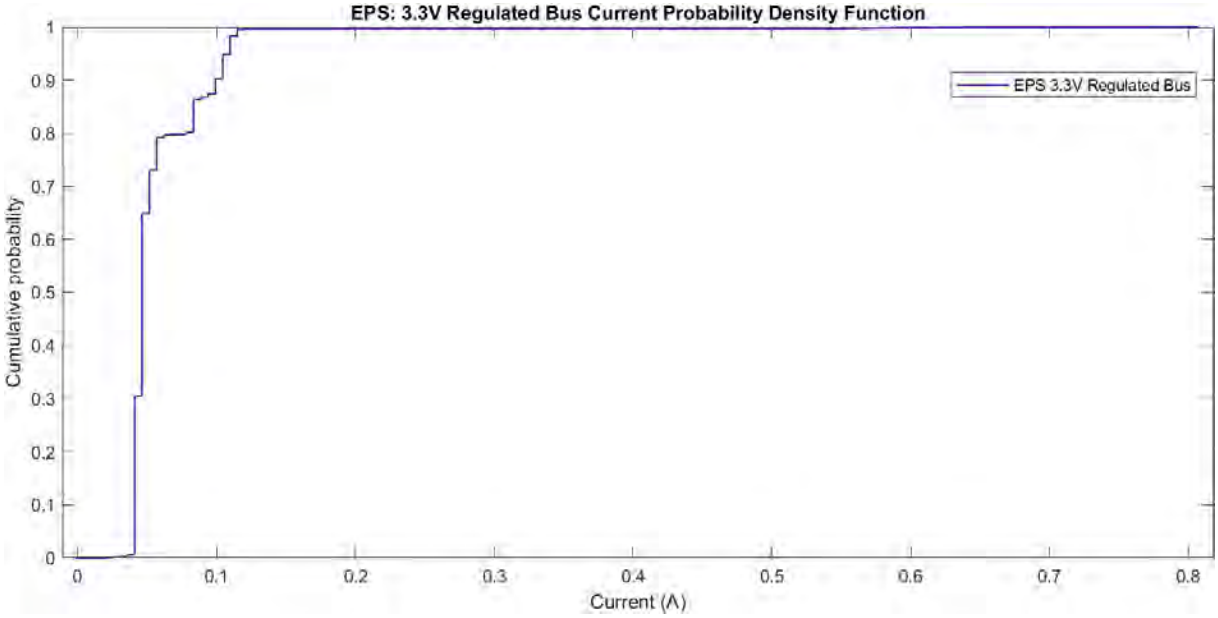

Figure B.11: EPS 3.3V Regulated Bus Current Probability Density Function

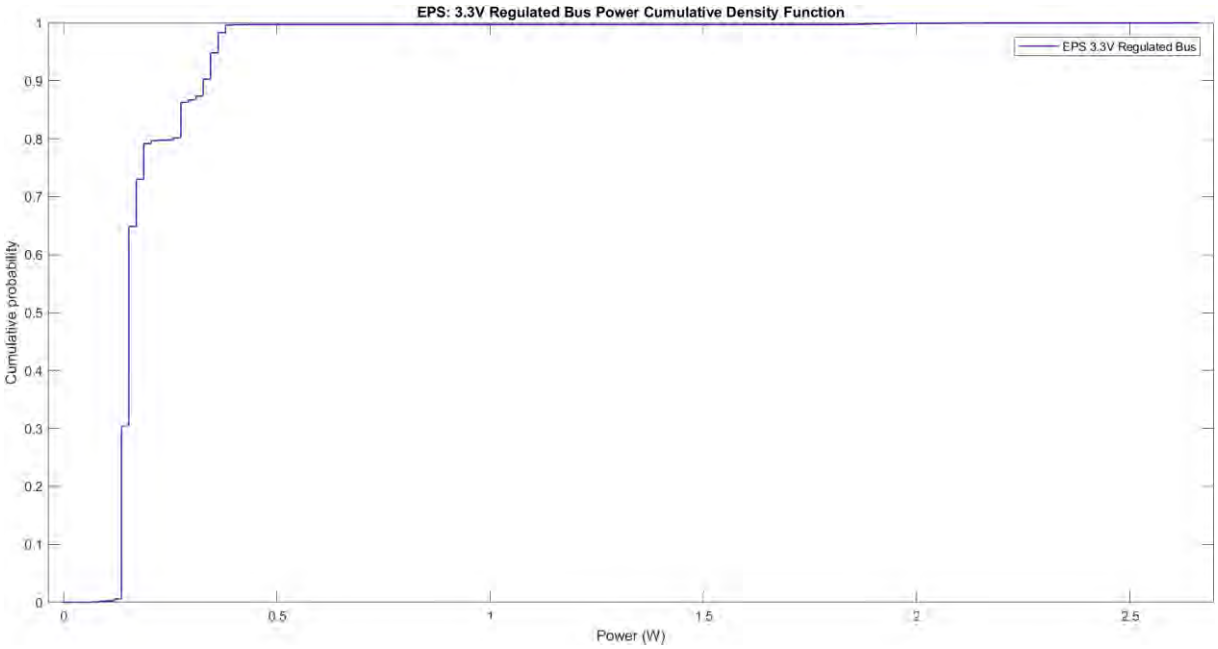

Figure B.12: EPS 3.3V Regulated Bus Power Cumulative Density Function

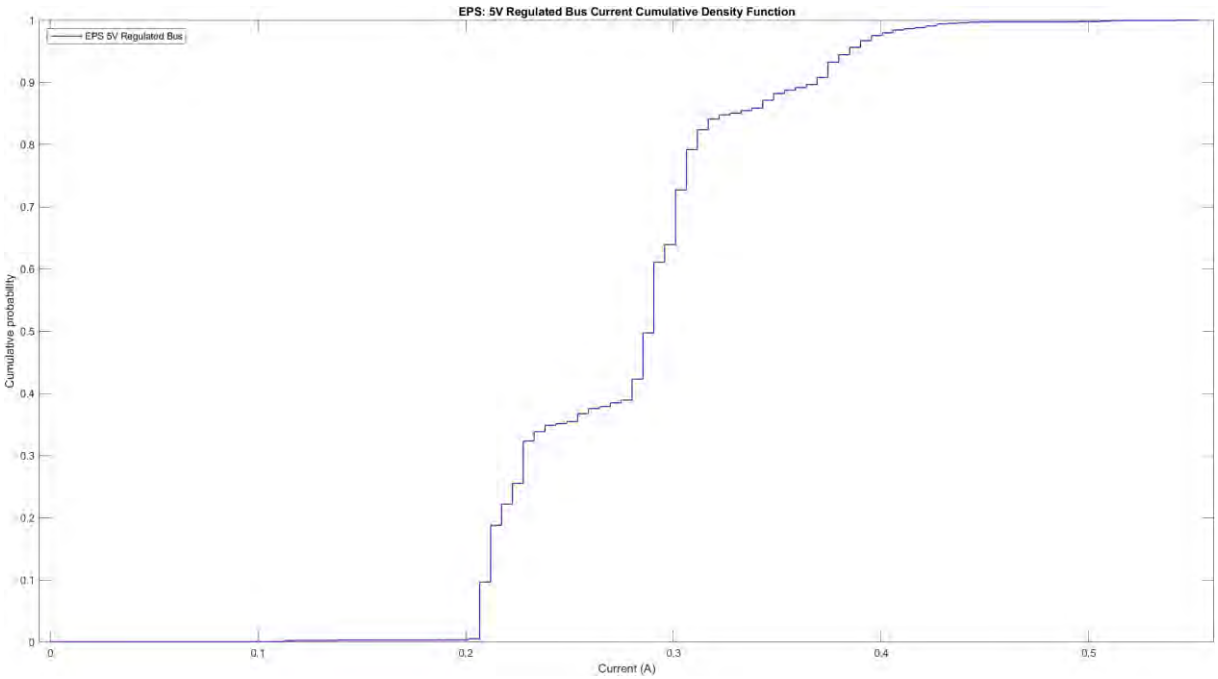

Figure B.13: EPS 5V Regulated Bus Current Cumulative Density Function

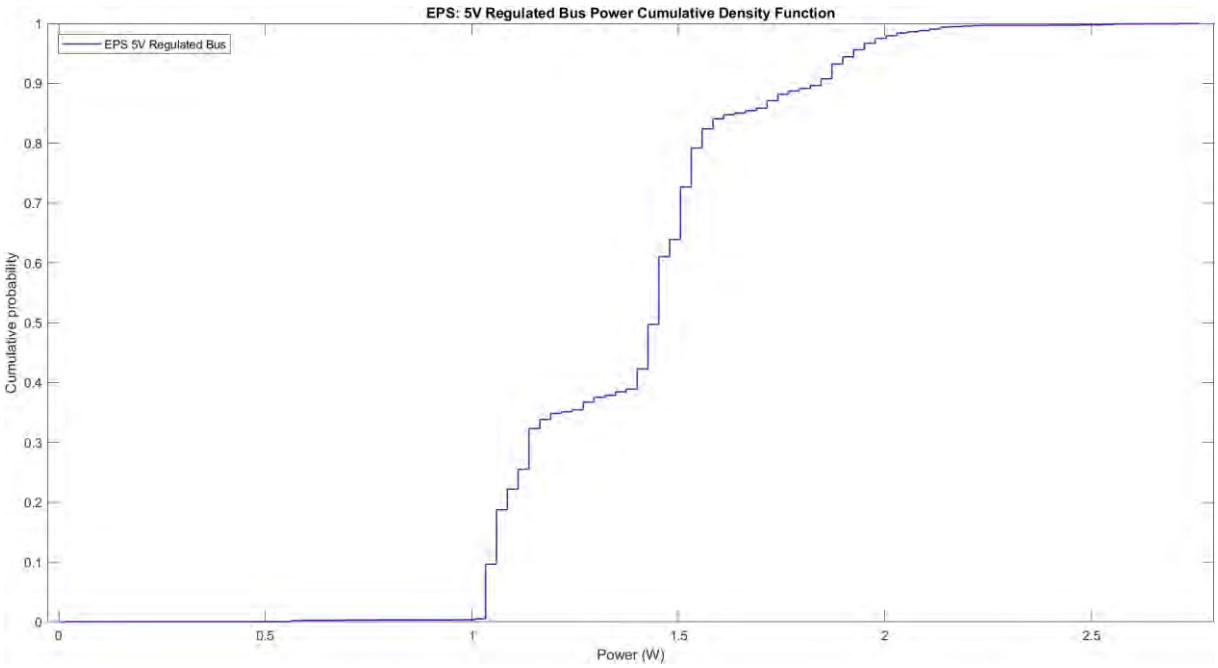

Figure B.14: EPS 5V Regulated Bus Power Cumulative Density Function

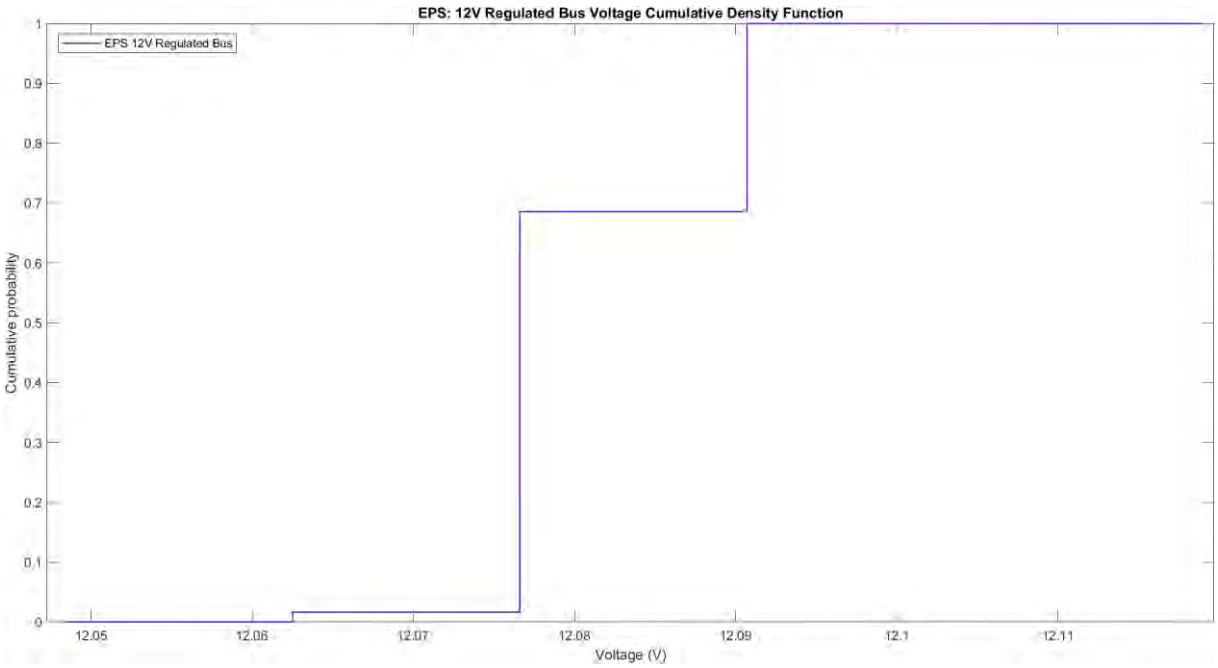

Figure B.15: EPS 12V Regulated Bus Voltage Cumulative Density Function

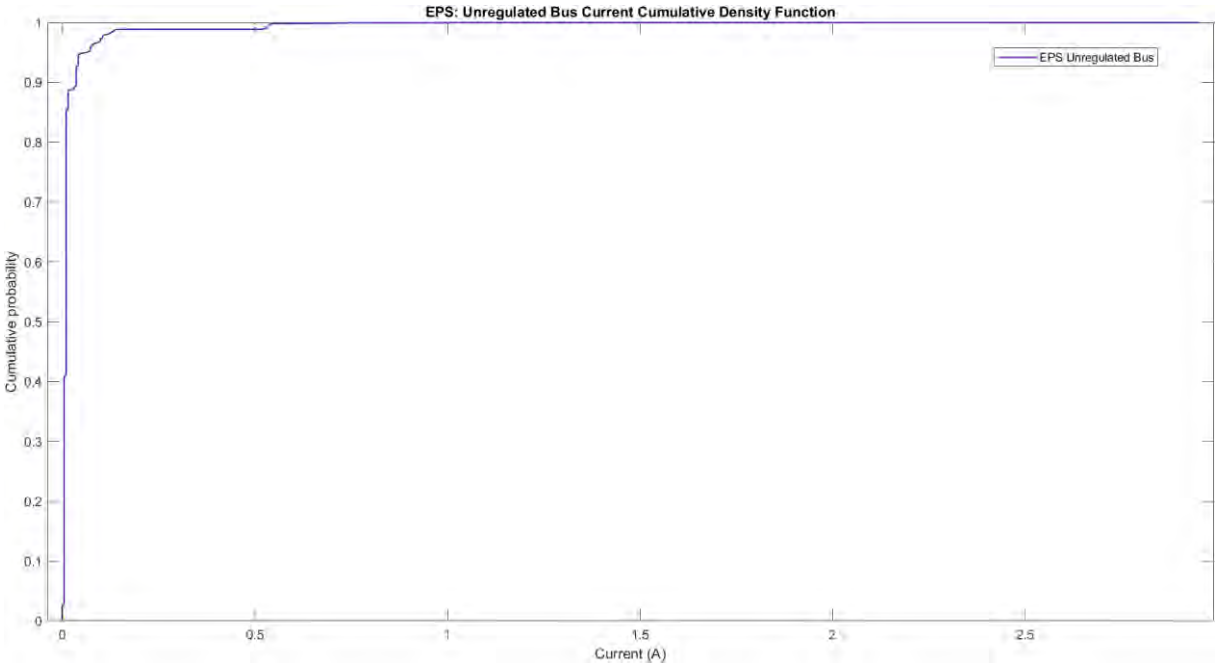

Figure B.16: EPS Unregulated Bus Current Cumulative Density Function

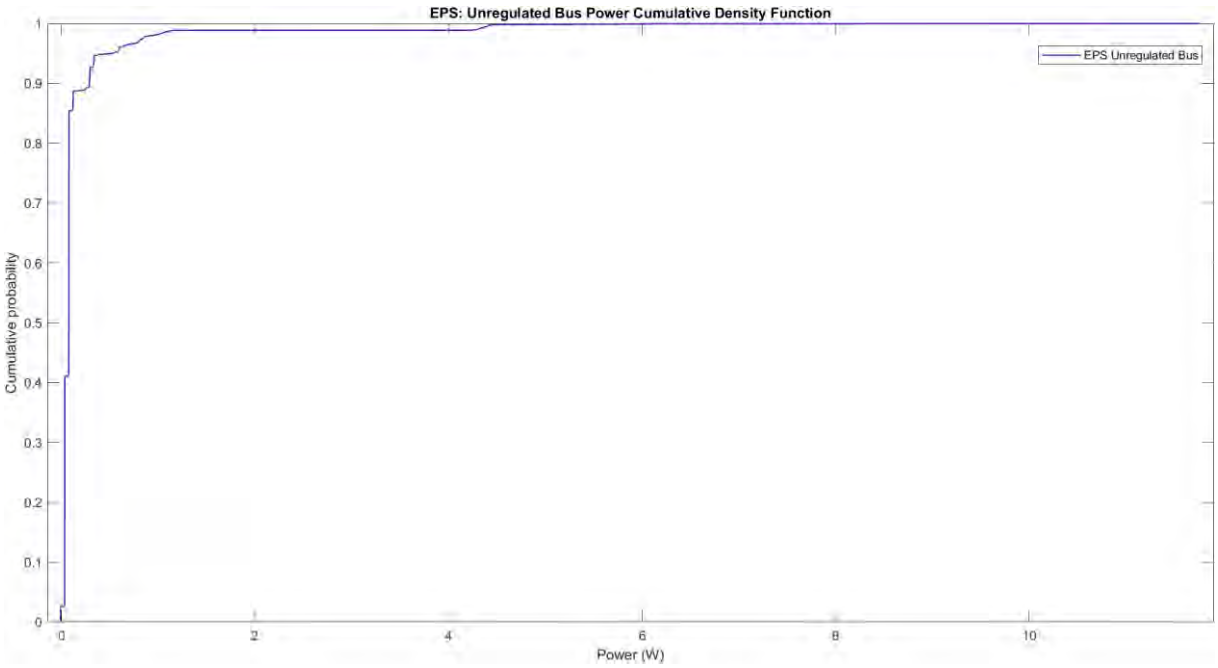

Figure B.17: EPS Unregulated Bus Power Cumulative Density Function

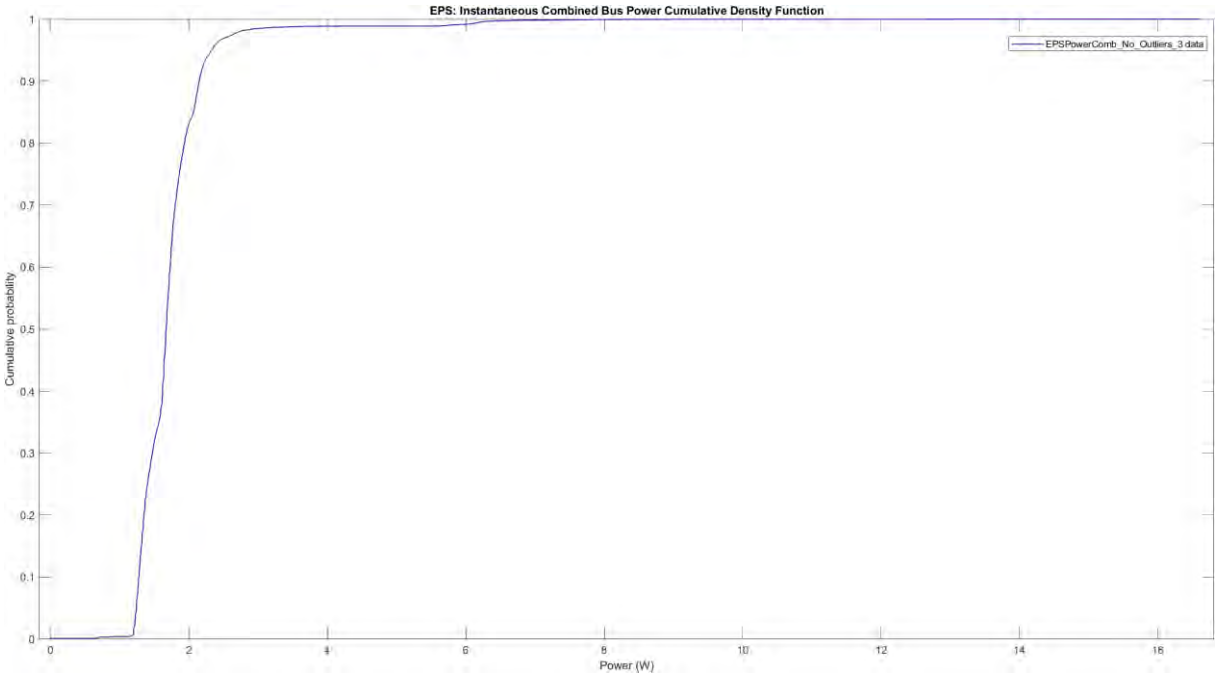

Figure B.18: EPS Instantaneous Combined Bus Power Cumulative Density Function

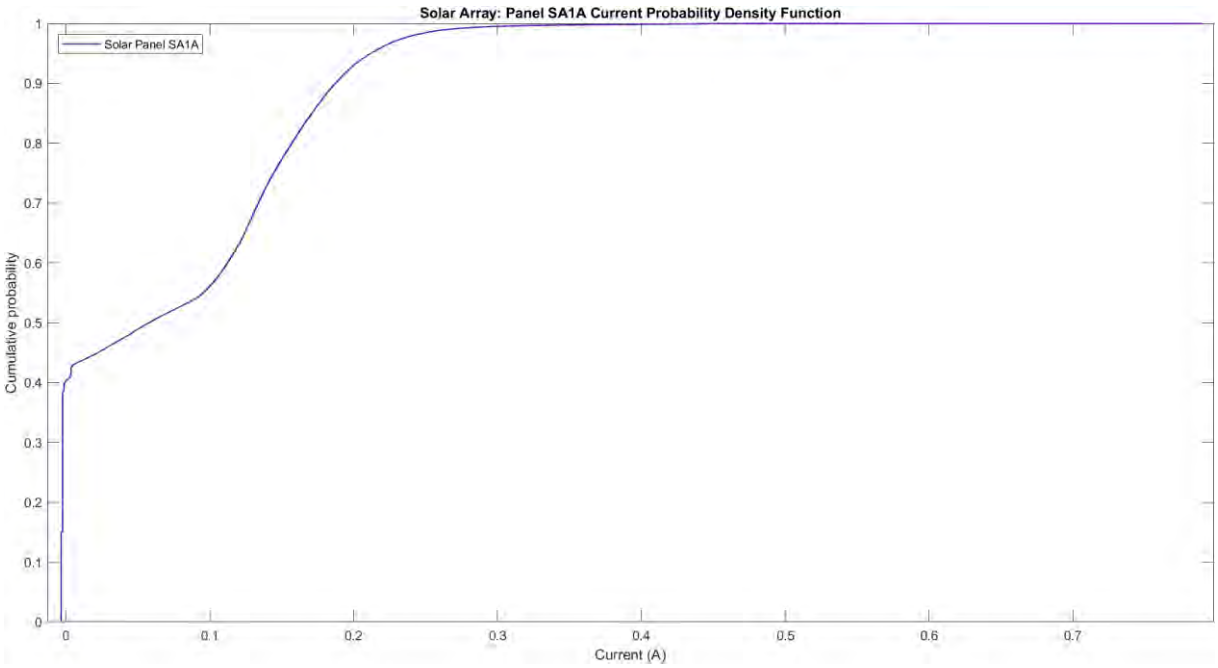

Figure B.19: Solar Array Panels SA1A and SA1B Current Cumulative Density Function

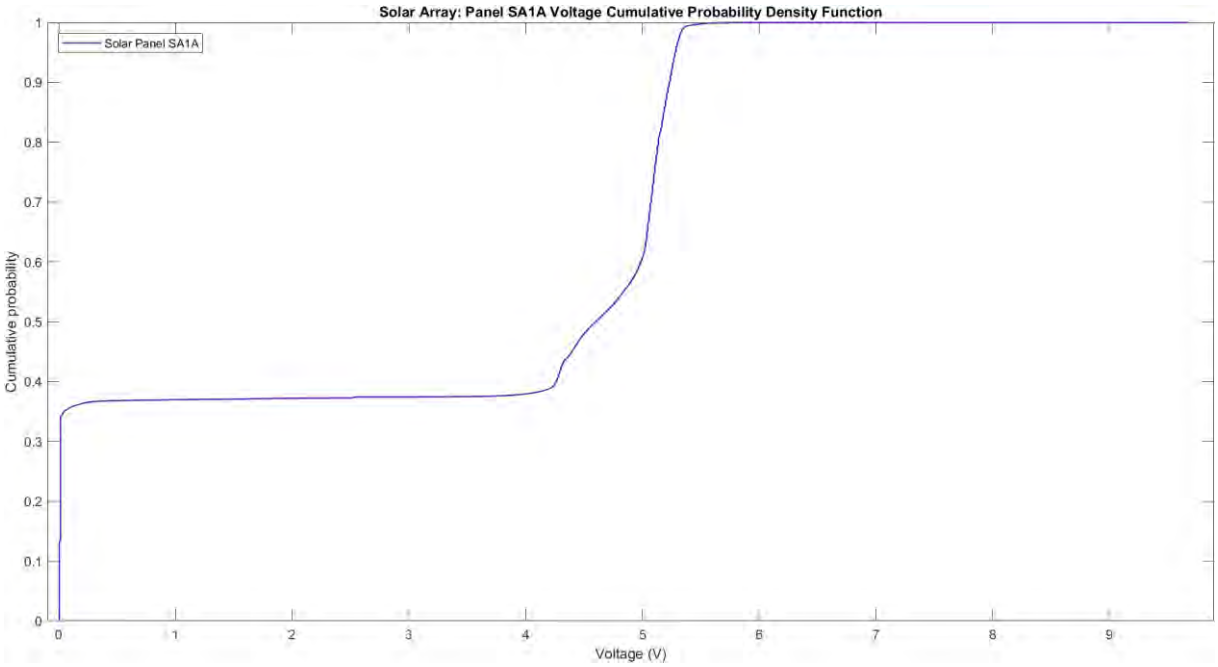

Figure B.20: Solar Array Panels SA1A and SA1B Voltage Cumulative Density Function

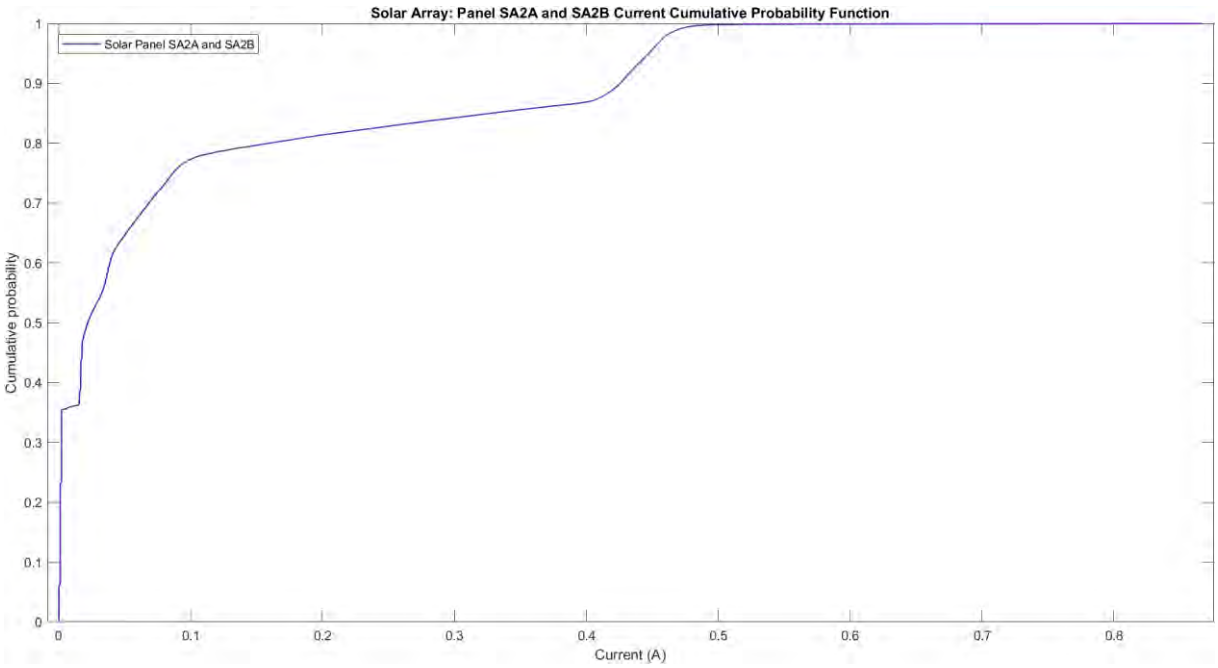

Figure B.21: Solar Array Panels SA2A and SA2B Current Cumulative Density Function

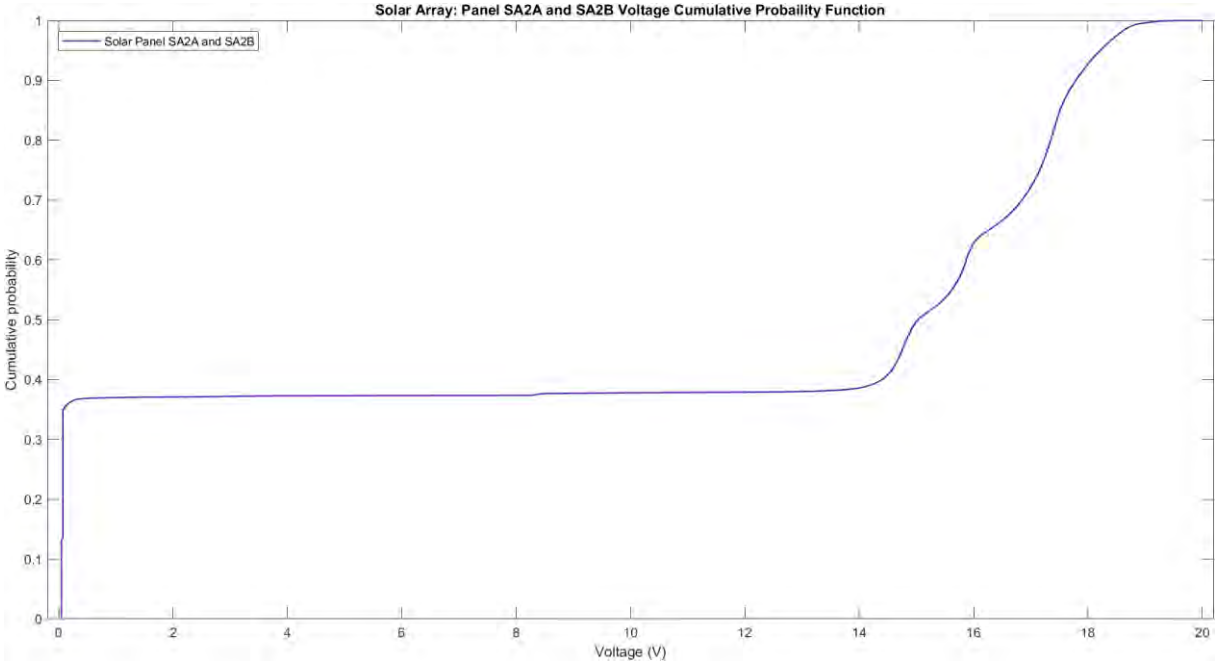

Figure B.22: Solar Array Panels SA2A and SA2B Voltage Cumulative Density Function

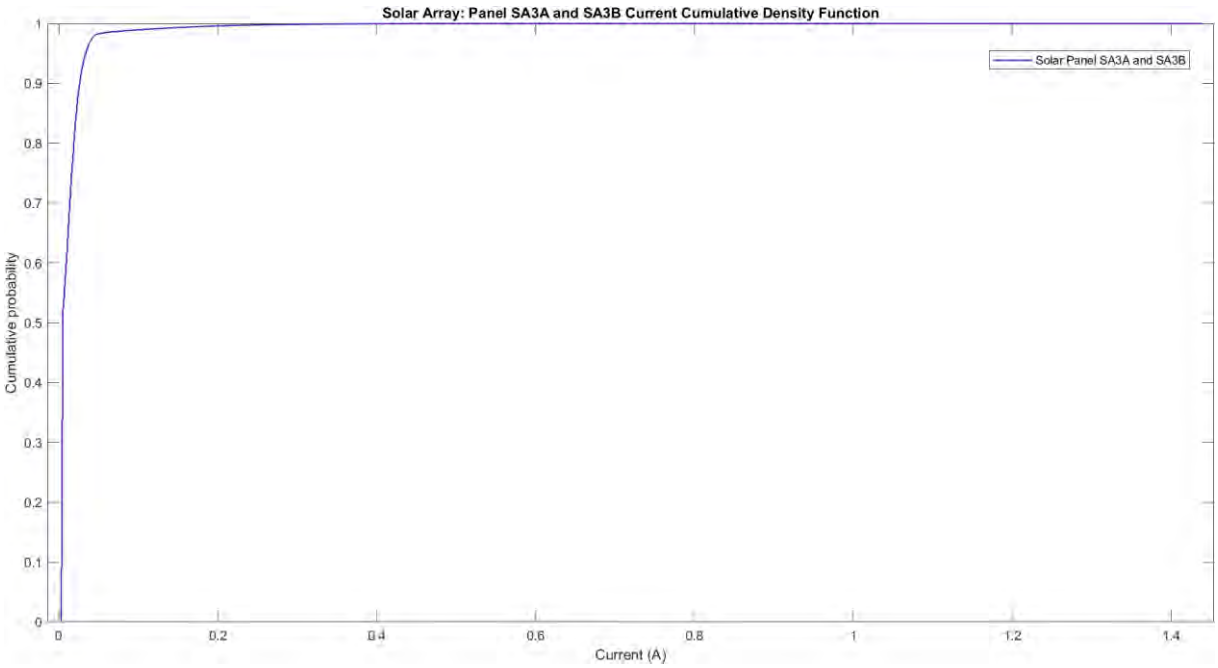

Figure B.23: Solar Array Panels SA3A and SA3B Current Cumulative Density Function

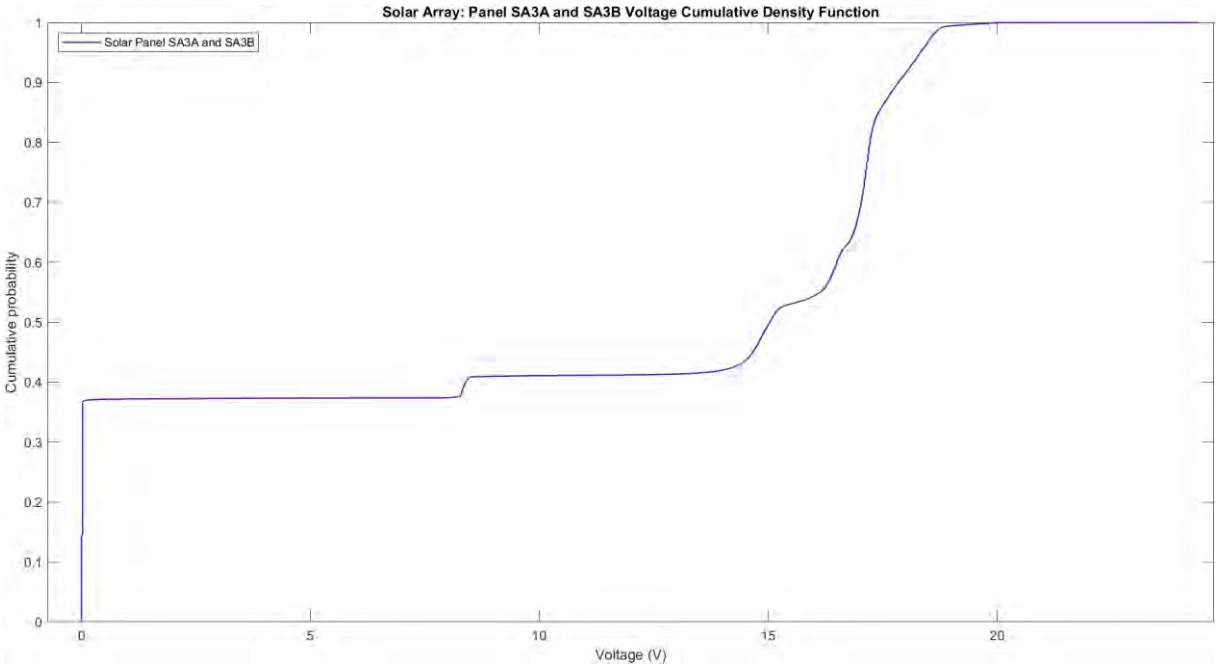

Figure B.24: Solar Array Panels SA3A and SA3B Voltage Cumulative Density Function

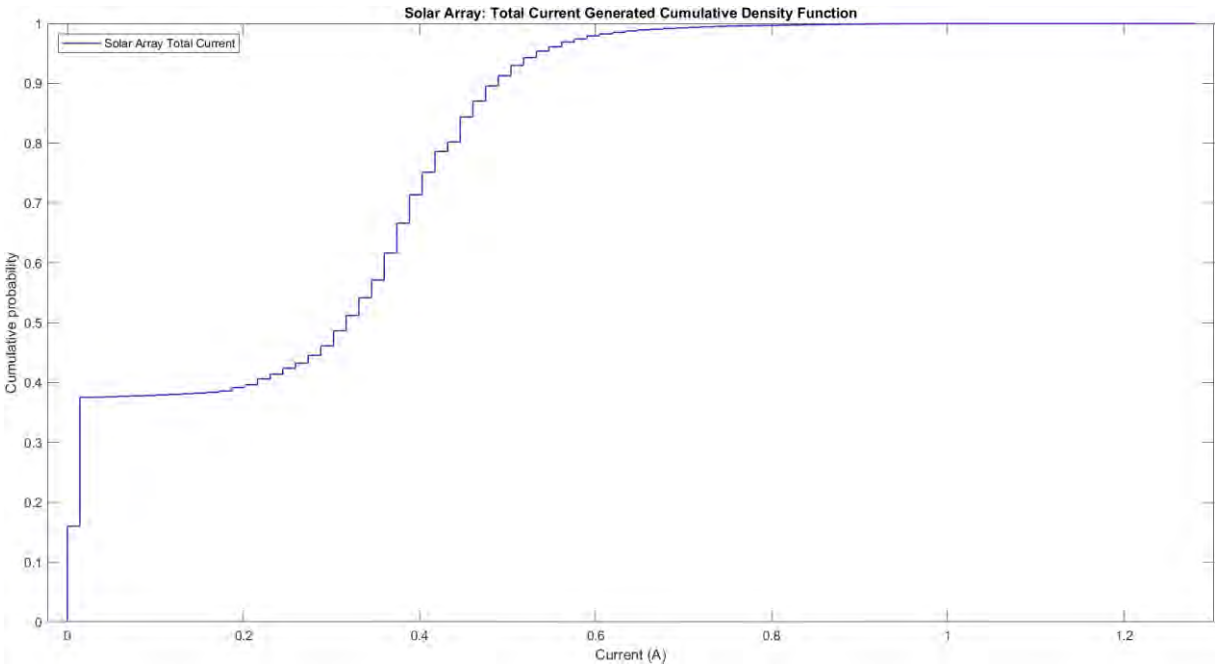

Figure B.25: Solar Array Total Current Generated Cumulative Density Function

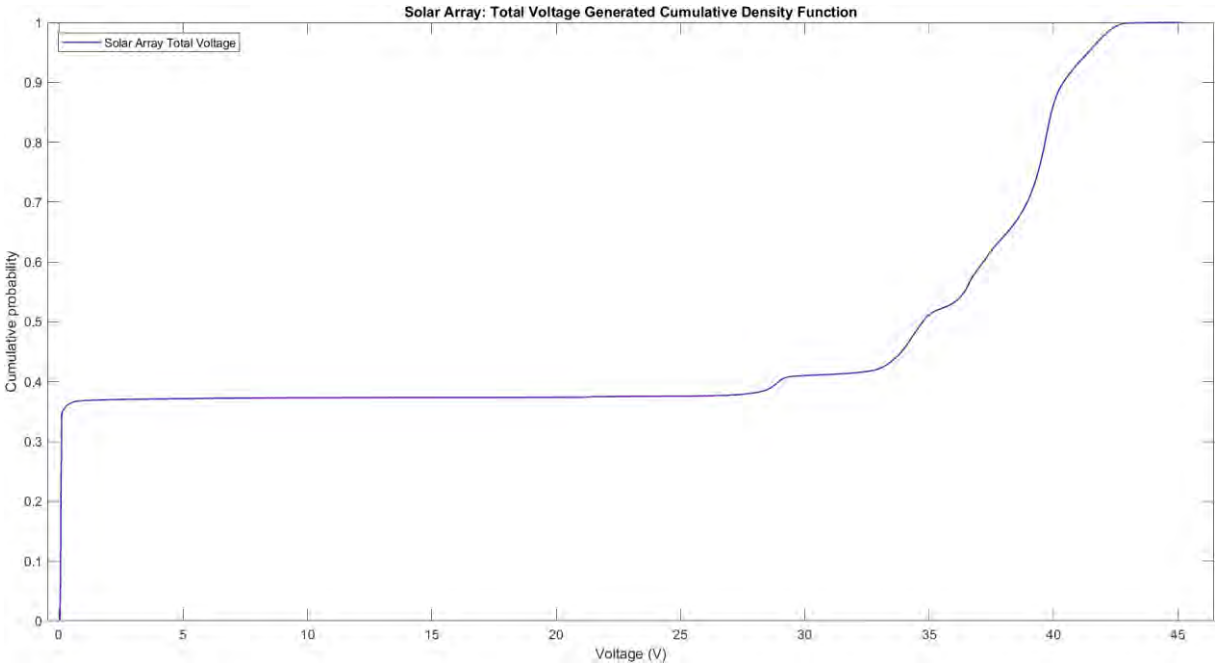

Figure B.26: Solar Array Total Voltage Generated Cumulative Density Function

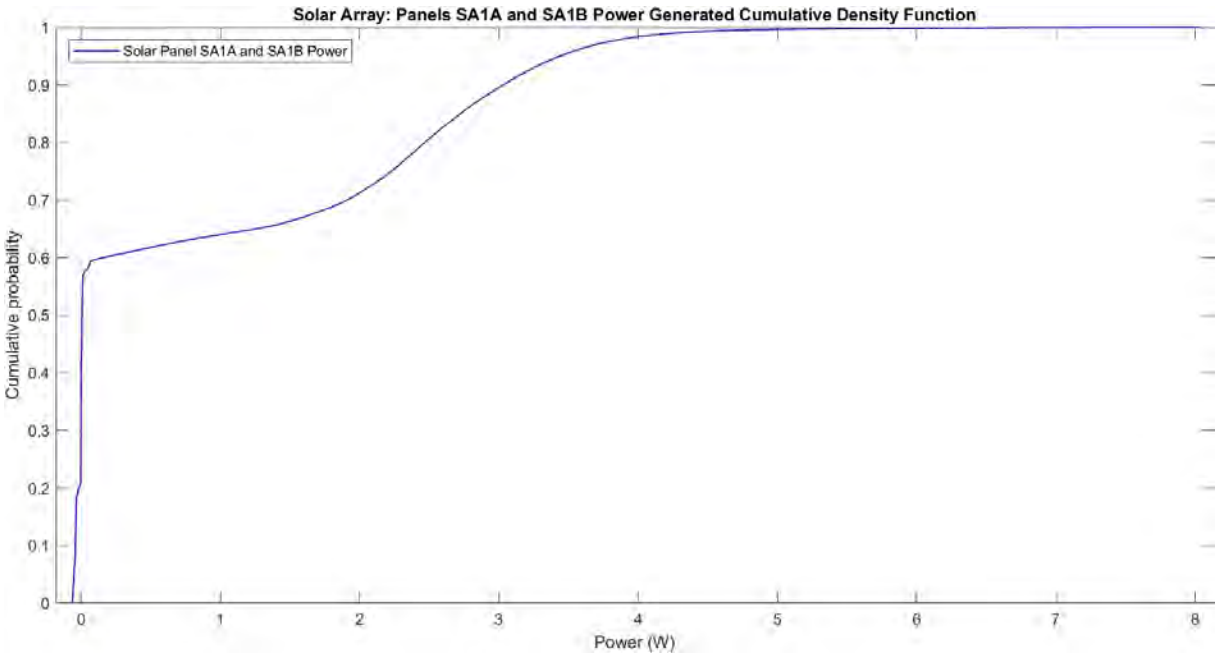

Figure B.27: Solar Array Panels SA1A and SA1B Power Generated Cumulative Density Function

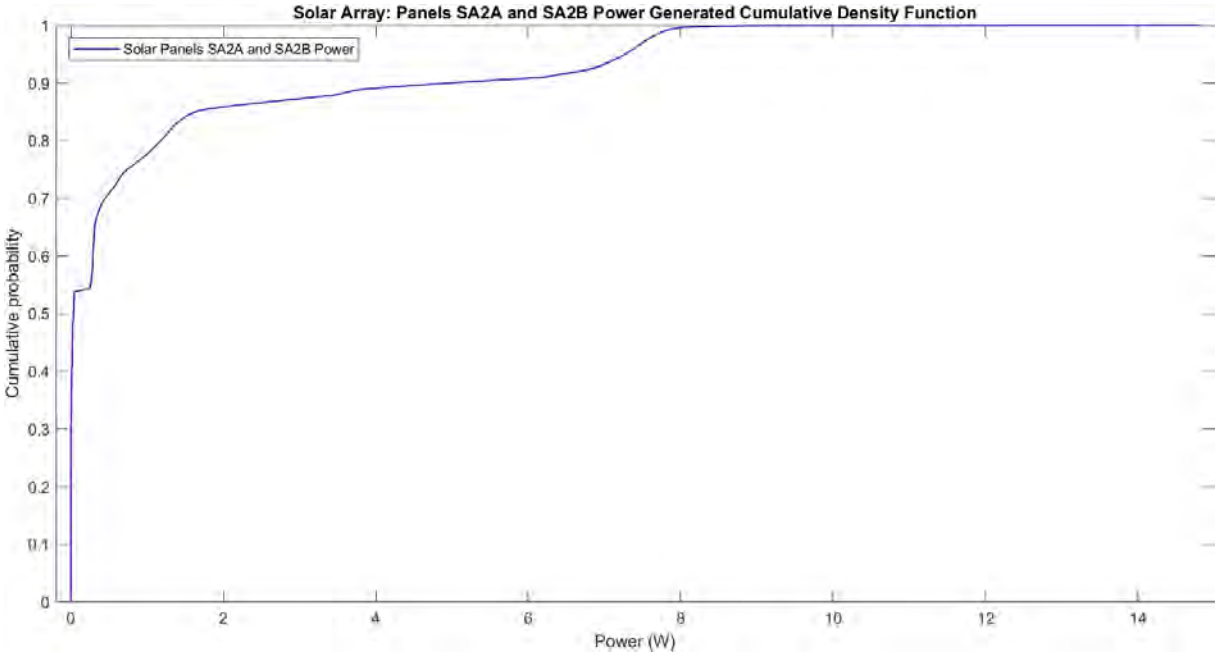

Figure B.28: Solar Array Panels SA2A and SA2B Power Generated Cumulative Density Function

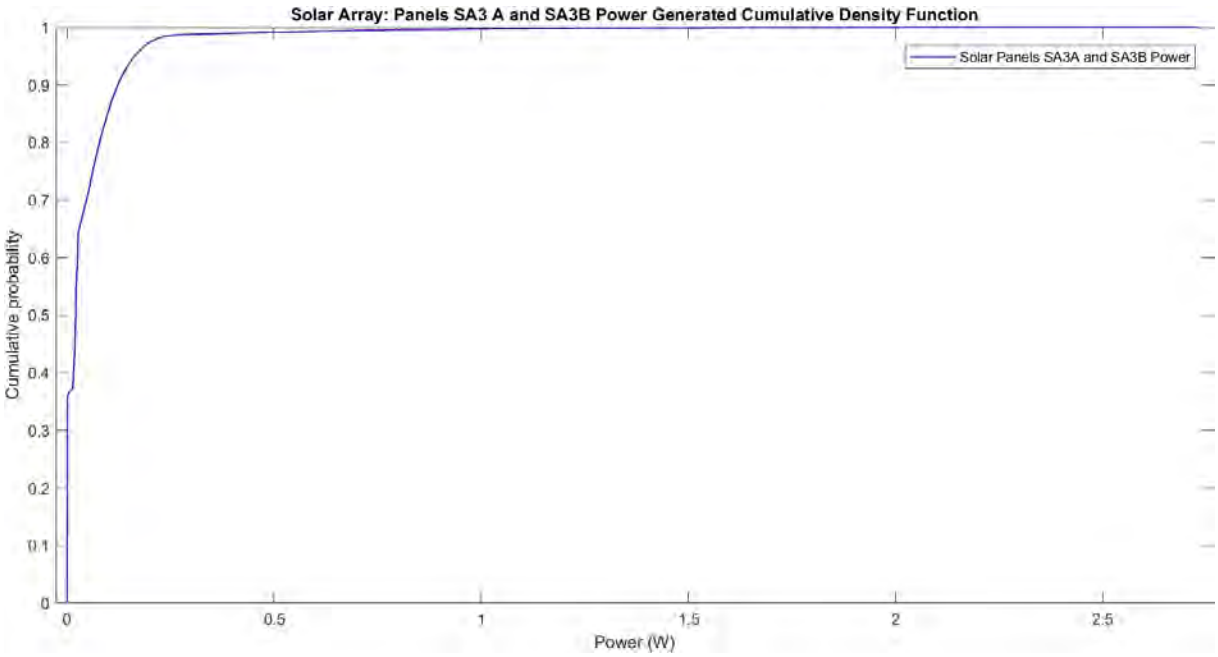

Figure B.29: Solar Array Panels SA3 A and SA3B Power Generated Cumulative Density Function

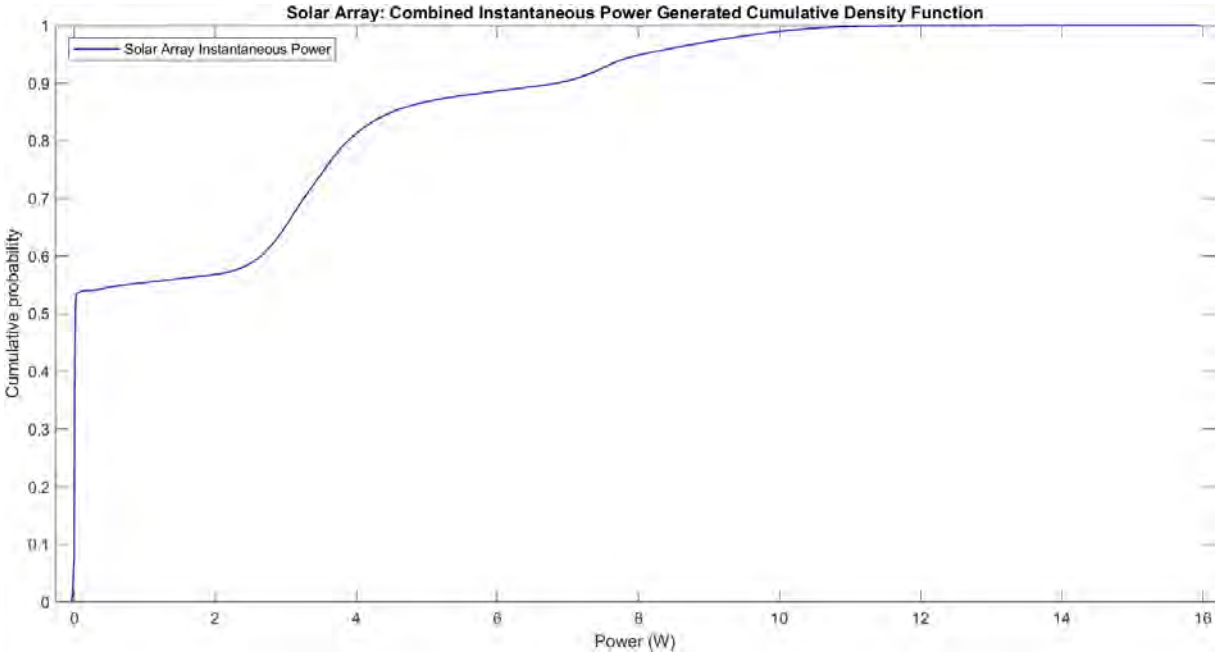

Figure B.30: Solar Array Combined Instantaneous Power Generated Cumulative Density Function

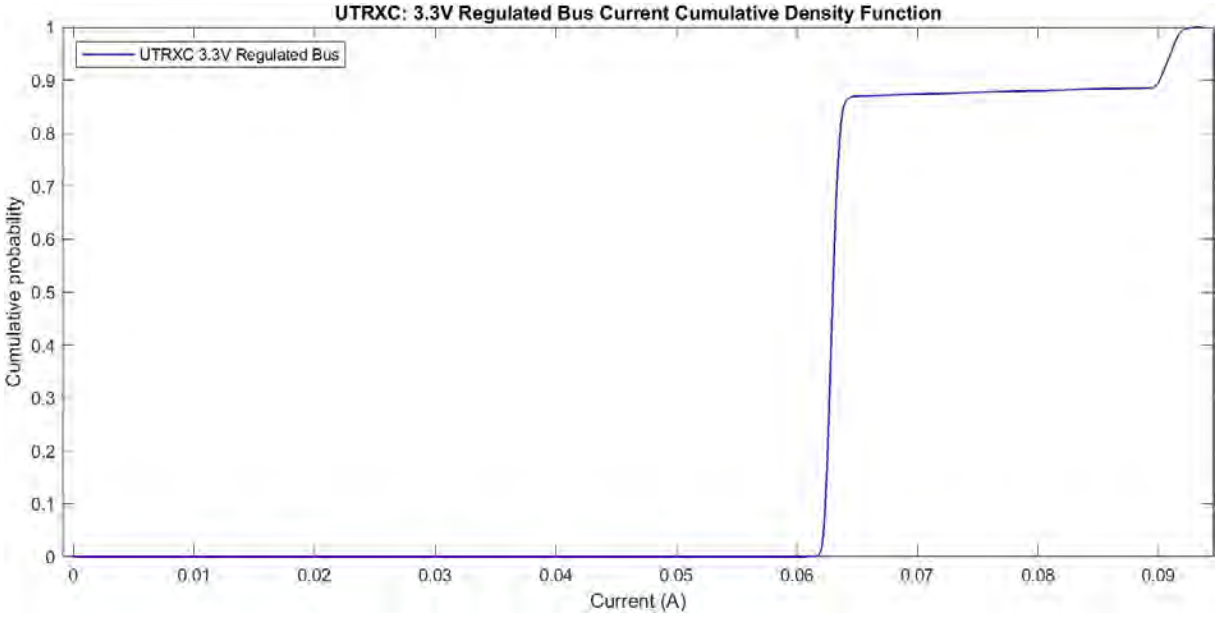

Figure B.31: UTRXC 3.3V Regulated Bus Current Cumulative Density Function

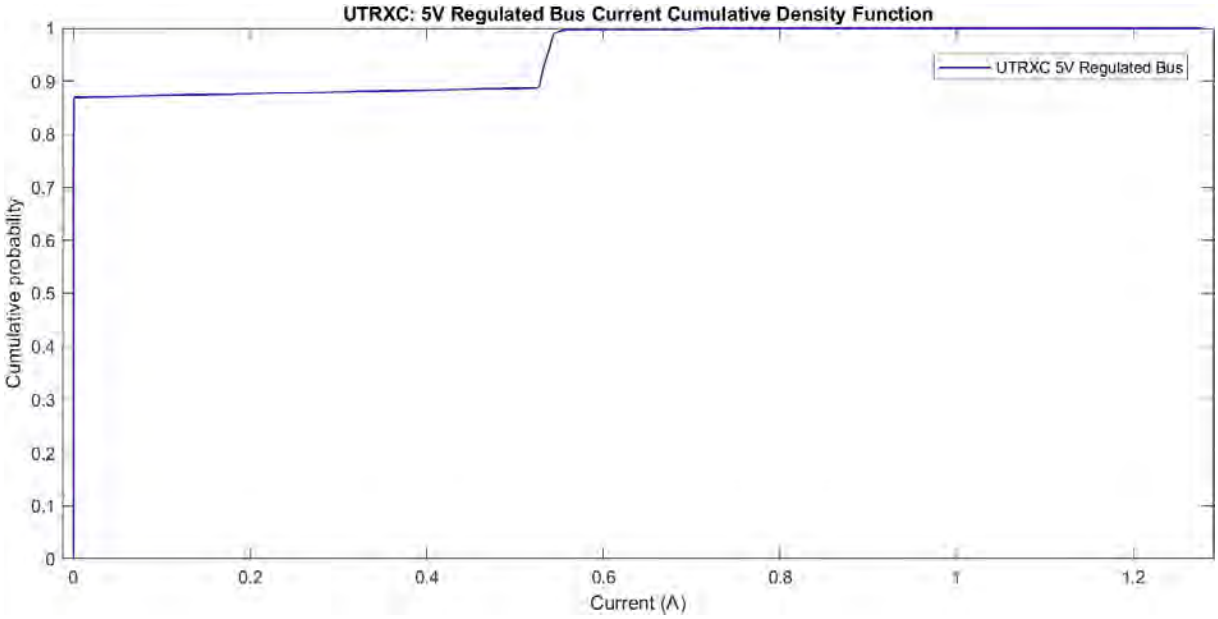

Figure B.32: UTRXC 5V Regulated Bus Current Cumulative Density Function

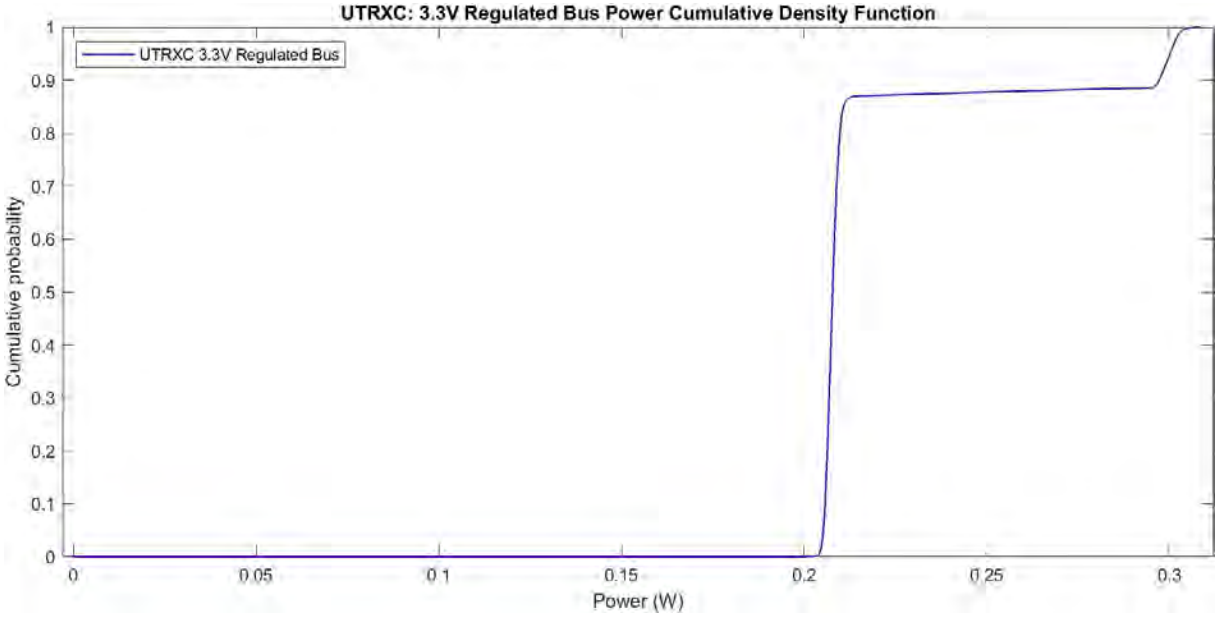

Figure B.33: UTRXC 3.3V Regulated Bus Power Cumulative Density Function

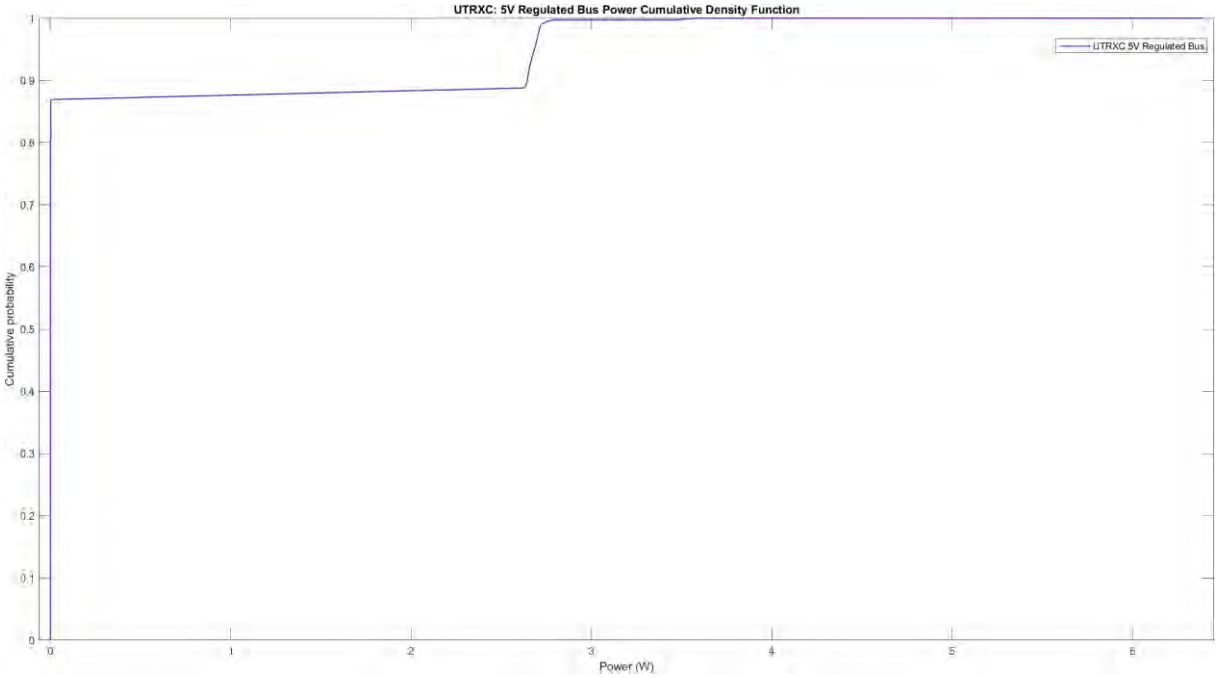

Figure B.34: UTRXC 5V Regulated Bus Power Cumulative Density Function

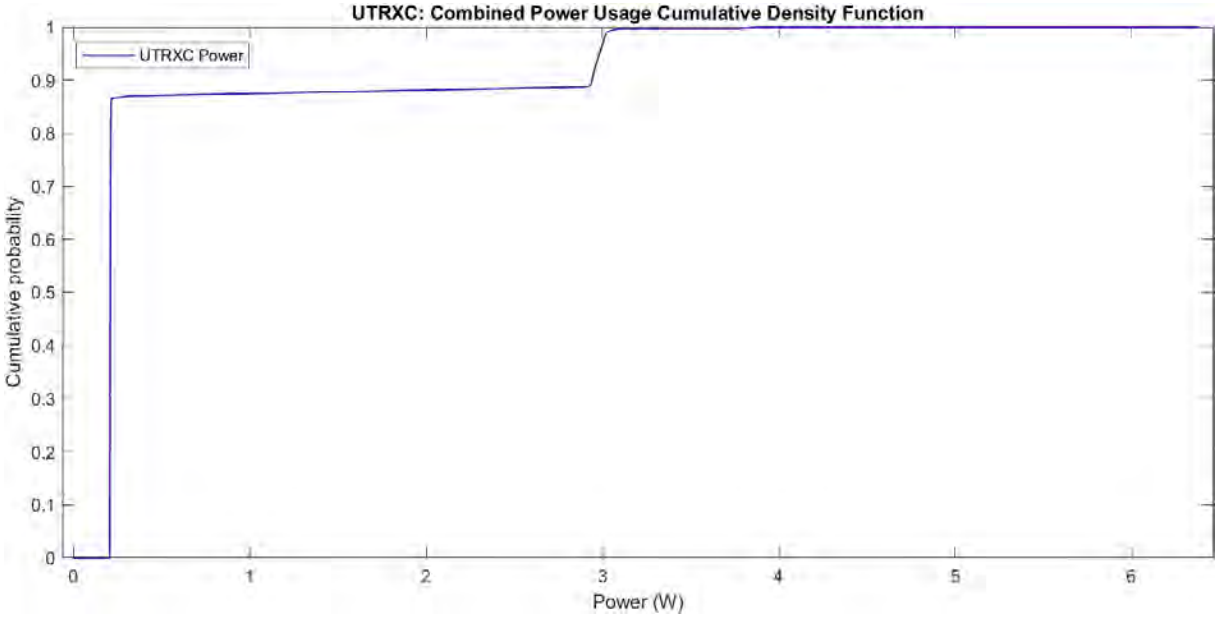

Figure B.35: UTRXC Combined Power Cumulative Density Function

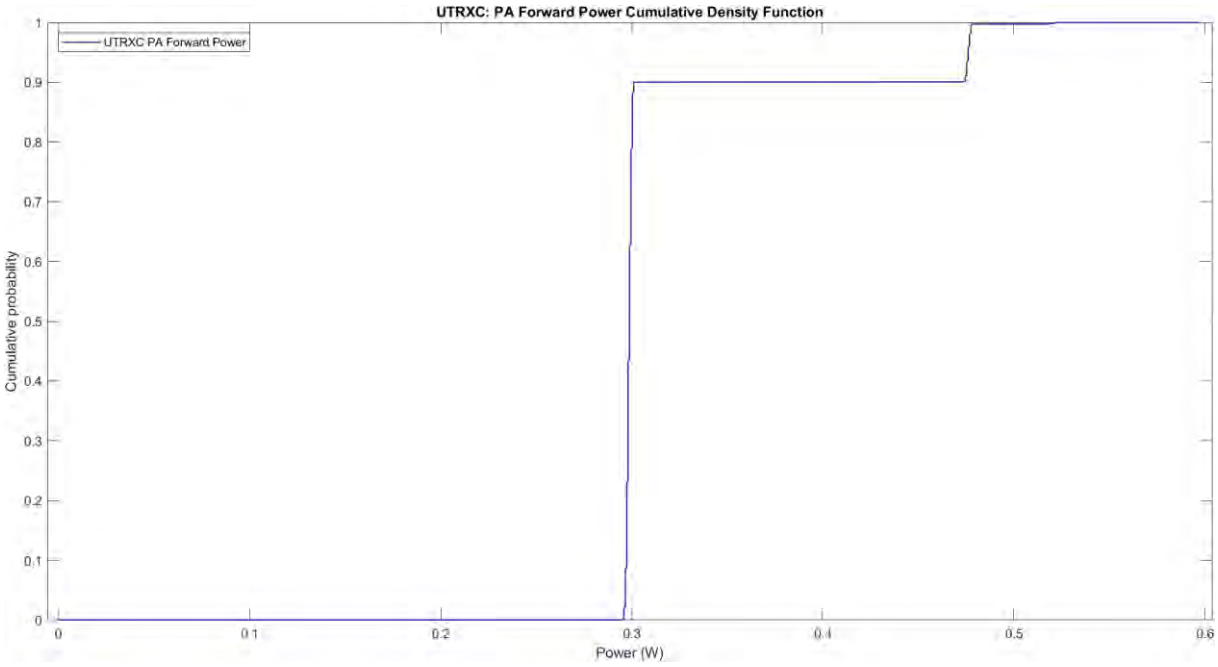

Figure B.36: UTRXC PA Forward Power Cumulative Density Function

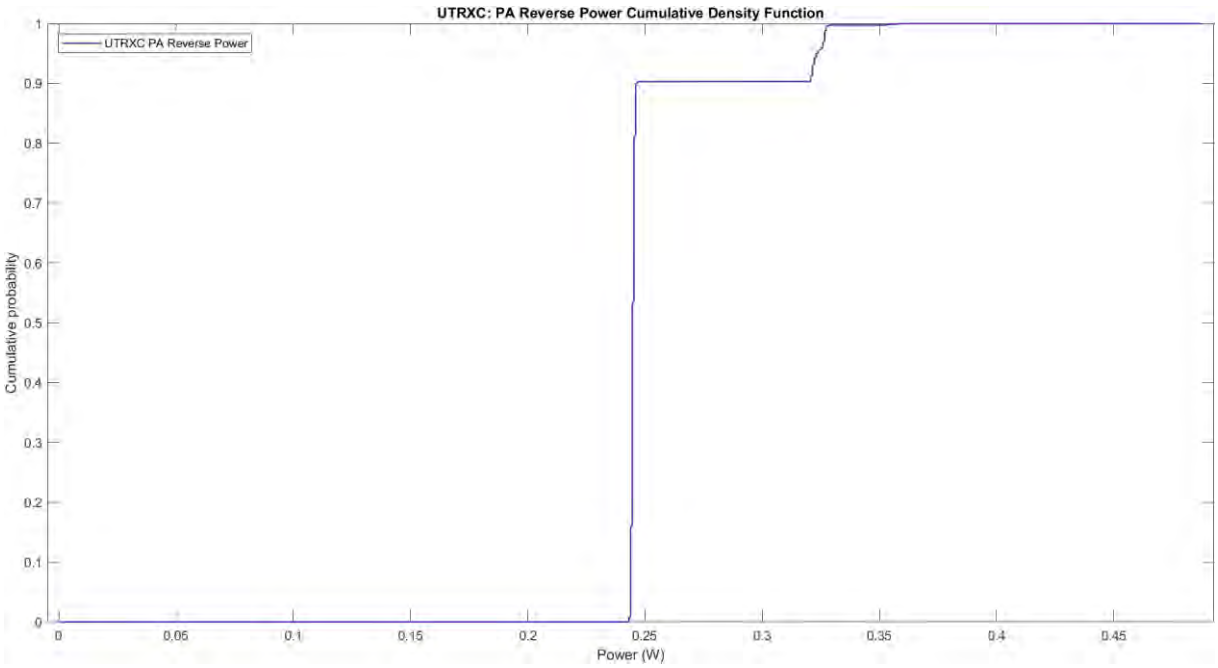

Figure B.37: UTRXC PA Reverse Power Cumulative Density Function

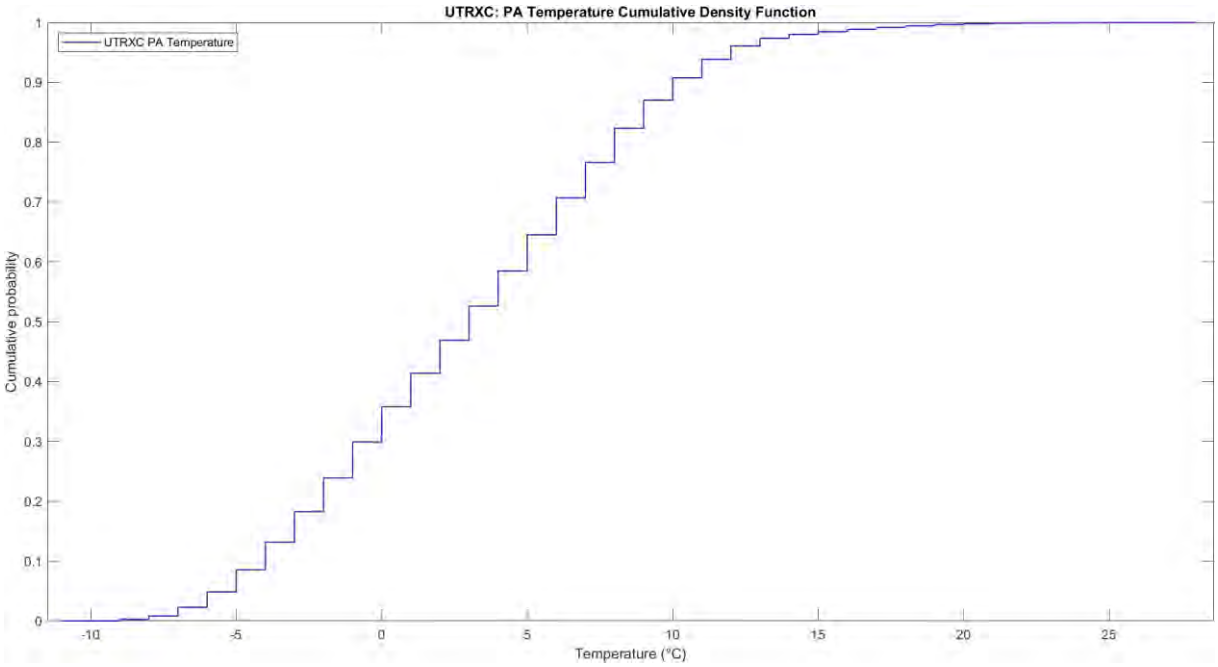

Figure B.38: UTRXC PA Temperature Cumulative Density Function

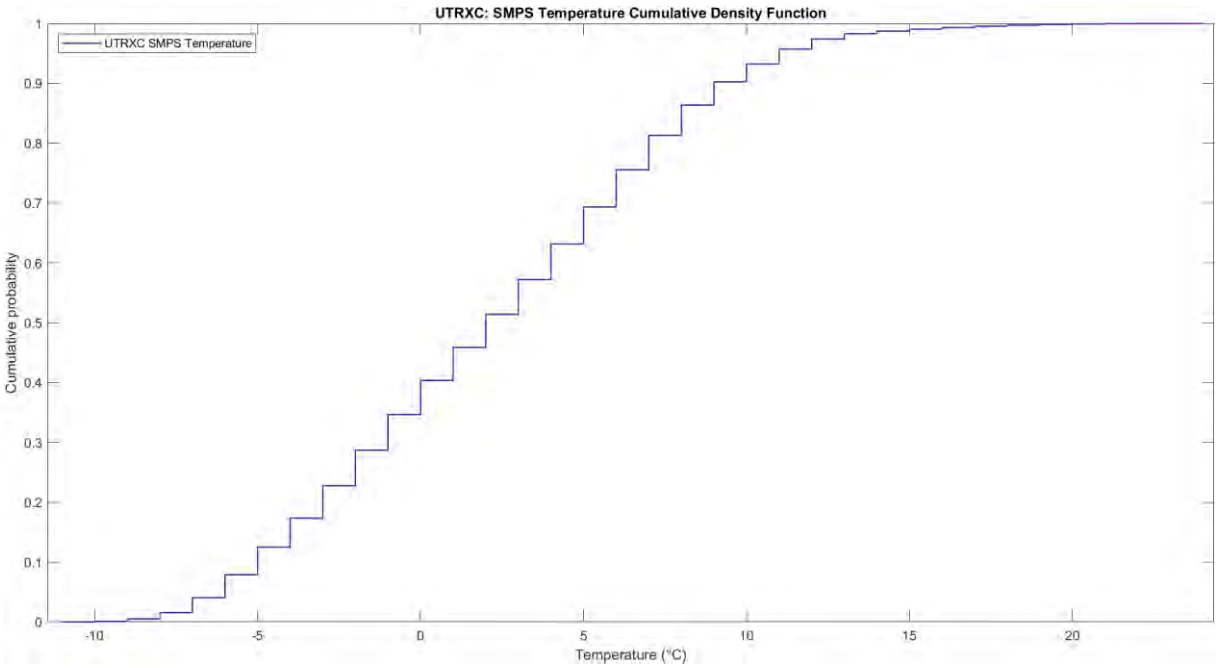

Figure B.39: UTRXC SMPS Temperature Cumulative Density Function